

Nagoya University
30th year of the Heisei period
Doctoral thesis

**Chemical Dealloying as optimized
by Combinatorial Method
for MEMS Application**

**Dept. of Micro-Nano Systems Eng.,
Graduate School of Eng.,**

Yusuke Yoshii

Contents

Chapter 1 Introduction.....	1
1.1 Background.....	1
1.1.1 Nanoporous materials	1
1.1.2 Nanoporous formation technique.....	6
1.1.3 Combinatorial materials synthesis	15
1.1.4 Chemical dealloying as optimized by combinatorial method	19
1.2 Purposes of this study	22
1.3 Structure of this thesis	25
Chapter 2 Chemical dealloying including high-temperature coarsening	28
2.1 Target	28
2.2 Fabrication of binary thin films via facing-target sputtering	28
2.2.1 New Facing Targets Sputtering (NFTS)	28
2.2.2 Principle of thin film deposition.....	32
2.3 Preliminary chemical dealloying test.....	33
2.4 Thermal coarsening technique	38
2.5 Nanoporous films fabricated via chemical dealloying including thermal coarsening	40
2.6 Summary	43
Chapter 3 Chemical dealloying including low-temperature coarsening.....	45
3.1 Target	45
3.2 Preliminary chemical dealloying test.....	46
3.3 Optimization of initial alloy compositions	49
3.3.1 Compositional gradients created by NFTS.....	49
3.3.2 Mechanism of compositional gradient	53
3.3.3 Fabrication of thin-film libraries for combinatorial search	55
3.4 Combinatorial search for nanoporous film.....	57
3.4.1 Optimization of initial alloy composition	57
3.4.2 Relationship between initial alloy composition and pore size	61
3.4.3 Relationship between initial alloy composition and porosity	63
3.5 Summary	66
Chapter 4 Chemical dealloying without thermal coarsening.....	68
4.1 Target	68
4.2 Preliminary chemical dealloying test.....	69
4.3 Fabrication of thin-film libraries for combinatorial search	71

4.4	Combinatorial search of nanoporous film	73
4.4.1	Optimization of initial alloy composition	73
4.4.2	Relationship between Cu–Cr film density and Cu etching rate	77
4.4.3	Influence of substrate type on final obtained nanostructure	84
4.5	Summary	92
Chapter 5	Nanoporous film for application in MEMS device	94
5.1	Target	94
5.2	MEMS sensor for monitoring moisture in oil	95
5.2.1	Motivations	95
5.2.2	Sensor design	97
5.3	Preliminary test	102
5.3.1	Fabrication process	102
5.3.2	First evaluation system	106
5.3.3	Experimental results and discussion	107
5.4	Sensors developed via the chemical dealloying including thermal coarsening.....	110
5.4.1	Conventional sensor model	110
5.4.2	Fabrication process	111
5.4.3	Experimental results and discussion	114
5.5	Sensors developed via the chemical dealloying without thermal coarsening	118
5.5.1	New sensor design.....	118
5.5.2	Fabrication process	119
5.5.3	Evaluation system in air	123
5.5.4	Experimental results and discussion	124
5.6	Final evaluation for sensors	134
5.6.1	Evaluation system in oil.....	134
5.6.2	Experimental results and discussion	136
5.6.3	Summary of sensor performances in air and oil.....	139
5.6.4	Future works	140
5.7	Summary	140
Chapter 6	Conclusions and future works	142
6.1	Conclusions.....	142
6.2	Future works	147
Appendix.....	149
Reference	152

Chapter 1 Introduction

1.1 Background

1.1.1 Nanoporous materials

Porous materials are known as three-dimensional (3D) interconnected morphologies with open pores, forming as a sponge-like structure. Materials including numerous >1 nm pores are defined as “porous materials”¹⁾. By contrast, materials containing below 1 nm pores are defined as “non-porous materials”, meaning a dense structure (Fig. 1.1). Moreover, the porous materials can be classified into two groups based on a pore size. In the range of 1–100 nm pores, the materials are specifically called as “nanoporous materials”, while that in the range of 100 nm to several micrometer pores are defined as “microporous materials”.

Porous materials are expected as many applications such as absorbent materials or catalysts due to their large specific surface area. By processing a pure Platinum (Pt) film into a nanoporous structure with below 10 nm pores, the nanoporous structure of Pt increases the true surface area by 170 times²⁾. This is because, nanoporous structures increase an apparent area three-dimensionally, increasing an effective surface area. Moreover, unlike dense structures, nanoporous structures consist of less amount of materials. Thus, it is also able to reduce a material utilization. Pt or palladium (Pd) have been earlier utilized as a hydrogen absorbing alloy, thereby hydrogen gas sensors including Pt or Pd are well known to date. Sensor performances highly depend on the electrochemical reactions involving adsorption, which include sensing of hydrogen by Pt or Pd. Therefore, the large catalytic action area generally promises an excellent sensor responsiveness. However, considering that the hydrogen absorbing alloys are comprised of precious Pt or Pd and the sensor device scale becomes larger, a less amount of Pt or Pd while keeping high catalytic performances is economic and desirable.

The feature of nanoporous Pt or Pd is very advantageous in this study. A. Abburi et.al³⁾ reported effective hydrogen gas sensors based on nanoporous Pt thin films as shown in Fig. 1.2(a). The sensors made with nanoporous Pt with <5 – 35 nm pores successfully demonstrated a significant change in resistance when exposed to hydrogen, whereas that with pure Pt thin film exhibited a poor sensitivity (Fig. 1.2(b)). These results could be achieved by that the hydrogen gas was easily trapped by nanoporous Pt owing to its high specific surface. Moreover, they succeeded in the reduction of Pt utilization.

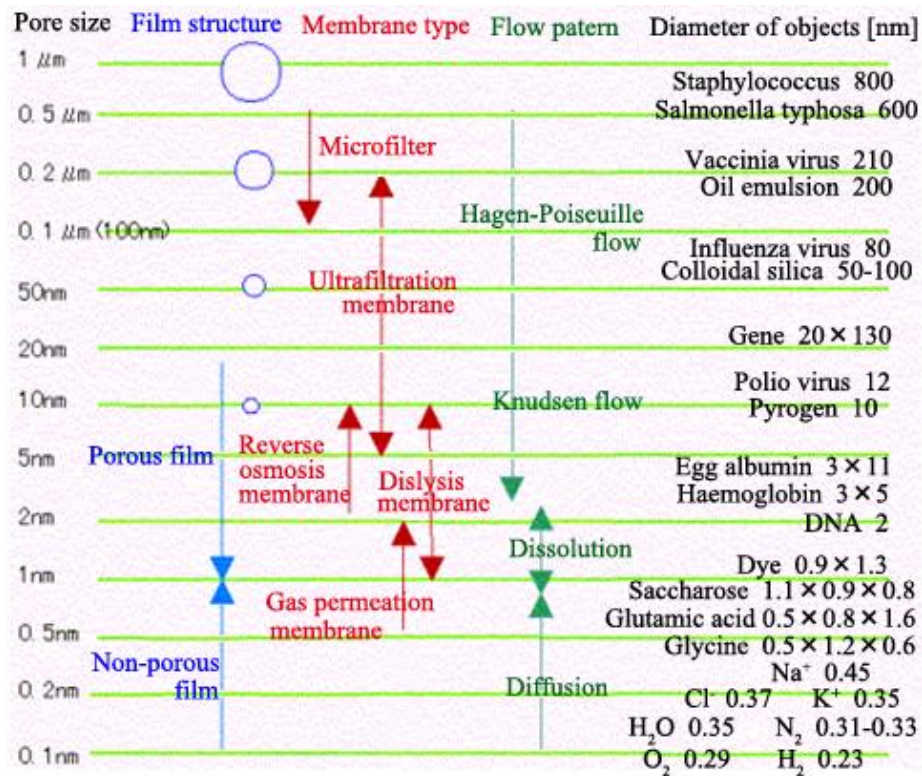


Fig.1.1 Classification of porous materials based on pore sizes (A. Ito¹⁾)
(Translated in English)

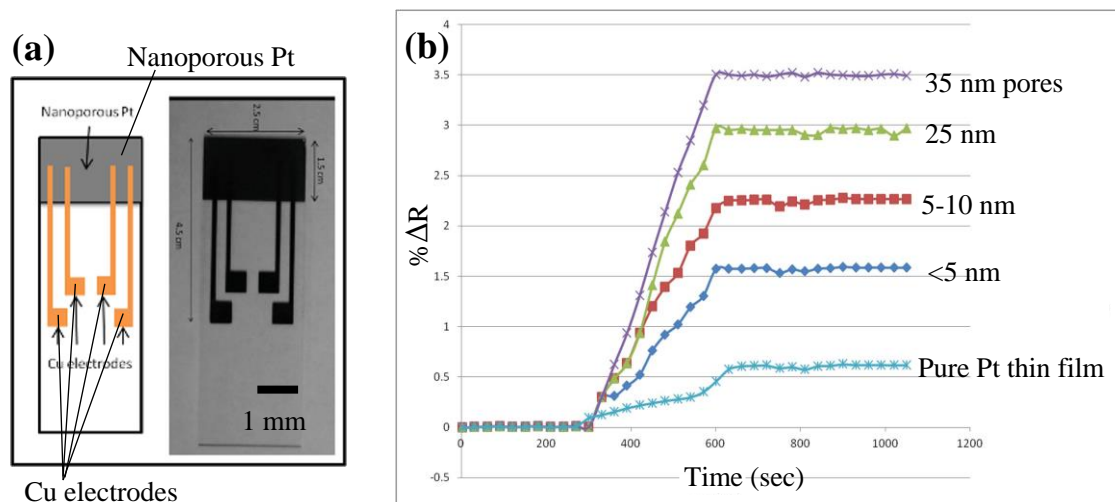


Fig. 1.2 Hydrogen gas sensor based on nanoporous Pt thin film; (a) sensor device, (b) sensor performances based on pore sizes (A. Abburi et.al³⁾)

For another report, W. C. Li et.al⁴⁾ revealed the relationship between stress change and hydrogen absorption/desorption of nanoporous Pd (pore size: approximately 10 nm). The nanoporous Pd film stress became increasingly compressive with higher hydrogen content in atmosphere. After flowing atmosphere with nitrogen, stress of nanoporous Pd film returned to approximately the initial value before exposure to hydrogen. The response times of dense Pd film and nanoporous Pd film to hydrogen were evaluated by exposing the Pd film to hydrogen between contents of 0 and 10 volume % (vol.%). Fig. 1.3(a) shows the image of nanoporous Pd used. As seen from Fig. 1.3(b) and (c), nanoporous Pd films exhibited a shorter response time for hydrogen absorption and desorption. This excellent response could be achieved based on the large specific surface area produced by nanoporous structures. This property promises an excellent hydrogen gas sensing. Consequently, they demonstrated that the catalytic performance improved significantly using nanoporous formation technique. In addition, this technology facilitates to fabricate small-scale devices with low consumption and material cost.

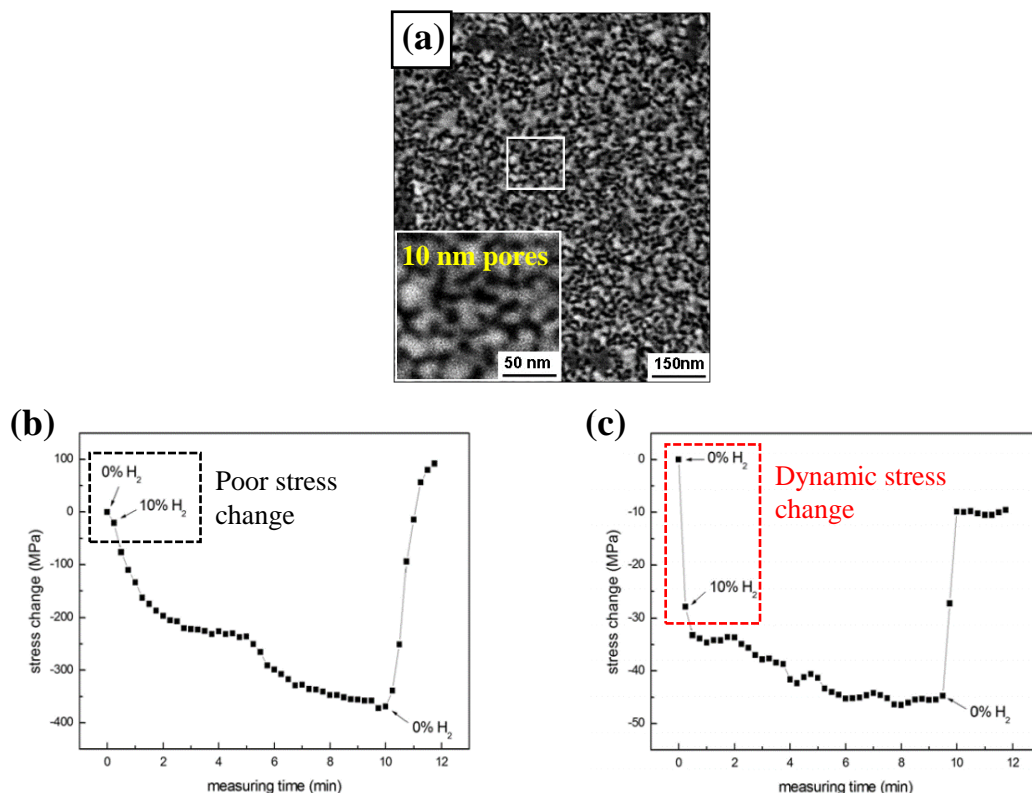


Fig. 1.3 Hydrogen absorption/desorption of nanoporous Pd thin films; (a) the obtained nanoporous Pd thin film, (b) responsiveness based on dense Pd thin film, (c) based on nanoporous Pd thin film (W. C. Li et.al⁴⁾)

Furthermore, nanoporous films have emerged to have significant importance in molecular filters. Membrane filtration is an attractive technology, and has been earlier developed for many applications used in bio-technology field, such as bacteria and viruses removal. S. T. Mostafavi et.al⁵⁾ reported nanofilters from carbon nanotubes for virus removal from water. The fabricated carbon nanotube bundles are about 45 nm in size (Fig. 1.4(a)), and these entangled carbon nanotubes bundles almost form the nanofilter with suitable porosity prepared by closely arranging the nanotubes (Fig. 1.4(b)). The velocity of water including initial virus concentration increased through nanofilter but mass transfer velocity of virus is low. Thus, the different mass transfer velocity causes that the virus concentration decreases. These results indicated that the fabricated nanofilters successfully could remove virus and nanoparticles from water at 20 °C.

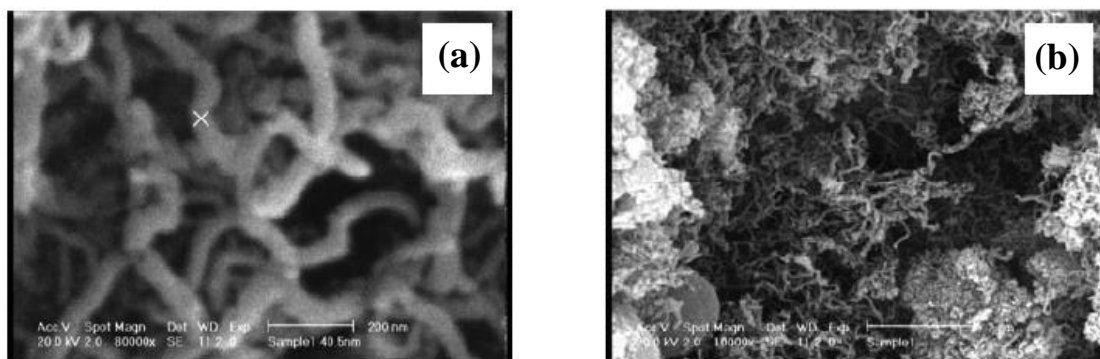


Fig. 1.4 Nanofilter from carbon nanotubes for application in virus removal from water, (a) carbon nanotubes bundle, (b) nanofilter formed by entangled carbon nanotubes bundles (S. T. Mostafavi et.al⁵⁾)

Moreover, innovative microfluidic chip using aluminum oxide membrane (Fig. 1.5(a)) was reported by F. Bunge et.al⁶⁾. In this study, anodized aluminum oxide (AAO) was the key process of the fabrication of molecular filters. The barrier layer was removed from the bottom side by dry-etching; the obtained mean pore diameter uniformly equals 32–44 nm (Fig. 1.5(b)). The mass-transport through the membrane was investigated by diffusion measurements with indigo carmine. The relative concentration of the indigo carmine was determined by assuming a linear correlation with the color. The measured concentration of indigo carmine that diffused from the top chamber 1 through the membrane to the bottom chamber 2 where it was flushed away, indicated that the concentration decreases exponentially; 95% of the indigo carmine was successfully removed within approximately 9 min.

Reflecting the rapid growth of the microelectromechanical systems (MEMS) field {e.g., bio- and medical MEMS⁷⁾, power MEMS devices⁸⁾ used in Internet of Things (IoT)}, nanoporous materials as well as nanoporous formation techniques have been paid attention. A wide variety of nanoporous formation techniques has been researched to date, revealing the differential final morphologies. As shown from the Fig. 1.4(b) and Fig. 1.5(c), the nanoporous structures that are ultimately obtained are different; while the obtained nanostructure in Fig. 1.4(b) has a complex and random porous network, that in Fig. 1.5(c) consists of uniform pores. The optimal nanoporous structures differ with each device concept. Therefore, suitable processing methods meeting the research goal should be used. In the next section, the author introduces nanoporous formation techniques previously reported, and additionally mentions advantages and disadvantages themselves.

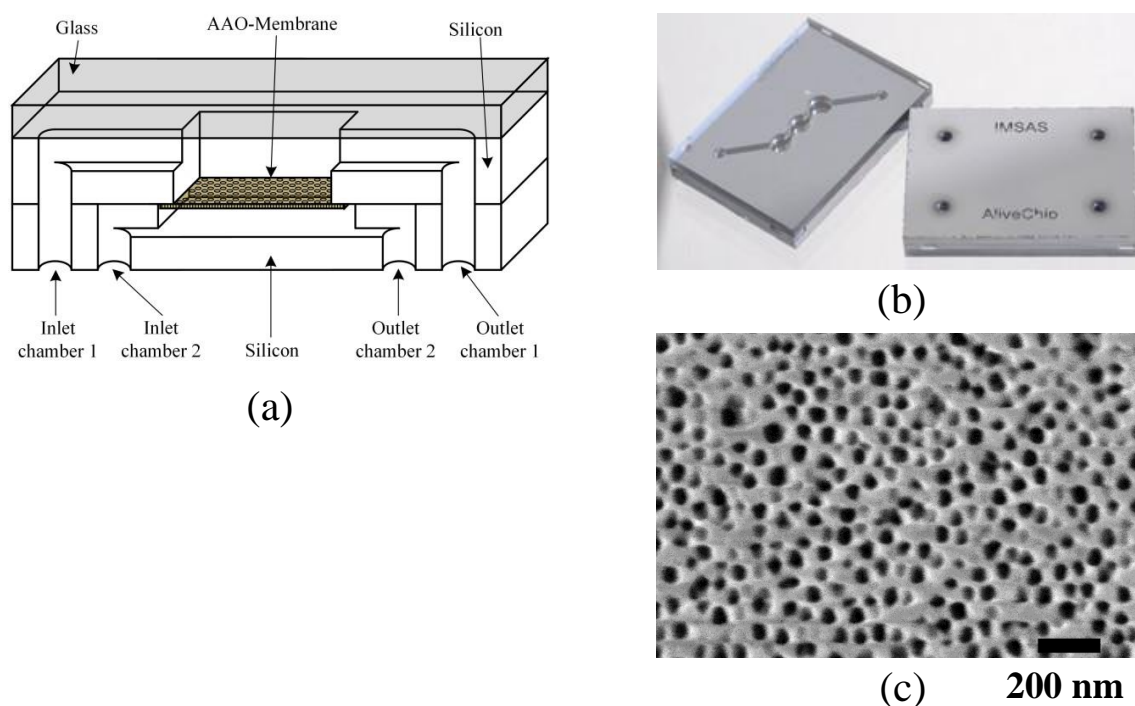


Fig. 1.5 Microfluidic chip; (a) concept of the device, (b) photo of the microfluidic chip with the dimensions of $6.5 \times 9.0 \times 1.3$ mm, (c) Top view of the AAO-Membrane (F. Bunge et.al⁶⁾)

1.1.2 Nanoporous formation technique

Nanoporous materials have been earlier developed based on hydrothermal growth⁹⁾⁻¹³⁾, AAO^{6),14)-17)}, carbon nanotubes^{5),18)-21)}, and chemical dealloying^{2)-4),22)-29)}. All processes promise structures with nanometer order pores, however their fabrication conditions (e.g., experimental setup, material, heat-treatment, etching liquid type, process time, or total cost) are different. Some fabrication methods require special conditions; thus, it is very important to select an optimal nanoporous formation technique fitting for a research goal. Below, the author introduces conventional nanoporous formation techniques, and reveals their advantages and disadvantages. Furthermore, the author develops a traditional nanoporous formation technique, and proposes a novel nanoporous formation technique that can be easily applicable to the micromachining with a short process time.

(1) Hydrothermal growth

The hydrothermal method allows to conduct a rapid crystal growth at relative low temperature (100–300 °C) and high pressures (over 1 atmosphere)⁹⁾. Water being under high temperature and high pressure exhibits differential properties comparing with that being at room temperature. In saturated steam pressure, water properties (e.g., density, viscosity, and dielectric constant) increase with increasing temperature. Moreover, ionic product of water becomes increasing with the increase of temperature, reaching maximum value at approximately 270 °C⁹⁾. Therefore, water at high temperature and high pressure promises an excellent ionic reaction, where ions and molecules are easily diffused, resulting in a rapid reaction velocity.

Recently, synthesizing ceramic powder is achieved by this hydrothermal growth. Synthesizing ceramic powder has been earlier developed by phase contact reaction, however it was time-consuming process, and required a high reaction temperature of 1000 °C⁹⁾. By contrast, thermal growth allows to create a target material under an extremely low- temperature due to the rapid reaction velocity produced by the high-temperature/pressure water. The crystal growth can be performed in an apparatus consisting of a steel pressure vessel called an autoclave. Starting materials and solutions or that working as reactants are prepared in the autoclave. Through the high temperature- and high pressure-treatment, starting materials are dissolved, and subsequently reacted with the solutions, which produces a new target crystal. Moreover, it is possible to control the crystal form by adjusting temperature, solution type or its concentration. Thus, hydrothermal

growth is also an important fabrication method for nanomaterials.

Nanowires or nanorods have been developed based on this technology. A. Syed et.al¹⁰⁾ reported hydrothermal growth of vertically-aligned zinc oxide nanowires on patterned seed layers. Fig. 1.8(a) shows a schematic diagram for growing ZnO nanowires on a defined Zn pattern. After patterning the silicon substrates with photoresist, Zn has been prepared. Hydrothermal growth has been performed at 90 °C for 17 h with a precursor solution formed of hexamethylenetetramine and zinc nitrate hexahydrate. After removing the photoresist, vertical nanowires were prepared on Zn micropatterns. From Fig. 1.8(b), vertically-aligned ZnO nanowires are seen on patterned zinc layer.

For another case, J. Wang et.al¹¹⁾ reported nanorods formed on fluorine-doped tin oxide (FTO) via hydrothermal synthesis. Fig. 1.9 shows a formation process of TiO₂ nanorods on FTO. A compounded solution and pre-treated FTO substrates with TiO₂ seed layer were placed in an autoclave, and then a hydrothermal reaction was conducted at 160–220 °C for 3–24 h. Fig. 1.10 reveal that the entire surface of FTO was covered uniformly with TiO₂ nanorod. The TiO₂ nanorods grew along the specific direction with the growth axis parallel to the substrate surface normal. The cross-sectional view reveals that bottom layer is the residual seed, and top layer is the nanorods allays, covering the seed layer uniformly.

As described above, hydrothermal growth is an attractive technique. With this method it is possible to grow crystals of compounds with high melting points at lower temperatures. The method is also particularly suitable for the growth of large good-quality crystals while maintaining control over their composition. However, there are some disadvantages; the need of expensive autoclaves and this method must include a heat-treatment with several hours. Processing that can be achieved with or without a heat-treatment in a short process time, may be desirable for all MEMS devices.

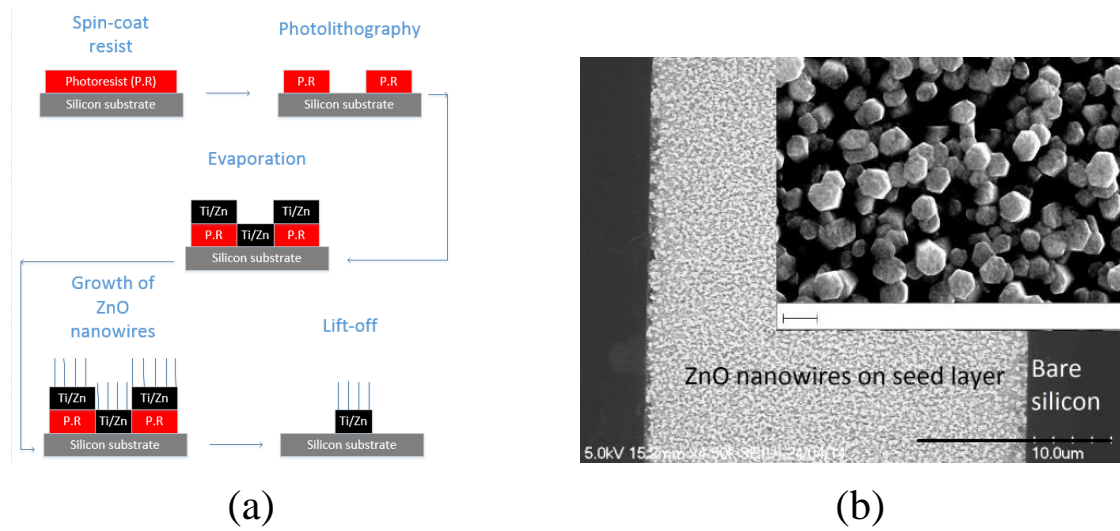


Fig. 1.8 (a) Schematic sequence of ZnO nanowires on a patterned Zn layer, (b) vertically-aligned ZnO nanowires formed on patterned Zn layer (A. Syed et.al¹⁰)

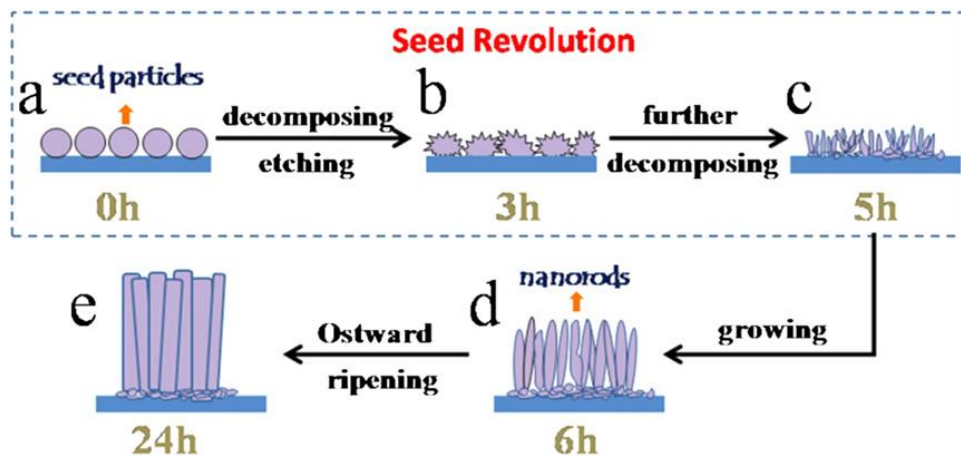


Fig. 1.9 Schematic sequence of TiO₂ nanorods (J. Wang et.al¹¹)

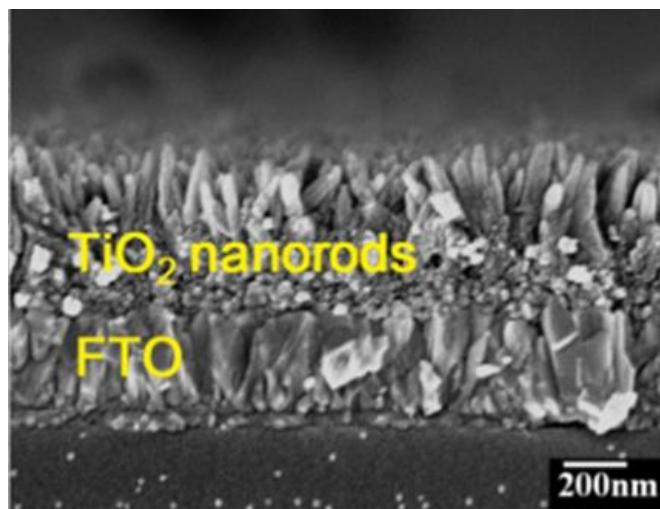


Fig. 1.10 Cross-section view of TiO_2 nanorod arrays grown on FTO substrate (J. Wang et.al¹¹)

(2) Anodized aluminum oxide

AAO is a self-organized material with honeycomb-like porous nanostructure, consisting porous layer growing top of a thin dense layer, called barrier layer¹⁴ (Fig. 1.11). The barrier layer has a non-porous structure. Fig. 1.12 shows the experiment setup for AAO. Normally, sulfuric acid, oxalic acid, phosphoric acid, or chromic acid are used for electrolytic solutions. First, DC voltage is applied between Aluminum (Al) substrates and cathodes in the sulfuric acid. Second, Al is easy to bond with O_2^- or OH^- by electrolysis. Subsequently an oxide film is formed on the Al substrate surface, finally becoming the barrier layer. The surface of the barrier layer is a non-uniform structure with a roughness. Sulfate ions are trapped by concavities¹⁵, thus the oxide films on concavities dissolve by becoming an aluminum sulfate, which open pores (Fig. 1.13(a)). In the final, highly ordered array of cylindrical shaped pores like Fig. 1.13(b) can be obtained through the growing of the oxide films, whereas that on concavities are dissolving.

AAO has been utilized in many products for almost a century, and nanoporous AAO is one of the most popular nanomaterials and applications including molecular separation⁶, catalysis³¹, sensors^{32,33}, drug delivery³⁴. The obtained porous nanostructure is electrically insulating, optically transparent, excellent chemically stable. Moreover, this process has a well control of pore sizes that can be achieved by optimization of applied voltage, acid type and its concentration^{16,17}.

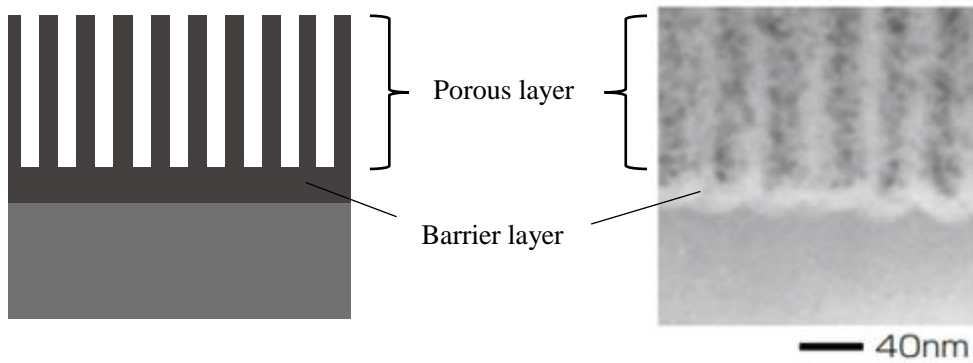


Fig. 1.11 Structure of anodized aluminum oxide (S. Ono et.al¹⁴)

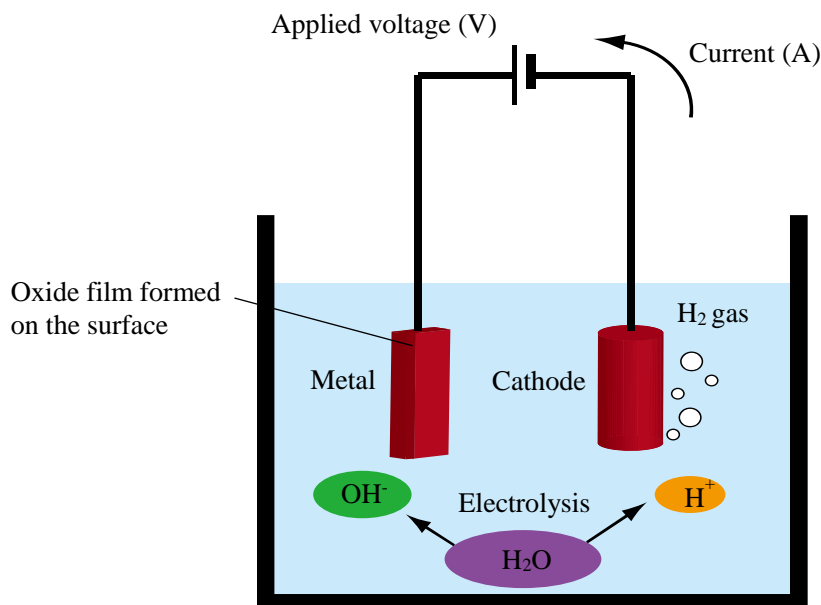


Fig. 1.12 Experimental setup for AAO

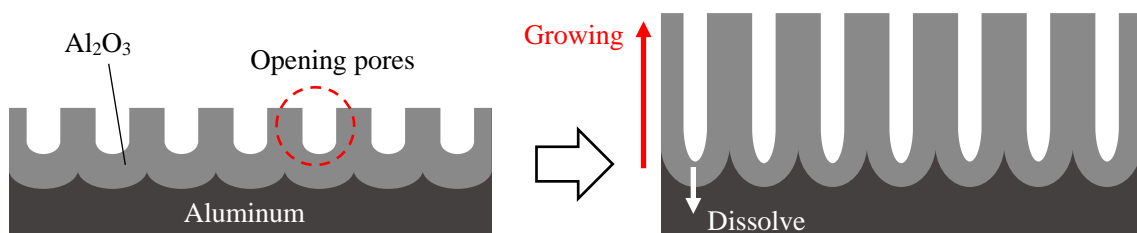


Fig. 1.13 Schematic sequence showing pore growth by anodic oxidation

In the use of nanoporous AAO for nanofilters, dense barrier layers however must be removed, because which may hamper the molecular separation. Microfluidic chip shown in Fig. 1.5 reported by F. Bunge et.al⁶⁾ could be achieved by removing barrier layers by DRIE-etching. Fig. 1.14 shows the fabrication process of the microfluidic chip. In the process (c), the silicon substrate including the barrier layer was fully DRIE-etched from the bottom side. The obtained nanoporous membranes after the process are shown in Fig. 1.15: (a) Left image exhibited a top view (i.e. the anodized side), and (b) right one shows a bottom view (i.e. DRIE-etched side) of the AAO membrane. The porosity of the membrane is about 22% on both sides, indicating that the barrier layer was successfully removed by DRIE-etching.

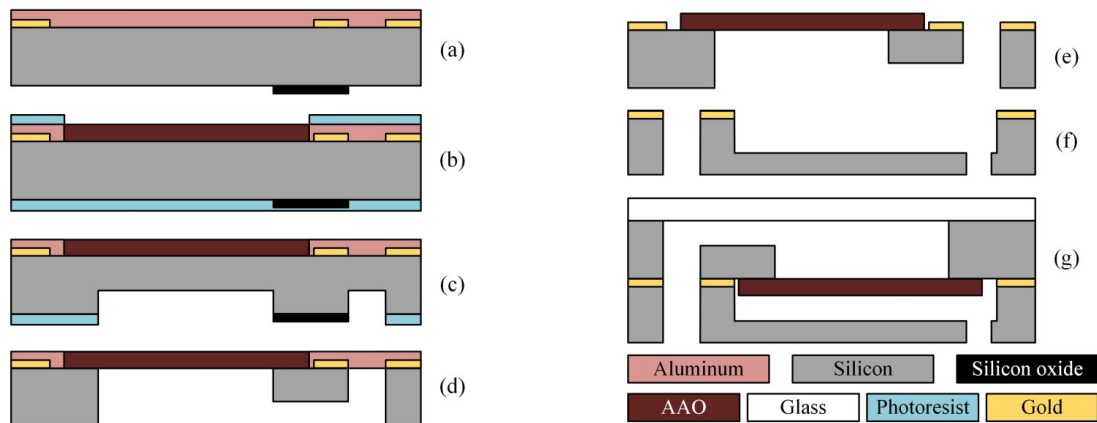


Fig. 1.14 Fabrication of the microfluidic chip: (a) silicon wafer with gold, silicon oxide and 2 μm of aluminum, (b) anodization in oxalic acid at 30 V, (c) DRIE-etching, (d) removal of the silicon oxide and DRIE-etching of silicon, (e) removal of aluminum and opening of the pores, (f) 2nd silicon wafer with gold and DRIE structures, (g) eutectic bonding of the silicon wafer and anodic bonding with glass wafer (F. Bunge et.al⁶⁾)

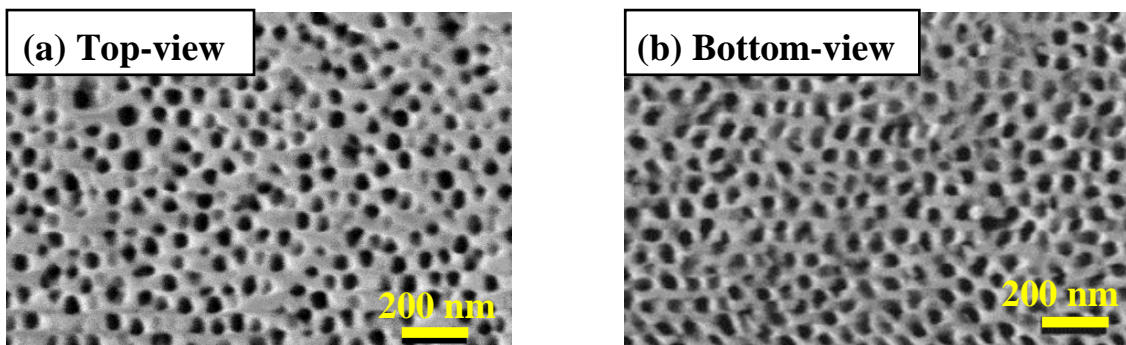


Fig. 1.15 The obtained AAO membrane: (a) top-, and (b) bottom-view (F. Bunge et.al⁶⁾)

(3) Carbon nanotubes

Carbon nanotubes have been played a role in advances in nanomaterials. Nanofilters based on carbon nanotubes⁵⁾ shown in Fig. 1.4 are fabricated by a continuous spray pyrolysis method (Fig. 1.16). This apparatus consisted of stainless steel gas and liquid flow lines, a vessel containing a catalyst and a carbon source and a two-stage heating system. Spray pyrolysis is a process in which a thin film is deposited by spraying a feed-solution on a heated surface, where the constituents react to form a chemical compound. This method is conducted in three steps as follows: (a) providing a carbon source gas and a catalyst gas thorough a nozzle onto a heater surface at 900 °C, (b) forming a carbon nanotube filter through a evaporation of a solvent and a materials synthesis, and (c) removing the carbon nanotube filter from the surface. To gain high-purity carbon nanotube filters with optimal density, three important parameters (catalyst concentration, temperature, and gas flow rate) must be carefully determined.

Furthermore, a great advantage of this method is that carbon nanotubes bundles are produced in only one step, without any prior substrate preparation¹⁸⁾. This method can produce a promising nanofilter in a short fabrication step. At the same time, however, it remains negative points: the available material is restricted to carbon, and it requires a 900 °C heat-treatment, which also limits future applications. Moreover, this method requires a special experimental setup, and seems to be over-skills.

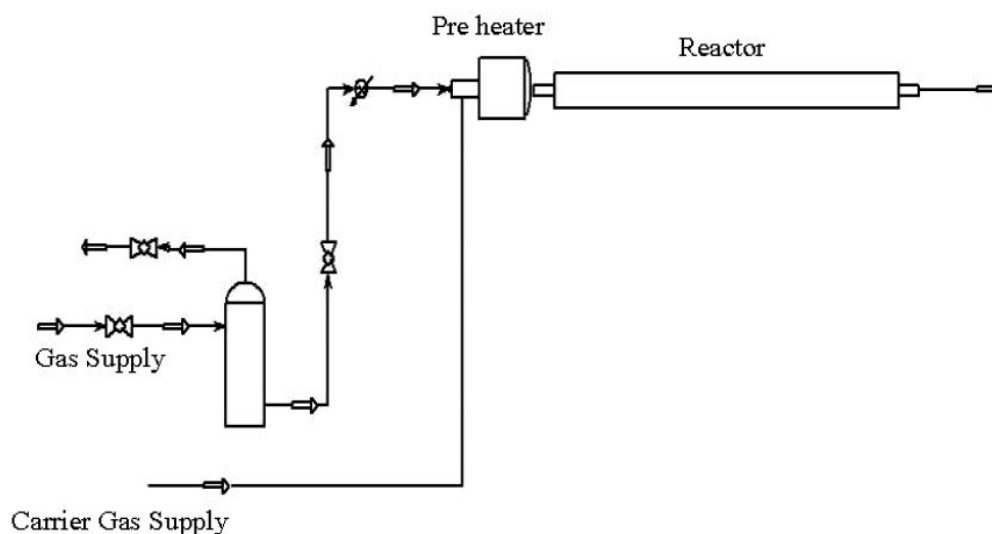


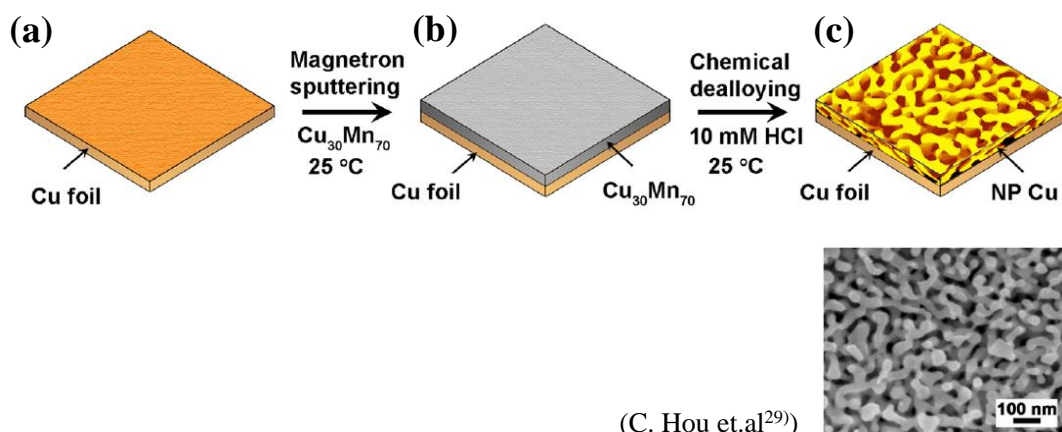
Fig. 1.16 Spray pyrolysis system (S. T. Mostafavi et.al⁵⁾)

(4) Chemical dealloying

Chemical dealloying^(2)-4),22)-29) is a simple process in which an element is selectively dissolved from an alloy, and a residual element forms a nanoporous structure by diffusion and self-organization. This selective dissolution process is known as a reliable process for obtaining porous structures from an alloy containing two or more metallic elements. Various chemical dealloying processes to produce nanoporous materials have been earlier researched by several groups.

Chemical dealloying of Cu–Mn alloy reported by C. Hou et.al²⁹⁾ (Fig. 1.17) consisted of two steps; (a) $\text{Cu}_{30}\text{Mn}_{70}$ film deposition on the Cu foil by magnetron sputtering, subsequently (b) selective dissolution of Mn elements from a binary $\text{Cu}_{30}\text{Mn}_{70}$ alloy by immersion the film in 10 mM HCl solution for 5 h at room temperature (25 °C). During Mn etching, the remained Cu was diffused, forming a 3D-interconnected nanoporous network. Finally, the initial binary Cu–Mn alloy fully turned to a Cu-based sponge-like structure with a pore size of ~50 nm (Fig. 1.17(c)).

Chemical dealloying is an excellent nanoporous formation technique because of easy pore- and patterning-control. Pore controlling can be simply conducted by adjusting the process parameters: the initial alloy composition³⁵⁾⁻³⁸⁾, dealloying time^{4),39),40)} and temperature⁴¹⁾, film thicknesses³⁹⁾, and thermal coarsening temperature³⁾. Moreover, two-dimensional metal patterns formed by sputtering completely turn into nanoporous structures through the dealloying, thus this easy patterning-control property is suitable for micromachining. Therefore, chemical dealloying can be considered for a promising technique for nanoporous structures for MEMS applications.



(C. Hou et.al²⁹⁾)

Fig. 1.17 Schematic sequence showing chemical dealloying of Cu–Mn: (a) $\text{Cu}_{30}\text{Mn}_{70}$ film deposition on Cu foil via magnetron sputtering, (b) Mn dealloying, and (c) opening pores

In addition to its easy fabrication process, wide applicable substrate types and materials are very attractive. Major substrates (e.g., SiO₂, Si, Alumina, and resist substrates) are available. Binary alloys (e.g., Au–Ag^{22-24,36,39}), Cu–Pt³, Al–Cu³⁵, and Ni–Pd^{4,40}) have been used as materials for chemical dealloying, and each fabricated nanoporous material shows different properties, such as optical appearance, electrical property, structure, catalyst, or chemical resistance. Thereby chemical dealloying can be widely utilized in various applications.

Recently, new materials are expected for electrodes used in storage batteries, and they have been researched focusing on the high-specific surface area and low-pressure loss. Nanoporous structures exhibit excellent high-specific surface area, however also exhibit high-pressure loss, remaining a problem in the use of electrodes. In contrast, microporous structures have relatively low-specific surface area, but have a merit in the low-pressure loss. Therefore, novel porous structures meeting the both high-specific surface area and low-pressure loss have been required. T. Fujita et.al⁴²) fabricated, for the first time, hybrid porous metal papers including two differential micro- and nano-pores (Fig. 1.18).

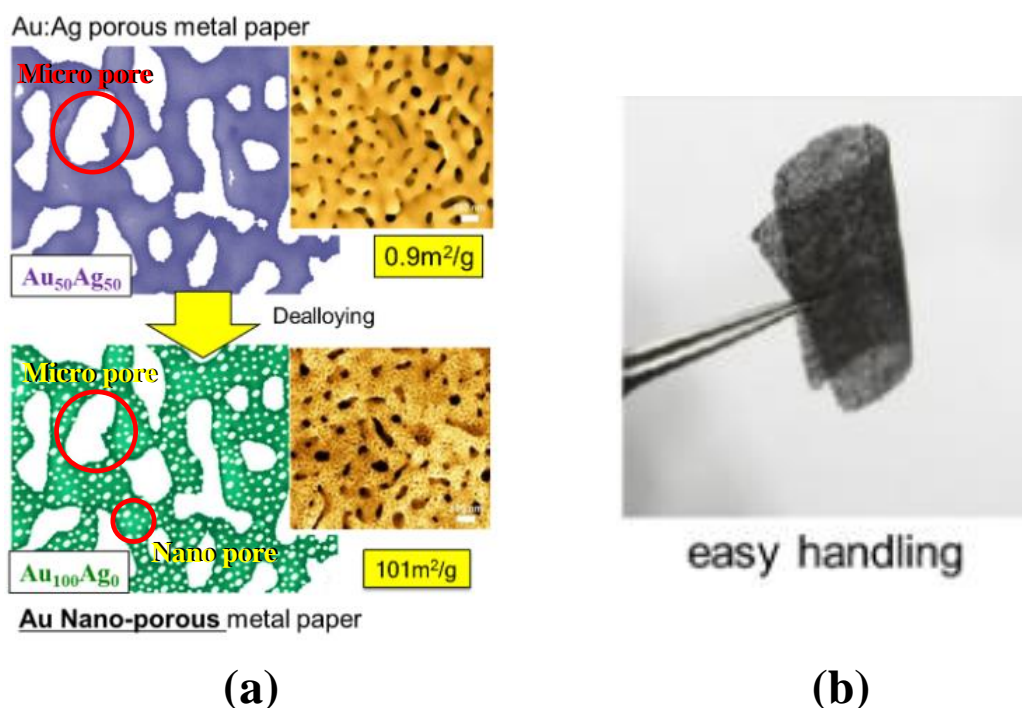


Fig. 1.18 Novel porous metal paper: (a) fabrication procedure, and (b) the obtained porous metal paper (T. Fujita et.al⁴²)

Au₅₀Ag₅₀ porous metal was further Ag dealloyed by electrochemical dealloying, and numerous nano pores were newly formed on the structure (Fig. 1.18(a)). This metal paper is an easy handling (Fig. 1.18(b)). Moreover, it exhibits high-specific surface area based on the nano pores, and also retains low-pressure loss owing to the micro pores. Therefore, it is expected as key materials for super capacitors, or electrodes for electrolysis of water. Hydrogen gas sensor shown in Fig. 1.2 and hydrogen absorption/desorption of nanoporous Pd thin films shown in Fig. 1.3 were also fabricated via chemical dealloying of Cu–Pt and Pd–Ni, respectively.

However, chemical dealloying remains two critical disadvantages. First, a large amount of sacrificial metals is necessary. Sacrificial metals are typically in rich side in binary alloys, which predominate average 70 atomic % (at. %). In the chemical dealloying of Au–Ag, 50–80 at.% precious Ag has to be removed by etching; it is no economic and not adaptable to industrial mass production. Second, complex fabrication conditions including the initial alloy composition, film thickness, or thermal coarsening etc. must be optimized. In general, optimization of the fabrication conditions for chemical dealloying is very time-consuming and difficult.

The author resolves the first problem using an inexpensive Cu for a sacrificial metal. Reasonable Cu has been often used for a sacrificial material in the micromachining, thus Cu is suitable. Furthermore, the second problem is resolved by using combinatorial technique. In this study, the author proposes a novel accelerated chemical dealloying of Cu-based alloy combined with a combinatorial method, whose detail is describe in the next section.

1.1.3 Combinatorial materials synthesis

Recent environmental performance, customer expectations, population expansion, and market globalization require new materials with optimized properties. Therefore, the opportunities and challenges to materials scientists worldwide have been greater. Discovering new materials have been in the limelight, and thereby the properties of materials have become better known. At the moment, there are 2,850 binary, 70,300 ternary, and 1,282,975 quaternary⁴³⁾. The ultimate properties of useful materials will also be a function of relative compositions and of processing conditions. This enormous number of possible combinations complicates the material search, and accordingly combinatorial materials synthesis and high throughput experimentation⁴⁴⁾⁻⁵⁵⁾ have emerged as a response to the challenges of materials development.

Combinatorial experimentation began to take off around 1990 in the pharmaceutical industry⁵⁶⁾ and 1995 in materials development^{57),58)}. Combinatorial and high-throughput approaches to the research of alloys means synthesizing a sample with multiple alloy compositions in parallel and

then screening the material libraries, subsequently studying their structures and properties simultaneously. In contrast with the conventional one alloy at a time process, this high-speed synthesis of combinatorial materials libraries combined with the high-throughput evaluation has a significant potential based on effective discovering novel materials (Fig. 1.19).

Combinatorial material synthesis has been reported by many researchers. P. J. McGinn⁵⁹⁾ used multiple masks that expose different regions of the substrate (Fig. 1.20). Binary alloy libraries are prepared by the process; (a) deposition of material A (first layer), (b) deposition of material B (first layer), (c) deposition of material A (second layer), (d) continue depositing intermixed pattern of A and B, (e) complete library, (f) binary alloy libraries after heat treatment. Through the process, materials having the differential compositions to be a function of positions can be formed on a single substrate. However, this synthesizing multiple materials technique is very time-consuming and complex, therefore more effective combinatorial materials synthesis has been researched.

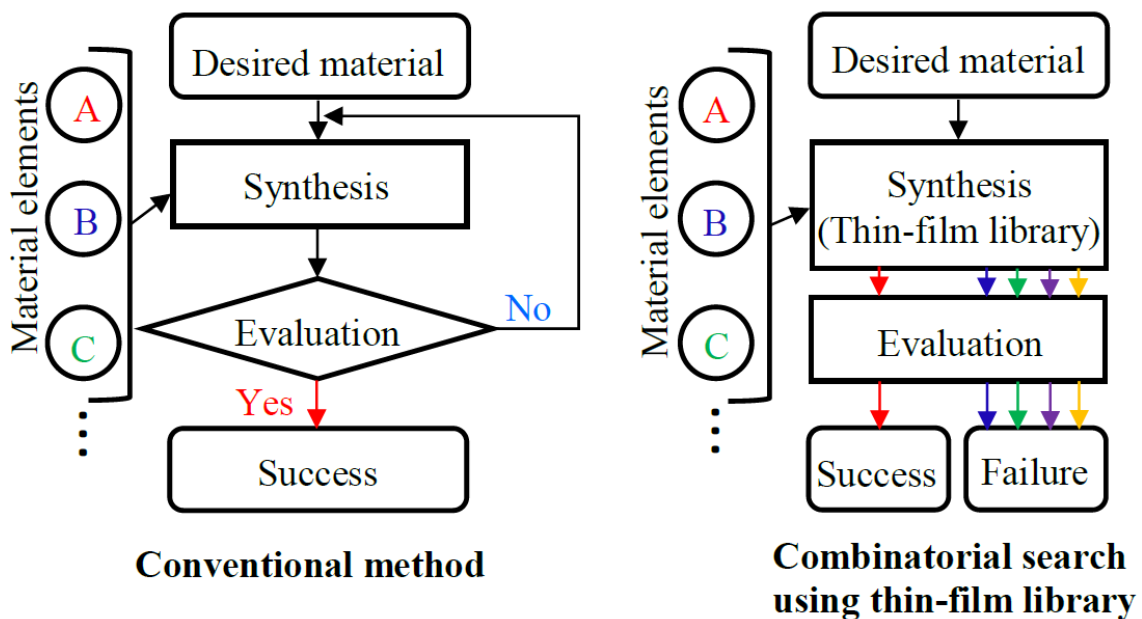


Fig. 1.19 Combinatorial optimization method

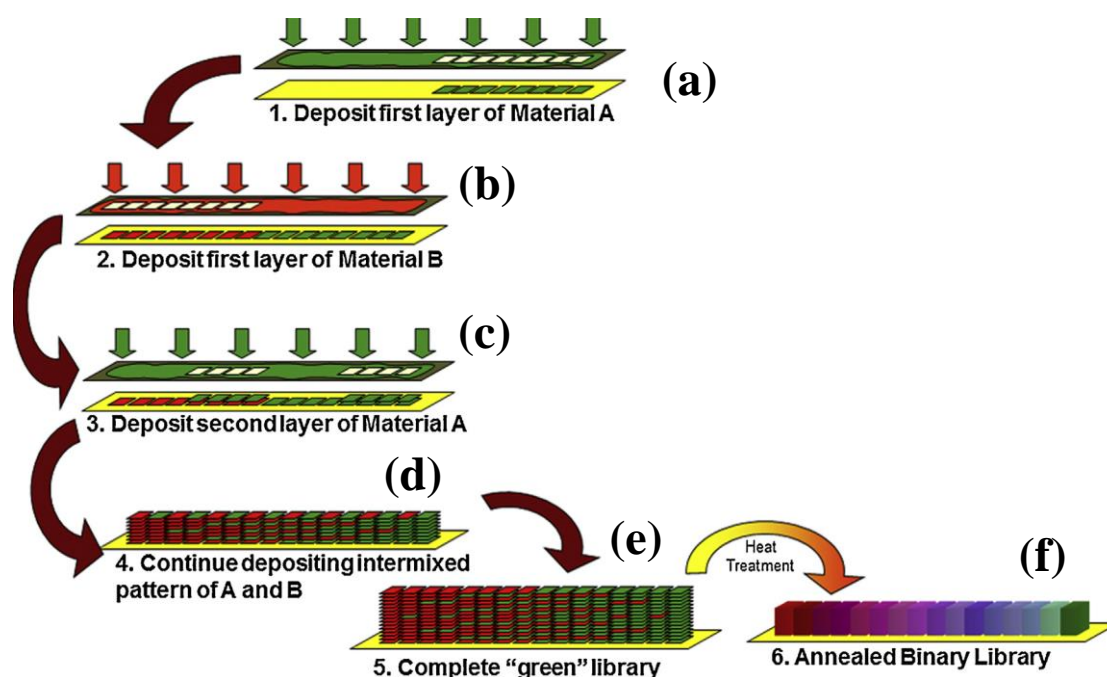


Fig. 1.20 Schematic sequence showing development of a thin-film library by deposition through contact masks: (a) deposition of material A (first layer), (b) deposition of material B (first layer), (c) deposition of material A (second layer), (d) continue depositing intermixed pattern of A and B, (e) complete library, (f) binary alloy libraries after heat treatment (P. J. McGinn⁵⁹)

Sequential deposition from multiple sputter combined with automatically moving masks⁵⁹ can be used to form thickness wedges (Fig. 1.21). Wedges with one-dimensional thickness gradient are achieved by combining constant velocity mask motion with a constant sputtering rate. By using this method, construction of a binary alloy libraries can be obtained faster than the conventional method shown in Fig. 1.20. Moreover, Co-sputtering is also attractive for a fabrication of gradient thin film libraries. Via simultaneous sputtering shown in Fig. 1.22 from two or more than two material sources, gradient composition binary or ternary films can be formed by one time sputtering⁵⁹. This process is faster than sequential deposition with moving masks in the fabrication of libraries.

The fabricated libraries enable a rapid material evaluation. M. Y. M. Chiang et.al⁶⁰ reported the combinatorial approach to the edge delamination test for thin film reliability. In their research, an effect of silicon substrate surface energy on the adhesion of polymethyl methacrylate thin films was studied. Fig. 1.23 shows a combinatorial edge delamination test to map the failure of thin film adhesion to substrates as a function of both temperature and film thickness. The library used had the film thickness gradient in one direction, and then it was cooled with a temperature gradient applied in the direction orthogonal to the thickness gradient (Fig. 1.23(a)). Film delamination was

evaluated based on critical stresses owing to the combination of each temperature and film thickness. Therefore, the stress concentration on a square pattern array of individual edge delamination samples (Fig. 1.23(b)) was efficiently varied in only one step experiment. Fig. 1.23(c) revealed the distribution of failure of a film on a substrate as a function of both temperature and film thickness. This result demonstrates that the proposed combinatorial approach was a rapid and effective. This technology must be valid for the evaluation of the adhesion between film and substrate as a function of multi-parameters.

Consequently, the combinatorial method definitely supports the chemical dealloying requiring the optimization of complex process parameters. Combinatorial method can be easily applicable in chemical dealloying. In this study, the author proposes a novel chemical dealloying as optimized by combinatorial method expected as an effective nanoporous formation technique.

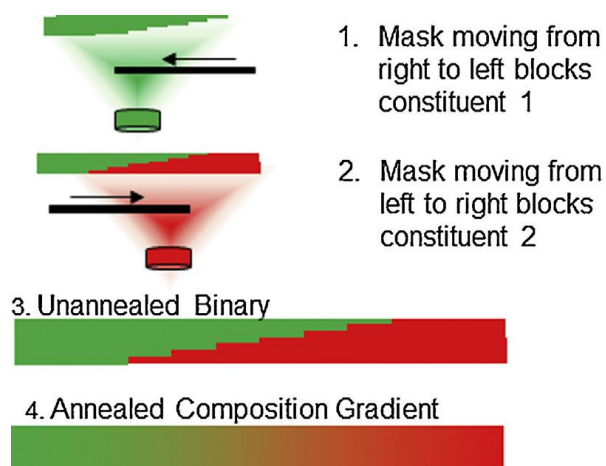


Fig. 1.21 Fabrication of a binary gradient library by the use of a moving masks (P. J. McGinn⁵⁹)

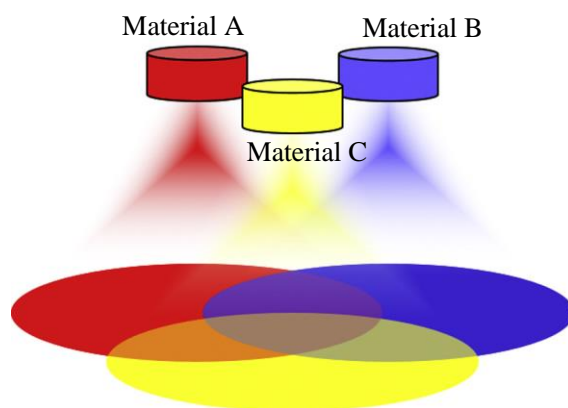


Fig. 1.22 Co-sputtering with overlapping fluxes (P. J. McGinn⁵⁹)

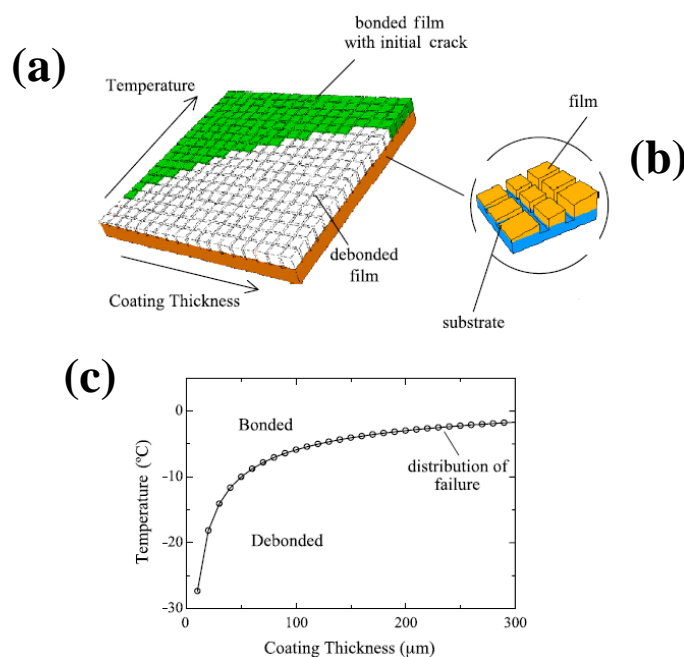


Fig. 1.23 Combinatorial approach to the edge delamination test: (a) multiple samples with film thickness and temperature gradients, (b) a square pattern array composed from edge delamination samples, (c) the distribution of failure of a film on a substrate as a function of both temperature and film thickness (M. Y. M. Chiang et.al⁶⁰⁾)

1.1.4 Chemical dealloying as optimized by combinatorial method

Carefully optimizing the pore size and porosity of the nanoporous film is important. The pore- and porosity-control in the chemical dealloying has been achieved mainly by adjustment of thermal coarsening temperature or initial alloy composition. A. Abburi et.al³⁾ revealed the temperature and pore size dependence on the chemical dealloying of Cu–Pt. In their study, nanoporous Pt from Cu₈₀Pt₂₀ thin film dealloyed in 93% H₂SO₄ showed there were no visible pores. The dealloying started with the Cu dissolution from the Cu–Pt alloy, however, Pt atoms diffused very slowly at room temperature, and finally the pore size could not grow up sufficiently. Therefore, opening pores were conducted by thermal coarsening; this processing mechanism is further described in chapter 2.

Thermal coarsening is to heat the sample in vacuum post dealloying. The dealloyed thin films were heated under vacuum at different temperature. And then the samples were cooled down to room temperature. Fig. 1.24(a)–(d) shows the obtained pore sizes with <5 nm for 250 °C, 5–10 nm for 300 °C, 25 nm for 400 °C and 35 nm for 500 °C. As increasing the heat temperature, the coarsening of the Pt particles is accelerated, becoming the pore scales gradually larger.

For another study, X. Lu et.al³⁶⁾ reported the influence of initial Au–Ag alloy composition on final morphology of nanoporous Au. Nanoporous Au formed by dealloying Au–Ag alloys

depends on the initial alloy composition, produce a variety of microstructural feature. The range of initial 22–45 at.% Au was investigated. Ag dealloying treatment was conducted with 32.5% HNO₃ solution for 10 h. The research revealed the porosity of nanoporous Au decreased noticeably with increasing initial Au content. SEM images shown in Fig. 1.25(a)–(c) corresponds on initial 41, 36, 24 at.% Au, respectively. Fig. 1.25(a) indicated, some pores with a diameter of 20–40 nm were seen, however it has not been fully Ag dealloyed, owing to the high initial Au composition. Fig. 1.25(b) shows there still some small islands that did not dealloying, which can also attributed in the high initial Au composition of 36 at.%. On the other hand, the structure presented in Fig. 1.25(c) produced a nanoporous with 20–50 nm pores covering the entire area. Thus, the Au–Ag film with an original composition of 24 at.% Au turned into completely the nanoporous with a high porosity, and the chemical dealloying was successfully achieved by using the certain initial composition.

The conventional optimization of process parameters (e.g., the coarsening temperature, initial alloy composition, or film thickness) has been conducted as follows: (a) preparation of one sample at a time process, and (b) studying the sample sequentially. This sequential procedure is extremely time-consuming, and it does not fully comprehend all process parameters, overlooking possible materials. Optimizing process parameters combined with the combinatorial method including a temperature gradient, composition or film thickness gradient such as Fig. 1.23, may be effective to discover optimal nanoporous films without omission. However, there is very few reports discussing about the combination of chemical dealloying and combinatorial method. Therefore, the author proposes an effective chemical dealloying as optimized by a combinatorial method. The schematic sequence of the proposed chemical dealloying is shown in Fig. 1.26. Various library samples (a)–(c) are dealloyed by immersion of them in etching liquid and studied (Fig. 1.26(d)). The dealloyed libraries (e) may produce an optimal nanoporous film evaluated based on the degree of dealloying, pore size, porosity, or nanoporous film adhesion to substrates.

Summary, optimal process parameters can be efficiently determined by using combinatorial searching. The author attempts to prepare nanoporous films via novel chemical dealloying as optimized combinatorial method, and demonstrates its efficiency in MEMS device fabrication.

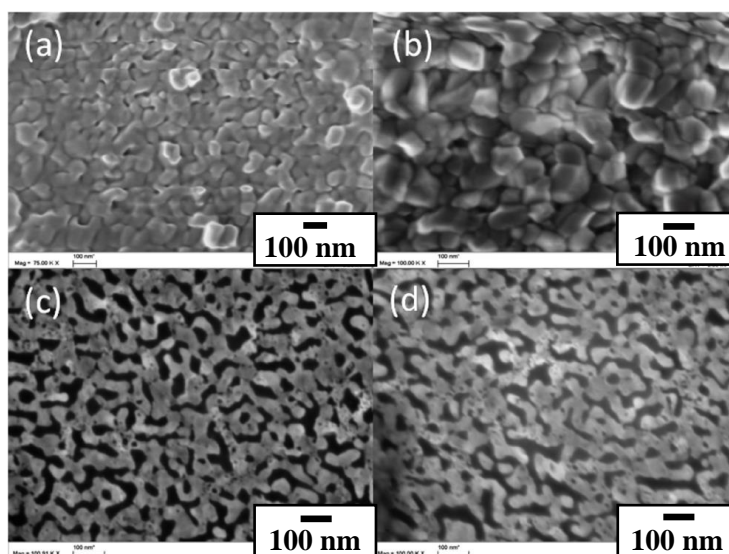


Fig. 1.24 Nanoporous Pt from $\text{Cu}_{80}\text{Pt}_{20}$ thin film dealloyed in 93% H_2SO_4 and coarsened at (a) 250 °C, (b) 300 °C, (c) 400 °C, and (d) 500 °C (A. Abburi et.al³⁾)

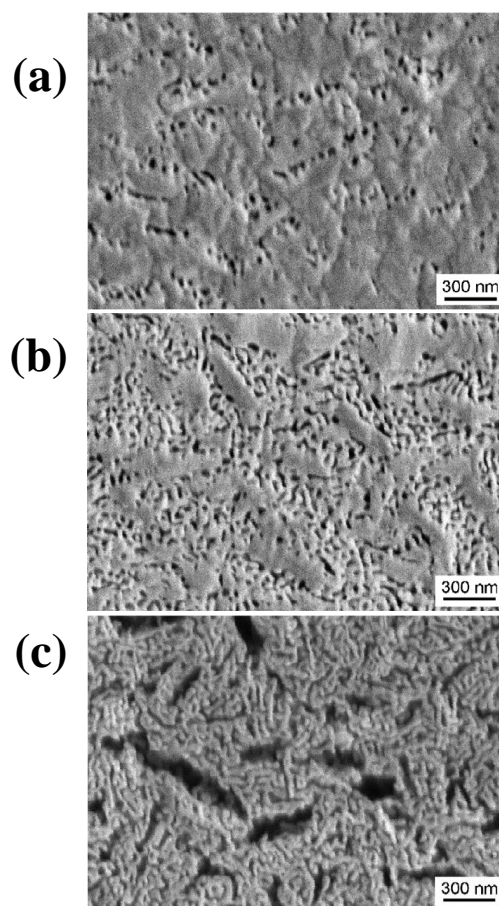


Fig. 1.25 The final obtained morphologies produced by individual initial Au compositions of (a) 41, (b) 36, (c) 24 at.% Au (X. Lu et.al³⁶⁾)

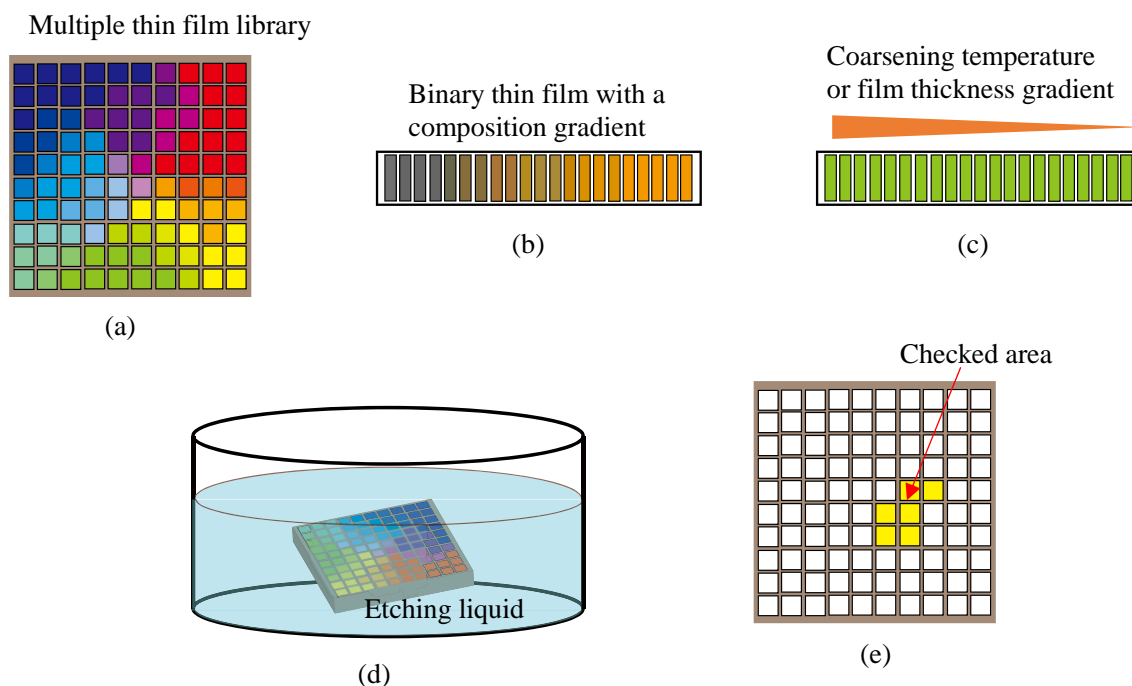


Fig. 1.26 Proposed chemical dealloying as optimized by combinatorial method: (a) multiple thin film library composed from more than two material sources, (b) binary thin film with a one-dimensional composition gradient, (c) specific binary thin film with a one-dimensional coarsening temperature or film thickness gradient, (d) dealloying treatment/screening, (e) combinatorial search.

1.2 Purposes of this study

One motivations in this study is to fabricate novel molecular filters working as an effective separation of water molecules from lubrication oil used in MEMS sensors; the sensor design and principle are further described in chapter 5. Fig. 1.27 shows a target sensor structure. The sensor comprises a capacitor with a sandwich structure: a nanoporous electrode film filter on the top, a polyimide film working as a moisture-sensitive film in the middle, and a dense electrode film on the bottom. The nanoporous film functions as a molecular filter to separate water molecules from oil and other contaminants. As shown from the Fig. 1.1, the diameter of a water molecule is approximately 0.3 nm, and the diameter of a colloidal oil particle is approximately 200 nm. A surface-active agent in the lubrication oil promotes the formation of an emulsion. Colloidal oil particles become larger than 200 nm with lapse of time, and the final diameter of oil particles would

be several micro meters³⁰). Therefore, the author hopes pore sizes being between approximately 10–50 nm. Summary, it needs a nanoporous formation technique giving a nanoporous film with about 10–50 nm pores that can be fixed on a polyimide film.

At the beginning, optimal nanostructure formation technique must be determined, which can be applicable to the device shown in Fig. 1.27. First, easy pore-control and fabrication process will be desirable. Second, for devices including non-heat resistant materials (e.g., polyimide film), processes are ideally that can be conducted with low-temperature treatment or without heat-treatment.

Unfortunately, hydrothermal growth requires an expensive autoclaves, and furthermore this process must include heat-treatment with several hours. Hence, this process has a limitation, and it dose not seem to be suitable in this study or other MEMS device fabrications.

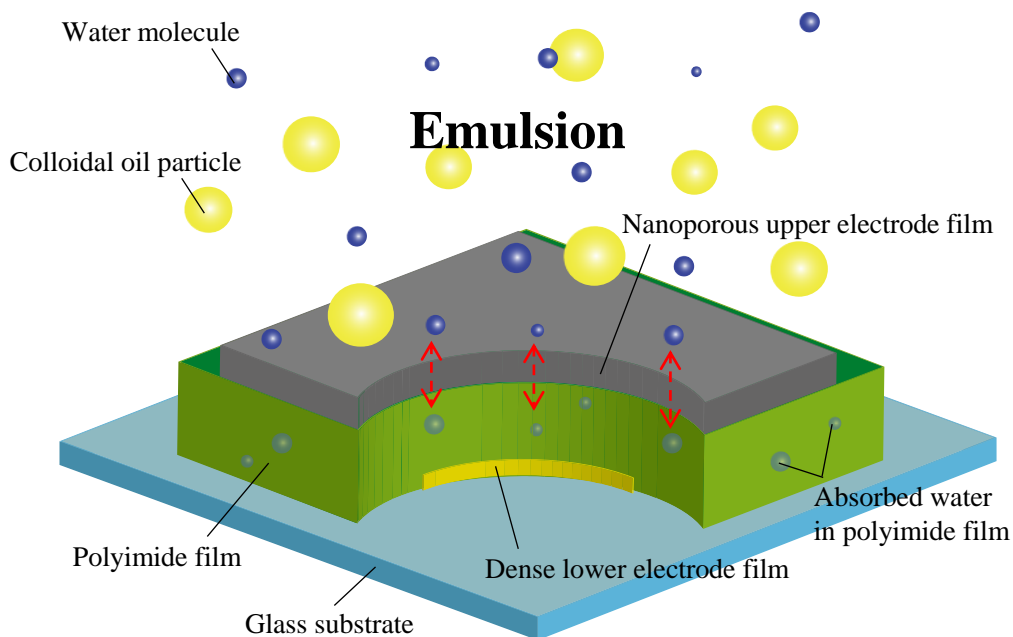


Fig. 1.27 Preparation of nanofilter fixed on polyimide film for MEMS sensor

On considering the barrier layer (Fig. 1.11), it may not be easy to apply the AAO membrane to the proposed devices. To realize the devices, the author must develop the membranes and sensor substrates separately, and then make bonding them together. But the bonding process may not be

easy. In addition, the carbon nanotubes developed based on a continuous spray pyrolysis also requires the bonding process; the heat resistance temperature of polyimide films is ca. 350 °C, therefore this continuous spray pyrolysis method conducted at 900 °C cannot be directly applied to the capacitive sensor. The only way to fabricate nanoporous films on polyimide films is to include a bonding process into this method. Moreover, some special experimental setups and over-skills for this method are also negative points.

In contrast to the above nanoporous formation techniques, chemical dealloying does not require a special experimental setup, a heat-treatment, and the bonding process too. Accordingly, the author utilizes chemical dealloying for a nanoporous formation technique. Here, the author develops novel nanoporous films via chemical dealloying as optimized by the combinatorial method. Furthermore, for the first time to the best of our knowledge, the author attempts to prepare the fabricated nanoporous films for application in MEMS sensors. Therefore, it is widely studied from the materials search to their advanced level. First challenges of this study are as follows:

(1) Chemical dealloying of Cu–Cr alloy

While chemical dealloying has been conducted on various binary alloys, including Au–Ag, Cu–Pt, Al–Cu, and Ni–Pd alloy, chemical Cu dealloying of Cu–Cr alloys to produce Cr-based nanoporous films has not been reported to date. In this study, Cu is selected as a sacrificial metal owing to its inexpensive material, covering the negative point of chemical dealloying. Moreover, Cr is suitable nanoporous metal, because of its excellent chemical resistance, and less costly than precious metals, and hydrophilicity⁶¹). Favorable chemical resistance has a great advantage for the use in sensor electrodes. Furthermore, binary alloys composed from the low cost of Cu and Cr are appropriate for industrial mass production. In addition, hydrophilicity based on Cr is an important property for the study. In this study, the fabricated nanoporous films are used as molecular filter for separation of water molecules from oil (see Fig. 1.27). Most metals are hydrophobic, and this property may hamper the filtration of water. By contrast, Al, Cr, and stainless are hydrophilic⁶²), indicating that Cr-based nanoporous films may work effectively on the separation of water molecules from oil.

Consequently, chemical dealloying of Cu–Cr alloy is challenging. The author reveals the dealloying mechanism, as well as demonstrates its utility and possibility.

(2) Combination of chemical dealloying and combinatorial method

The author proposes optimized chemical dealloying via combinatorial method. For the first try, the author optimizes initial alloy compositions for chemical dealloying by using binary thin film with a composition gradient (Fig. 1.26(b)). This technology will be helpful to form nanoporous films via chemical dealloying at a room or low temperature (0 or 300 °C). Moreover, this systematic chemical dealloying may become a powerful tool for the future applications. The author believes that these experimental results will be an importance to materials engineering field (e.g., chemical dealloying, or materials discovery).

(3) Fabrication conditions and final obtained morphologies dependence

There are extremely few reports explaining about detailed fabrication conditions for chemical dealloying such as sputtering pressure, as-deposited film density, initial alloy composition, dealloying time, or substrate type used. The author clarifies those conditions dependence on the chemical dealloying procedure, as well as morphologies that are ultimately obtained.

(4) Nanoporous films for application in nanofilter used in MEMS sensor

Based on a combinatorial analysis aimed at materials discovery, initial Cu–Cr alloy compositions are selected in chemical dealloying experiments as candidates for incorporation in sensors for the first time. Through the evaluation of nanoporous films based on sensor performances, it is demonstrated that the obtained materials exhibit effective nanoporous structures and filtration property.

1.3 Structure of this thesis

A structure of this thesis is as follows:

Chapter 1 Introduction

The author mentions a major attraction of porous materials to gas sensors, filtration technology or other applications. In response to the future MEMS applications, a wide variety of nanoporous formation technologies has been researched. Each preparation technique has advantages and disadvantages, and the author reveals them while referring the previous researches.

Moreover, the author proposes a newly developed nanostructure formation aimed at MEMS

device fabrication. Motivations, purposes and final destination of this study is cleared.

Chapter 2 Chemical dealloying including high-temperature coarsening

The author proposes chemical dealloying of Cu–Cr including high-temperature coarsening. At first, the author mentions about our chemical dealloying procedure and detailed fabrication conditions used. Formation of binary thin films through New Facing Targets Sputtering (NFTS) will be specifically described.

Furthermore, to enhance the chemical dealloying, the author introduces a thermal coarsening with high temperature (Coarsening temperature: 700 °C). The principle of the thermal coarsening is initially explained, and the author demonstrates the importance of this pre-heat treatment. The dealloyed binary films are evaluated by the use of energy-dispersive X-ray spectroscopy (EDX), stylus-type step profiler, X-ray diffraction (XRD), and field-emission scanning electron microscopy (FE-SEM), and the obtained results are discussed. In the final, the author also mentions about the possibility of the use of obtained nanoporous films for applications.

Chapter 3 Chemical dealloying including low-temperature coarsening

The author proposes more practical chemical dealloying of Cu–Cr that includes low-temperature coarsening. The chemical dealloying reported in chapter 2 requires the high-temperature heat treatment at 700 °C, and therefore its applications are limited. Because the heat-resistant temperature of the polyimide film is approximately 350 °C, the author attempts to form nanoporous films via new chemical dealloying, where the initial alloy compositions are carefully optimized while the thermal coarsening temperature can be kept in 300 °C.

For optimization of initial alloy compositions, binary thin films with a composition gradient such Fig. 1.26(b) are used. NFTS has a great advantage in the fabrication of libraries, and the author explains how to fabricate libraries by using NFTS. Through the chemical dealloying combined with the combinatorial method, the author clarifies a relationship between initial alloy compositions and level of Cu dealloying. Moreover, the author reports a relationship between initial alloy compositions and final obtained pore sizes, whose results will demonstrate a merit of the combinatorial method used in the chemical dealloying.

Chapter 4 Chemical dealloying without thermal coarsening

The author proposes more developed chemical dealloying without heat treatment. In which process, all steps can be conducted at room temperature. For applications including non-heat resistance materials (e.g., plastic substrate), a process that can be achieved without heat treatment is desirable. This novel chemical dealloying would be achieved by further optimizing initial alloy compositions, as well as controlling as-deposited film densities. The author determines each process parameter for chemical dealloying, and evaluates the final obtained materials using EDX, stylus-type step profiler, FE-SEM, and XRD. Moreover, the author reveals an influence of substrate types used on final dealloyed morphology.

Chapter 5 Nanoporous film for MEMS device

The author evaluates nanoporous films based on sensor performances. The proposed MEMS sensor measuring moisture in lubrication oil has a sandwich structure. First, the author mentions about the motivations why such sensor is required today. Second, the author explains about the sensor design and its principle. Moreover, sensor fabrication procedure is clearly mentioned by using schematic sequence.

Process parameters for chemical dealloying are identified in author's combinatorial search developed based on chapter 2–4. Alloy compositions and film thicknesses after each process are determined by EDX and stylus-type step profiler, respectively. Moreover, optical microscope and FE-SEM are employed for recording an appearance and structures before and after dealloying.

Sensor performances are evaluated in air and oil with a reference sensor. Before testing in oil, all data from the newly proposed sensors and the commercial reference sensor are simultaneously recorded in air and compared in terms of time-series responsiveness and hysteresis. The target value for the hysteresis is less than 10.0% Full Scale (FS). Next, the performance of the fabricated sensors in oil is determined based on the transient moisture content in the oil. The sensor performances including 90% response time in oil are evaluated, and possibilities of the newly proposed sensors are discussed. The target value for the 90% response time is less than 10 min.

Chapter 6 Conclusions and future works

The author summarizes the study, and mentions that the purposes in this study described in 1.2 are successfully achieved. Furthermore, the author mentions about future works.

Chapter 2 Chemical dealloying including high-temperature coarsening

2.1 Target

In this section, the author attempts to fabricate Cr-based nanoporous films via chemical dealloying of Cu–Cr alloy. At the beginning, a sputtering system used to deposit the Cu–Cr films in this study is introduced. Next, the author explains a chemical dealloying sequence as well as evaluation systems. First tried chemical dealloying tests are revealed, and the author mentions technical problems remained.

To develop the first chemical dealloying, the author proposes a new step called “Thermal coarsening”. Mechanism of newly proposed chemical dealloying including high-temperature coarsening is clarified, and the author demonstrates its efficiency. In the final, the author discusses about experimental results, and mentions about some future applications.

2.2 Fabrication of binary thin films via facing-target sputtering

2.2.1 New Facing Targets Sputtering (NFTS)

Thin film formations^{63,64} have been earlier developed based on sputtering⁶⁵⁻⁶⁷, chemical vapor deposition (CVD)^{68,69}, electroplating^{70,71}, dip- and spin-coating⁷². Generally, the metal deposition on a substrate is made by sputtering under dry vacuum conditions in a well-controlled atmosphere. Sputtering is performed on the manufacturing of disk drives, CDs, and optical devices industries. Advantages of sputter technology are known as well-control of film thicknesses and alloy compositions, which can be basically adjusted as a function of sputtering time⁷³ and sputtering power⁷⁴, respectively. Moreover, metallic compounds with high melting points or alloys each having different melting points are allowable for the use as targets⁶⁴. Also introducing O₂ or N₂ gas to the chamber atmosphere allows deposition of either metal-oxide or metal nitride films. Sputtering theory (Fig. 2.1) is as follows: (a) high-voltage applied argon (Ar) gas becomes ionized and positive Ar ions are accelerated to the negatively charged cathode and attack the target surface with high energy, (b) the flicked target atoms are sputtered as a coating on the opposite substrate with excellent uniformity and adhesion, (c) the secondary electrons produced by collision of positive Ar ions and the target promote new Ar ions. Thus, repeating the process (a)–(c) allows to deposit thin film layer with short process time.

However, general sputtering has remained a problem; deposition of insulating materials is

typically difficult because positively charged targets repel Ar ions, causing a slow sputtering rate.

Magnetron sputtering⁷⁵⁾⁻⁷⁹⁾ or RF (Radio Frequency) sputtering⁸⁰⁾⁻⁸²⁾ has been employed for improvement technology. John S. Chapin is known as a person who invented the first magnetron sputtering in 1974⁸³⁾. Magnetron sputtering deposition uses magnets behind the negative cathode to trap electrons over the negatively charged target. Hence, those electrons are not free to damage the substrates, allowing for faster sputtering rates with excellent film qualities. However, DC sputtering has limitations when perfectly using dielectric target materials. During DC sputtering, the dielectric targets gradually become positively charged, which terminate the discharge of sputtering atoms. RF sputtering is helpful to prevent the dielectric targets from getting into a positive charged state. This sputtering alternates the electrical potential of the current at radio frequencies to avoid the insulating targets becoming a positive charged state.

In general, the substrate is placed inside the plasma, so it will be invariably damaged by charged particles such as secondary electrons. Moreover, the enhanced substrate temperature by the heated targets may lead a post deposition anneal. Facing target sputtering (FTS) system⁸⁴⁾⁻⁹²⁾ not only retains the advantages of conventional magnetron sputtering methods, but also eliminates the damage of charged particles on the substrate. Fig. 2.2 shows a schematic diagram of the FTS system reported by C. Lin et.al⁸⁴⁾. In this system, two targets are placed face to face in a cathode box. Proper magnetic field formed by magnets directly oriented behind the targets enter and leave the targets perpendicularly. This magnetic field restricts the facing plasma between two targets, while the substrate is placed outside the plasma region. Thus, low substrate temperature and damage free against the substrate are achieved, allowing to form the high-quality film (e.g., ITO film^{87),91)}).

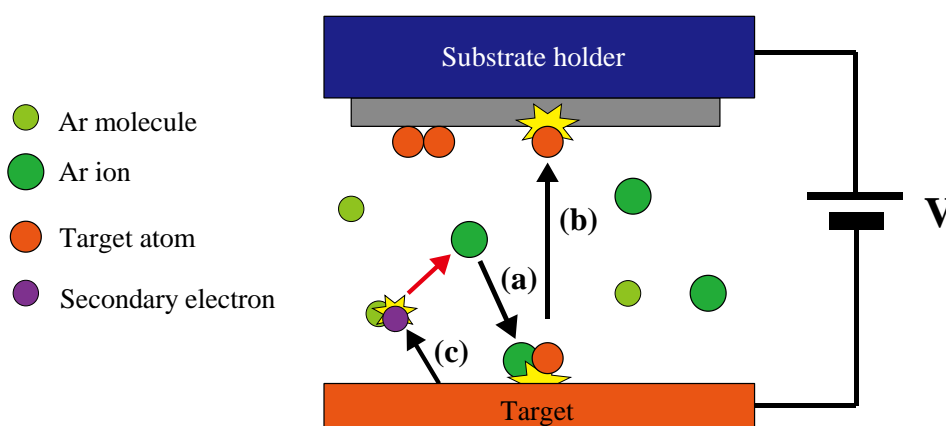


Fig. 2.1 Schematic diagram of sputtering

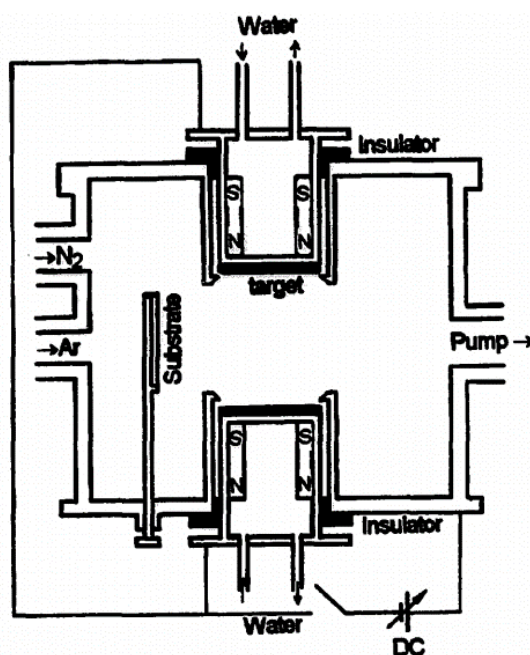


Fig. 2.2 Facing-Targets Sputtering (FTS) (C. Lin et.al.⁸⁴)

In this study, the author used more improved FTS system called “New Facing Targets Sputtering (NFTS)”. In the conventional FTS system, the facing plasma intensively enhances the erosion near the center of the target, whereas the erosion near the fringe area tends to be difficult, remaining a problem to efficiently use the targets. Reflecting such a background, NFTS was realized based on technologies of M. Naoe et.al.⁹³. Fig. 2.3 and 2.4 are a photo of NFTS system used and a schematic diagram of the cathode box (top-view), respectively. While permanent magnets are originally oriented at the target’s back, the magnets used in NFTS are arranged at the target’s fringe. Owing to this design, magnetic field can be formed not only between the two targets but also on the surface of individual targets. Therefore, two differential plasmas (facing plasma and magnetron plasma) can be realized in NFTS (because magnets fixed on the target’s fringe form magnetron plasmas by their self-return), promising a stable and high-density plasma for the sputtering (Fig. 2.4). Furthermore, the target surface is uniformly eroded by two plasmas. Thus, the target utilization can be improved. This technology is also attractive for the use of large-size targets. The stable and high-density plasma between two large-size targets has led to a successful sputtering on a large area. In the next section, the author mentions the theory of the film deposition in NFTS.

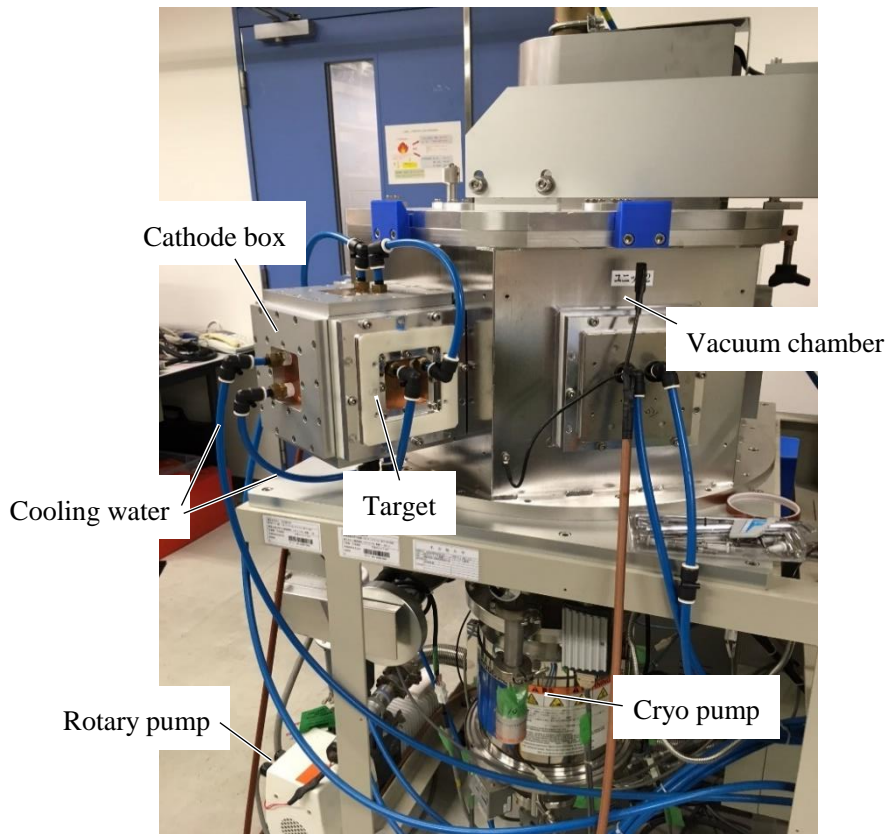


Fig. 2.3 New Facing-Targets Sputtering (NFTS)

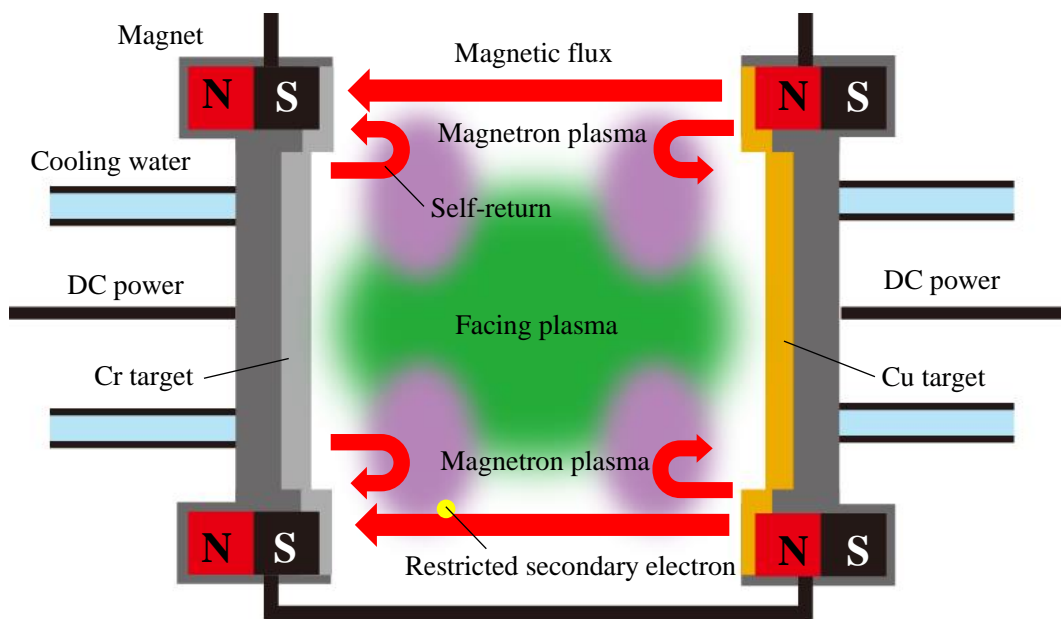


Fig. 2.4 Schematic diagram of a cathode box used in NFTS (top-view)

2.2.2 Principle of thin film deposition

Fig. 2.5 is a detailed NFTS system (top-view). In this system, the Cu and Cr targets are opposed to each other in a cathode box. Magnets are arranged in the fringe areas of the targets to form a magnetic field that confines the plasma and secondary electrons between the targets. Thus, the system can achieve co-sputtering without damaging the substrates. The adaptable sputtering pressure is lying between 0.1–2.5 Pa. In general, film deposition in NFTS is conducted under sputtering pressure of 0.5 Pa in argon. Because co-sputtering performed under 0.5 Pa in argon generally promises a dense film with a uniform composition (non-compositional gradient zone).

Substrate holder is composed from three supports A–C with a rolling mechanism. Hence, this DC sputtering can be conducted on three times in a row by one-preparation. TS (Target-Substrate) distance can be adjusted in the range of 66–98 mm. Generally, 82 mm corresponding to center position is selected as TS distance for sputtering. The average base-pressure is 2.0×10^{-4} Pa that is recognized as well-vacuum atmosphere, in which all sputtering in this study was conducted.

Angular distribution of the traveling sputtered particles was assumed to be “cosine law”⁹⁴⁾⁻⁹⁷⁾. As the angle, that emitting direction of particles make with the normal line of the target, is defined as “ θ ” (Fig. 2.6), in this rule, deposition rate varies as a function of the cosine θ . Therefore, compositional gradients can also be created in NFTS by the other process parameter adjustment, which is described in more detail in next chapter 3.

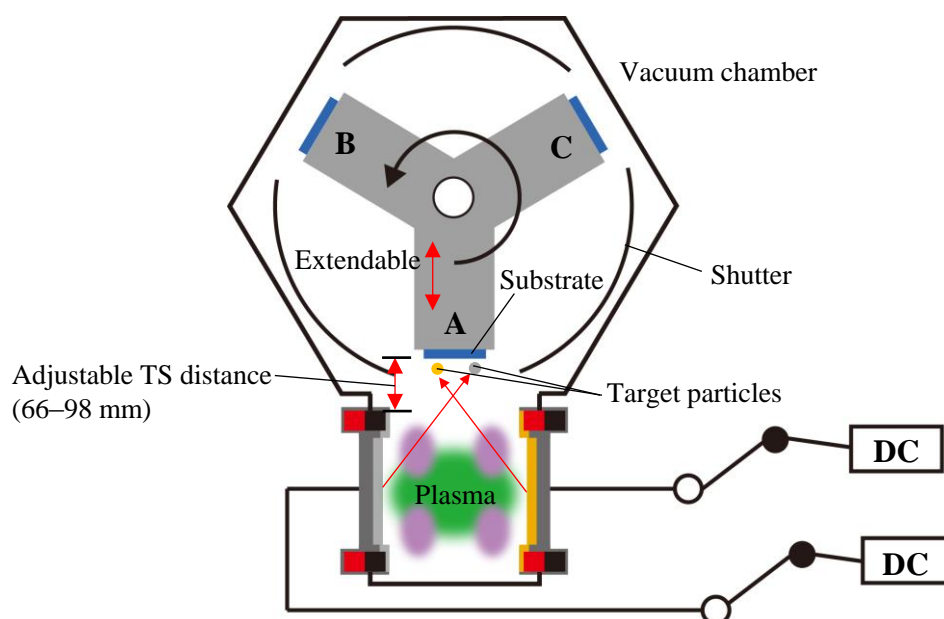


Fig. 2.5 NFTS setup

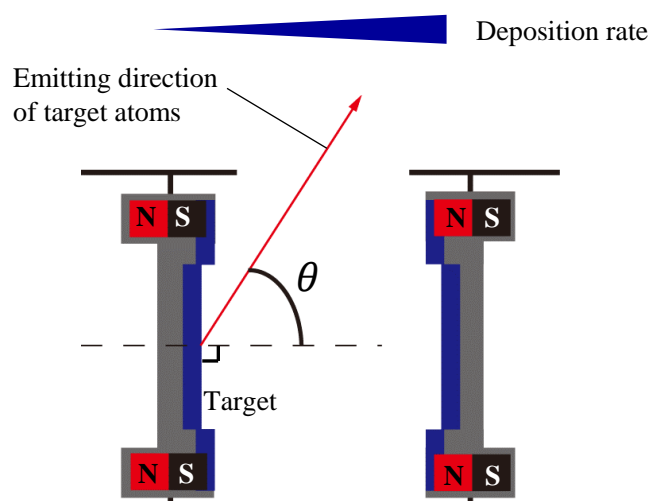


Fig. 2.6 Angular distribution of the sputtered particles obeying cosine law

2.3 Preliminary chemical dealloying test

Fig. 2.7 shows a schematic sequence of proposed chemical dealloying of Cu–Cr. First, the glass substrate with dimensions of 26 mm × 26 mm was sonicated in acetone at 100 kHz for 5 min (Honda Electronics Inc., Model W-113)). It was then rinsed with ethanol and then rinsed with deionized water by the ultrasonic cleaning under the same condition. The cleaned substrate was blow dried with air. Subsequently, the dried substrate was placed on a hotplate, and heated at 110 °C for 5 min, removing the residual water (Fig. 2.7 (a)).

Second, the cleaned substrate was loaded in NFTS, and Cu and Cr were simultaneously sputtered onto the substrate (Fig. 2.7 (b)). The pure Cu and Cr targets (Toshiba Manufacturing Inc.) were used. Most Cu-based binary alloys used in chemical dealloying contain high Cu contents of approximately 70–80 at.%²³⁾. Thus, upon the first challenging, the Cu–Cr alloy with a composition of Cu₆₈Cr₃₂ (at.%) was initially tested. Table 2.1 shows the sputtering conditions. The film thickness was 1.0 μm. The so fabricated Cu–Cr film was Cu dealloyed by immersing it in dilute nitric acid (HNO₃) for 15 h at room temperature (Fig. 2.7 (c)).

HNO₃ solution was suitable for an etching liquid used in the chemical dealloying of Cu–Cr. In general, Cr becomes a passive state in the solution⁹⁸⁾, remaining during the dealloying, whereas Cu is dissolved in the solution⁹⁹⁾. Prior to dealloying, the author tested the HNO₃ solution to assess its etching performance. Seen from the study by X. Lu et.al³⁶⁾, the concentration of the etching solution was determined in 32.5%.

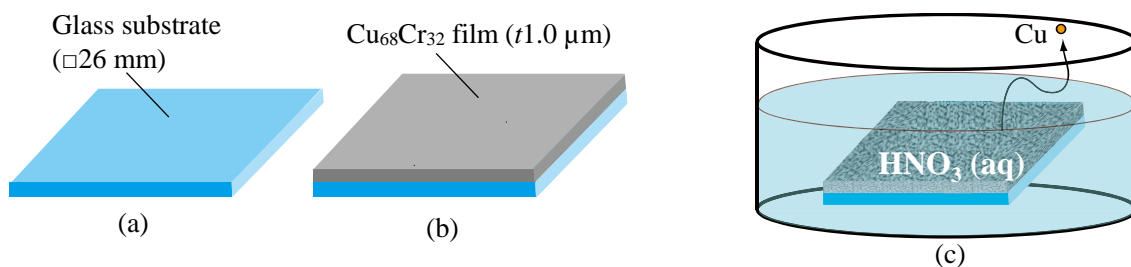


Fig. 2.7 First chemical dealloying of Cu–Cr; (a) substrate cleaning, (b) co-sputtering in NFTS, and (c) Cu dealloying with HNO₃ solution for 15 h at room temperature

Table 2.1 Sputtering conditions

Composition (at. %)	Cu ₆₈ Cr ₃₂
Sputtering pressure (Pa)	0.5
Sputtering power (W)	Cu target: 180
	Cr target: 220
Sputtering time (min)	30
TS distance (mm)	82
Deposition area (mm)	26 × 26

Immediately upon immersion in the solution, the pure Cu film was completely dissolved. The pure Cr film, however, was intact after 15 h. Moreover, the thickness of the Cr film was unchanged after the immersion. These results indicated that the selected solution may preferentially remove Cu from the Cu–Cr alloy, producing a Cr-based nanoporous structure.

The dealloyed samples were evaluated using EDX (SHIMADZU Inc., Model μ EDX-1300), stylus step profiler (Kosaka Laboratory Ltd., Model ET200), XRD (Rigaku Inc., Model RINT RAPID-S), and FE-SEM (JEOL Ltd., Model SPG-724). EDX is performed on the composition analysis by using an X-ray technique (Fig. 2.8). A beam of X-rays is focused into the compositionally unknown samples. An atom being in the sample involve ground state electrons. The incident beam excites an electron in an inner shell, ejecting it from the shell (Fig. 2.8 (a)). Therefore, an electron hole is newly created. Other electron being in an outer shell shifts to the hole, and new characteristic X-ray based on the level difference in energy between the higher-energy shell and the lower energy shell is emitted (Fig. 2.8 (b)). The wave length of the newly

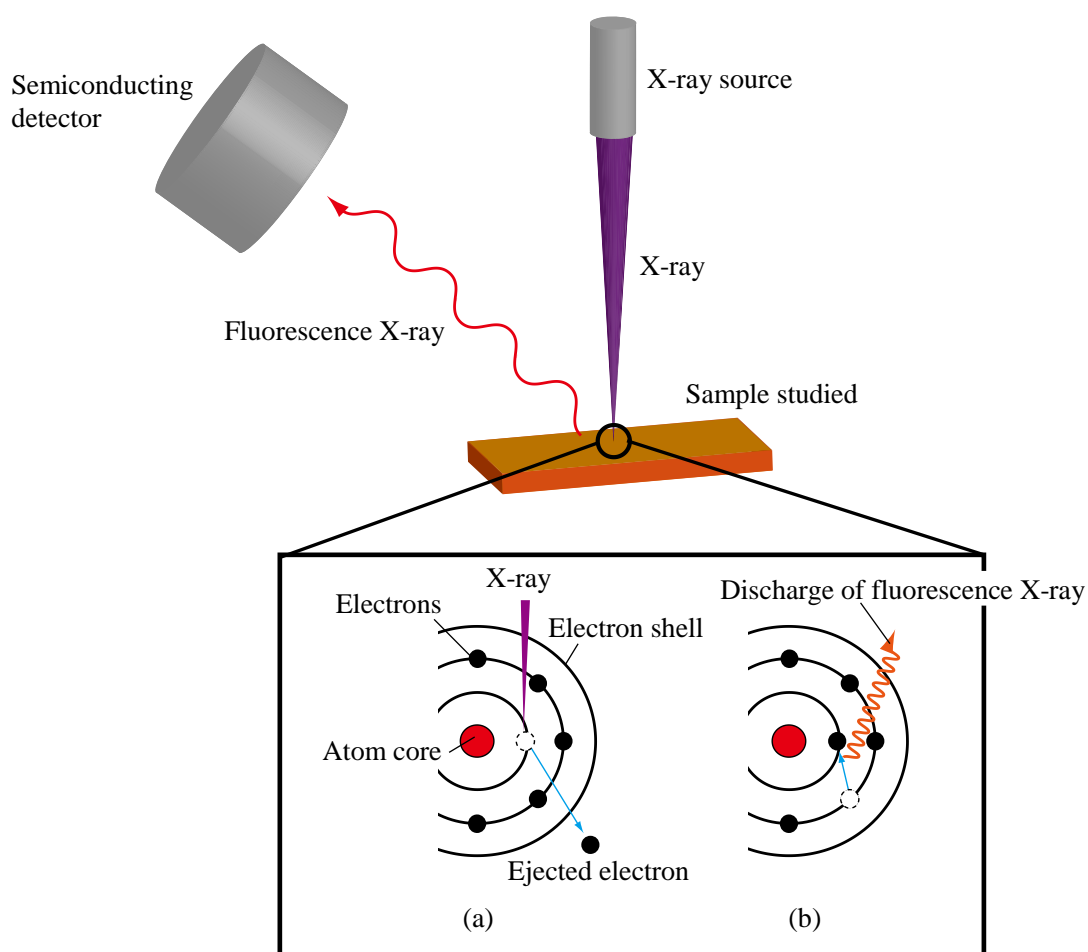


Fig. 2.8 Principle of energy-dispersive X-ray spectroscopy (EDX)

emitted X-ray corresponds to each substance. By analyzing these signals, EDX allows the qualitative testing. Moreover, quantitative analysis can be performed through the measurement of X-ray intensities.

Stylus step profiler is utilized for measuring film thicknesses, which is capable of analyzing two dimensional step heights. This stylus typed setup was performed in before and after dealloying to assess the film thickness.

XRD⁽¹⁰⁰⁾ are utilized for the identification of crystalline phases of various materials. When an incident beam of X-rays interacts with a target material, those X-rays are scattered by the regularly arranged structure material, where the scattered X-rays undergo constructive and destructive interference. This process is diffraction. The diffraction of X-rays by crystals can be explained by Bragg's Law^(101),102) (Eq. 2.1).

$$m\lambda = 2d \sin \theta \quad (2.1)$$

where m is an integer, λ is the characteristic wavelength of the incident X-rays on the crystallize sample, d is the lattice spacing, and θ is the angle of the X-ray beam with respect to these planes. The incident X-rays are in phase and parallelly reflected to the top beam that hit the top layer (Fig. 2.9). The second beam hitting the next layer must travel the extra distance $AB + BC$. When the incident angle is equal to the reflected angle, and the extra distance ($AB + BC$) is equal to an integral multiple of wavelengths (when the formula shown in eq. 2.1 was satisfied), the scattered X-rays becomes constructive interference. The detector records the number of X-rays observed at each angle 2θ . Thus, an X-ray diffraction pattern plotting the X-rays scattered intensity at different angles can be obtained. This own 2D pattern can be an important information identifying the crystal structure as well as material type and grain size.

Moreover, FE-SEM was used to examine the surface and cross-sectional structures. Fig. 2.10 is a principle of technique in FE-SEM. FE-SEM allows to observe micro- or nano-order small structures. Electrons are emitted from a field emission electron gun and accelerated in a high electrical field. Subsequently, the electrons are focused and deflected by electronic lenses and coils to produce a narrow scan beam that detects the sample. By irradiating the electron beam toward the sample, secondary electrons are emitted from the sample. Signals (angle and velocity of these secondary electrons) are reflecting the surface structure. These signals are amplified and transformed to a scan image by a detector. Through the process, users can investigate the surface or cross-sectional structures and their electronic properties.

The chemical dealloying shown in Fig. 2.7 was carried out and experimental results were revealed. Unfortunately, it was not possible to do Cu dealloying for the $\text{Cu}_{68}\text{Cr}_{32}$ thin film. The final composition and film thickness remained the same even when the dealloying time was prolonged. Moreover, the appearance of the sample was also unchanged after dealloying. These results may have resulted from the dense film structure with high initial Cr composition ratio. As shown from the Fig. 2.11, the dense film structure with high initial Cr composition hindered the infiltration of the HNO_3 solution into the film. Due to this, Cu particles tended to be difficult to be removed from the Cu–Cr alloy. One of way to do fully Cu dealloying is to include a new step into the process. It is a process called thermal coarsening, which is described in the next section.

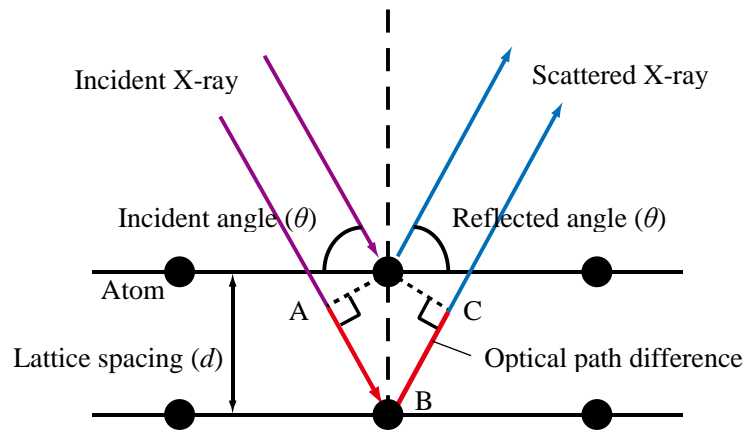


Fig. 2.9 Constructive interference of scattered X-rays based on Bragg's Law

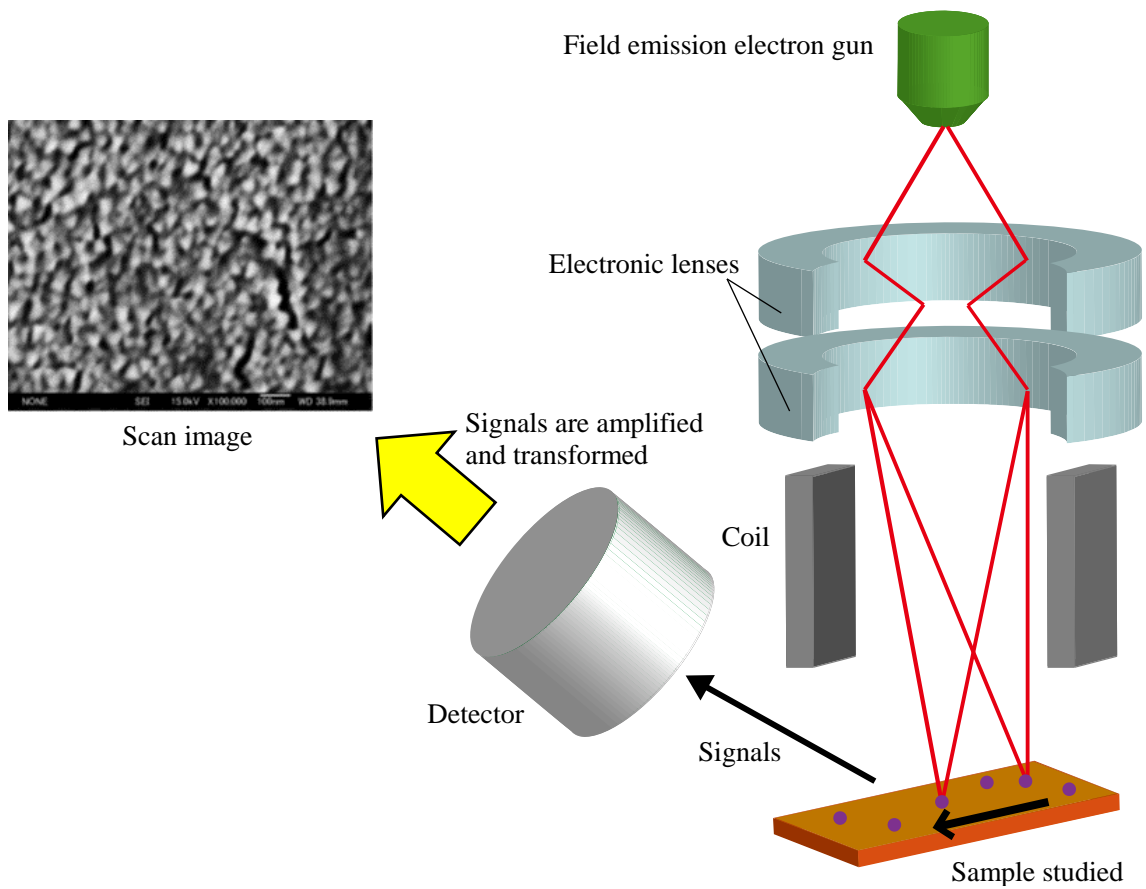


Fig. 2.10 Principle of field-emission scanning electron microscopy (FE-SEM)

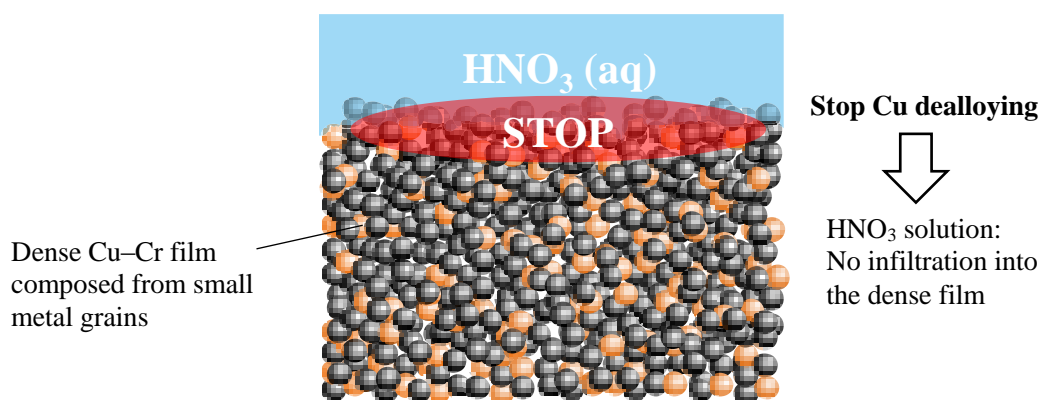


Fig. 2.11 Schematic of the film structure used in the first tried chemical dealloying

2.4 Thermal coarsening technique

In a high temperature, metal particles are thermally diffused over time. Materials are recovered through the elimination or rearrangement of dislocations, and then crystals grains with less dislocation density and high-angle boundary are newly formed, reaching recrystallization^{103),104)}. After recrystallization, thermal coarsening¹⁰³⁾⁻¹⁰⁷⁾ at highly temperature atmosphere offers a grain growth. The grain boundary energy provides the driving force for this process. This can be explained by the following theory: the grain boundary areas decrease with increase of grain sizes, where grain boundary energy works as the driving force for the grain growth. Therefore, thermal coarsening permit to develop the materials sterically in the level of grains (Fig. 2.12). However, this grain boundary energy is extremely smaller than stain energy working on the recrystallization. Accordingly, higher temperature than recrystallization temperature (at least half value of melting point) is required for the thermal coarsening¹⁰⁴⁾.

S. K. Nakatani et.al¹⁰⁵⁾ utilized the thermal coarsening technique for pore-control of nanoporous Au. As shown in Fig. 2.13, the pore sizes became larger with the increase of coarsening temperature. Therefore, the author newly included thermal coarsening step. The as-deposited film, in which the small Cr grains densely packed, may be better structures for dealloying through the thermal coarsening process (Fig. 2.14). Fig. 2.15 shows the newly proposed chemical dealloying of Cu-Cr. The process was conducted in four steps as follows:

After prior Al₂O₃ substrate cleaning (Fig. 2.15(a)), uniform Cu₆₈Cr₃₂ films were deposited on the substrates via co-sputtering in NFTS (Fig. 2.15(b)). Sputtering conditions were same as Table 2.1.

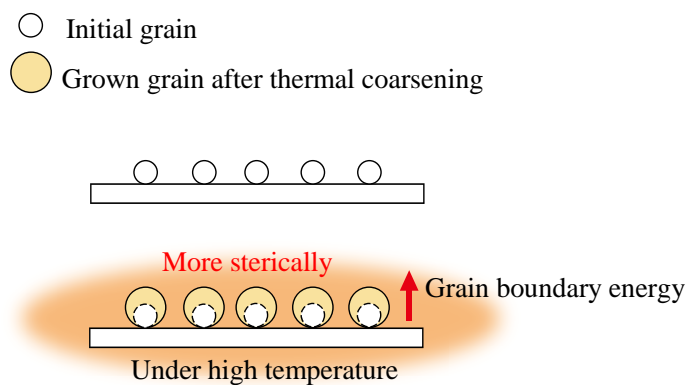


Fig. 2.12 Schematic of grain-growth produced by thermal coarsening

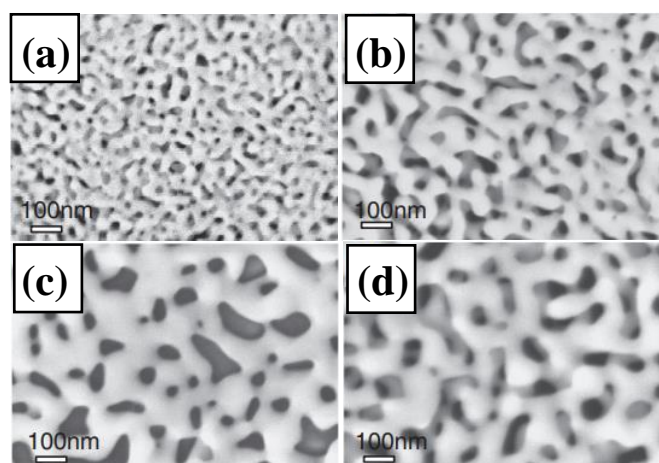


Fig. 2.13 Nanoporous Au coarsened in vacuum for 4 h at various temperatures; (a) initial state, (b) 200 °C, (c) 300 °C, and (d) 400 °C (S. K. Nakatani et.al¹⁰⁵)

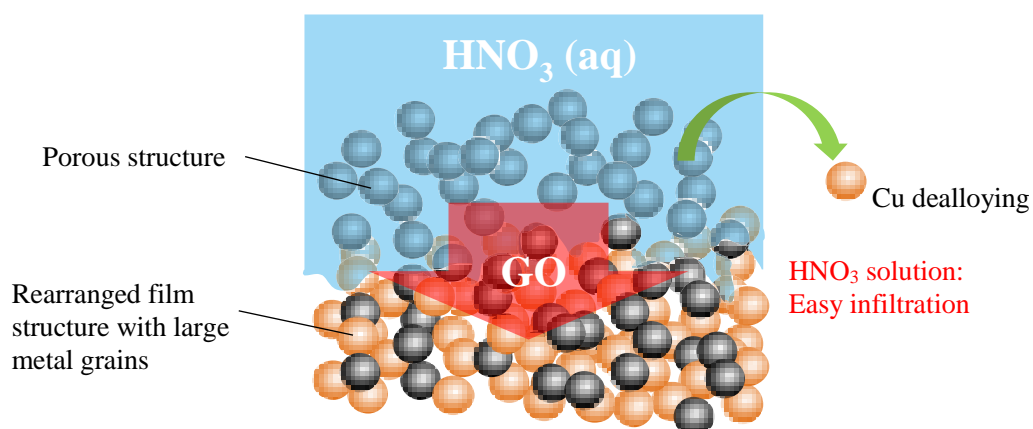


Fig. 2.14 Rearranged film structure via thermal coarsening assists Cu dealloying

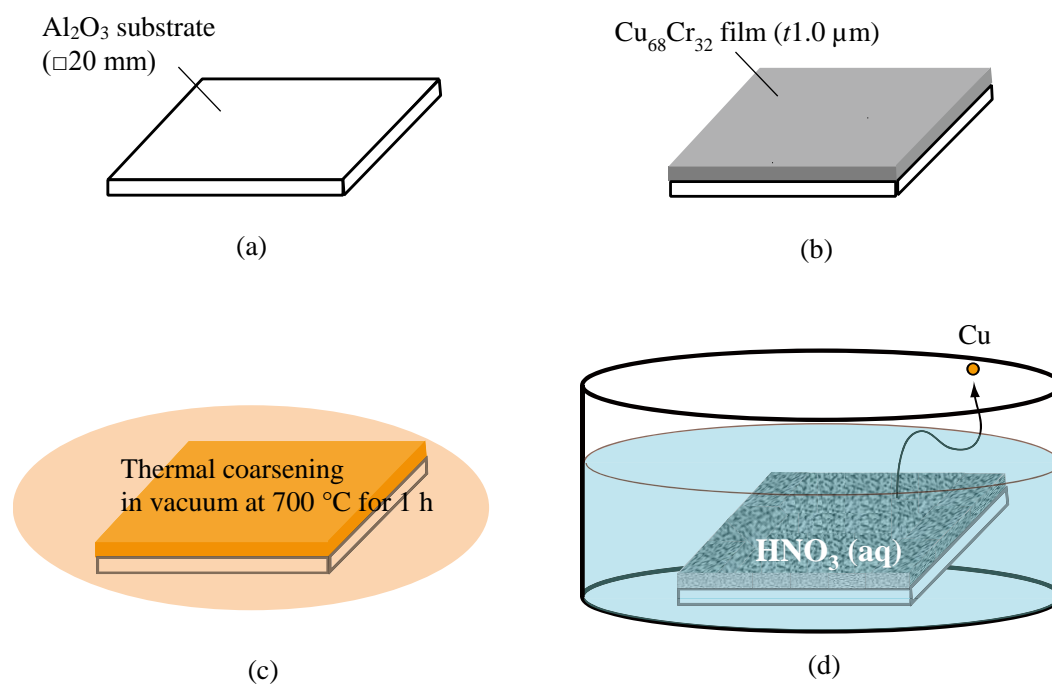


Fig. 2.15 Schematic sequence of new chemical dealloying of Cu–Cr; (a) substrate cleaning, (b) co-sputtering in NFTS, (c) thermal coarsening in vacuum at 700 °C for 1 h, and (c) Cu dealloying with HNO₃ solution for 15 h at room temperature.

Next, the samples wrapped in titanium-foils were loaded in the vacuum heating furnace (ULVAC Inc., Model MILA-3000), and thermal coarsened at 700 °C for 1 h under high vacuum at 2.0×10^{-4} Pa (Fig. 2.15(c)). Melting point of Cu–Cr alloy is approximately 1000 °C¹⁰⁸, thus the thermal coarsening was conducted 700 °C, which was a bit higher than half melting point. In the last step, the thermal coarsened samples were Cu dealloyed by immersion in HNO₃ solution for 15 h at room temperature (Fig. 2.15(d)). The experimental results are mentioned in the next section.

2.5 Nanoporous films fabricated via chemical dealloying including thermal coarsening

The sample after each treatment was shown in Fig. 2.16; (a) the appearance post as-depositing represented silver color, which may have resulted in Cr, (b) after the thermal coarsening, the appearance changed from silver to copper brown. This can be attributed into that Cu and Cr were thermally diffused with a grain growth, and Cu-rich binary alloy (Cu₆₈Cr₃₂) dominated the appearance, (c) the Cu dealloying altered the film appearance to gray color. The film thickness

was unchanged during the procedure.

The elemental compositions were determined by EDX, where three points were measured (Fig. 2.17). As seen from Table 2.2, Cu was successfully removed from the Cu–Cr alloy. The residual Cu composition was approximately average 1.0 at.%, indicating that Cu was almost not contained in the dealloyed film, while maintaining the film thickness. Summary, as-deposited Cu–Cr films were composed from small grains with high density, thus HNO_3 solution could not reach the interior of the Cu–Cr films. The grain growth allowed the Cu–Cr film structure sterically with excellent inter-diffusion. After the process, this binary thin film structure became a favorable one for Cu dealloying.

The XRD spectra in Fig. 2.18 shows some peaks owing to the Al_2O_3 substrate, and another several peaks corresponding to Cr. Cu peaks were absent, because Cu was fully dealloyed from the binary film. Cu and Cr grains were thermally grown up, and subsequently phase-separated by high temperature coarsening. After Cu dealloying, the large Cr grains were clearly remained, resulting in the Cr peaks.

Next, the dealloyed sample was evaluated by FE-SEM for recording the structures. Fig. 2.19(a) and (b) exhibited a surface structure (top-view) and a cross-sectional structure (side-view), respectively. From the image (a), porous structures were entirely formed throughout the surface. The estimated pore size was 200–300 nm. Moreover, image (b) showed the favorable porous structures throughout the film thickness. The obtained Cr nanoporous films with 200–300 nm open pores are expected in the use of catalysts, absorbent materials, or nanofilters.

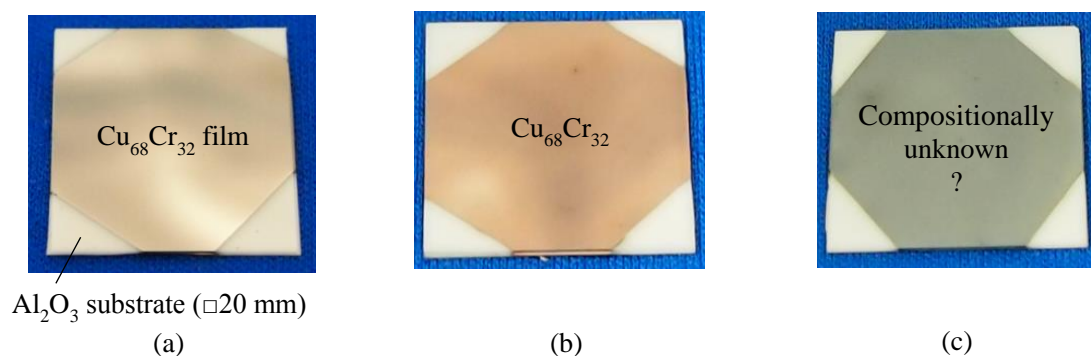


Fig. 2.16 Obtained $\text{Cu}_{68}\text{Cr}_{32}$ film after each treatment; (a) as-deposited state, (b) after thermal coarsening, and (c) after Cu dealloying

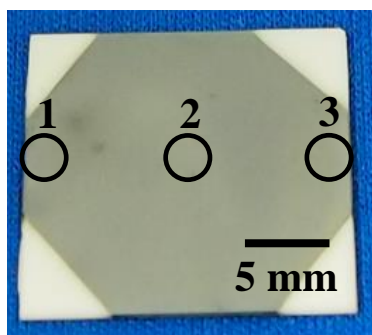


Fig. 2.17 Three measurement points were tested by EDX

Table 2.2 EDX analysis after Cu dealloying

	Measurement points		
	1	2	3
Cu (at.%) (Initial composition: 68)	1.2	1.5	1.6
Cr (at.%) (Initial composition: 32)	98.8	98.5	98.4

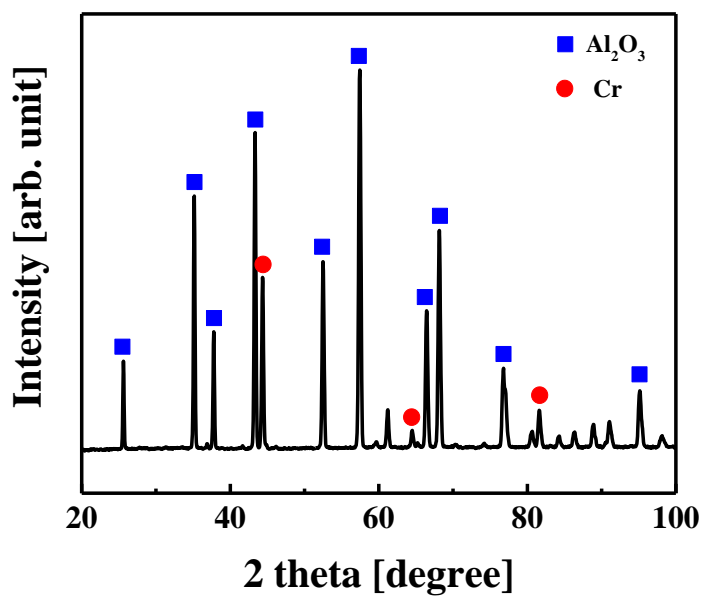


Fig. 2.18 XRD pattern of the film after Cu dealloying

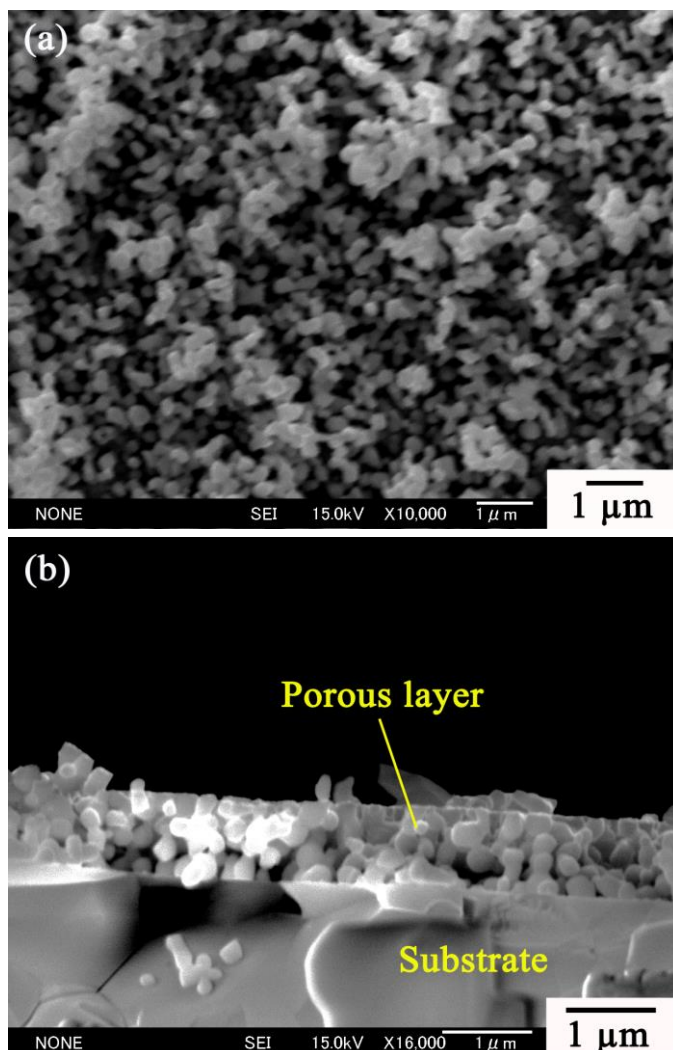


Fig. 2.19 FE-SEM images of the Cu dealloyed film; (a) surface- (top-view), (b) cross-sectional structure (side-view)

2.6 Summary

The author successfully fabricated Cr nanoporous films (pore size: 200–300 nm) via chemical dealloying of Cu–Cr including thermal coarsening. Newly introduced thermal coarsening complied with the theoretical expectations and offered an effective grain growth, resulting in the excellent Cu dealloying. This section is summarized below.

First, the author mentioned about the details of NFTS system. NFTS had a unique structure, which was explained how NFTS system differs from other FTS systems. In this work, NFTS was employed in co-sputtering of Cu–Cr.

Second, the author mentioned about the first model of chemical dealloying. Fabrication conditions (initial alloy composition, dealloying time, etching liquid type and its concentration) were carefully determined, while referring previous reports. Employed evaluation equipment and their detecting principles (EDX, stylus step profiler, XRD, and FE-SEM) were also explained.

Unfortunately, first tried chemical dealloying ended up in the failure. As-deposited $\text{Cu}_{68}\text{Cr}_{32}$ film had a densely packed structure of small metal grains, resulting in a low Cu etching rate. Furthermore, due to its high initial Cr composition (32 at.%), Cu could not be sufficiently etched out from the binary film. Regarding these remained problems, all mechanisms and ideas were explained using the schematic diagrams. In order to etch the Cu region in the binary film, the author included a new step in the early process.

The new extra step was thermal coarsening, demonstrating its efficiency in this work. First thermal coarsening was conducted at 700 °C for 1 h in a high-vacuum atmosphere, in which Cu and Cr were fully diffused. Moreover, grain growth was effectively occurred. Final film structure was in the best condition, and the author proved that thermal coarsening was very helpful for improving the Cu dealloying performance. Final obtained alloy compositions were dominated by Cr (98 at.% Cr). Moreover, the almost Cr based-materials showed 200–300 nm open pore structure, indicating that the first challenge was successfully achieved. The obtained Cr nanoporous films are expected in the use of catalysts, absorbent materials, or nanofilters. Moreover, it is also found out that micro pores (200–300 nm) could be generated through 700 °C coarsening, indicating that the permissible pore range was wider than expected. Grain growth can be adjusted through the coarsening temperature, and this wide controllable pore size has a great advantage in the filtration property.

In this method, however, thermal coarsening at 700 °C must be included in the process. This high temperature treatment may affect negatively on other non-heat resistance materials (e.g., polyimide film, glass, silicon or plastic substrate). Then, the author attempts to lower the heat temperature. In next chapter 3, the new chemical dealloying including low-temperature coarsening but also retaining the excellent dealloying performance was studied.

Chapter 3 Chemical dealloying including low-temperature coarsening

3.1 Target

In chapter 2, the author reported the chemical dealloying of Cu–Cr including the high-temperature coarsening, which has led to the successful porous structures with 200–300 nm pores. However, this method requires the heat-treatment with 700 °C, limiting applications composed from highly heat resistant materials. Generally, micro- or nanoporous films have gained much attention in application areas such as actuators, sensors, and electrodes. To meet various devices including non-heat resistant materials (e.g., resists or plastic substrates), the author offers novel chemical dealloying including low-temperature coarsening.

On considering the heat-resistant temperature of polyimide films (350 °C), the author initially tried a chemical dealloying of Cu–Cr thin film, where thermal coarsening is simply conducted at 300 °C. The author mentioned in the last chapter that thermal coarsening of Cu–Cr films had to be conducted at least with 500 °C. Therefore, heat-treatment with 300 °C may be insufficient for a grain growth, which possibly hinders HNO₃ solution to enter to the interior of Cu–Cr films. However, Cu grains have a tendency to grow even at as-depositing. Thus, the author considered that high Cu compositions zone may permit an easy infiltration of HNO₃ solution into Cu–Cr films, resulting in effective Cu dealloying.

The first challenging was evaluated by EDX and stylus step profiler analysis, where compositions and film thicknesses before and after dealloying were measured, respectively. Afterwards, the author discussed about the results and technical problems remained.

Next, the author attempts to overcome this challenge by further adjustment of initial Cu–Cr alloy compositions. It is typically difficult to select an appropriate initial composition from numerous candidate compounds. Upon these experiments, the author uses a combinatorial investigation. Composition libraries with many distinct regions of gradient composition are employed, where composition varies one-dimensionally across libraries. Fabricated libraries with a rapid screening via dealloying possibly facilitates the identification of process parameters used in the chemical dealloying.

Combinatorial film deposition has been done based on co-sputtering by NFTS. At first, the author describes details about the combinatorial film processing by NFTS. General libraries fabricated by NFTS are introduced. After that, to assess the conventional theory being true of the

author's co-sputtering, the author verifies the simultaneous deposition mechanism of Cu–Cr, and reveals the relationship between compositional gradient (Δx at.% Cr) and sputtering pressure. After testing, optimal sputtering parameters (sputtering pressure, power, and time) are determined, and the author prepares target libraries for the study.

Afterwards, the author rapidly screens the libraries through the dealloying process. The level of Cu dealloying as a function of initial alloy compositions are carefully investigated by EDX and stylus step profiler analysis. Next, the author studies initial alloy composition and pore size dependence by using FE-SEM. Subsequently dependence of initial alloy composition on porosity of films are evaluated by an image data processing.

Finally, the author demonstrates that the chemical dealloying as optimized by combinatorial method can be greater than with traditional methods. Nanoporous properties (residual Cu composition, film thickness, pore size, and porosity) depending initial alloy compositions are effectively revealed. Moreover, the author determines an optimal composition region that can realize the proposed novel chemical dealloying.

3.2 Preliminary chemical dealloying test

The author is motivated with the aim of fabricating nanoporous films on polyimide films. In this section, therefore the author first determines a coarsening temperature focusing on polyimide films. Generally, polyimide films (TORAY Inc., PW-1500) are cured at approximately 350 °C¹⁰⁹), indicating that heat-treatment with 300 °C serves as an allowance without causing large change of physical properties of polyimide films. Therefore, the author proposes a chemical dealloying of Cu–Cr including the thermal coarsening with 300 °C. Fig. 3.1 shows a schematic sequence of first tried chemical dealloying, and the author confirms the possibility for the processing.

Prior to the experiment, a glass substrate was washed in acetone, and then rinsed with ethanol, subsequently with deionized water (Fig. 3.1(a)). Next, a polyimide film (2.0 μm thick) was deposited on a glass substrate via lithography (Fig. 3.1(b)). Polyimide films were prepared by dilute (75 wt.%) polyimide precursor solution (TORAY Industries Inc. Photoneece PW-1500). Photo sensitive polyimide was spin-coated (MIKASA Inc., Model 1H-DX) on the glass substrate. The masked substrate was patterned through the lithographic process (MIKASA Inc., MA-20), and then cured under N₂ atmosphere, forming polyimide films with optimal dimensions. Afterwards, the polyimide film was masked, and Cu and Cr were co-sputtered on an exposed

surface area of $2.5 \text{ mm} \times 3.5 \text{ mm}$, which was positionally restricted to be within the polyimide boundary (Fig. 3.1(c)). In this preliminary test, $\text{Cu}_{68}\text{Cr}_{32}$ and $\text{Cu}_{78}\text{Cr}_{22}$ films (500 nm thick) were used. Sputtering conditions are shown in Table 3.1.

The fabricated $\text{Cu}_{68}\text{Cr}_{32}$ and $\text{Cu}_{78}\text{Cr}_{22}$ films were wrapped in titanium-foils to prevent the samples becoming oxidation, and loaded in a vacuum heating furnace. The samples were thermally coarsened at $300 \text{ }^\circ\text{C}$ for 1 h under high-vacuum at $2.0 \times 10^{-4} \text{ Pa}$ (Fig. 3.1(d)). In the final, the two samples were Cu dealloyed in HNO_3 solution for 15 h (Fig. 3.1(e)).

Unfortunately, it was not possible to achieve Cu dealloying for the $\text{Cu}_{68}\text{Cr}_{32}$ films. The resulting $\text{Cu}_{68}\text{Cr}_{32}$ film could not be fully Cu dealloyed, and its composition ended up with $\text{Cu}_{45}\text{Cr}_{55}$. This result indicated that the grain growth did not occur due to the low-temperature coarsening (Fig. 3.2). The used coarsening temperature ($300 \text{ }^\circ\text{C}$) was less than half melting point of Cu–Cr film (approx. $500 \text{ }^\circ\text{C}$). Generally, half melting point is at least required for the thermal coarsening¹⁰⁴. Therefore, grain growth as well as phase separation were imperfectly with $300 \text{ }^\circ\text{C}$, resulting the poor Cu dealloying.

Moreover, the initial Cr composition of 32 at.% would be too high to etch Cu region in films (Fig. 3.2). This can be explained by the dealloying of $\text{Cu}_{78}\text{Cr}_{22}$ film. In the case of $\text{Cu}_{78}\text{Cr}_{22}$, the film was completely dissolved during the dealloying treatment (Fig. 3.3). This may be attributed in part to the low initial Cr composition, which prevented the formation of a nanoporous structure. This result means that reducing the initial Cr content to below 32 at.% might allow Cu dealloying to produce a Cr-based nanoporous film. To realize the excellent Cu dealloying without the Cu–Cr film dissolution, the author optimized a proper initial Cu–Cr alloy composition.

There is probably certain initial Cr compositions between 32 and 22 at.%. In order to discover the optimal initial Cr compositions, the author used a combinatorial technique accompanied with a thin film with a gradient composition containing an initial 32–22 at.% Cr (thin-film library). Concepts of this study and approaches are mentioned in more detail below.

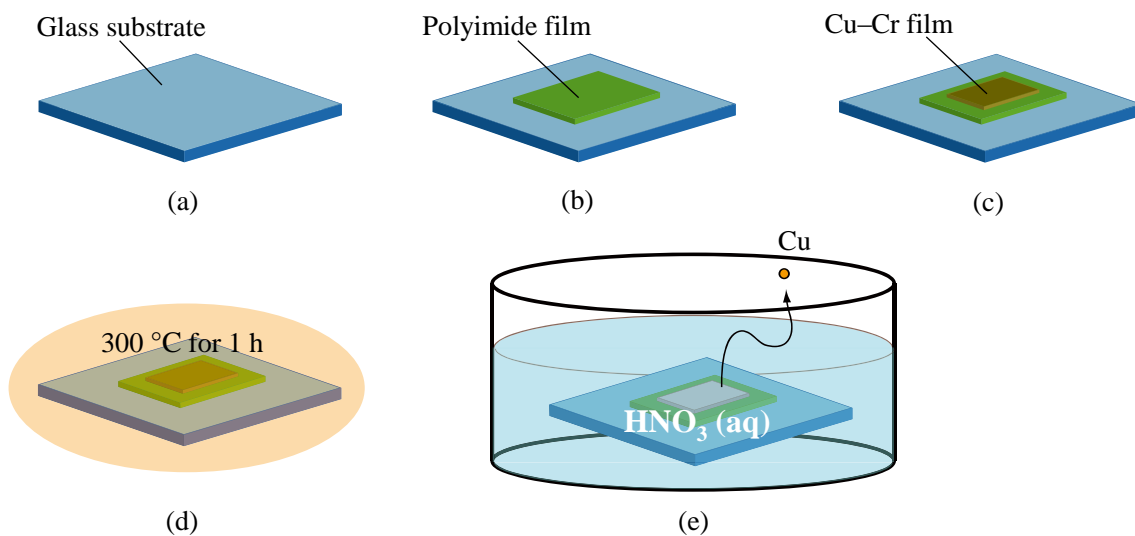
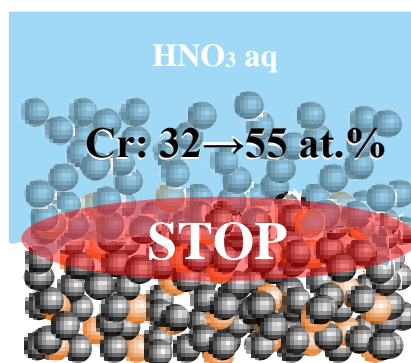
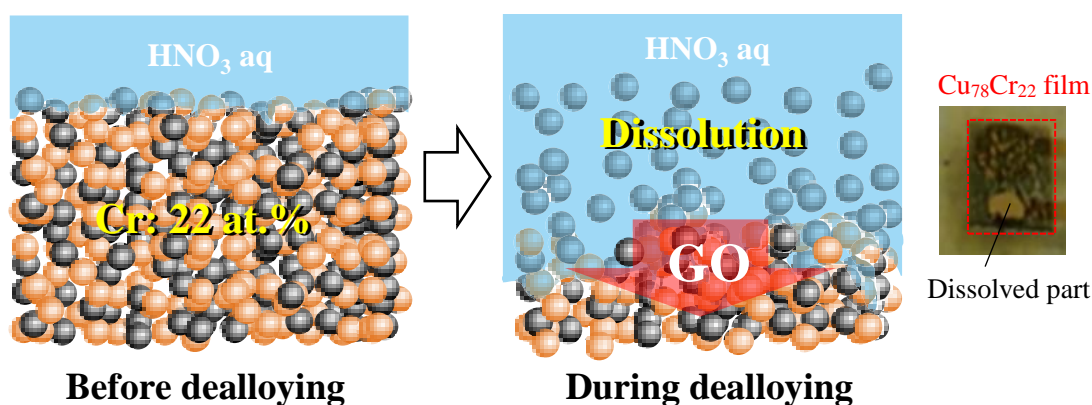


Fig. 3.1 Preliminary chemical dealloying test; (a) substrate cleaning, (b) deposition of a polyimide film on a glass substrate via lithography, (c) co-sputtering of Cu–Cr film onto the polyimide film in NFTS, (d) Thermal coarsening at 300 °C for 1 h under high-vacuum state, and (e) Cu dealloying in 32.5% HNO₃ for 15 h at room temperature.

Table 3.1 Sputtering conditions

		Tested samples	
		(a) Cu ₆₈ Cr ₃₂	(b) Cu ₇₈ Cr ₂₂
Sputtering pressure (Pa)		0.5	0.5
Sputtering power (W)	Cu	180	220
	Cr	220	130
Sputtering time (min)		15	15
TS distance (mm)		82	82
Deposition area (mm)		2.5 × 3.5	2.5 × 3.5

Fig. 3.2 Schematic diagram of chemical dealloying of $\text{Cu}_{68}\text{Cr}_{32}$ Fig. 3.3 Schematic diagram of chemical dealloying of $\text{Cu}_{78}\text{Cr}_{22}$

3.3 Optimization of initial alloy compositions

3.3.1 Compositional gradients created by NFTS

Combinatorial investigation using thin-film libraries is currently employed for a rapid and easy discovery of optimal process parameters. Widespread materials synthesis has been often performed by simultaneous deposition from more than two or three sources. Sputter co-deposition ensures intimate mixing of the library in a short process time, and multiple compositions varies continuously as a function of single substrate position. Moreover, because process parameters of sputtering (sputtering pressure, sputtering power and time, and TS (Target-Substrate) distance) strongly influence the thin-film composition library, it enables us to design profiles in the combinatorial libraries (e.g., composition range or film thickness) thorough the calculation.

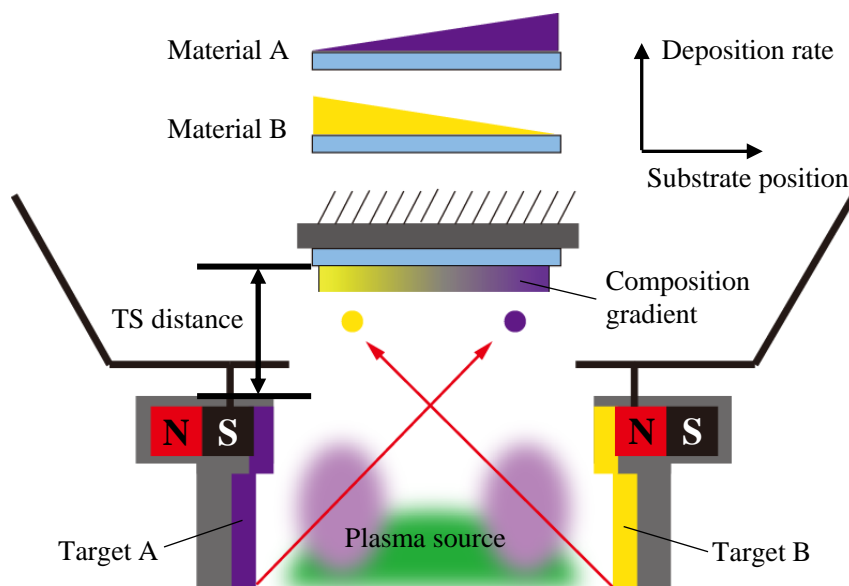
The target thin-film libraries in this study were prepared by co-sputtering in NFTS system. As mentioned in chapter 2, NFTS is also possible to generate compositional gradients due to its characteristic sputtering geometries. Because substrates are stationary during sputtering, and

because the two targets are oriented symmetrically and perpendicularly to substrates, composition gradients are created in one-dimensional direction (horizontal direction) on substrates (Fig. 3.4 (a) and (b)). This standard NFTS sputtering generates no compositional gradient along the vertical direction. However, there is a report that setting the substrate position has enabled generating expanded compositional gradients, such as two-dimensional gradient zone¹¹⁰.

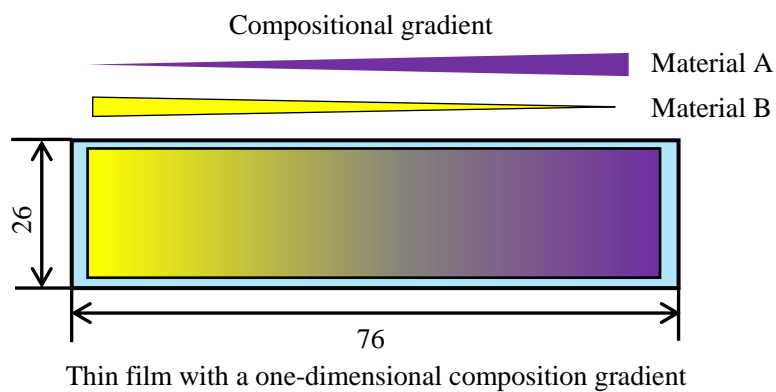
Angular distribution of the traveling sputtered particles is assumed to be cosine law. So in principle, deposition gradients can be formed while obeying the rule of cosine law. In this rule, sputtering rate of each material increases as deposited positions are separated from the targets. In Fig. 3.4(b), material A can generate a linear gradient varying from a maximum in the region (right part) to a minimum where the distance between the target A and the deposited position becomes the shortest (left part).

N. Mori¹¹⁰ reported the deposition mechanism in NFTS. In his research, the Zr–Cr films with a compositional gradient were experimentally revealed. He showed that the gradient range depends on the sputtering (argon) pressure, and an inclined level expands with decrease of sputtering pressure. Through the experiments, he explained that the co-sputtering of Zr–Cr followed the cosine law. This is because, as the sputtering pressure decreases, the mean free path of each sputtered particle increases¹¹¹ (Fig. 3.5); hence, the sputtered particles have high kinetic energy and are likely to reach the far edge of the substrate. Accordingly, sputtering rate was enhanced based on above mechanism and cosine law, expanding the compositional gradient in the low sputtering pressure.

To assess this theory being true of the author's co-sputtering of Cu–Cr, compositional gradients created via NFTS were researched. Cu–Cr films with compositional gradients were sputtered at pressures of 0.3, 1.0, 1.5, and 2.5 Pa (Fig. 3.6). In this study, glass substrates with dimensions of 26 mm × 76 mm were used. The cleaned substrate was loaded into the sample holder of NFTS, and Cu and Cr were simultaneously sputtered following Table 3.2. As illustrated in Fig. 3.7, the total 15 points were analyzed by EDX along the centerline at 5 mm intervals from the center of the sample. The author compared the newly obtained results with that reported by N. Mori in Cu–Zr alloy system. Details about the results are mentioned below.



(a)



(b)

Fig. 3.4 Schematic diagram of general materials synthesis in NFTS; (a) deposition mechanism of thin films with a composition gradient, (b) fabricated thin-film libraries.

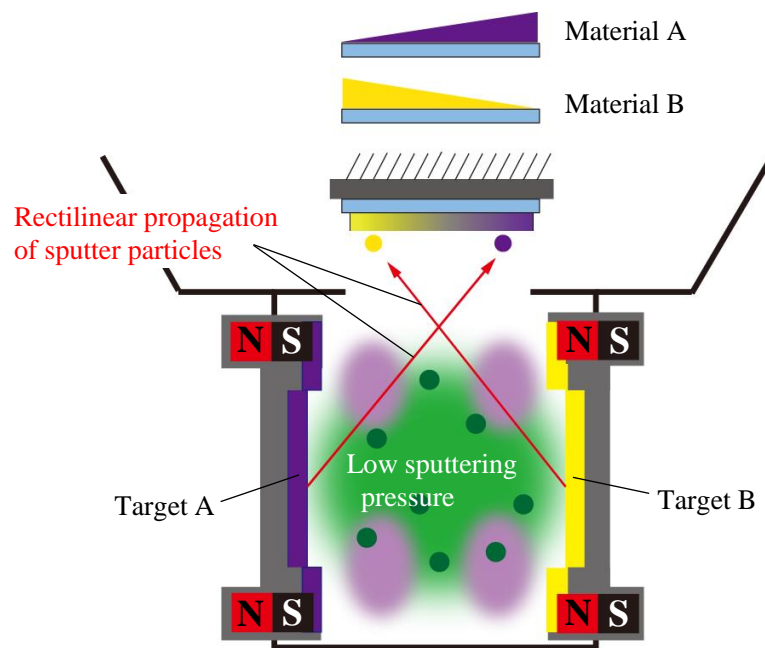


Fig. 3.5 General co-sputtering at low sputtering pressure in NFTS

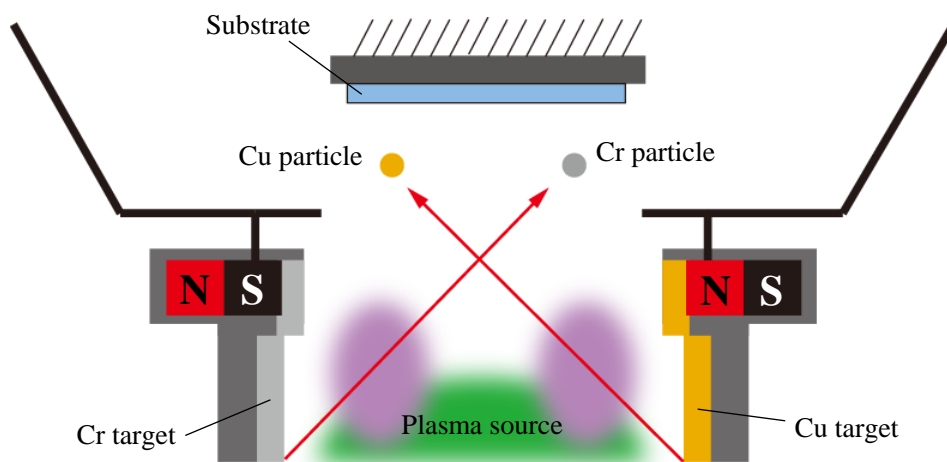


Fig. 3.6 Predicted co-sputtering of Cu-Cr in NFTS

Table 3.2 Sputtering conditions

Sputtering pressure (Pa)	0.3/1.0/1.5/2.5
Sputtering power (W)	Cu target: 500
	Cr target: 500
Sputtering time (min)	30
TS distance (mm)	82
Deposition area	26 × 76

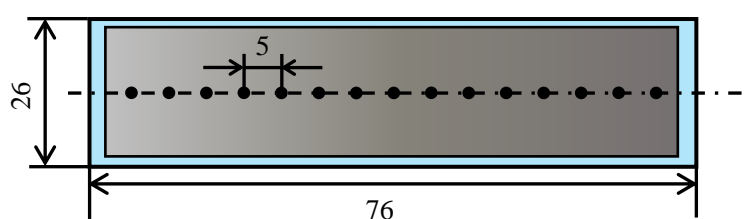


Fig. 3.7 Measurement points for EDX analysis (total: 15 points)

3.3.2 Mechanism of compositional gradient

Fig. 3.8 shows the compositional gradients obtained at different sputtering pressures. The results show that the range of the compositional gradient increased as the sputtering pressure was increased, which was markedly different from the results previously reported by N. Mori. Contrary to expectations, a thin film with a uniform composition can be formed by sputtering at low sputtering pressures (0.3 Pa). The measured compositional gradient (Δx at.%) was 1.2 at.% in the range of 76 mm.

In the case of 1.0 Pa in argon, the compositional gradient ($\Delta 5.1$ at.%) was attained, becoming wider than that with 0.3 Pa in argon. These results are contrary to the theory of N. Mori. As seen from this tendency, in the combination of Cu and Cr targets, target particles are originally less likely to reach the far edge of the substrate. Moreover, as the sputtering pressure increases, the mean free path of each sputtered particles decreases (thermalization)¹¹²⁾ (Fig. 3.9); hence, the sputtered particles have less kinetic energy. Therefore, target particles tend to be delivered more difficult on the far side, providing the wide compositional gradient. Deposition rate basically follows cosine law, however it alters depending on the combination of targets. This is because co-sputtering is conducted based on multiple targets, and sputter particles flicked off are transported in complexity. Thus, the distribution of sputtered particles does not always obey a cosine law.

Some researchers reported the same phenomenon¹¹³⁾⁻¹¹⁵⁾. J. Williams et.al¹¹⁶⁾⁻¹¹⁸⁾ studied the differential sputtering yield, and revealed that the distribution of ejected sputter particles did not simply obey a cosine law. When xenon ion beam (150–1500 eV) was vertically applied to the targets (molybdenum or carbon composite materials), deposition rate became strongest with 45–60° between the normal line of the target and the incident direction of the xenon beam. Prediction of the transportation of sputter particles during the ions bombardment has been studied much¹¹⁹⁾⁻¹²¹⁾. Based on the simulation model (e.g., monte carlo simulation), film deposition technology, such as gas motion or tracing the sputtered particles were more cleared. Although that simulation must be helpful, experimental analysis will be also necessary.

The author revealed the mechanism of simultaneous depositions of Cu–Cr. As seen from the Fig. 3.8, the widest compositional gradient ($\Delta 10.6$ at.% Cr) was attained under 2.5 Pa in argon; this condition was also used to fabricate the thin-film libraries, whose results are shown in the next section.

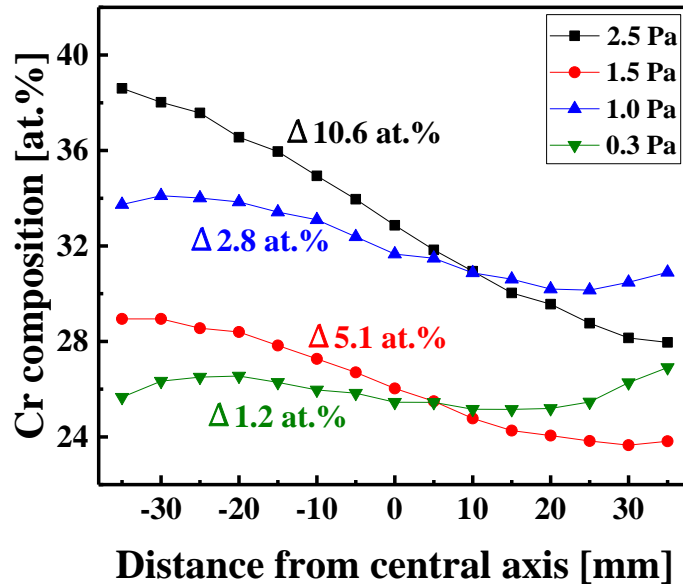


Fig. 3.8 Relationship between sputtering pressure and Cr compositional gradient

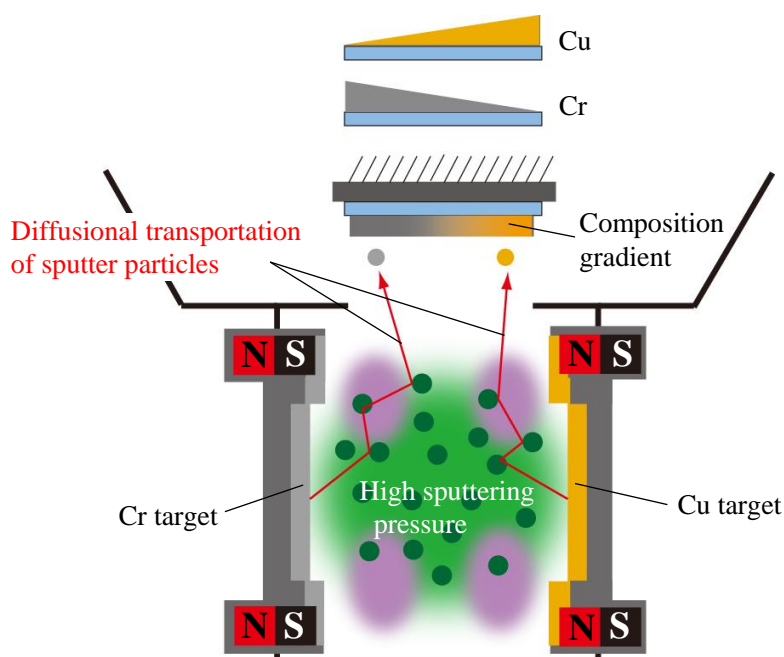


Fig. 3.9 Co-sputtering of Cu–Cr at high sputtering pressure in NFTS

3.3.3 Fabrication of thin-film libraries for combinatorial search

The thin-film library containing the initial composition of 32–22 at.% Cr was prepared by NFTS. A glass slide with dimensions 26 mm × 76 mm was used as the substrate. The substrate was first sonicated in acetone for 5 min. It was then rinsed with ethanol, followed by a rinse with deionized water, and then blow dried with air. The cleaned substrate was loaded into the sample holder of NFTS system. In general, the composition and film thicknesses change linearly in proportion to the sputtering power and time, respectively. Thus, it is possible to estimate composition and film thickness profiles in combinatorial libraries. In this study, the author targets the compositional gradient being in the range of 32–22 at.% Cr, and the film thickness having approximately 500 nm thick. Cu and Cr were simultaneously sputtered in accordance with the estimated sputtering conditions shown in Table 3.3. Fig. 3.10 shows the fabricated thin-film library.

Afterwards, the sample compositions were analyzed by EDX along the centerline at 5 mm intervals from the center of the sample. Fig. 3.11 shows the result of the compositional analysis. This result indicates that an gradient composition between 32–22 at.% Cr was successfully achieved.

Next, thicknesses of the sample were measured using the stylus step profiler. Fig. 3.11 shows

the thickness results, indicating successfully 400–500 nm thick. The so synthesized thin-film library was then screened via dealloying, and the author identified possible process parameters.

Table 3.3 Sputtering conditions for thin-film library

Sputtering pressure (Pa)	2.5
Sputtering power (W)	Cu target: 500
	Cr target: 429
Sputtering time (min)	30
TS distance (mm)	82
Deposition area	26 × 76



Fig. 3.10 Thin-film libraries fabricated under the conditions in Table 3.3

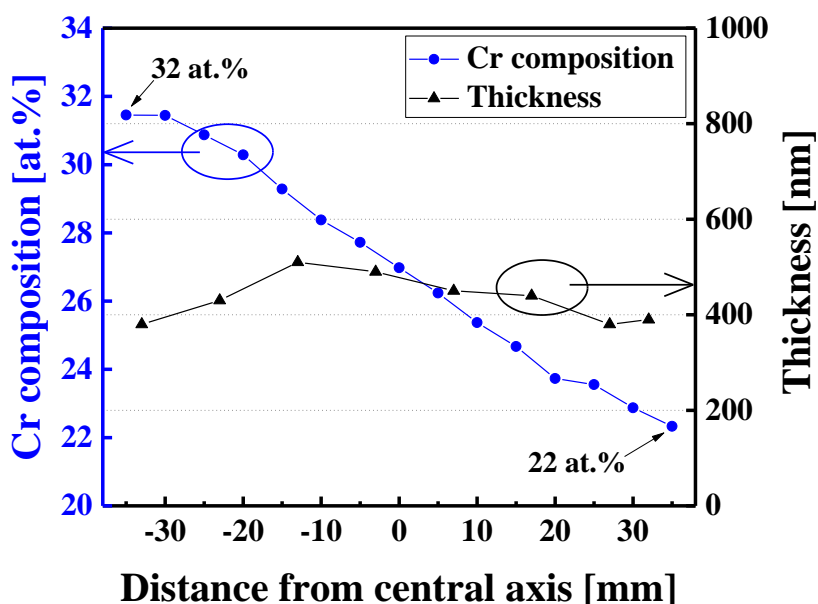


Fig. 3.11 EDX and stylus step profiler analysis of the fabricated thin-film library

3.4 Combinatorial search for nanoporous film

3.4.1 Optimization of initial alloy composition

Dependence of initial alloy compositions on final obtained nanoporous properties (Cu dealloying performance, film thickness, pore size, and porosity) was revealed by the chemical dealloying as optimized by the combinatorial method. Through the combinatorial approach, the author rapidly determined optimal initial alloy compositions. A schematic sequence of this experiment is as follows:

In the first step, thin-film libraries containing optimal compositions and film thicknesses are prepared by NFTS (Fig. 3.12(a)). The author already showed that the synthesized thin-film library having the target properties. In the second step, the fabricated thin-film library was wrapped in a titanium-foil. This processing is due to prevent the library becoming an oxidation during heat-treatment (Fig. 3.12(b)). In the third step, the sample wrapped in the titanium-foil was vacuum-enclosed in a glass (pyrex) tube at base-pressure of $7.0\text{--}8.0 \times 10^{-3}$ Pa (Fig. 3.12(c)). This processing allows a vacuum heating of large-size samples. In the fourth step, the vacuum enclosed sample was loaded in an electric furnace, and then heated at 300 °C for 1 h. After heating, the sample was allowed to cool down to room temperature in the furnace (Fig. 3.12(d)). After removing the library from the glass tube (Fig. 3.12(e)), it was then Cu dealloyed in HNO₃ solution for 15 h at room temperature (Fig. 3.12(f)).

The obtained sample after each treatment was shown in Fig. 3.13; (a) after as-depositing, (b) after vacuum heating, and (c) after Cu dealloying. It was seen that the appearance of the sample changed from silver to black through the dealloying process.

After dealloying, the sample was then rinsed with ethanol and deionized water and blow dried with air. Next, compositions and film thicknesses of the dealloyed sample were analyzed. For analyses, EDX and stylus step profiler were employed. Fig. 3.14 shows the composition analysis before and after dealloying. As shown from the result, the initial Cr composition, which was 32–22 at.%, became 79–97 at.% after dealloying.

It is especially interesting to note that initial Cr composition between 28–22 at.% (herein referred to as region A) resulted in 9–3 at.% residual Cu, which was a favorable result since the desired Cu composition is less than 10 at.%.

The obtained combinatorial analysis did not coincide on the first chemical dealloying of Cu₆₈Cr₃₂ shown in Table 3.1(a); Initial 32 at.% Cr for the thin-film library became 79 at.% Cr,

whereas the first Cu dealloying altered the initial Cr composition from 32 to only 55 at.% Cr even so the same experimental conditions. This can be attributed to the sputtering pressure, where the thin-film library was deposited at 2.5 Pa in argon, and the first $\text{Cu}_{68}\text{Cr}_{32}$ film was deposited at 0.5 Pa in argon. As explained using schematic diagram shown Fig. 3.9, kinetic energy of the transported target particles depends on the sputtering pressure.

For example, under low sputtering pressure (0.5 Pa), the mean free path of each sputtered particle increases; hence, the kinetic energy of each sputtered particle increases, thus probably resulting in higher film density (e.g., the first $\text{Cu}_{68}\text{Cr}_{32}$ film). In contrast, thin films fabricated under higher sputtering pressures (2.5 Pa) exhibit relatively low densities because the sputtered particles have less kinetic energy, leading to greater porosity in the formed film (e.g., the thin-film library). The film density may have a significant influence on the Cu etching rate. It can be considered that the low density thin-film library might allow the favorable infiltration of HNO_3 solution into the film, resulting in better Cu dealloying (initial 32→79 at.% Cr for 15 h Cu dealloying). This hypothesis is clearly explained in chapter 4.

In general, as-deposited film density is also characterized by sputtering power. The kinetic energy of sputtered particles increases with increasing of sputtering power, promising the highly-density film. As seen from Table 3.1 and 3.3, the Cu dealloying on the thin-film library originally should be slow based on the both high sputtering power for the Cu (500 W) and Cr target (429 W). But in fact, the prepared thin-film library was more favorable for Cu dealloying than the $\text{Cu}_{68}\text{Cr}_{32}$ film deposited under Table 3.1, because the sputtering pressure strongly determined the final film density. The author considered that the sputtering pressure was preferential process parameter, and the film characteristics may not be strongly affected by the sputtering power. Especially for high sputtering pressure, the transport of the sputtered particles becomes rather diffusion state, therefore the difference of each sputtering power does not have great influence on the as-deposited film characteristics. From the above, the author did not exactly optimize the sputtering power in this work.

Later, sample thicknesses were evaluated using the stylus step profiler. Fig. 3.15 shows that there is almost no change in thickness before and after dealloying. The average thickness was approximately 430 nm and 450 nm before and after dealloying, respectively. Although the film with an original composition of 22–23 at.% Cr locating in the edge was partially dissolved, this result means that the author could successfully remove Cu from the Cu–Cr films without film

dissolution.

In conclusion, region A could produce an excellent Cu dealloying performance without film dissolution. Moreover, new chemical dealloying where initial compositions were carefully adjusted, successfully offered the Cu dealloying even at low-temperature coarsening.

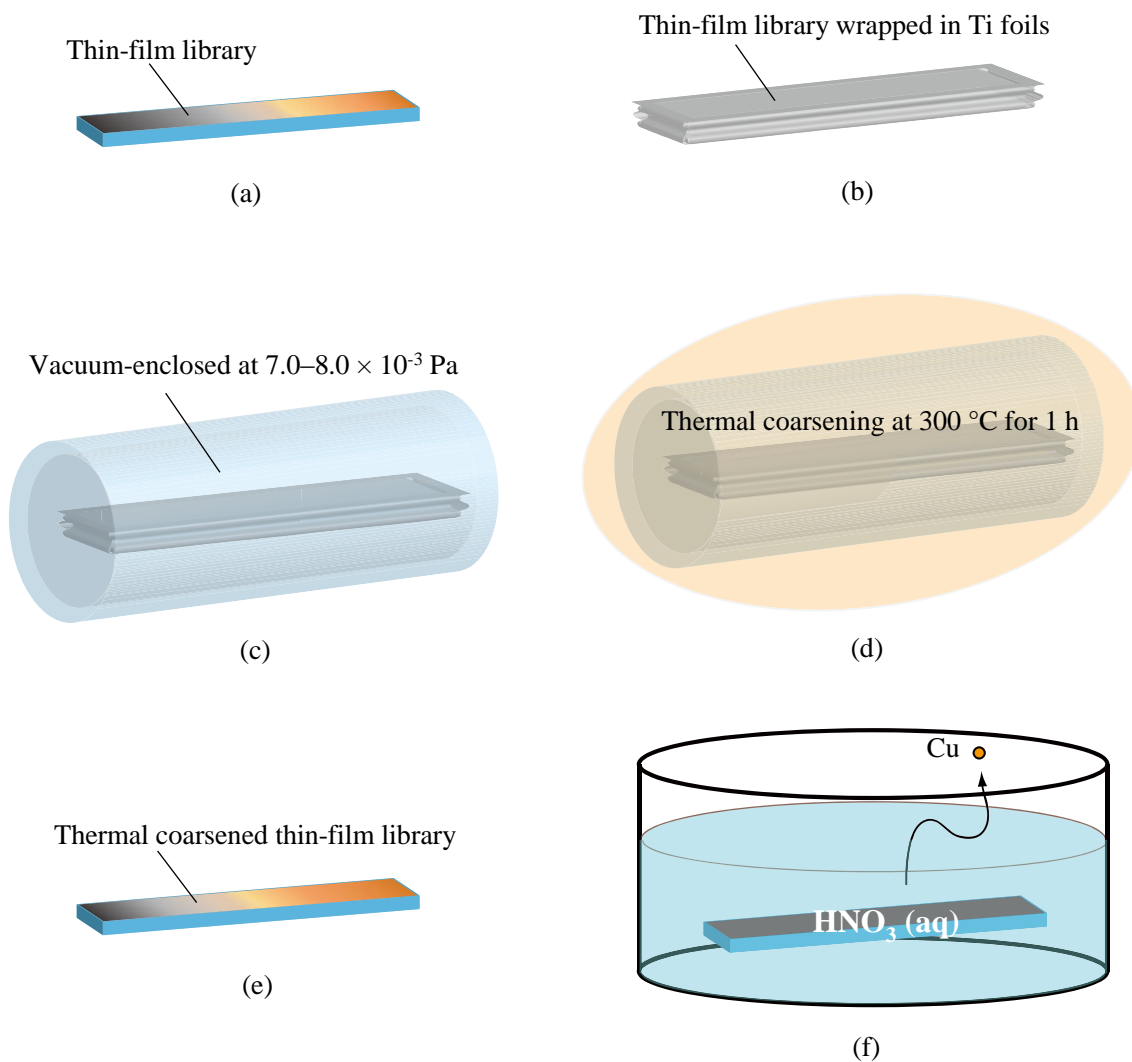


Fig. 3.12 Chemical dealloying as optimized by combinatorial method; (a) fabrication of a thin-film library in NFTS, (b) The thin-film library was swathed in a titanium foil to prevent the sample becoming in oxidation state, (c) the sample is vacuum-enclosed in a glass-tube (base pressure: $7.0-8.0 \times 10^{-3}$ Pa), (d) thermal coarsening at 300 °C for 1 h, (e) remove the sample from the glass-tube, and (f) Cu dealloying in 32.5% HNO₃ for 15 h at room temperature.

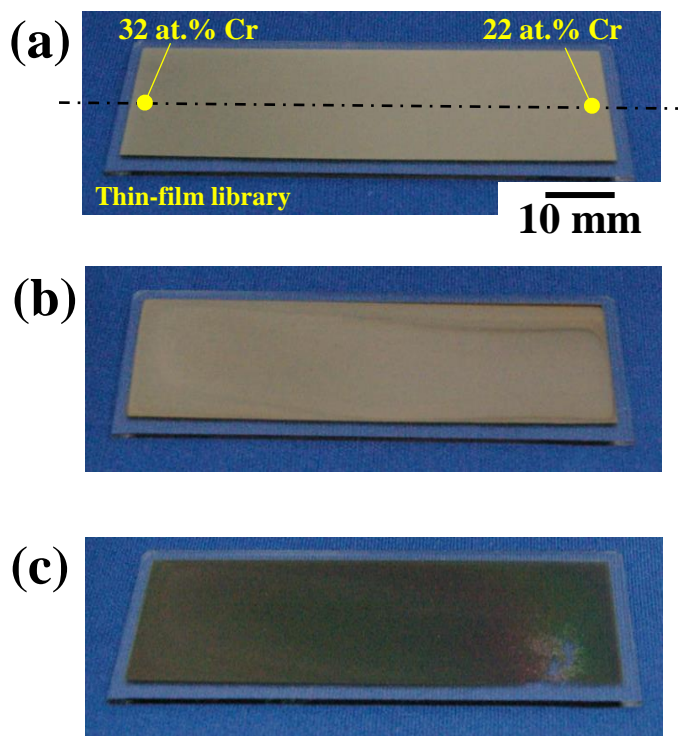


Fig. 3.13 Obtained thin-film library; (a) after as-deposition, (b) after thermal coarsening, and (c) after Cu dealloying

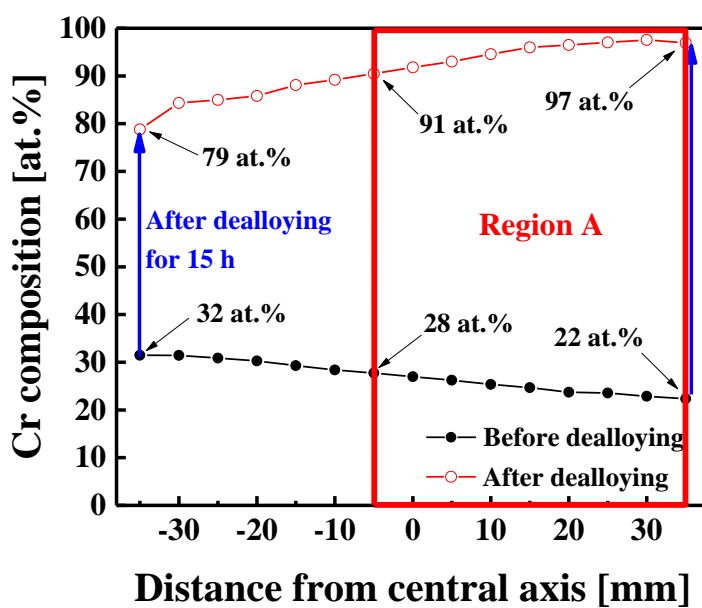


Fig. 3.14 Compositional analysis by EDX before and after dealloying

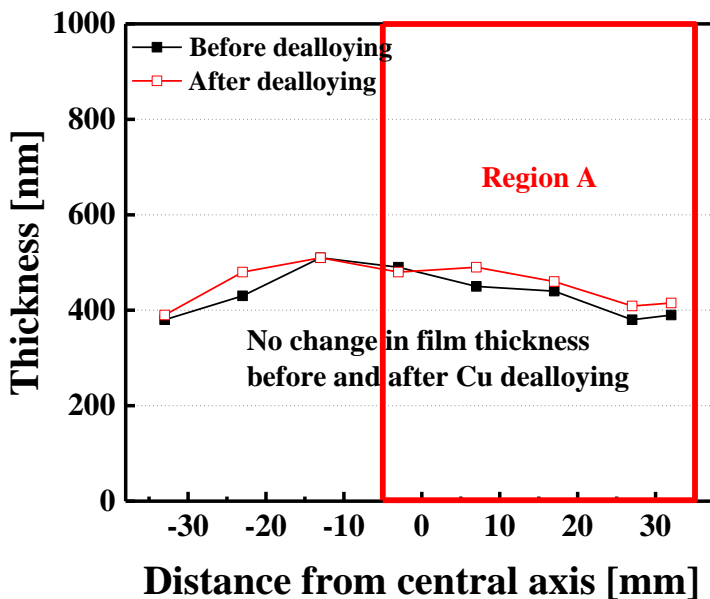


Fig. 3.15 Film thickness analysis by stylus step profiler before and after dealloying

3.4.2 Relationship between initial alloy composition and pore size

Surface characterization using the secondary electron mode on the FE-SEM was performed on the dealloyed film for pore size measurements. As seen from Fig. 3.16, four points (a)–(d), corresponding to initial Cr compositions of 32, 28, 25, 22 at.%, respectively, were observed by using FE-SEM. The FE-SEM images in Fig. 3.17, taken after the dealloying process, show that the pore size obtained increased as the initial Cr composition decreased. The pore sizes obtained were avg. 70 nm for initial 22 at.% Cr (Fig. 3.17(a)), avg. 54 nm for initial 25 at.% Cr (Fig. 3.17(b)), avg. 36 nm for initial 28 at.% Cr (Fig. 3.17(c)), and avg. 24 nm for initial 32 at.% Cr (Fig. 2.17(d)), respectively. The author summarizes the pore size measurements in Fig. 3.18. Obtained pore size sharing the excellent Cu dealloying in region A was estimated at avg. 36–70 nm. These pore sizes were ideally, and expected for the target molecular filters.

It is easy to find that the pore size and porosity increase with decrease of initial Cr composition. X. Lu et.al.³⁶⁾ also reported that less non-dealloyed content correlated with a higher porosity. Fig. 3.17(c) and (d) were unclear because charging readily occurred when an electron beam irradiated the sample. Poor electrical conduction property represents a low volume density of the film, suggesting a high film porosity. Next, the author evaluated the relationship between initial Cr compositions and porosities. To assess porosities, image data processing was used.

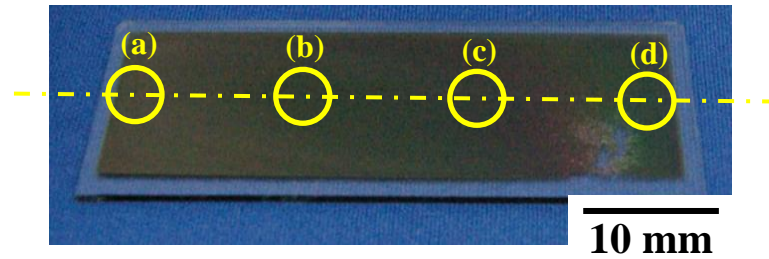


Fig. 3.16 Observation points (total: 4 points) for FE-SEM

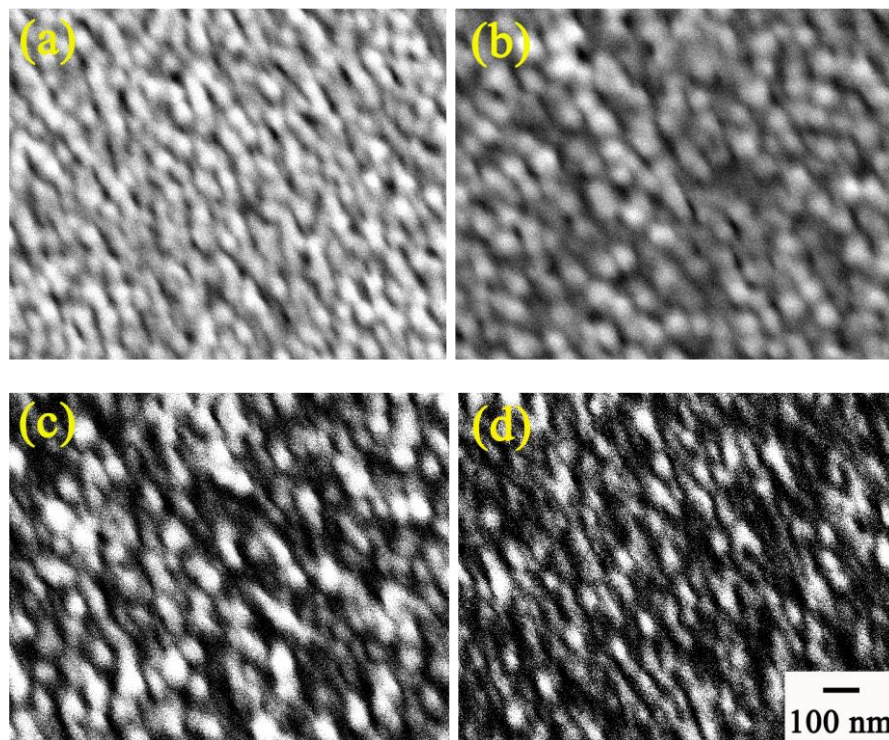


Fig. 3.17 FE-SEM images of the Cu dealloyed films from an area with an initial composition of (a) 32 at.% Cr, (b) 28 at.% Cr, (c) 25 at.% Cr, and (d) 22 at.% Cr. The estimated pore sizes were avg. 24 nm for 32 at.% Cr, avg. 36 nm for 28 at.% Cr, avg. 54 nm for 25 at.% Cr, and avg. 70 nm for 22 at.% Cr.

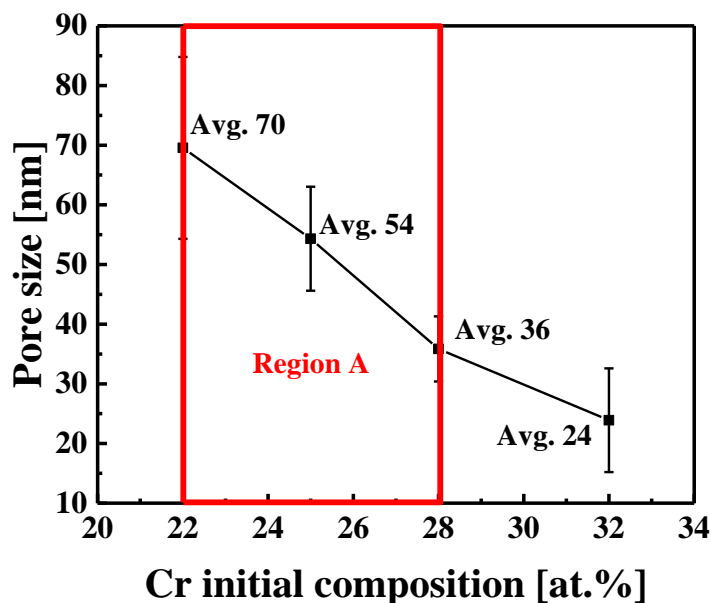


Fig. 3.18 Relationship between initial Cr composition and final pore size

3.4.3 Relationship between initial alloy composition and porosity

Porosities were determined based on area ratio by image processing (Software: GIMP). The FE-SEM images (Fig. 3.17(a)–(d)) were binarized, generating such binary images (Fig. 3.19(a)–(d)). A rate of pixels in the porous area to all pixels in the binary image was calculated. Through the processing, the author studied the relationship between initial alloy composition and porosity. Fig. 3.20 shows that the porosity decreases with the increase of initial Cr composition. The measured porosities of the dealloyed sample were 59% for initial 22 at.% Cr, 42% for initial 25 at.% Cr, 24% for initial 28 at.% Cr, and 20% for initial 32 at.% Cr. Hence, the porosity lying in region A was 24–59%.

The author summarizes the combinatorial analyses obtained in Fig. 3.21. The proposed combinatorial search combined with the rapid screening by dealloying offered successfully optimal initial alloy compositions. Under the initial alloy compositions in region A, the residual Cu after dealloying was found less than 10.0 at.%, demonstrating that the Cu dealloying can be allowed even at low-temperature coarsening. Furthermore, pore size of avg. 70–36 nm could be achieved under the fabrication condition in region A. Therefore, chemical dealloying as optimized by combinatorial method accelerated a discovery of process parameters as well as final properties of nanoporous films by only one experiment.

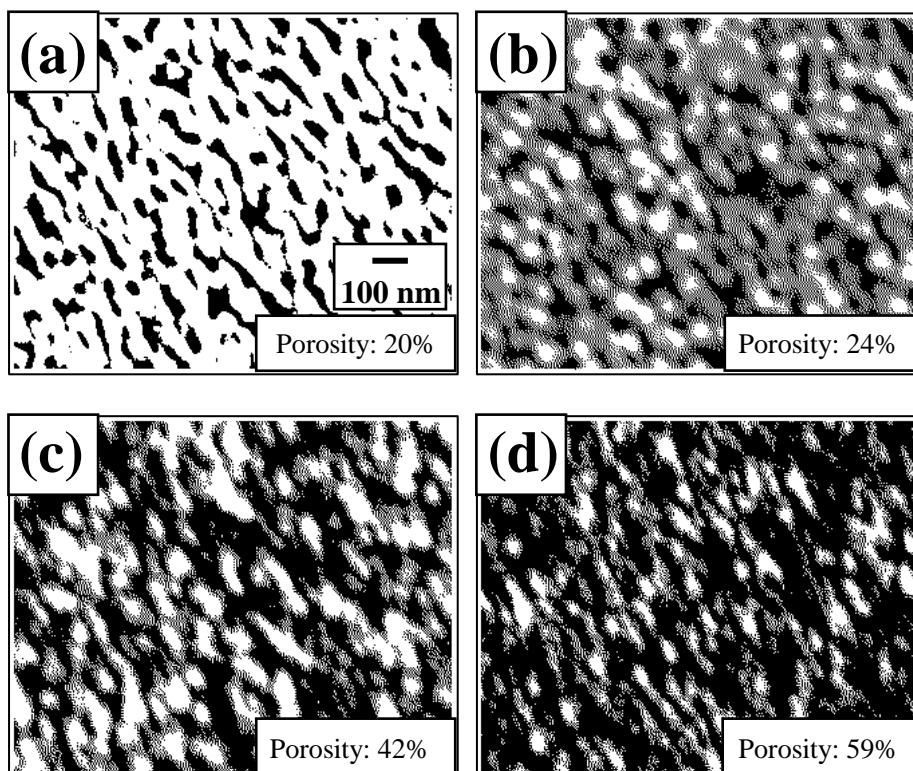


Fig. 3.19 Binary images (a)–(d) generated from FE-SEM images (a)–(d), respectively. The estimated porosities were 20% for initial 32 at.% Cr, 24% for initial 28 at.% Cr, 42% for initial 25 at.% Cr, and 59% for initial 22 at.% Cr.

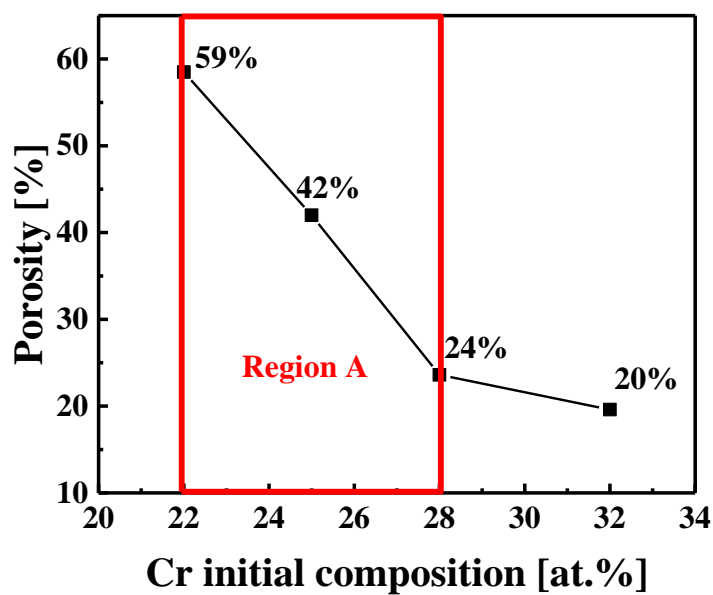


Fig. 3.20 Relationship between initial Cr composition and porosity

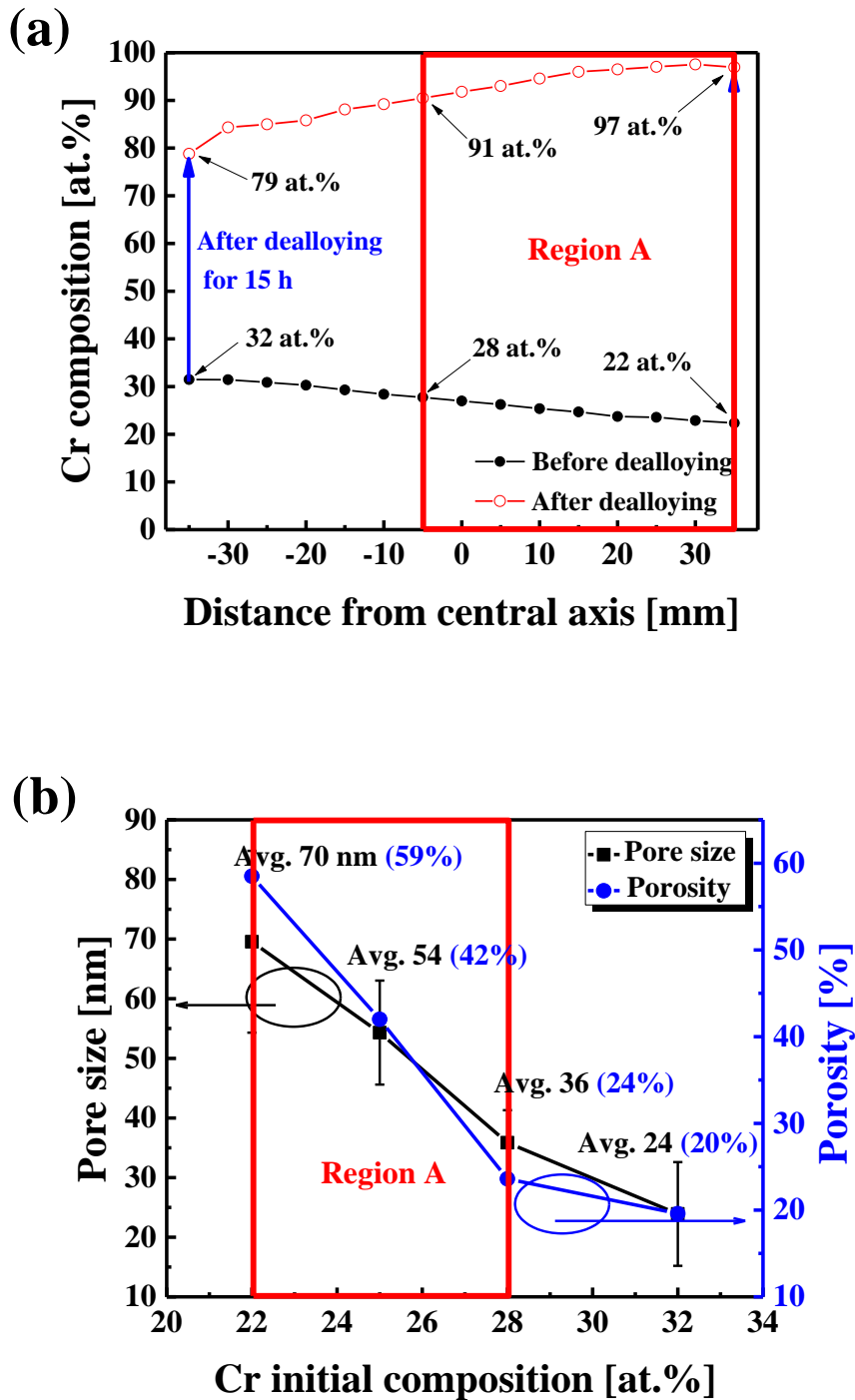


Fig. 3.21 Summary of the combinatorial approach to determine the optimal initial Cu–Cr compositions for chemical dealloying; a Cu–Cr film with a compositional gradient of 32–22 at.% Cr was used. Between 28–22 at.% Cr (Region A), dealloying produced nearly pure Cr-based nanoporous film as seen from (a), and the estimated pore size and porosity lying in region A were in the range of avg. 36–70 nm and 24–59%, respectively.

3.5 Summary

This chapter presented the first challenging chemical dealloying combined with the low-temperature coarsening. The author targeted to fabricate nanoporous films fixed on polyimide films via chemical dealloying, and tried to lower the required coarsening temperature from 700 °C to 300 °C. Originally, it was impossible to achieve this chemical dealloying, since this heat temperature was extremely small and unsatisfied for a thermal coarsening. As expected, the preliminary test demonstrated the author's hypothesis; the $\text{Cu}_{68}\text{Cr}_{32}$ film could not be fully Cu dealloyed owing to the poor grain growth based on the low-temperature coarsening. The original elemental composition ended up with $\text{Cu}_{45}\text{Cr}_{55}$ after dealloying. Generally, 500 °C is at least required for the thermal coarsening for Cu–Cr films. Therefore, grain size did not grow significantly with 300 °C. The author concluded that this poor grain growth might hamper the infiltration of the HNO_3 solution into the film.

However, another preliminary test showed signs of success; the $\text{Cu}_{78}\text{Cr}_{22}$ film was, in contrast, completely dissolved during the dealloying. This may have been resulted from the low initial Cr composition, which prevented the formation of a nanoporous structure. This result means that reducing the initial Cr content to below 32 at.% might allow Cu dealloying to produce a Cr-based nanoporous film.

Response to the previous study, the author employed the combinatorial investigation. The author prepared the thin-film libraries synthesizing multiple compositions varying continuously from 32–22 at.% Cr. The thin-film libraries were fabricated by NFTS. First, the author described the deposition mechanism in NFTS. General materials synthesis in NFTS was cleared. Furthermore, the author investigated the influence of sputtering pressure on the Cr compositional gradient. By comparing the author's combinatorial film sputtering with the previous results, the author investigated the technical difference among them, revealing the co-sputtering of Cu–Cr did not follow a cosine law.

Next, the author determined the sputtering conditions, and prepared the target libraries. The so fabricated libraries were rapidly screened through the dealloying process. In the part of the film with an initial Cr composition in the range of 28–22 at.% (= region A), the dealloying treatment resulted in sufficient Cu dealloying (the final Cr composition in region A was 91–97 at.%, which was almost Cr-based films) without dissolving the film. Therefore, the combinatorial approach efficiently clarified the relationship between the initial Cu–Cr composition and the degree of Cu

dealloying. Moreover, it was markedly to note that further adjustment of initial alloy compositions enabled the sufficient Cu dealloying, even if the coarsening temperature was smaller than the minimum required value.

Afterwards, the author examined the microstructures of dealloyed films using FE-SEM. The measured pore sizes were closely related to the initial alloy compositions; the final pore size increased as the initial Cr composition decreased. The pore sizes obtained were avg. 70 nm for initial 22 at.% Cr, avg. 54 nm for initial 25 at.% Cr, avg. 36 nm for initial 28 at.% Cr, and avg. 24 nm for initial 32 at.% Cr; the pore range lying in region A was estimated in avg. 36–70 nm, which were ideally for the author's target molecular filters.

Furthermore, the author studied the dependence of initial alloy composition on film porosity. The porosity of the film was also position-dependent, showing 59% for initial 22 at.% Cr, 42% for initial 25 at.% Cr, 24% for initial 28 at.% Cr, and 20% for initial 32 at.% Cr; the region A produced the 24–59% porosity.

Summary, the author successfully determined the possible process parameters for the new chemical dealloying. This could be achieved by the chemical dealloying combined with the combinatorial approach. Optimizing the process parameter from numerous candidates were achieved in a short time, suggesting a significant economic benefits.

In this chapter, however, the author was specially focusing the fabrication of nanoporous films applied to polyimide films. To meet various devices including such as plastic substrates (heat resistance temperature: 100–200 °C¹²²), the author further challenges a novel chemical dealloying without a thermal coarsening. Detailed experiments are mentioned in more detail in the next chapter.

Chapter 4 Chemical dealloying without thermal coarsening

4.1 Target

In chapter 3, the low-temperature coarsening in combination with the combinatorial technique successfully achieved the excellent Cu dealloying. Especially, effective initial alloy composition adjustment allowed significantly the Cu etching performance. Moreover, the dependence of initial alloy composition on pore size and porosity was rapidly determined through the one step experiment. However, heat-treatment with 300 °C was necessary in this method. Due to this requisites condition, the technology was still unsatisfied, limiting the selection of applications.

Accordingly, there is currently a need in the art for chemical dealloying of Cu–Cr with no requirement of thermal coarsening. In this chapter, the author newly proposes chemical dealloying without thermal coarsening. Another strong advantage of this process is that it does not require the heat-treatment processes, also promising the short process time. As mentioned in chapter 2, the chemical dealloying of Cu–Cr normally could not produce Cu dealloying and nanoporous films without thermal coarsening (see Fig. 2.7 and 2.15 in chapter 2). The previous chemical dealloying has been successfully achieved based on the grain growth produced by the thermal coarsening. As-deposited Cu–Cr films under low sputtering pressure were densely composed from small grains, thus HNO₃ solution could not reach the interior of the Cu–Cr films. The grain growth allowed the Cu–Cr film structure sterically with excellent inter-diffusion and phase separation. Therefore, binary thin films became favorable structures for chemical dealloying.

In order to achieve the chemical dealloying not depending thermal coarsening, the author additionally optimizes initial alloy composition and sputtering pressure. The author attempts to overcome this challenge by further readjustment of initial alloy compositions, as well as by optimizing Cu–Cr film densities. The author expects that low-density Cu–Cr films may permit the sufficient dealloying of Cu to produce Cr-based nanoporous films.

First, the author simply tests a chemical dealloying without thermal coarsening. In chapter 3, the author already reported the test using the Cu₆₈Cr₃₂ films. This process failed in the Cu dealloying owing to the high initial Cr composition. Thus, the author initially tries Cu₇₈Cr₂₂ films. This first challenge is carefully evaluated by EDX and stylus step profiler, where compositions and film thicknesses before and after dealloying are measured. Afterwards, the author mentions experimental results, and discusses about technical problems remained.

In order to complete a sufficient Cu dealloying without thermal coarsening, the author proposes a further adjustment of initial alloy compositions. The same as before, the author prepares new thin-film libraries using NFTS. Based on the preliminary analysis, the author first estimates sputtering conditions. The fabricated libraries are rapidly screened via chemical dealloying, and the author identifies an optimal initial alloy composition (herein referred to as $\text{Cu}_x\text{Cr}_{100-x}$).

Moreover, the author studies a relationship between the $\text{Cu}_x\text{Cr}_{100-x}$ film density and the Cu etching rate. The binary film density may strongly relate to the selective metal dissolution. However, studies regarding the influence of the film density on the dealloying performance have not been reported to date. In co-sputtering, film density can be controlled by sputtering pressure. The author compares high- and low-density $\text{Cu}_x\text{Cr}_{100-x}$ films based on the Cu etching rate. The dealloyed films are evaluated using EDX, stylus step profiler, XRD, and FE-SEM.

In the final, the author also reveals an influence of substrate type used on final dealloyed morphology. The author expects that different substrate type may yield a rich variety of characteristic of the resulting nanoporous films. In this study, $\text{Cu}_x\text{Cr}_{100-x}$ films are deposited on glass substrates or polyimide films. Two samples are Cu dealloyed under the same experimental conditions, and subsequently the final nanostructures formed on different substrates are compared.

4.2 Preliminary chemical dealloying test

The aim of the present study was to fabricate nanoporous films with optimal pore size (10–50 nm) via chemical dealloying without thermal coarsening. Fig. 4.1 shows the process of chemical dealloying of $\text{Cu}_{78}\text{Cr}_{22}$. A glass substrate (26 mm × 26 mm) was used. The substrate was first sonicated in acetone at 100 kHz for 5 min. It was then rinsed with ethanol and then rinsed with deionized water at 100 kHz for 5 min, respectively. After blow drying the substrate with compressed air, it was placed on a hot plate, and heated at 110 °C for 5 min. Through the process, the water remained on the substrate was fully removed (Fig. 4.1(a)).

The cleaned substrate was loaded in NFTS, and then Cu and Cr were simultaneously sputtered onto the glass substrate to deposit a $\text{Cu}_{78}\text{Cr}_{22}$ film (500 nm thick) with a uniform composition (Fig. 4.1(b)). Table 4.1 shows the sputtering conditions. The as-deposited $\text{Cu}_{78}\text{Cr}_{22}$ film was readily immersed in 22.5% HNO_3 for 15 h at room temperature (Fig. 4.1(c)).

The resulting $\text{Cu}_{78}\text{Cr}_{22}$ film was slightly dealloyed only at the surface, and its composition changed to $\text{Cu}_{76}\text{Cr}_{24}$ (Fig. 4.2). The final composition remained the same even when the

dealloying time was prolonged. The limited dissolution of Cu is likely attributed in part to the high initial Cr composition, which hindered the infiltration of the HNO_3 solution into the film (Fig. 4.3). Thus, reducing the initial Cr composition to below 22 at.% might allow Cu dealloying to produce a Cr-based nanoporous film. As proved in chapter 3, a combinatorial investigation will be helpful for the determination of the optimal alloy composition ($\text{Cu}_x\text{Cr}_{100-x}$). Consequently, the author fabricated Cu–Cr thin film libraries with a compositional gradient containing to below 22 at.% Cr. The fabrication procedure is described in more detail below.

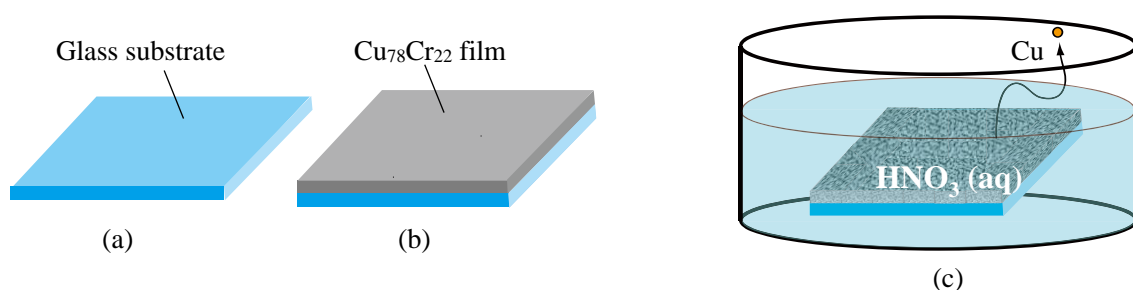


Fig. 4.1 Schematic sequence of initial chemical dealloying; (a) substrate cleaning, (b) co-sputtering of $\text{Cu}_{78}\text{Cr}_{22}$ film, and (c) Cu dealloying in 22.5% HNO_3 for 15 h at room

Table 4.1 Sputtering conditions

Sputtering pressure (Pa)	0.5
Sputtering power (W)	Cu target: 212
	Cr target: 138
Sputtering time (min)	15
TS distance (mm)	82
Deposition area	26×26

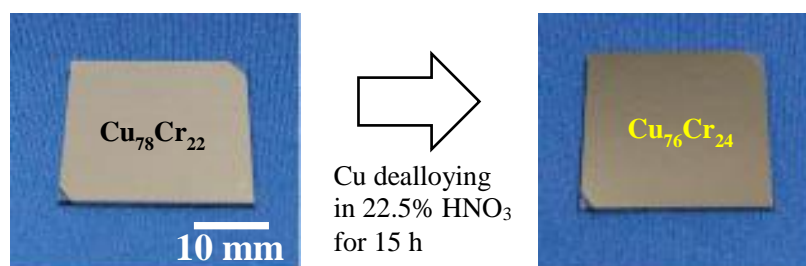


Fig. 4.2 Initial chemical dealloying of before and after Cu dealloying

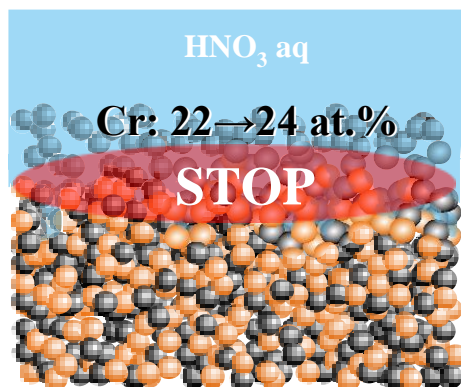


Fig. 4.3 Schematic diagram of chemical dealloying of $\text{Cu}_{78}\text{Cr}_{22}$

4.3 Fabrication of thin-film libraries for combinatorial search

The substrate used was the same dimension with 26 mm \times 76 mm. The substrate was first sonicated in acetone at 100 kHz for 5 min. It was then rinsed with ethanol, followed by a rinse with deionized water at 100 kHz for 5 min. After blow drying and heat treatment, the substrate was set into the sample holder of NFTS system, and subsequently co-sputtering was done (Fig. 4.4). In the previous work concerning NFTS, the achieved maximum compositional gradient was approximately 10/76 at.%/mm at 2.5 Pa in argon (see Fig. 3.8). Therefore, the author targeted the desired compositional gradient and film thickness in 22–12 at.% Cr, and 350 nm thick, respectively. It was easy to determine new sputtering conditions based on Table 3.3 (because the composition and film thicknesses change linearly in proportion to the sputtering power and time, respectively). Table 4.2 summarizes the estimated sputtering conditions.

Fig. 4.5 shows an as-deposited thin-film library. 15 points were compositionally detected by EDX (Fig. 4.6(a)), and Fig. 4.6(b) showed that they were position-dependent, successfully containing the close target range of 22–15 at.% Cr. Additionally, the obtained film thickness was approximately 380 nm, which is close to a target value (350 nm thick). Summary, the author successfully synthesized the optimal properties of Cu–Cr films on the single glass substrate. The fabricated thin-film library was employed to discover the optimal initial alloy composition ($\text{Cu}_x\text{Cr}_{100-x}$).

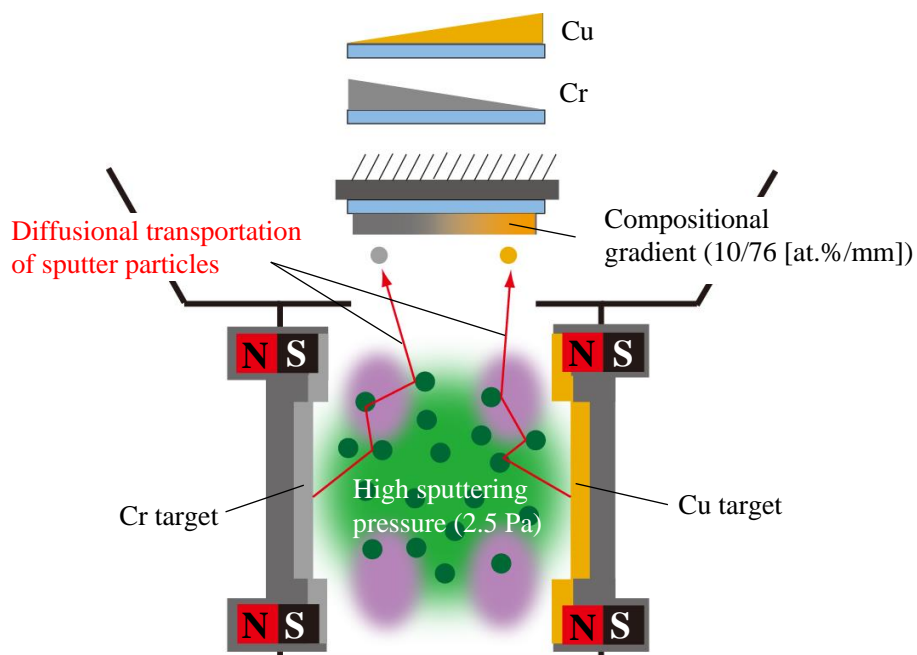


Fig. 4.4 Preparation of thin-film libraries in NFTS

Table 4.2 Sputtering conditions for thin-film library

Sputtering pressure (Pa)	2.5
Sputtering power (W)	Cu target: 500
	Cr target: 257
Sputtering time (min)	9
TS distance (mm)	82
Deposition area	26 × 76

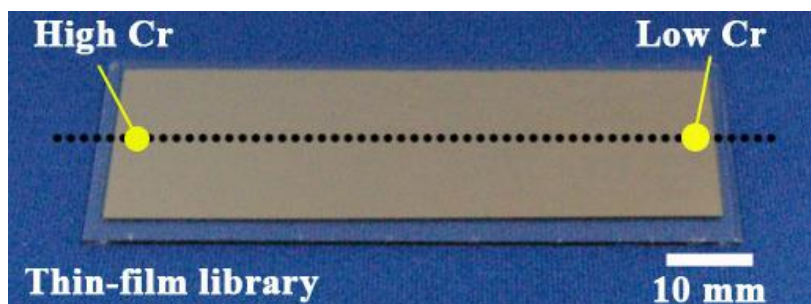


Fig. 4.5 The fabricated thin-film library

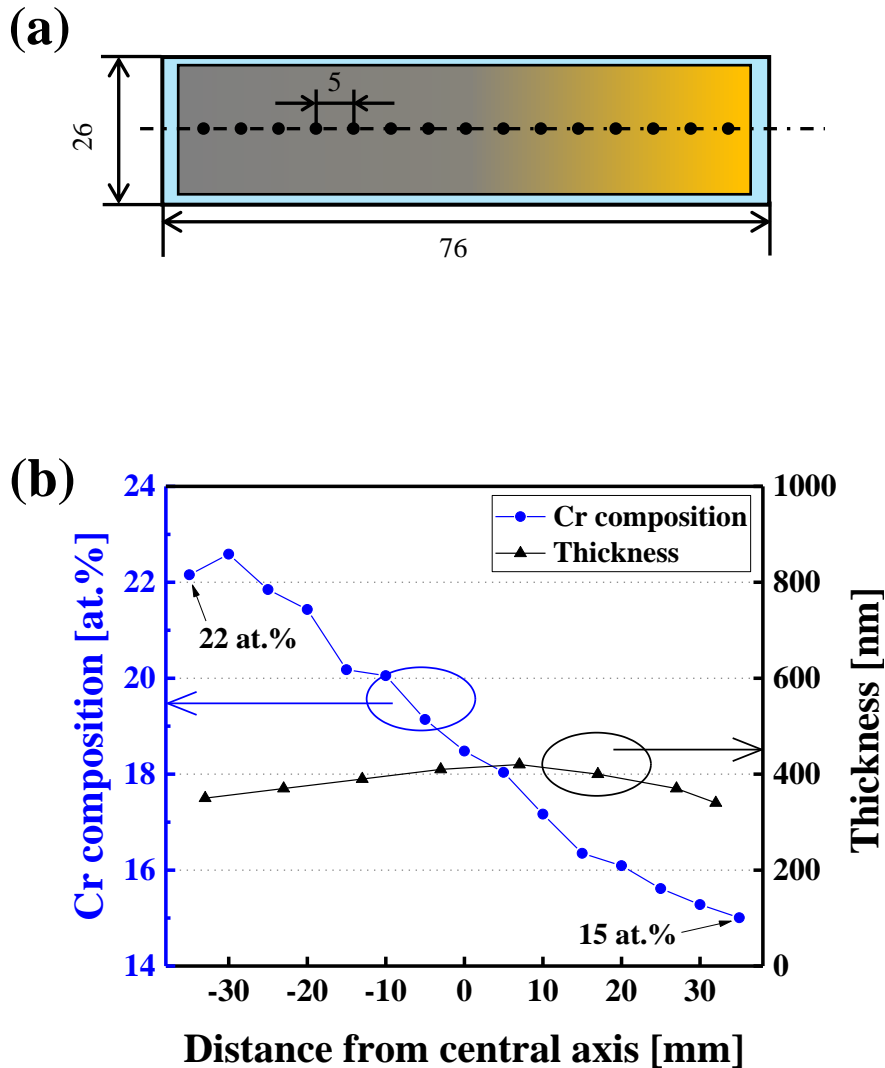


Fig. 4.6 EDX analysis in the fabricated thin-film library; (a) measurement points (total 15 points), and (b) EDX analysis indicating that compositions were position-dependent, successfully containing the near target range of 22–15 at.% Cr and avg. 380 nm thick.

4.4 Combinatorial search of nanoporous film

4.4.1 Optimization of initial alloy composition

The fabricated thin-film library was Cu dealloyed followed by the experimental procedure shown in Fig. 4.7. The dealloyed sample showed a dramatic change through the 15 h Cu dealloying treatment. The appearance of the film represented brown before dealloying (Fig.

4.7(a)), and varied as the Cu was dealloyed as shown in Fig 4.7(b). Moreover, the film was divided into two regions based on the composition and thickness of the Cu–Cr film before and after Cu dealloying as shown in Fig. 4.8(a) and (b), respectively. At all locations in region 1, the Cr concentration increased as Cu was dissolved. In this region, the film remained after dealloying (i.e., the film thickness was unchanged), and the initial Cr content (22–18 at.%) increased to 33–80 at.% after dealloying.

In region 2, the film was completely dissolved because the low Cr composition in this region prevented the formation of nanoporous structures. The results also show that an initial Cr composition of 18 at.% resulted in sufficient Cu dealloying without film dissolution. Summary, the combinatorial thin film composition mapping ensured a rapid discovery of materials or process parameters¹²³⁾⁻¹³⁰⁾. These 2D maps shown in Fig. 4.7(a) and (b) suggest that initial 18 at.% Cr may be a point between success and failure in chemical dealloying of Cu–Cr. In other word, initial Cr composition of 18 at.% is a minimum permissible concentration that can keep the dealloyed film stability. Cr-based nanostructures could be maintained well during the Cu dealloying, and finally it may produce 3D interconnected morphologies.

Under the initial 18 at.% Cr, however, the residual Cu composition after dealloying was 20 at.%. This result was over the target range (0–10 at.% Cu). This limited Cu dealloying can be attributed to the small Cr grains that were rather densely packed in the Cu–Cr film, resulting in the insufficient infiltration of HNO₃ solution into the film. The author attempted further Cu etching by prolonging the dealloying time, but the Cu dealloying could not be completed. Long time dealloying hampered the stability of Cu–Cr films, and their edges were partially dissolved. It may be that some of the Cu was necessary for maintaining the dealloyed film stability.

Comparing with the above chemical dealloying of Cu₈₂Cr₁₈, the chemical dealloying of Cu₆₈Cr₃₂ including high-temperature coarsening at 700 °C produced excellent Cu dealloying. The dealloyed Cu–Cr films were almost Cr-based nanoporous films; the final Cr composition was approximately 99 at.% Cr (see Table 2.2). This excellent Cu dealloying performance could be achieved based on the high initial 32 at.% Cr and thermal coarsening. High initial Cr content (32 at.%) prevents the dissolution of films during the dealloying. Moreover, thermal coarsening offered the sufficient grain growth as well as inter-diffusion. In this process, large Cr and Cu particles produced by thermal coarsening were fully diffused, forming ideal binary alloys with a uniform structure. Therefore, Cu was easily etched out, while high initial 32 at.% Cr could also

maintain the porous structures even if the residual Cu became less than 2.0 at.%. This has led to the successful Cu dealloying and Cr-based nanoporous films.

In principle, as-deposited films by sputtering own the unfavorable structure, where thin films were closely consisted from small each metal grains with poor phase separation. Therefore, the early structures may hinder the infiltration of the HNO_3 solution into the film. Selective dissolution from such binary alloys was difficult, resulting in the observed limited Cu dissolution.

Although the newly proposed chemical dealloying step did not completely remove all Cu from the film, the best initial alloy composition ($\text{Cu}_x\text{Cr}_{100-x} = \text{Cu}_{82}\text{Cr}_{18}$) was successfully optimized. This initial composition ($\text{Cu}_{82}\text{Cr}_{18}$) has still possibility, and therefore the author selected it as the optimal initial alloy composition to fabricate the nanoporous film herein.

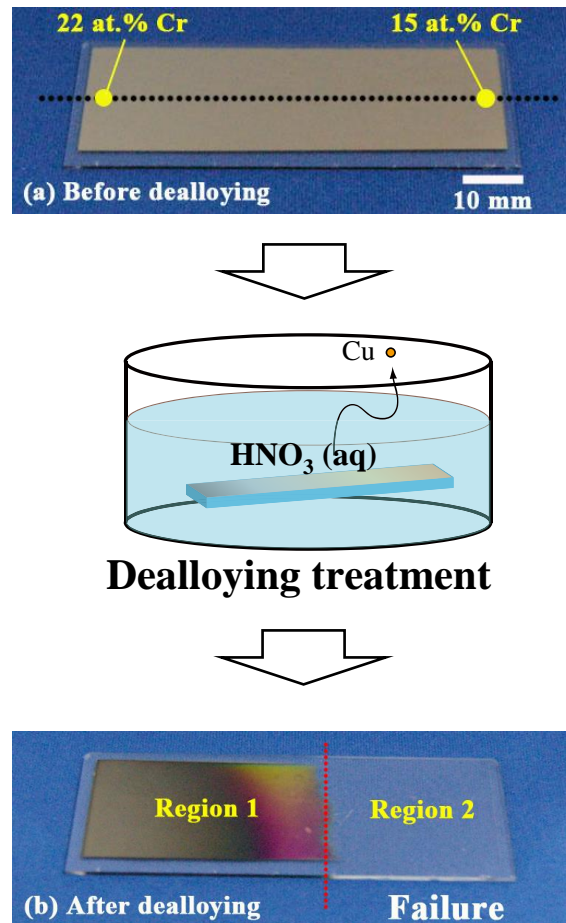


Fig. 4.7 Chemical dealloying procedure using the thin-film library; (a) preparation of the thin-film library in NFTS, through the Cu dealloying, and (b) the screened thin-film library.

4.4.2 Relationship between Cu–Cr film density and Cu etching rate

The relationship between the Cu–Cr film density and the Cu etching rate was characterized in $\text{Cu}_{82}\text{Cr}_{18}$ films (dimension: 3.6 mm \times 5.0 mm) under differential sputtering pressures of 0.5 and 2.5 Pa in argon. The density of the sputtered film strongly depends on the sputtering pressure. For example, under low sputtering pressures, the mean free path of each sputtered particle increases; hence, the kinetic energy of each sputtered particle increases, resulting in higher film density (Fig. 4.9(a)). In contrast, thin films fabricated under higher sputtering pressures exhibit relatively low densities because the sputtered particles have less kinetic energy, resulting in greater porosity in formed film (Fig. 4.9(b)).

The film density may have a significant influence on the Cu etching rate. Fig. 4.10 is the author's images of the dealloying mechanism in $\text{Cu}_{82}\text{Cr}_{18}$ films fabricated under differential sputtering pressures of 0.5 and 2.5 Pa. While the $\text{Cu}_{82}\text{Cr}_{18}$ film deposited at 0.5 Pa exhibit high film density, the film deposited at 2.5 Pa may exhibit lower density. The dense $\text{Cu}_{82}\text{Cr}_{18}$ film may hinder the infiltration of aqueous HNO_3 into the film (Fig. 4.10(a)). On the other hand, the porosity of the low-density $\text{Cu}_{82}\text{Cr}_{18}$ film is expected to allow the aqueous HNO_3 to easily reach the interior of the Cu–Cr film (Fig. 4.10(b)). Thus, it was hypothesized that reducing the Cu–Cr film density by increasing the argon pressure may result in better Cu dealloying and yield a Cr-based nanoporous film. Hence, the sputtering pressure for chemical dealloying was optimized.

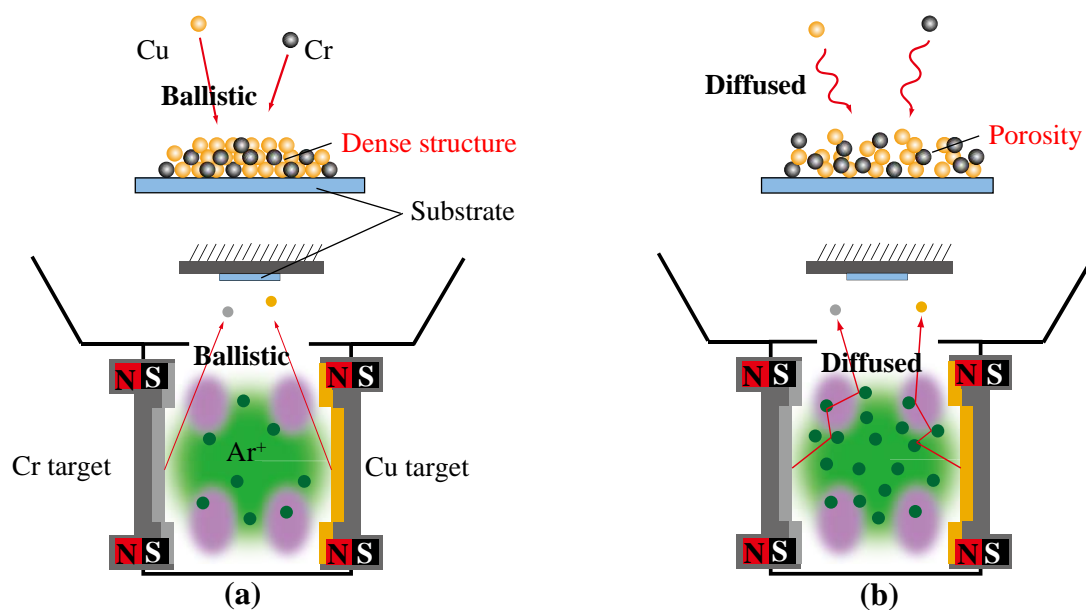


Fig. 4.9 Film density depending on sputtering pressure; (a) low- and (b) high-pressure

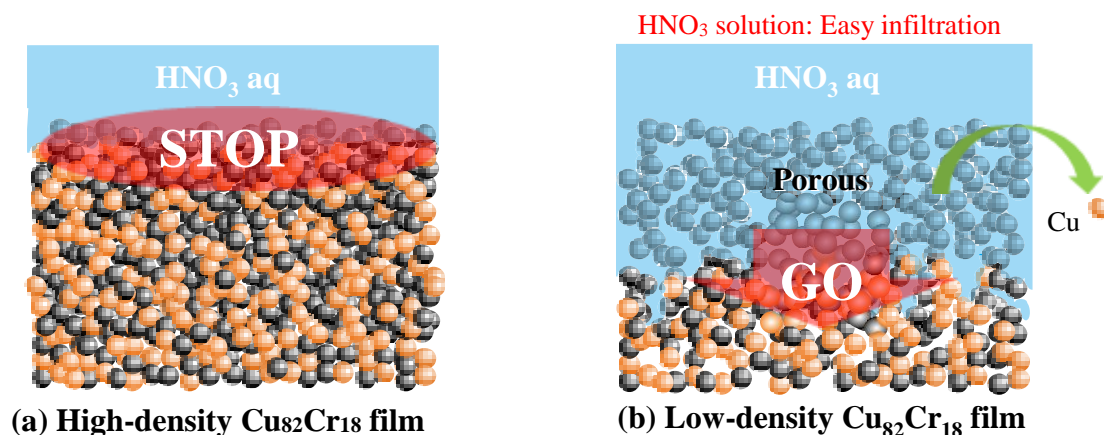


Fig. 4.10 Cu etching performance depending on film density

Fig. 4.11 shows a schematic sequence of the experiment. After cleaning of glass substrates, the substrates were loaded in NFTS. Afterwards, Cu and Cr were simultaneously sputtered at 0.5 or 2.5 Pa in argon. The estimated sputtering conditions were summarized in Table 4.3. It is interestingly to note that the both experiments successfully resulted in a uniform $\text{Cu}_{82}\text{Cr}_{18}$ film (no compositional gradient zone). As mentioned in chapter 3, sputtering pressure at 2.5 Pa generates a composition gradient in NFTS. For the testing the Cu etching rate depending on the film density, a uniform initial composition should be maintained and only the film density should be adjusted by controlling the sputtering pressure.

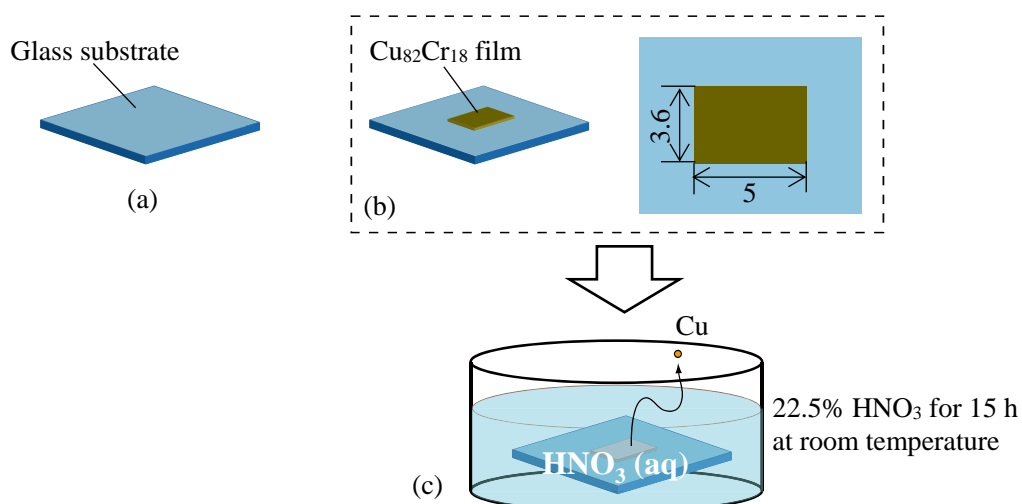


Fig. 4.11 Experimental procedure; (a) substrate cleaning, (b) co-sputtering of $\text{Cu}_{82}\text{Cr}_{18}$ film (350 nm thick) onto the substrate at differential sputtering pressure (0.5/2.5 Pa), and (c) Cu dealloying.

Table 4.3 Sputtering conditions

		Tested samples	
		(a) 0.5 Pa in argon	(b) 2.5 Pa in argon
Initial alloy composition (at.%)		Cu ₈₂ Cr ₁₈	Cu ₈₂ Cr ₁₈
Film thickness (nm)		350	350
Sputtering power (W)	Cu	223	175
	Cr	113	80
Sputtering time (min)		15	35
TS distance (mm)		82	82
Deposition area (mm)		3.6 × 5.0	3.6 × 5.0

Thus, compositional gradients (Δx at.%) generated with a sputtering pressure of 0.5 or 2.5 Pa over an area of 3.6 mm × 5.0 mm were measured (Fig. 4.12). Three points were compositionally determined by EDX. The measured compositional gradient (Δx at.%) was 0.5 at.% at 0.5 Pa and 0.7 at.% at 2.5 Pa, which were below the acceptable limit of 1.0 at.% (because the resolution of EDX used was 1.0 at.%). Thus, forming the films (dimension: 3.6 mm × 5.0 mm) with uniform compositions at both 0.5 and 2.5 Pa in argon was possible.

Fig. 4.13 was FE-SEM images recorded after sputtering, showing a different surface structure. The image (b) showed that the resulting surface was coarser at 2.5 Pa in argon than the image (a) generated under 0.5 Pa in argon.

First, a dealloying test was conducted on a Cu₈₂Cr₁₈ film fabricated at 0.5 Pa in argon. The result shown in Fig. 4.14 indicates that the Cu dealloying was not sufficient. The initial Cr composition of 18 at.% increased to 21 at.% for 15 h but only increased slightly with longer dealloying times, reaching 22 at.% after 30 h of dealloying. Moreover, after Cu dealloying for 30 h, the gradient was only $\Delta 4$ at.% Cr. Surface structures taken by FE-SEM revealed the diffusion and self-organization during the dealloying treatment. As the Cu dealloying treatment advanced, Cr particles were diffused and clumped together, forming a porous network. However, the Cu etching has been conducted at only the surface, resulting in the incomplete Cu dealloying. These results can also be explained from cross sectional FE-SEM images, showing no visible pores throughout the film thickness. Moreover, the bottom appearance of the dealloyed film represented initial Cu brown, indicating aqueous HNO₃ could not enter to the interior of the film.

Second, a chemical dealloying of the porosity of the low-density Cu₈₂Cr₁₈ film was carried out,

showing a dramatic difference in the Cu etching performance. Fig. 4.15 shows a comparison of the Cu etching rates in the $\text{Cu}_{82}\text{Cr}_{18}$ films fabricated on glass substrates with sputtering pressures of 0.5 and 2.5 Pa in argon. The Cu etching rate was 0.1 at.%/min under 0.5 Pa and 30 times higher (3.0 at.%/min) under 2.5 Pa, confirming the hypothesis that a higher sputtering pressure would result in better Cu etching. Fig. 4.16 summarized the chemical dealloying test with 22.5% HNO_3 for 20 min at room temperature. The composition of the dealloyed dense $\text{Cu}_{82}\text{Cr}_{18}$ film was $\text{Cu}_{80}\text{Cr}_{20}$, where Cu was not sufficiently removed. By contrast, the porosity of the low-density $\text{Cu}_{82}\text{Cr}_{18}$ film was easily Cu dealloyed, showing its composition changed from $\text{Cu}_{82}\text{Cr}_{18}$ to $\text{Cu}_{22}\text{Cr}_{78}$, as measured by EDX. Moreover, the film thickness was unchanged after dealloying.

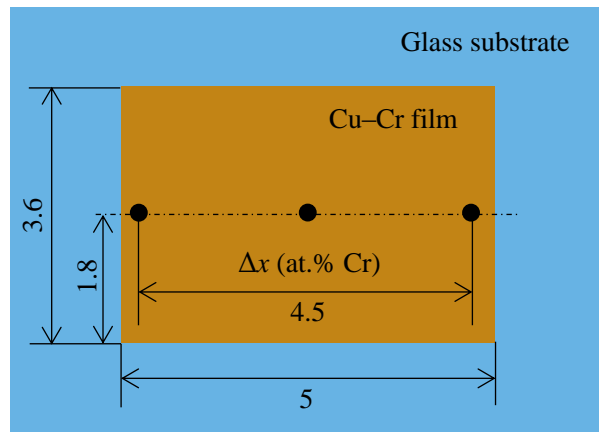


Fig. 4.12 Compositional gradient created by NFTS in area of 3.6 mm × 5 mm.

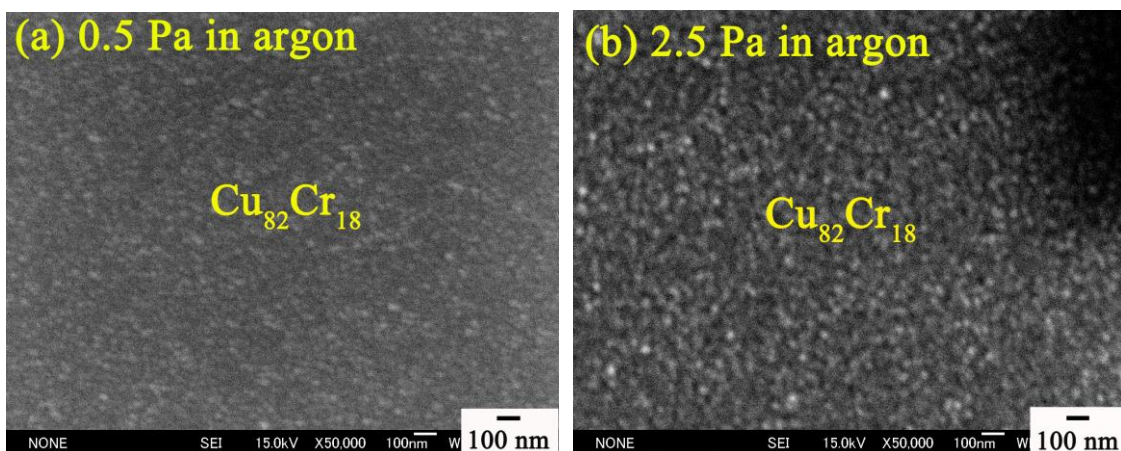


Fig. 4.13 FE-SEM images taken post as-depositing; (a) 0.5 Pa in argon, and (b) 2.5 Pa in argon.

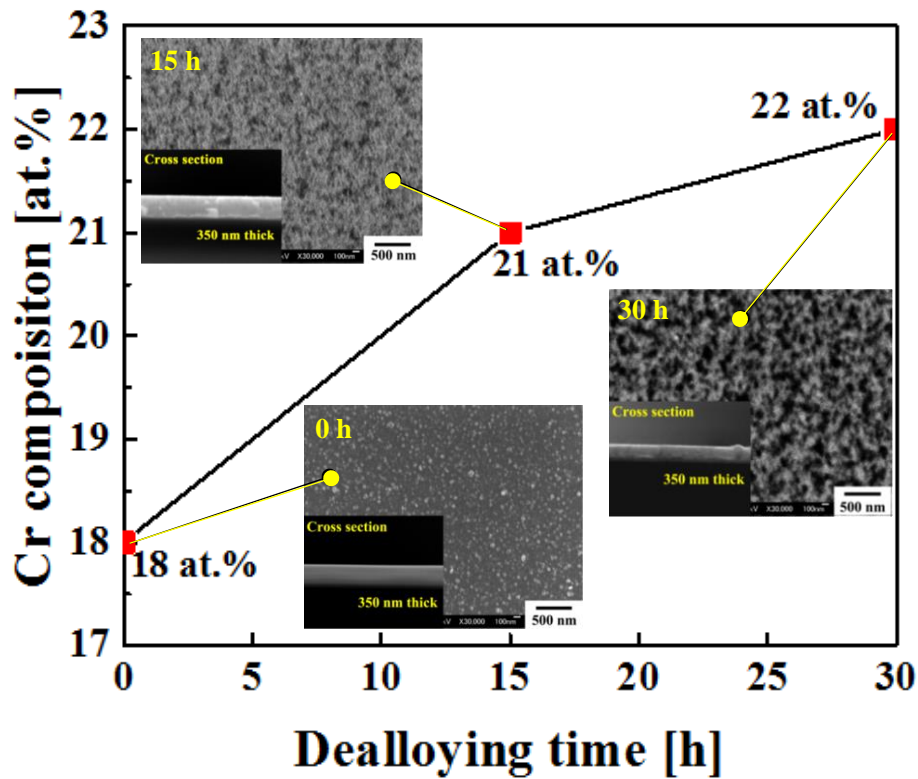


Fig. 4.14 Changes in Cr composition and nanostructures of $\text{Cu}_{82}\text{Cr}_{18}$ film at dealloying times from 0 to 30 h. The initial Cr composition of 18 at.% increased to 21 at.% for 15 h but only increased slightly with longer dealloying times, reaching 22 at.% after 30 h of dealloying.

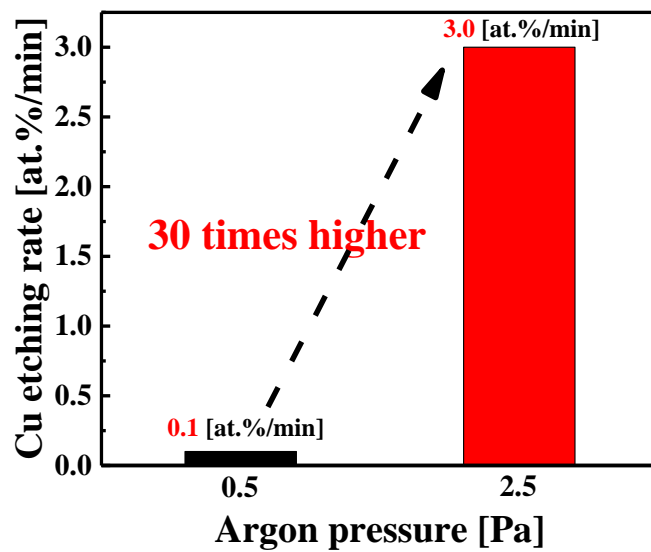


Fig. 4.15 Cu etching rate dependence on sputtering pressure in NFTS

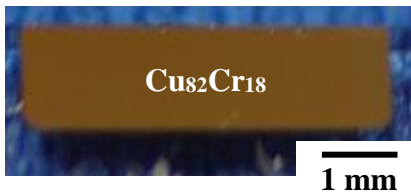
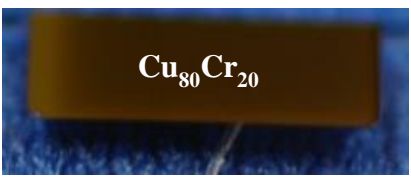
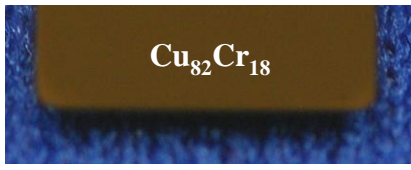
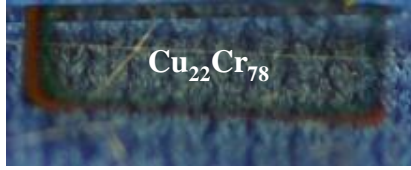
	Dealloying with 22.5% HNO₃ for 20 min	
	Before dealloying	After dealloying
0.5 Pa	 Cu ₈₂ Cr ₁₈ 1 mm	 Cu ₈₀ Cr ₂₀
2.5 Pa	 Cu ₈₂ Cr ₁₈	 Cu ₂₂ Cr ₇₈

Fig. 4.16 Changes in appearance of Cu–Cr films through the Cu dealloying at different sputtering pressures.

The author considered that the incomplete Cu dealloying in the preliminary chemical dealloying (Fig. 4.1) has resulted not only from the high initial Cr composition (22 at.%), but also from the low sputtering pressure (0.5 Pa). This theory can be explained from Fig. 4.8(a), where initial 22 at.% Cr changed to 33 at.% Cr thorough the Cu dealloying for 15 h. In contrast to the preliminary test in Fig. 4.1 (initial 22→24 at.% Cr), Cu was more dealloyed in this time, because the thin-film library was deposited in NFTS at 2.5 Pa in argon. Thus, the fabricated thin-film library originally had a porosity, resulting in the enhanced Cu etching.

Curiously, the Cu₈₂Cr₁₈ film deposited in 2.5 Pa in argon changed in appearance from brown to transparent after Cu dealloying (Fig. 4.16). The resistance of the dealloyed film measured using the two-terminal method indicated an insulation state. The transparency of the film after dealloying may be attributed to the formation of Cr₂O₃. Accordingly, the crystal structure of the film was evaluated using XRD.

Fig. 4.17 shows the XRD patterns of the Cu–Cr film before and after Cu dealloying. Only peaks corresponding to Cu are found in the XRD pattern of the as-deposited Cu₈₂Cr₁₈ film because the low concentration of Cr was dissolved in the Cu layer with low crystallinity. Most of them, sputtering in NFTS is conducted at room temperature¹³¹), therefore deposited metal particles diffuse slowly, resulting in a poor crystallinity¹³²). Due to this, Cr peaks were absent before

dealloying. After Cu dealloying, the Cu peaks disappeared, and some Cr_2O_3 peaks newly appeared. This suggests that the observed film transparency and insulation state can be attributed to the formation of Cr_2O_3 .

As seen in Fig. 2.18 (in chapter 2), Cr peaks were observed in XRD analysis after dealloying step (not Cr_2O_3 peaks). This has resulted from the Cr grain growth based on the thermal coarsening at 700 °C, emphasizing the presence of Cr. Cr was exactly becoming the oxidation in HNO_3 solution, however the final volumed Cr nanoporous film with large particles (approximately 200–300 nm pores) enhanced the intensities of Cr peaks, resulting in the absence of Cr_2O_3 peaks.

On the other hand, the as-deposited film without thermal coarsening was made up with small Cr grains, which easily oxidized in HNO_3 solution. Due to this, the film appearance represented the transparency. Subsequently, the film structures before and after dealloying were examined using FE-SEM, which is described below.

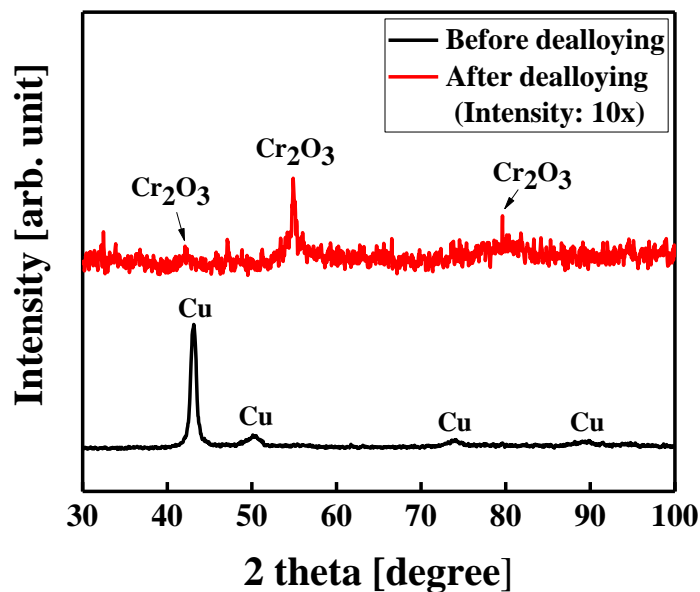


Fig. 4.17 XRD analysis before and after Cu dealloying

4.4.3 Influence of substrate type on final obtained nanostructure

The surface structures of the initial and dealloyed Cu–Cr film were observed using FE-SEM. While the initial film showed a smooth surface (Fig. 4.18(a)), the dealloyed films had cracks throughout the film, and no clear nanopores were observed (Fig. 4.18(b)). The cracking was attributed to internal stress in the as-deposited film^{4),36),37)}. Mechanical stresses in small-scale structures (e.g., thin film on substrates) often reach several hundred MPa after processing or during service^{36),133)}. Thus, in this study, the relief of internal stress when dealloying began resulting in cracking throughout the surface of the film.

There has been many reported about this problem (Fig. 4.19). All studies (a)–(c) successfully produced nanostructures, however also remained cracks. Those cracks cause a poor mechanical toughness, and therefore removal of cracks has been researched. Unfortunately, there are few reports succeeding in the fabrication of ideal nanoporous films without film cracking. The research by W. C. Li et.al⁴⁾ revealed that crack-free Pd nanoporous films could be achieved with an optimum initial Pd–Cu composition. Film cracks typically appear when there is too little Pd in the initial alloy (too much Pd leads to incomplete Cu dealloying). Therefore, careful investigation of initial alloy compositions may resolve the problem.

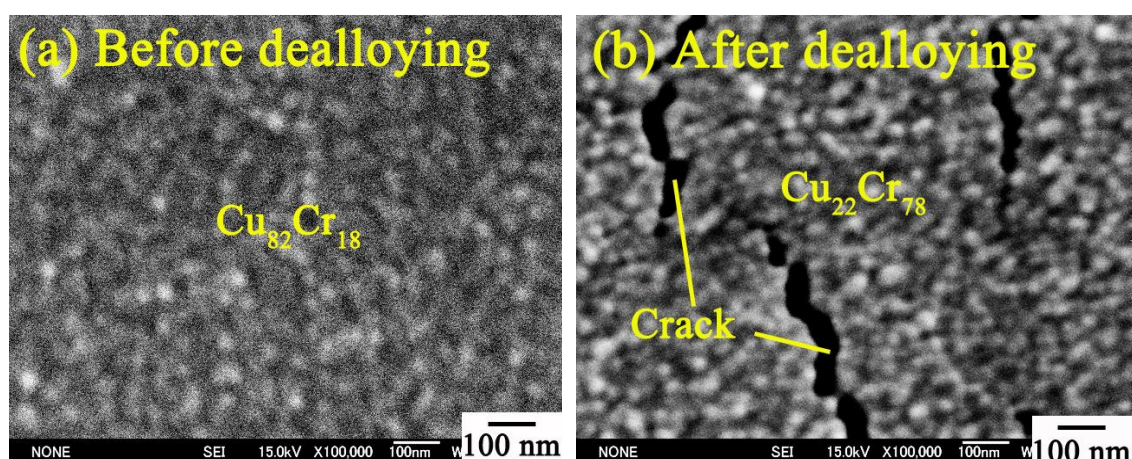
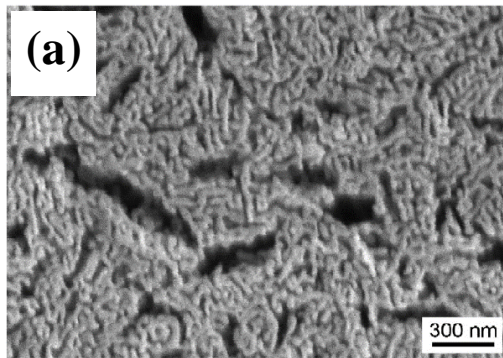
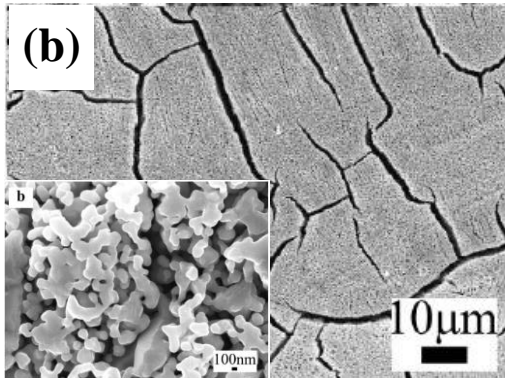


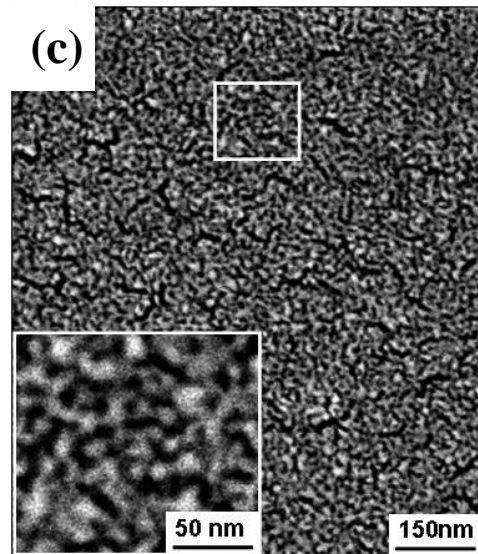
Fig. 4.18 FE-SEM images of (a) the initial and (b) dealloyed Cu–Cr film (top-view)



(a)
Nanoporous Au films fabricated
via chemical dealloying of Au–Ag



(b)
Nanoporous Cu films fabricated
via chemical dealloying of Al–Cu



(c)
Nanoporous Pt films fabricated
via chemical dealloying of Pd–Ni

Fig. 4.19 Film cracks appeared after dealloying have been reported by many researchers; (a) X. Lu et.al.³⁶⁾, (b) Z. Qi et.al.³⁷⁾, and (c) W. C. Li et.al.⁴⁾.

Nanoporous structure could not be observed in the cross-sectional image either (Fig. 4.20). The author considered that the pore growth can be determined by diffusion of metal particles. J. Erlebacher et.al.²²⁾ reported, in the Au–Ag alloy, the dealloying process began with the dissolution of surface silver atoms. The residual Au atoms gradually diffused to the surface, and formed a three dimensional morphologies with open pores. Au atoms are easy to diffuse during Ag dealloying, promising to create large pores. However, in our case, the residual Cr atoms have a very small self-diffusion coefficient at room temperature ($4.7 \times 10^{-59} \text{ m}^2/\text{s}$)¹³⁴⁾ compared to the Au atom ($1.6 \times 10^{-36} \text{ m}^2/\text{s}$)¹³⁴⁾. Therefore, poor diffusion of Cr atoms could not produce open pores.

Hence, the author saw no visible pores on the film.

The same phenomenon was reported by A. Abburi et.al.³⁾. They presented chemical dealloying of Cu–Pt. $\text{Cu}_{80}\text{Pt}_{20}$ films (150 nm thick) were deposited by co-sputtering, and the thin films were Cu dealloyed by immersing the sample in 93% sulfuric acid at room temperature. Cu was selectively removed from the binary alloy and a film with only Pt was produced. However, FE-SEM image taken after Cu dealloying showed, there was no visible pores (Fig. 4.21); even full Cu was perfectly removed from the Cu–Pt alloy, open pores were not seen. They also concluded that no visible pores due to the small self-diffusion coefficient of Pt atoms (self-diffusion coefficient (Pt): $8.7 \times 10^{-54} \text{ m}^2/\text{s}$)¹³⁴⁾. In the author's case, self-diffusion coefficient of Cr atoms is smaller than Pt atoms. Thus, unclear pores shown in Fig. 4.18(b) and Fig. 4.20 may be resulted from the same reason for A. Abburi et.al.

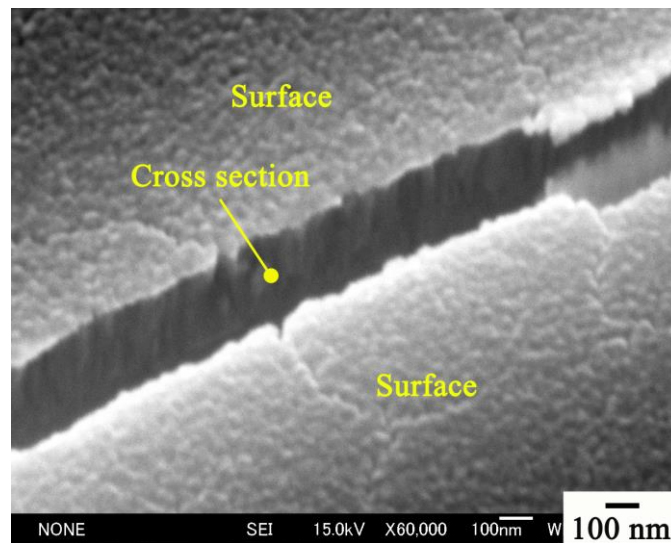


Fig. 4.20 Cross-sectional structure after Cu dealloying

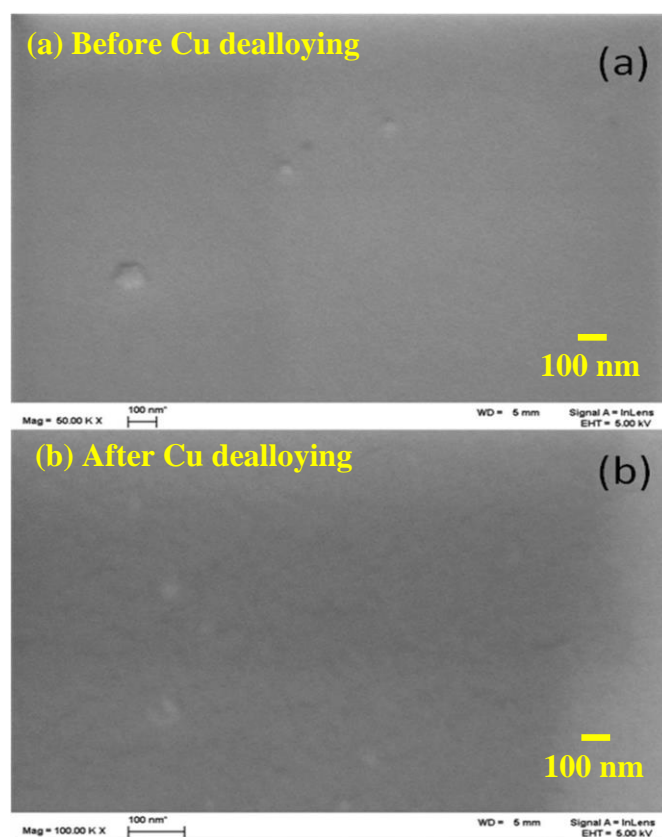


Fig. 4.21 FE-SEM images of (a) before dealloying of $\text{Cu}_{80}\text{Pt}_{20}$ film and (b) after dealloying. Pore structures were not seen from the image (b). (A. Abburi et.al³⁾)

A. Abburi et.al finally obtained visible open pores by introducing thermal coarsening. The author has already reported that this heat treatment could realize a grain growth, becoming effectively pore size larger. However, to achieve the chemical dealloying of Cu–Cr without thermal coarsening, the author investigated another technique not depending on thermal coarsening. The author attempted to fabricate a nanoporous Cu–Cr film on a softer polyimide film under the same dealloying conditions.

The author considered that no visible pores may be also attributed to the hard glass substrate; this hard glass substrate strongly restricted the above Cu–Cr films, hindering the growth of the pore sizes and self-organization (Fig. 4.22(a)). Softer polyimide films should not strongly restrict the above Cu–Cr films, allowing the pore scales to grow easily (Fig. 4.22(b)). Moreover, H. Matsuyama¹³⁵⁾ reported that polyimide films discharge H_2O -based gas during sputtering, and this gas changes the film characteristics. Thus, depositing the $\text{Cu}_{82}\text{Cr}_{18}$ films on polyimide is expected to enhance the film porosity because Cu–Cr films contain gas.

A $\text{Cu}_{82}\text{Cr}_{18}$ film with the same dimensions and thickness (sputtering conditions: Table 4.3(b)) was formed on a polyimide film (2 μm thick) and then dealloyed with 22.5% HNO_3 for 30 min. After dealloying, the composition of the Cu–Cr film changed from $\text{Cu}_{82}\text{Cr}_{18}$ to $\text{Cu}_{25}\text{Cr}_{75}$, and the appearance of the film changed from brown to transparent (Fig. 4.23), as for the film deposited on a glass substrate. Furthermore, the film thickness remained unchanged.

The FE-SEM images before and after Cu dealloying are shown in Fig. 4.24. While the initial surface structure had no pores, pores with diameters of 20–40 nm were successfully observed after dealloying. Moreover, the cross sectional image of the dealloyed film (Fig. 4.25) showed a nanoporous structure throughout the film thickness. The final structures were totally different at the substrate type used. This result proved that the polyimide films enhanced the dealloyed Cu–Cr film porosity. The fabricated nanoporous film is expected to be useful as a nanofilter used in the author's devices.

Unfortunately, large cracks (approximately 100 nm wide and several μm long) were formed on the nanoporous film when polyimide film was used for substrate (Fig. 4.26(a)). Large cracks resulted from the relief of internal stresses, and eliminating cracking on the film surface will be a future work. The author's chemical dealloying combined with thermal coarsening at 300–700 $^{\circ}\text{C}$ could produce ideal nanoporous films without film cracking. Because thermal coarsening results in relief of internal residual stresses, softening, homogenizing and transformation of the grain structure into more stable state. Therefore, film cracks were not seen on the film surface even after the Cu dealloying treatment were carried out.

To remove film crack not depending the thermal coarsening, the author considers further adjustment of initial alloy compositions or film thicknesses. Moreover, reducing the Cu–Cr film thickness by decreasing the sputtering time may permit to lower internal stresses of the film. If the amount of film cracks can be successfully reduced, the mechanical toughness of the nanoporous film would be better.

Although the author mentioned the negative aspects about this study, the width of the cracks was fortunately approximately 100 nm (Fig. 4.26(b)). This scale is slightly larger than pore size (20–40 nm), which will not be a fatal problem upon the separation of water molecules (0.3 nm) from colloidal oil particles (200 nm to several micro meters).

Summary, the author succeeded in the fabrication of novel Cr-based nanoporous films via the chemical dealloying without thermal coarsening. This fruit was achieved by the combinatorial

analysis as well as the optimization of film density and substrate type. The fabricated nanoporous films can be expected to be useful as nanofilters for separating water molecules from oil.

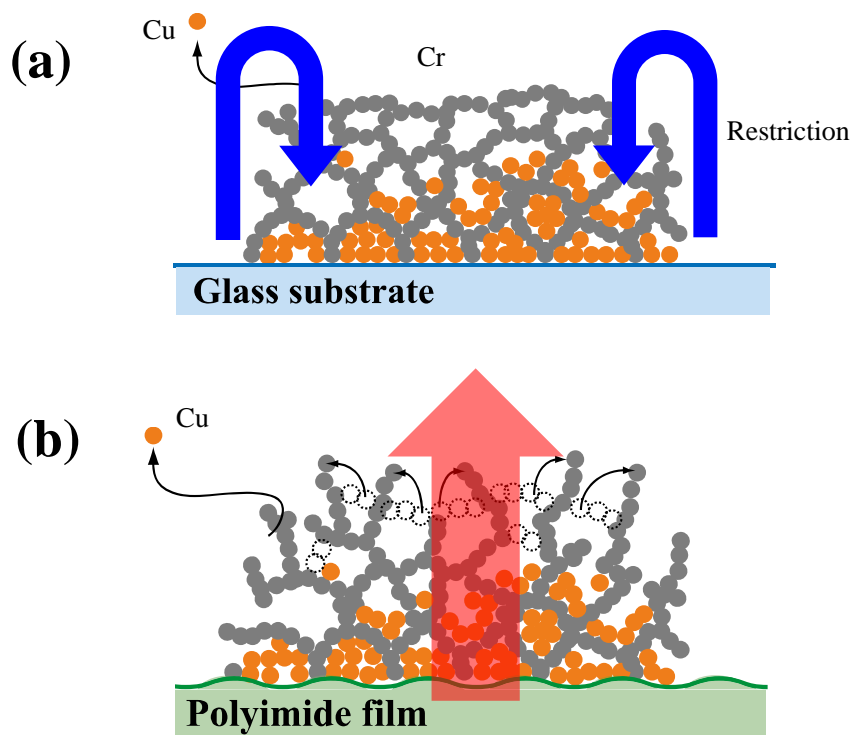


Fig. 4.22 The author's hypothesis: (a) hard glass substrate may hamper the pore growth, but (b) soft polyimide may enhance the pore growth because it does not strongly restrict the above Cu–Cr film as well as discharged gas from the polyimide film provide a film porosity.

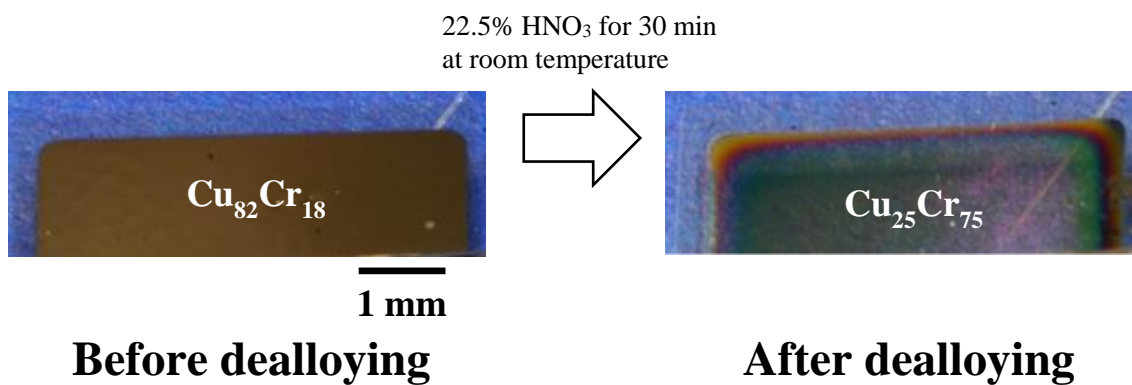


Fig. 4.23 Changes in appearance of the Cu–Cr film; (a) before and (b) after Cu dealloying

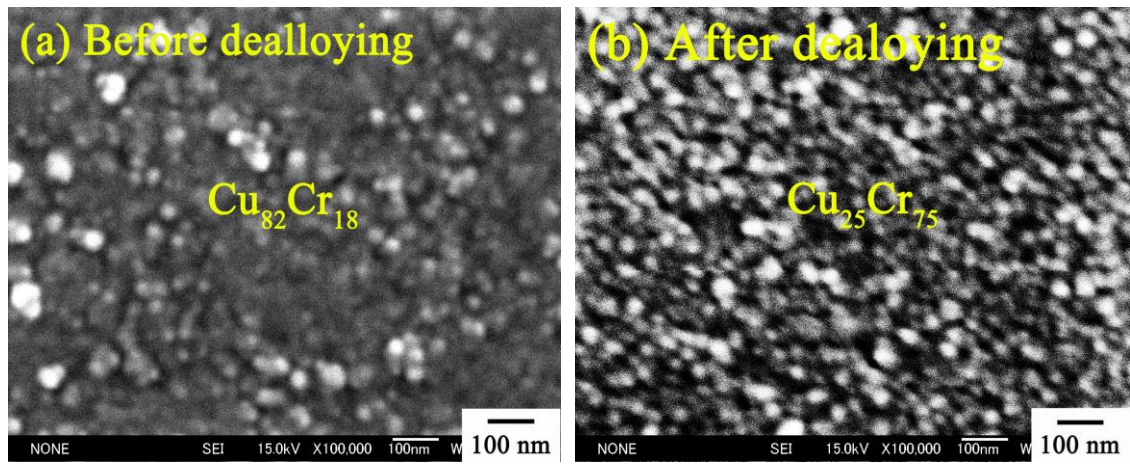


Fig. 4.24 FE-SEM images of (a) the initial and (b) dealloyed Cu–Cr film on the polyimide film (top-view)

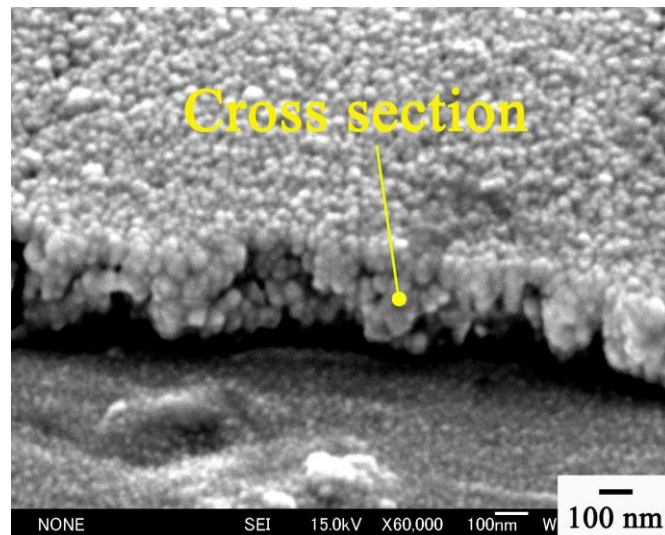


Fig. 4.25 Cross sectional structure taken by FE-SEM

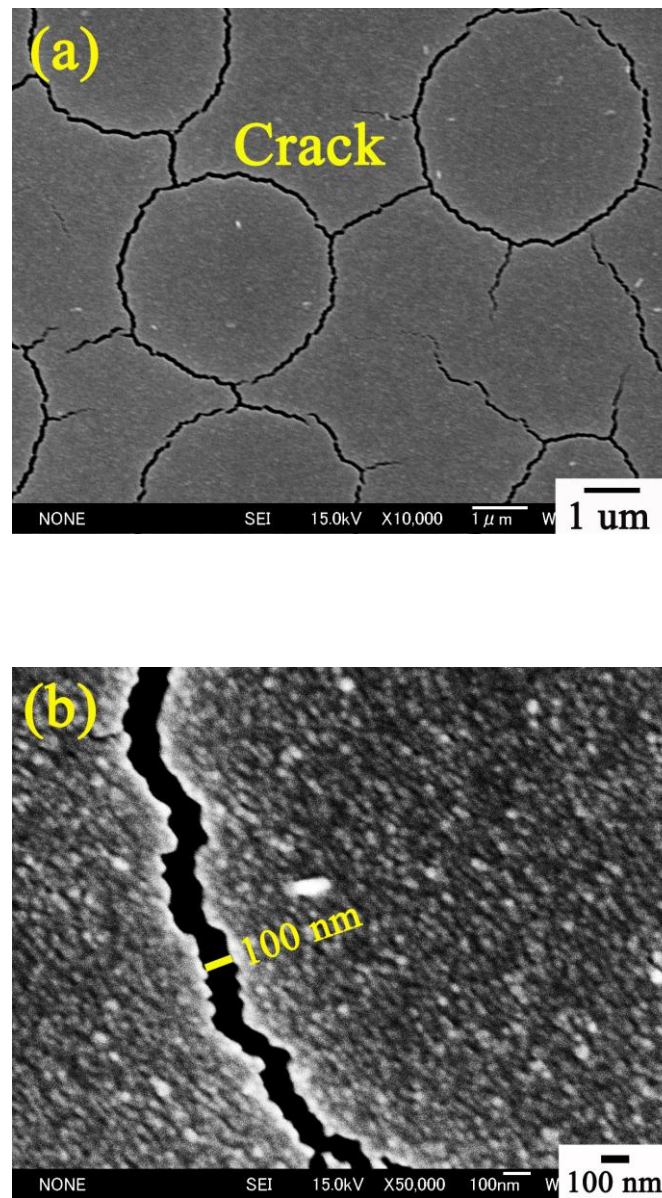


Fig. 4.26 Film cracking appeared after Cu dealloying; (a) FE-SEM image (X10,000) showing cracks created throughout the film surface, and (b) FE-SEM image (X50,000) showing crack size. The width of cracks was estimated in approximately 100 nm.

4.5 Summary

In this chapter, the author attempted to fabricate nanoporous films via chemical dealloying of Cu–Cr without thermal coarsening. Response to applications including non-heat resistant materials, chemical dealloying with no requirement of thermal coarsening will be better. Furthermore, this short process is also attractive for mass production.

The preliminary test was helpful, and suggested the possibility for Cu dealloying at room temperature. Based on the findings, it was hypothesized that reducing the initial Cr composition to below 22 at.% might result in better Cu dealloying and yield a favorable Cr-based nanoporous film. Hence, the combinatorial analysis was employed, as for chapter 3.

Thin-film libraries (dimension: 26 mm × 76 mm) containing the initial 22–15 at.% Cr (Avg. 380 nm thick) were successfully prepared in NFTS. The libraries were Cu dealloyed with 22.5% HNO₃ for 15 h at room temperature, and successfully gave the possible initial alloy compositions. Cu dealloying performance and film dissolution test were characterized as a function of substrate position. By tracing the locus of them, the author found that the optimal initial alloy composition could be determined in Cu₈₂Cr₁₈. The best Cu₈₂Cr₁₈ alloy permitted the sufficient Cu dealloying (residual Cu was 20 at.%), but its thickness remained unchanged.

Moreover, the influence of film density on Cu etching rate was studied. Cu₈₂Cr₁₈ films with the dimension (3.6 mm × 5.0 mm) and thickness (350 nm thick) were prepared by NFTS at 0.5 and 2.5 Pa in argon. While Cu₈₂Cr₁₈ films prepared at 0.5 Pa in argon showed the dense structures, that prepared at 2.5 Pa exhibited the porosity of the low-density films. This was because, as the sputtering pressure increased, the mean free path of each sputtered particle decreased; hence, the sputtered particles have less kinetic energy, resulting in the formation of low-density films. As expected, the porosity of the low-density Cu₈₂Cr₁₈ films were easily Cu etched, and the dealloying performance was 30 times higher. The sufficient Cu dealloying was successfully achieved for only 20 min.

The appearance of the dealloyed films changed from brown to transparent as Cu was etched out. Moreover, the resistance values of the dealloyed films indicated an insulation state. XRD analysis indicated the formation of Cr₂O₃ during Cu dealloying. However, FE-SEM images taken immediately after the dealloying process showed there were no visible pores. The author concluded that this might be attribute into the poor diffusion of Cr.

Pore growth not depending the thermal coarsening was necessary, and the author tried the same

dealloying test using the $\text{Cu}_{82}\text{Cr}_{18}$ film deposited on the polyimide film. Because the author considered that the substrate type might influence the final porous morphologies; the softer polyimide film may not restrict the pore growth as well as the discharged gas from the polyimide film may change the $\text{Cu}_{82}\text{Cr}_{18}$ film characteristics.

While the dealloyed film on glass substrate had no clear visible pores, the dealloyed film on polyimide exhibited a nanoporous surface and cross section with pore sized of 20–40 nm. This result proved that the polyimide films enhanced the dealloyed Cu–Cr film porosity. Although some cracks (approximately 100 nm wide and several μm long) were created on the film surface, the fabricated nanoporous film is expected to be applied as a nanofilter.

Through chapter 2–4, the author has been focusing to fabricate nanoporous films via chemical dealloying. Next, the author attempts to prepare nanoporous films for application in molecular filters used in MEMS sensors. In this study, fabricated nanoporous films are evaluated as molecular filters based on sensor performances. The motivations and experimental procedures are described in more detail in next chapter 5.

Chapter 5 Nanoporous film for application in MEMS device

5.1 Target

The author fabricated Cr-based nanoporous films with the wide porous range (approximately 20–300 nm) via many types of chemical dealloying of Cu–Cr. Thermal coarsening, optimization of initial alloy composition and film density, and further selection of substrate type have successfully driven the achievement of chemical dealloying. The obtained nanoporous films have many possibilities for applications, and the aim of this study is also to demonstrate its functionality.

In addition, evaluating nanoporous films based on their application performances will be also reliable to judge their properties (e.g., pore size, porosity, mechanical toughness and film thickness). Best properties of the nanoporous film can be also determined by outputs of its application. In this section, prepared nanoporous films are characterized and studied for application in separation of water molecules from oil. This filtration properties are carefully evaluated based on MEMS sensor performances.

First, the author introduces MEMS sensors to monitor the water concentration of oil in real time. The author mentions a motivation why such MEMS sensors are required today. After giving an explanation for devices, the author touches the sensor design and its principle. The prepared nanoporous films function as upper electrode film filters in sensors. The author also refers that the nanoporous film will be a key-material in order to realize the moisture sensors for oil.

Second, the author describes the first challenge of this study. Sensor fabrication process as well as their evaluation method are clearly mentioned. For preliminary test, the author initially utilizes dense films in place of nanoporous films. The fabricated sensors are first evaluated in air, because it is difficult to control the relative humidity (RH) in oil. Fabrication results and sensor performances are reviewed, and then future directions are discussed.

On considering the heat-resistant temperature of polyimide films (approximately 350 °C), the upper nanoporous electrode film filters are first prepared via the chemical dealloying including low-temperature coarsening. Optimal fabrication conditions for sensors are identified in the previously reported combinatorial search. The author mentions the fabrication recipes and subsequently tries to fabricate effective sensors. After all processing, the fabricated sensor performances are studied and discussed.

The author prepares another nanoporous electrode film filters using chemical dealloying

without thermal coarsening. The author believes that the developed fabrication procedure may demonstrate the possibility for designing effective sensors. Dependence of level of Cu dealloying on sensor performance is carefully determined in air first, indicating the interesting sights.

Next, the author measures sensor performances in oil. Experimental setup is explained using a schematic diagram. Each sensor performance in oil at different nanostructures is studied, and the author optimizes the best fabrication conditions for sensors. In the final, the author concludes the study, demonstrating that the all targets of this study are successfully achieved.

5.2 MEMS sensor for monitoring moisture in oil

5.2.1 Motivations

Lubrication oil is widely used in mechanical system, such as ships or wind-driven power generators, to reduce friction between machine elements. However, when the machinery is used in close contact with water, the oil may become contaminated by water¹³⁶. Not limited to such a special environment, oil becoming mixed with water can easily occurred everywhere, in which water leakage from oil cooler or coolant used in machine tools may be the cause of trouble. This presence of unexpected water can cause the oil to degrade and allow bacteria to grow, thereby corroding the machine elements¹³⁷. Moreover, viscosity lowering and oxidative degradation of oil are mainly caused by the same problem¹³⁸. Accordingly, oil condition monitoring is an essential technology, and research is ongoing on the design and development of sensors or systems.

Oil conditions are normally determined by total acid number (TAN)^{139,140}. The total acid number is defined as effective amount of potassium hydroxide (KOH) for neutralizing acid component included in 1 g sample. Table 5.1 summarized the total acid number of lubrication oil¹⁴¹. This table explains the level of degradation of two type oils; pure oil (300 ml) and oil being mixed with water (60 ml). O₂ gas was constantly introduced to the oils at 93 °C, and after processing time (3,000 h), the total acid numbers were 0.13 mgKOH/g at pure oil and 0.78 mgKOH/g at contaminated oil by water, respectively. This result indicates that the water existence drastically enhanced the degradation of oil. Fig. 5.1 shows an influence of water content on degree of oxidative degradation for fresh oil¹⁴¹. With increase of the water content in oil, the oxidative degradation was becoming enhanced. It is markedly note that the graph curve declined sharply after 0.2 vol.% water content. Therefore, water content in oil has been generally controlled in 0.1–0.2 vol.%.

Although approximately 20–100 ppm water is extant in even fresh oil, this water content can

perfectly dissolve in oil layer. However, when RH in oil becomes more than saturated steam pressure of oil (RH = 100%), water layer called “free water” is newly generated while completely separated from oil layer (Fig. 5.2)^{142),143)}. The incorporation of free water in the oil layer may result in abnormal friction between machine elements. These effects can lead to malfunctions of marine equipment. Thus, developing sensor to monitor the water content of oil in real time is important.

The conventional way of monitoring water content is by taking a representative sample and sending it to a laboratory of analysis, such as Karl Fischer titration¹⁴⁴⁾. While this method is reliable and accurate, the disadvantage is the lag time between sampling and obtaining the analysis results. On the other hand, a capacitive water sensor can perform real-time monitoring and can be used as a control device. Thereby, this type of capacitive water sensor for oil can be expected as an intelligent IoT device, and the author describes the sensor design and its principle below.

Table 5.1 Influence of water existence on oxidation of oil¹⁴¹⁾

Water (ml)	Evaluation time (h)	Total acid number (mgKOH/g)
0	3,000	0.13
60	3,000	0.78

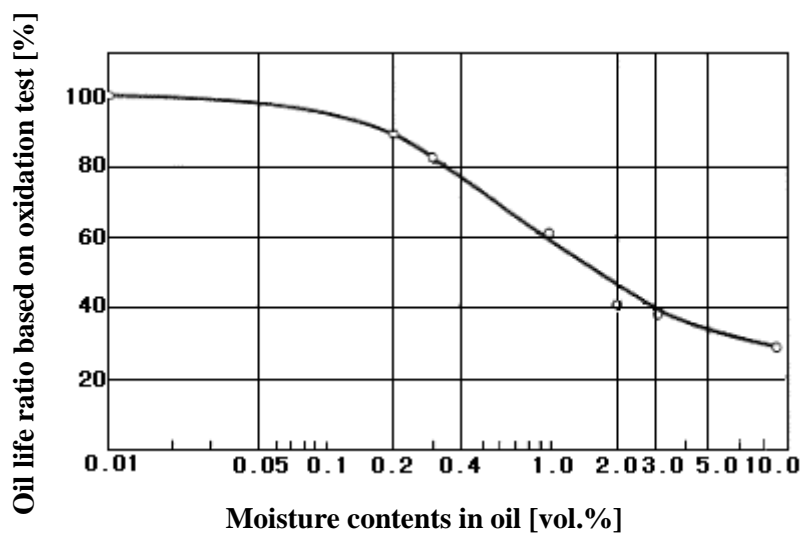


Fig. 5.1 Effect of moisture content on oil degradation¹⁴¹⁾

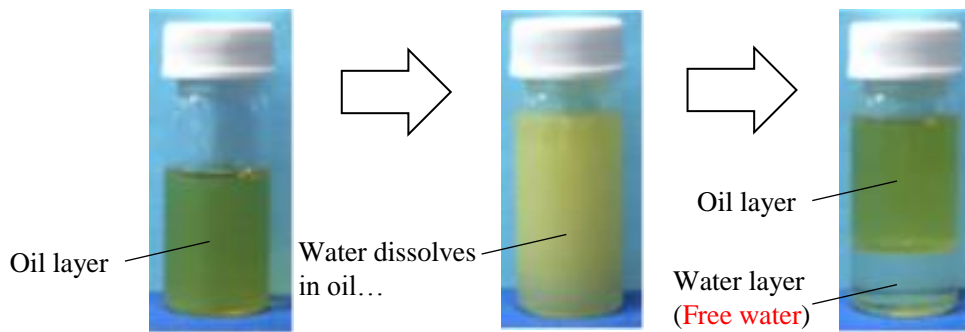


Fig. 5.2 Generation of free water in oil, causing a lot of problems.

5.2.2 Sensor design

Fig. 5.3(a) shows a schematic diagram of the basic capacitive water sensor for oil. This type of capacitive water sensor consists of a sandwich structure: a nanoporous film filter electrode on the top, a polyimide film in the middle, and an Au electrode film on the bottom. The ideal pore size of nanoporous film filter electrodes may be 10–50 nm. As illustrated in Fig. 5.3(b), the diameter of water molecule is about 0.3 nm, and the diameter of a colloidal oil particle is about 200 nm–5.0 μm ; therefore, the nanoporous film electrode functions as a molecular filter to separate water molecules from oil and other contaminants.

The diameter of colloidal oil particle alters with the degree of water concentration in oil. In the low water concentration in oil (0–10% RH), forming emulsion tends to be difficult, therefore the diameter of oil particles may be smaller than 10 nm. Such smaller oil particles can easily become trapped in the pores of the film filters, thereby decreasing the sensor response. Generally, it is very difficult to predict the diameter of oil particles, because this oil particle size depends on the oil type, level of water absorption in oil, or oil temperature. However, the most importance of the device is to work well to prevent the generation of free water. Accordingly, the author designed the pore size focusing on the sensor device operating well in the range 90–100% RH. In such environment, the emulsion state is enhanced, and therefore 10–50 nm pores may deserve of the separation of water molecules (0.3 nm) from colloidal oil particles (200 nm–5.0 μm).

Polyimide films function as moisture-sensitive films. The polyimide film absorbs water molecules from the oil through the nanoporous film filter until its RH equilibrates with that of the oil. The dielectric constant (ϵ_r) of the polyimide film changes as it absorbs water, which affects the electric capacity (C) of the sensor according to the following linear function (Eq. 5.1):

$$C = \varepsilon_0 \varepsilon_r (S/d) \quad (5.1)$$

where ε_0 is the dielectric constant in a vacuum, S is the surface area of the lower Au electrode film, and d is the thickness of the polyimide film. In conclusion, detecting the electric capacity of the sensor enable us to monitor the RH of the oil.

The dielectric constant (ε_r) of the polyimide film used is 2.8–3.0, and the ε_r of water is about 80. Therefore, the ε_r of the polyimide film increases significantly with the level of water absorption, promising a highly-sensitive sensor response. In order to design the sensor devices, the two unknown parameters (S and d) of Eq. 5.1 were determined. The author attempted to fabricate a millimeter-ordered sensor device, which can be applicable to IoT system. Sensor output (C) was first measured to be approximately 100 pF in the initial state (RH = 0%). For $d = 2 \mu\text{m}$, S can be determined by Eq. 5.1, where $\varepsilon_0 = 8.9 \times 10^{-6} \text{ pF}/\mu\text{m}$ and $\varepsilon_r = 3.0$. The calculated S was approximately 7.5 mm^2 . The ε_r of polyimide at $25 \text{ }^\circ\text{C}$ was approximately 3.5 at 50% RH and 4.0 at 90% RH¹⁴⁵). Therefore, the predicted sensor output was approximately 117–134 pF for 50%–90% RH (i.e., estimated sensitivity is ca. 17/40 pF/RH). The difference between the sensor output and the designed output value can be attributed to error in the polyimide film thickness, which can be compensated by a controlling circuit. The upper nanoporous film filter electrode and the lower dense Au electrode film were determined on 350–500 nm thick, and 300–500 nm thick, respectively.

By increasing the pore size of the film filter, the moisture-sensing properties are enhanced, but oil or contaminants in the oil can easily become trapped in the pores of the film filters, thereby decreasing the responsiveness of the sensor. Hence, the author determines the optimal pore size for the sensor. Especially, the author focuses the minimum allowable pore size for the sensor, which can allow the excellent sensor response.

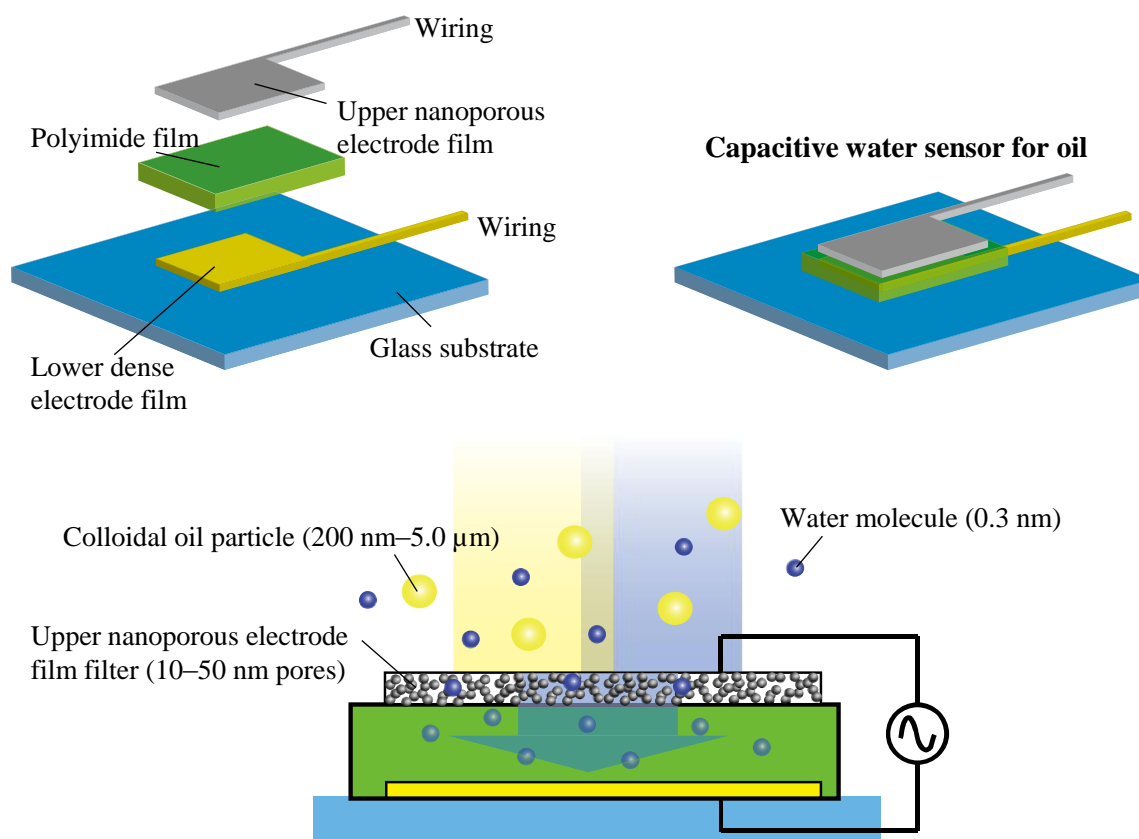


Fig. 5.3 Schematic diagram of the moisture sensor for oil; (a) capacitive water sensor consists of a sandwich structure, and (b) cross-sectional structure of sensor.

Fig. 5.4 shows the first sensor design. The scale of sensor chip is a millimeter order. The author partially removed the bottom left of the lower electrode film (see shape of yellow electrode in the figure) as well as the polyimide film (green), so that the upper wiring could connect to the subsequently formed upper nanoporous film filter electrode. The both lower electrode film and upper nanoporous film filter electrode has the same dimension ($3.5 \text{ mm} \times 2.4 \text{ mm}$). The dimension of polyimide film was $4.5 \text{ mm} \times 3.4 \text{ mm}$, which was analogously larger than that of the upper nanoporous electrode film filter. This sufficiently wide polyimide film can prevent the upper nanoporous electrode film filter from being electrically connected with the lower electrode film.

Moreover, the author additionally prepared new sensor design as illustrated in Fig. 5.5. The first designed sensor shown in Fig. 5.4 may cause a sensor output loss (Fig. 5.6). The upper electrode film has the same dimension as the lower electrode film, and furthermore, this upper electrode film is first prepared by sputter deposition through a metal mask and subsequent chemical dealloying. Therefore, the pattern placement error of the alignment marks between metal

mask and substrate is easy to happen. This accidently caused reduction of the effective surface, resulting in sensor output loss. To prevent such output loss, the lower electrode film was designed to be smaller than the upper electrode film. The predicted sensor output was approximately 30–47 pF for 50%–90% RH (i.e., estimated sensitivity is same ca. 17/40 pF/% RH).

Multiple sensors are synthesized on a single glass substrate (dimension: 60 mm × 60 mm), as shown in Fig. 5.7. The sensors were prepared via sputtering, lithography technology, and chemical dealloying, which are mentioned clearly below.

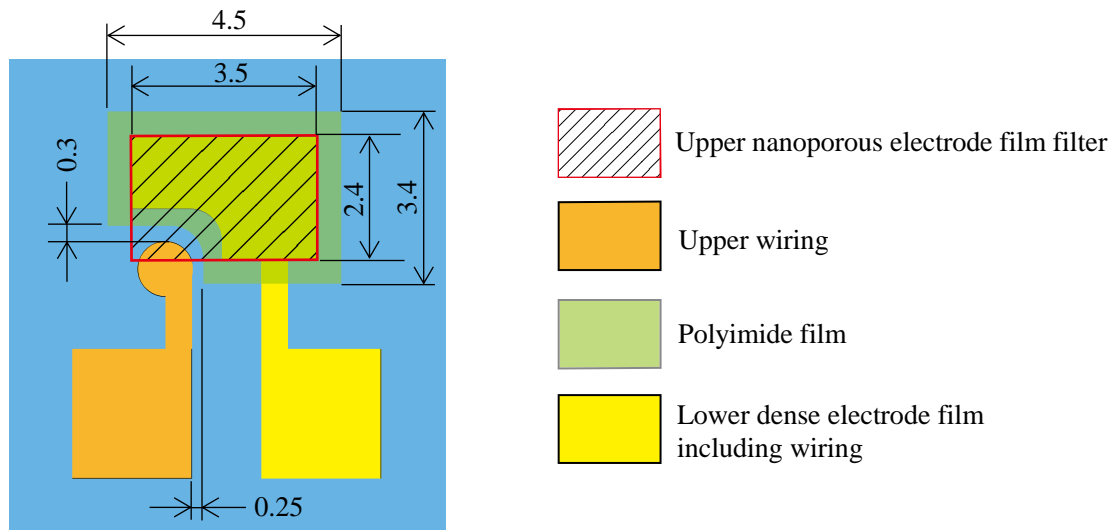


Fig. 5.4 First sensor design

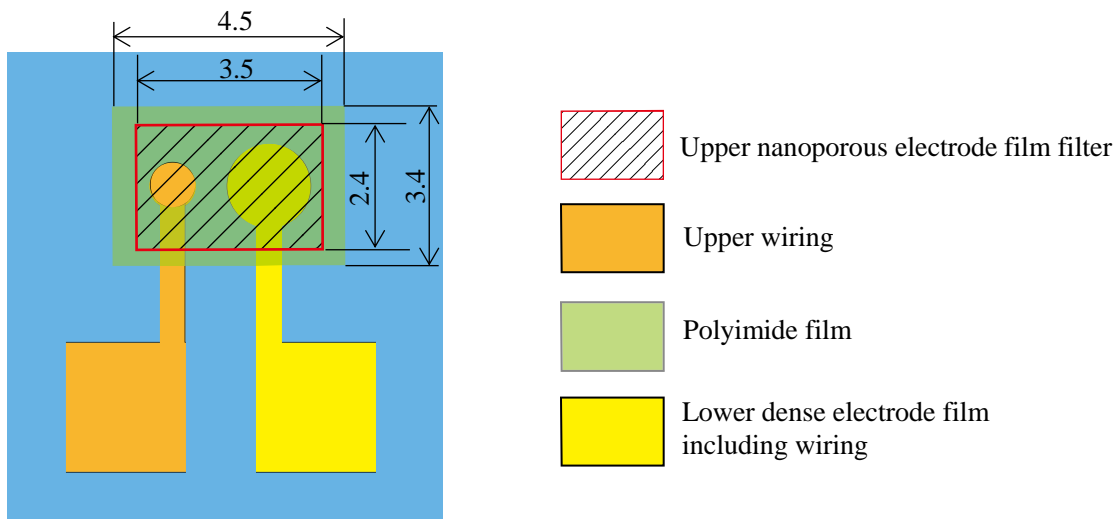


Fig. 5.5 Second sensor design

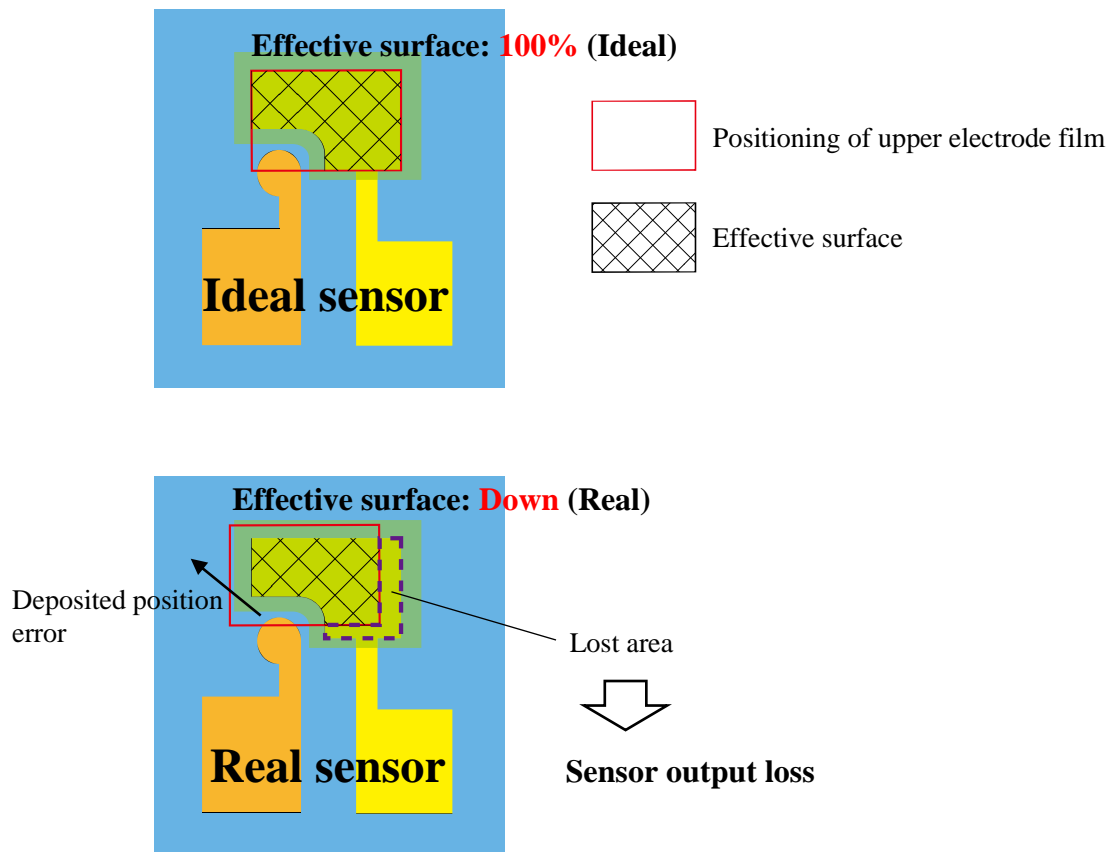


Fig. 5.6 Sensor output loss resulted from reduction of effective surface of capacitor

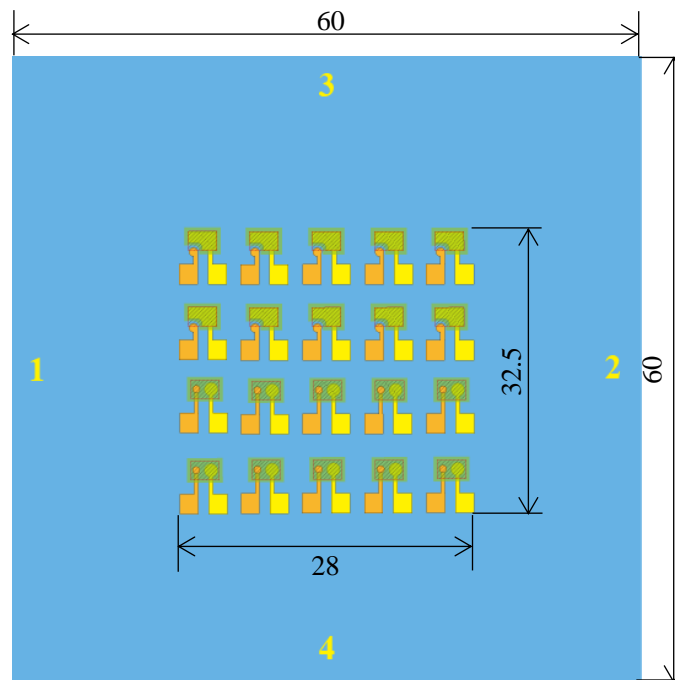


Fig. 5.7 Multiple sensors synthesized on single substrate

5.3 Preliminary test

5.3.1 Fabrication process

Through chapter 2–4, the author has been fabricated nanoporous films for MEMS sensors. However, the author did not quite show if the moisture sensor for oil really needs upper nanoporous electrode film. Dense type upper electrode film may work well on the sensor performance. Therefore, the author first utilized a dense structured upper electrode film. It was studied how the fabricated sensor would operate. Moreover, these experimental results will be important information upon designing the ideal sensor structure.

Fig. 5.8 and 5.9 shows a schematic sequence of the sensor fabrication process. A glass substrate (dimension: 60 mm × 60 mm) was first prepared through the ultrasonic cleansing in acetone for 5 min, and then in ethanol for 5 min, subsequently rinsed in water for 5 min. Afterwards, the substrate was dried through the air blow and heat-treatment in air at 110 °C for 5 min {step (a)}.

Next, the masked glass substrate was loaded in sputtering system (Canon Anelva Inc., Model SPF-430H), and a lower Au electrode film (500 nm thick) including wirings was sputtered {step (b) and (c)}. The metal mask was removed after Au sputtering {step (d)}, a polyimide film was prepared via lithographic process. Fabrication conditions were summarized in Table 5.2. 75% diluted polyimide precursor solution (Toray Inc., Model Photoneece PW-1500) was spin-coated (Mikasa Inc., Model 1H-DX) on the wafer. Afterwards, the coated wafer was prebaked by hot plate in air (Mikasa Inc., Model DP-1S), and further masked wafer was UV-exposed at 325 mJ/cm² for 50 sec by exposure machine (Mikasa Inc., Model MA-20). Finally, the treated wafer was dipped in a developing solution (Tokyo Ohka Kogyo Inc., Model NMD-3) at room temperature for 90 sec, patterning itself on a form of shadow mask {step (e)}. The so prepared wafer was cured in N₂ atmosphere following the conditions shown in Table 5.2. The polyimide film thickness resulted in approximately 2.0 μm. The prepared wafer was shown in Fig. 5.10(a). Multiple sensors are synthesized on a single glass substrate (dimension: 60 mm × 60 mm).

In the final step, the masked wafer using metal mask {Fig. 5.10(b)} was loaded in NFTS, and an upper electrode film (400 nm thick) was formed onto the polyimide film with an area with dimensions 3.5 mm × 2.4 mm exposed to the sources {step (f)}. Fig. 5.11 illustrates a schematic diagram of NFTS sputtering. Cr was simultaneously sputtered by facing Cr targets in accordance with conditions described in Table 5.3. The tested sputtering pressures were in the low range (0.1 and 0.5 Pa in argon), where normally dense metal thin films can be formed. Each sample was

referred as sensor 1 (0.1 Pa) and sensor 2 (0.5 Pa) herein.

After sputtering, the microstructures of deposited films in NFTS were examined using SEM (JEOL Inc., Model JSM-6010LV). The fabricated sensor performances were then determined, which procedure was described in the next section.

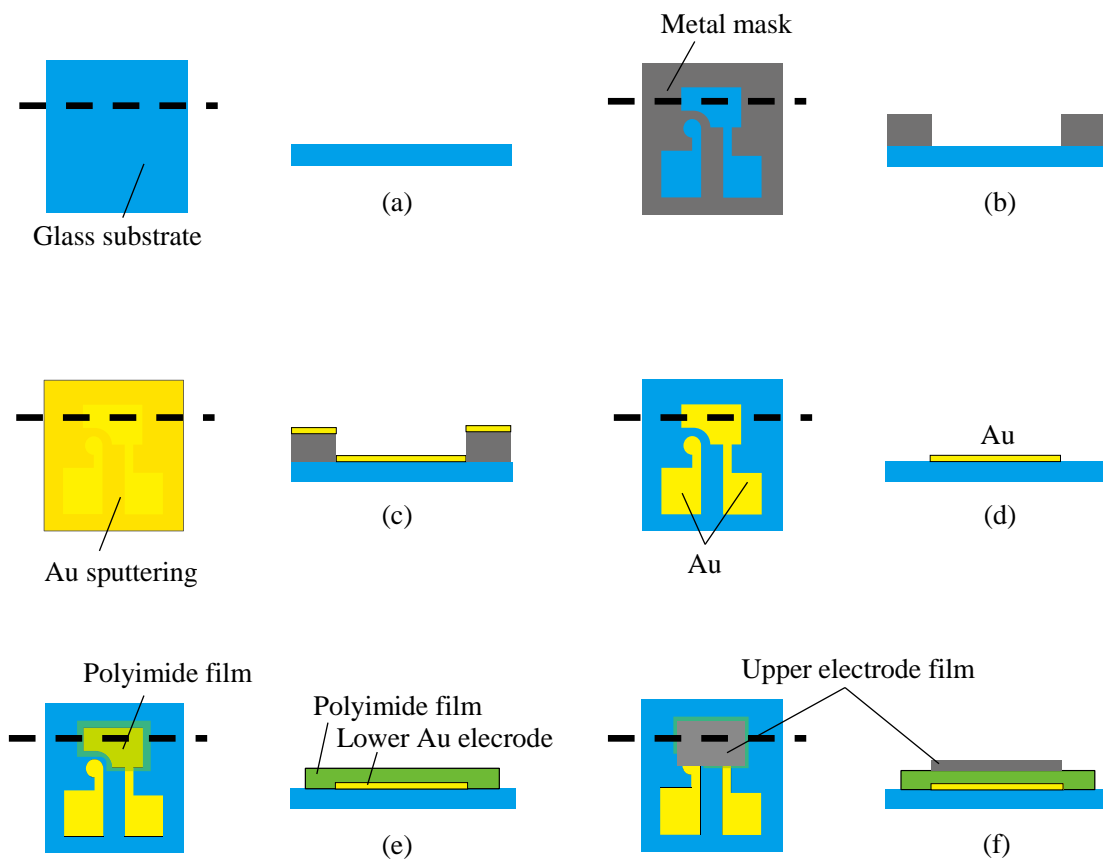


Fig. 5.8 First sensor fabrication process: (a) substrate cleaning, (b) masked substrate using metal mask, (c) deposition of upper wiring and lower Au electrode film including lower wiring, (d) removal of metal mask, (e) deposition of polyimide film, and (f) deposition of dense upper electrode film.

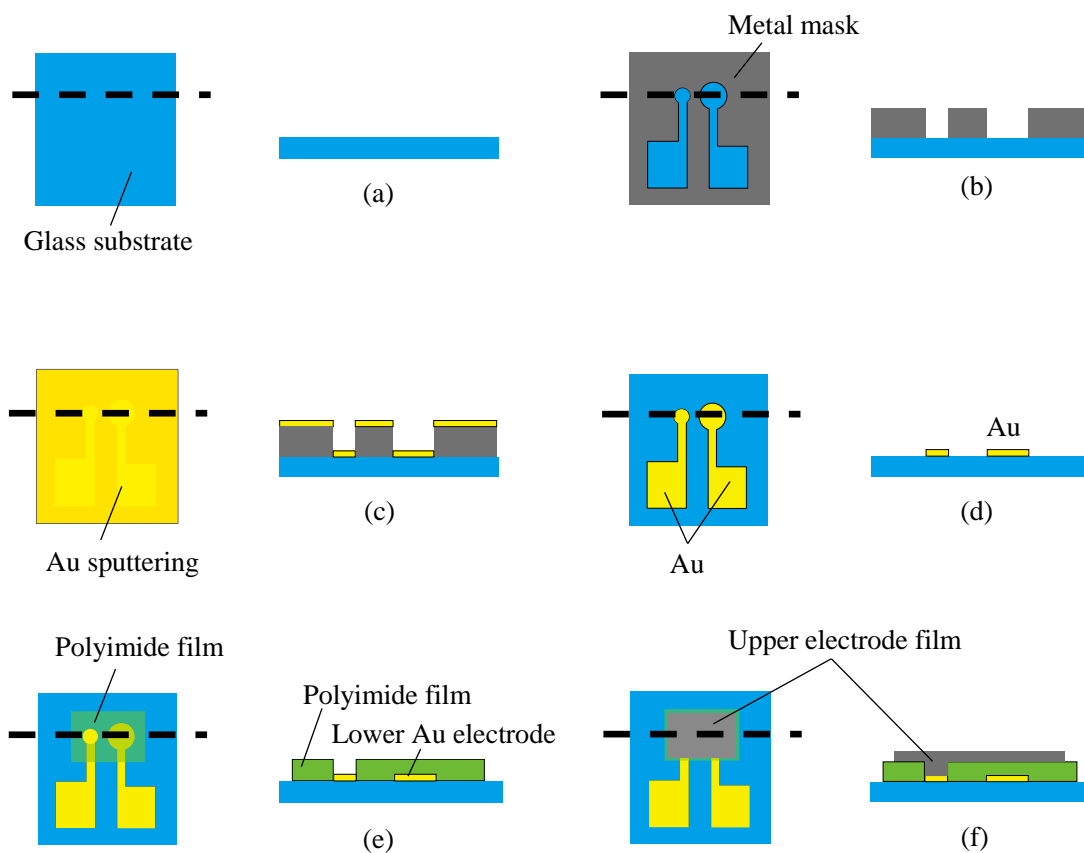


Fig. 5.9 Second sensor fabrication process: (a) substrate cleaning, (b) masked substrate using metal mask, (c) deposition of upper wiring and lower Au electrode film including lower wiring, (d) removal of metal mask, (e) deposition of polyimide film, and (f) deposition of dense upper electrode film.

Table 5.2 Deposition conditions for polyimide film

Spin coat	200 rpm × 10 s → 700 rpm × 10 s → 1800 rpm × 30 s → 2200 rpm × 0.5 s
Pre bake	130 °C × 5 min
Exposure	325 mJ/cm ² for 50 s
Development	NMD-3 for 90 s
Cure	140 °C × 5 min → 240 °C × 5 min → 340 °C × 5 min

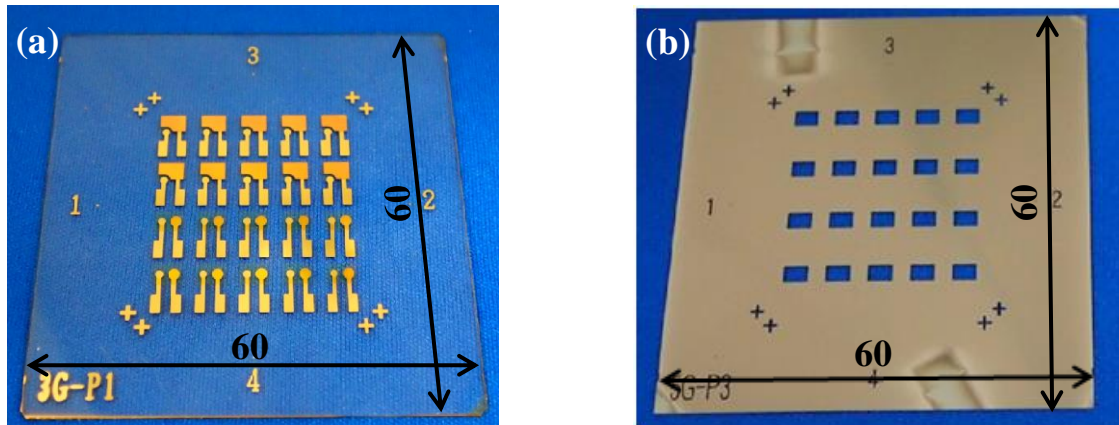


Fig. 5.10 Preparation of wafers; (a) wafer after the fifth step, and (b) metal mask used for deposition of upper electrode film.

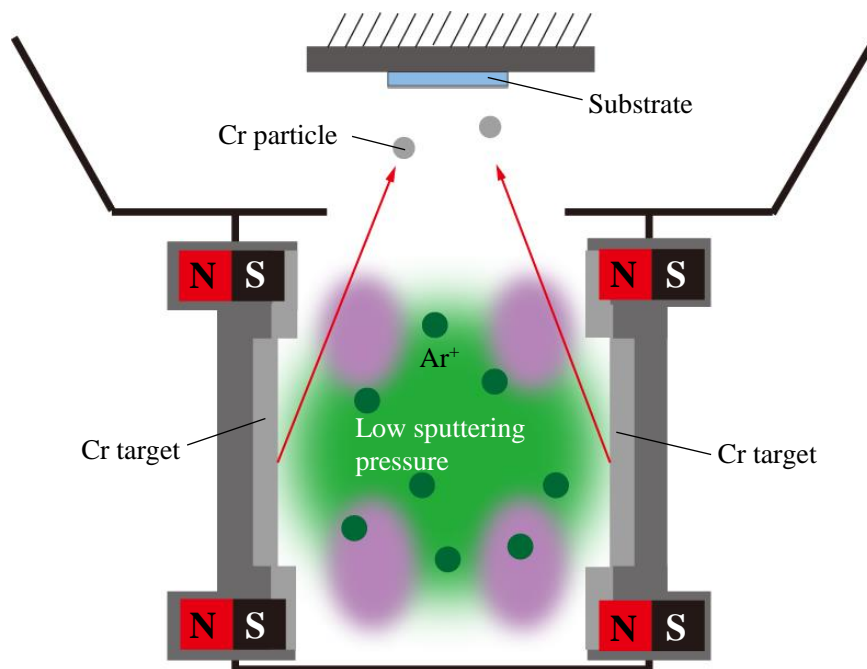


Fig. 5.11 Schematic diagram of NFTS system for deposition of dense upper electrode film

Table 5.3 Sputtering conditions in NFTS

		Sensor 1	Sensor 2
Sputtering pressure (Pa)		0.1	0.5
Sputtering power (W)	Cr	500	500
	Cr	500	500
TS distance (mm)		82	82
Deposition area (mm)		3.5×2.4	3.5×2.4
Film thickness (nm)		420	450

5.3.2 First evaluation system

The fabricated sensors were first evaluated in air (because it is difficult to control the RH in oil). The measurement setup for air, shown in Fig. 5.12, comprised a humidity- and temperature-controlled chamber (ESPEC Inc., Model LHU-113, Controllable range: 30%–90% RH), a reference moisture sensor (VAISALA Inc., Model MMT330), and an LCR meter (Keysight Technologies Inc., Model 4285A, Measuring frequency: 100 kHz) connected to a PC (Software: Agilent VEE Pro 9.2). The reference sensor and the fabricated sensor were simultaneously measured, which records were analyzed using software on the PC. The time-series responsiveness and hysteresis of each fabricated sensor was evaluated using an electrostatic-capacity-transient method, in which the change in the electrostatic capacity was measured between different RH values (50%–90% RH) at 25 °C.

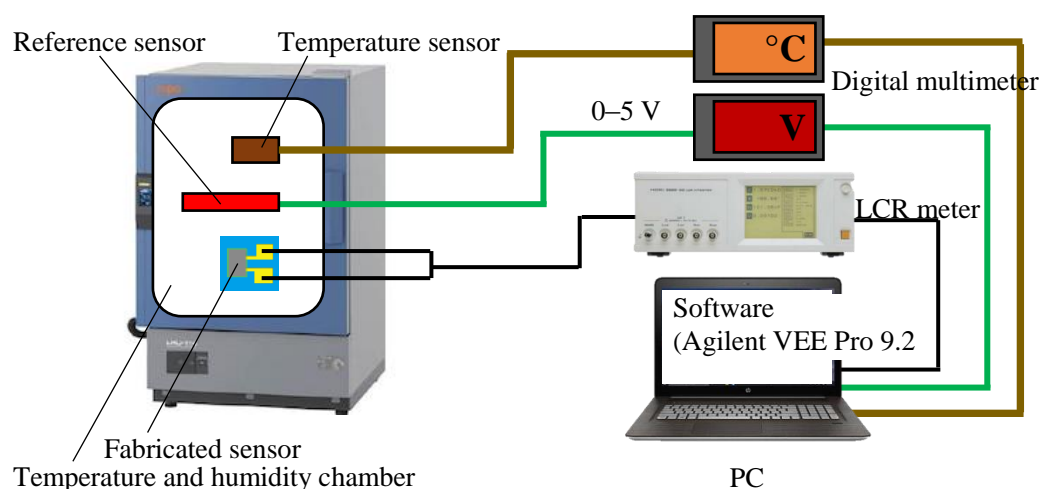


Fig. 5.12 Measurement setup for testing the sensors in air.

5.3.3 Experimental results and discussion

The prepared sensors were first characterized using SEM. The structural observation results are shown in Fig. 5.13. SEM images (a) and (b) were corresponding to sensor 1 and sensor 2, respectively. While the image (a) showed a smooth structure throughout the film surface, the image (b) showed additional cracks to the dense structure. Those cracks may be attributed into the thermal stress, in which polyimide films are thermally shrank under the high temperature. In general, a low substrate temperature can be realized during the sputtering in NFTS, however cooling water might be accidentally not enough, causing an unintentional high substrate temperature. Next, the sensors having the two differential structures were evaluated and compared in terms of the sensor performances.

Fig. 5.14 shows the time-series response of the sensor 1 having the pure dense upper electrode film. The data indicate that the fabricated sensor unfortunately did not react. This have resulted from the poor moisture permeability of the upper film. Dense structure hampered its permeability to water molecules. Hence, the electric capacity of the sensor 1 did not change between different RH values.

Fig. 5.15(a) shows the time-series response of the second sensor having the dense and cracked upper electrode film. It can be seen that the fabricated sensor 2 reacted to the changes in RH, however, there was poor repeatability. Moreover, the measured hysteresis was 35.8% Full Scale (FS), indicating the non-linearity (Fig. 5.15(b)).

In addition, the obtained sensitivity was also extremely low; the designed sensitivity was 17/40 pF/% RH, whereas that of sensor 2 was only 2.5/40 pF/% RH. This resulted from the poor water permeability based on the dense upper film. Cracks created on the film surface allowed the slight water permeability, thus the changes in the electric capacity of the sensor could be observed. However, this sensor performance was far from complete, remaining a lot of problems.

Consequently, the author certified that nanoporous structured upper film are necessary for the sensor. The author expects that the nanoporous electrode film filter may successfully enhance the moisture permeability, as well as may promise an excellent sensor response.

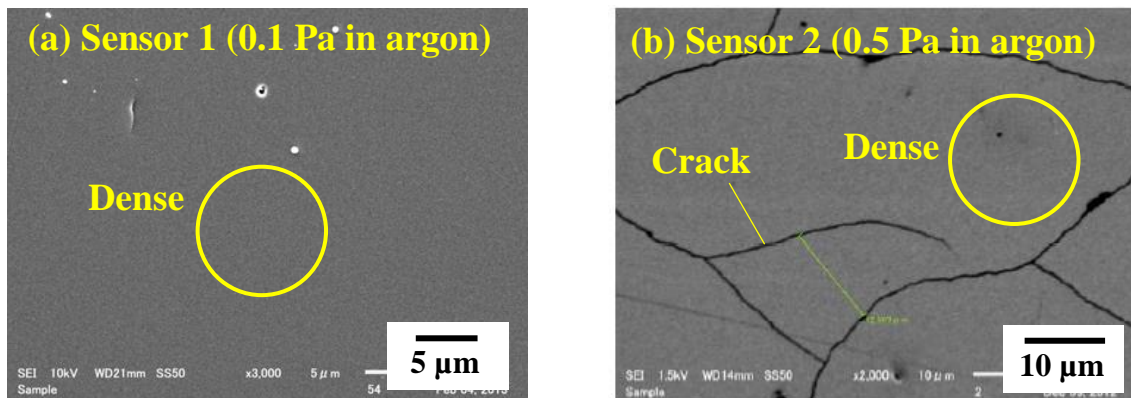
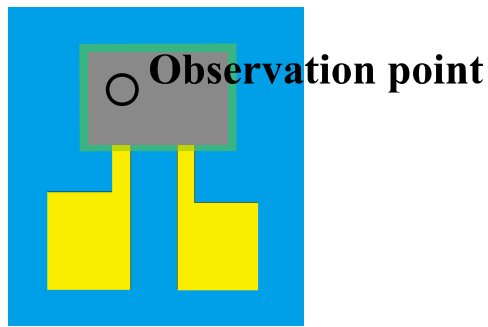


Fig. 5.13 SEM images of upper electrode film structure deposited at (a) 0.1 Pa in argon, and (b) 0.5 Pa in argon.

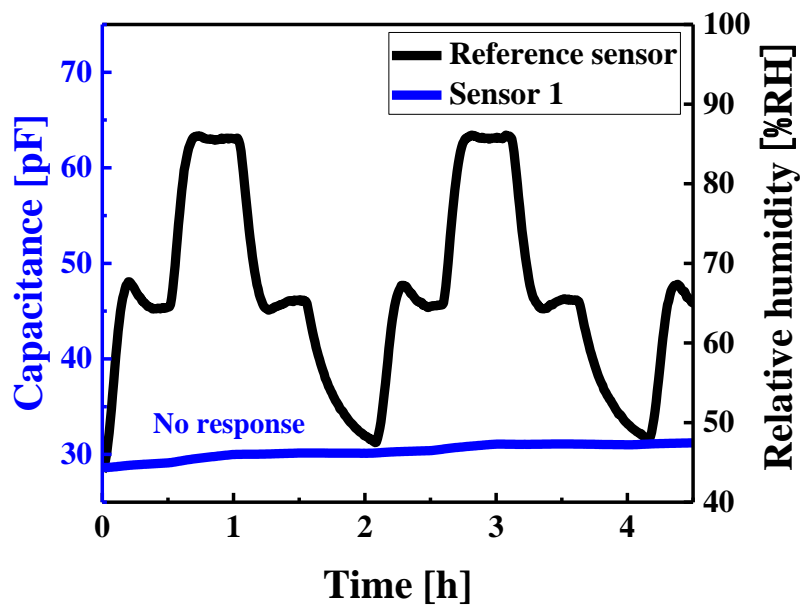


Fig. 5.14 Time-series response of the sensor 1 having dense upper electrode film.

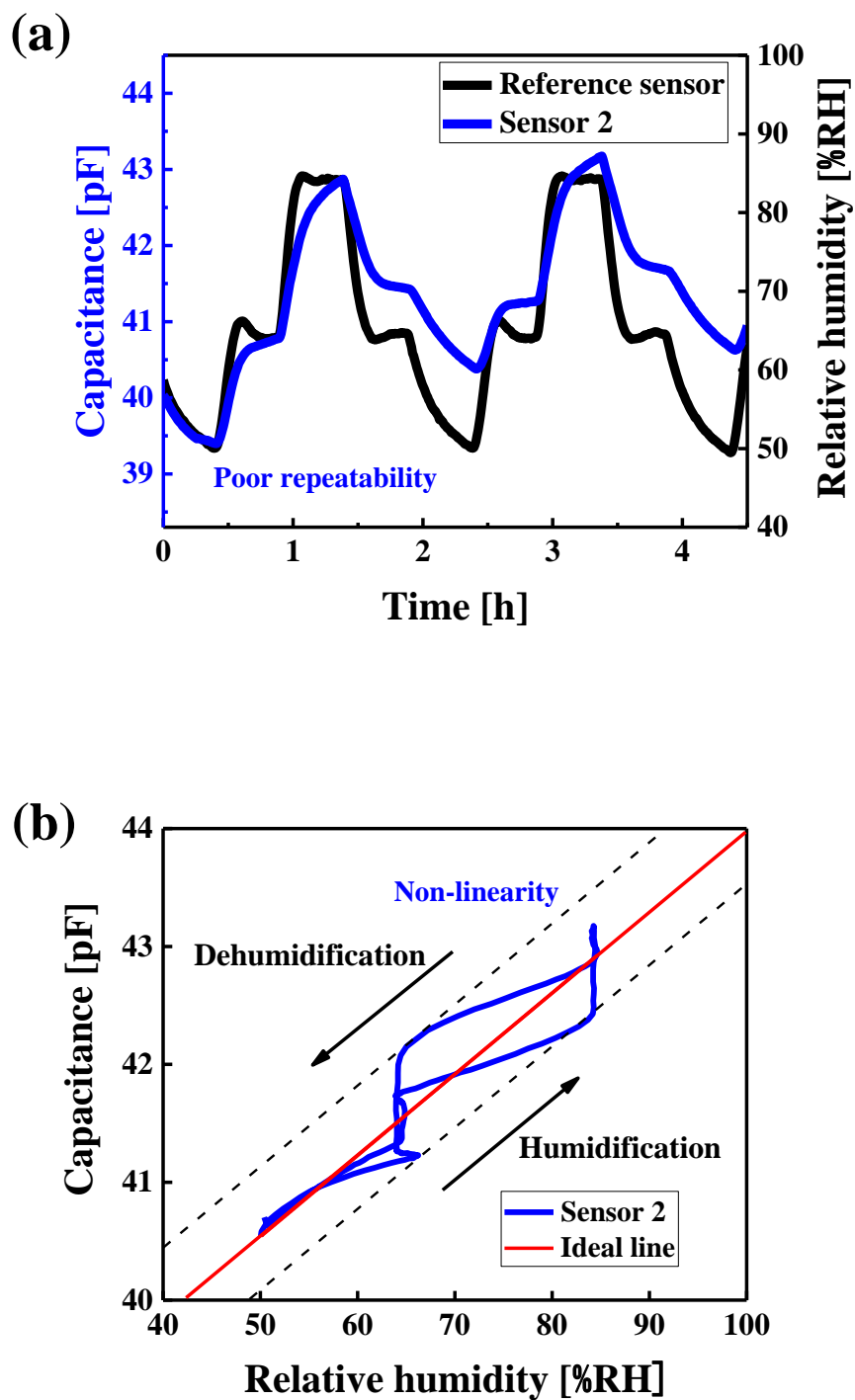


Fig. 5.15 (a) Time-series response and (b) hysteresis of sensor 2 in air at 50%–90% RH and 25 °C.

5.4 Sensors developed via the chemical dealloying including thermal coarsening

5.4.1 Conventional sensor model

A commercially available moisture sensor for oil (Nabtesco Inc., Model N-WIO-006H) has been developed based on our previous research¹⁴⁶⁾ and has also the same condenser structure and exhibit a well responsiveness in oil. Thus, the author used the sensor in this work as the reference sensor. The upper nanoporous electrode films used in the reference sensor have been prepared using oblique incidence film deposition¹⁴⁷⁾⁻¹⁵⁴⁾.

Oblique incidence film deposition is a simple method for fabricating a nanostructure. J. L. Plawsky et.al¹⁵⁵⁾ reported a representative oblique incidence film deposition technique (Fig. 5.16). The incident vapor flux reaches at the substrate at an angle θ , in which the geometric shadowing effect enhanced the formation of the directed nanorods. While the created self-shadowed region by incident vapor flux can hardly receive the target particles, taller islands can continuously receive the target particles and grow longer. The proper nanocolumnar structure in the final cross-section can be seen in Fig. 5.16. This thin film structure promises a well porosity, and has been used as the sensor electrode. However, it is typically difficult to regulate the pore sizes at the nanoscale because oblique incidence film deposition is simply based on sputtering, and the transport of a target particle during sputtering is almost uncontrollable. Moreover, the obtained final film structure has no visible pores, which cannot entirely suggest the pore morphology. It is desirable for a molecular filter to consist of well controllable pore sizes.

The author considered that the chemical dealloying as optimized by combinatorial method could overcome the poor controlling of the pores. Moreover, the effect of pore sizes on sensor performances can be also determined, which may further improve the sensor performance. The author aims to fabricate more effective sensors via chemical dealloying of Cu–Cr alloys with compositions that were optimized by a combinatorial method. Further experimental information were described below.

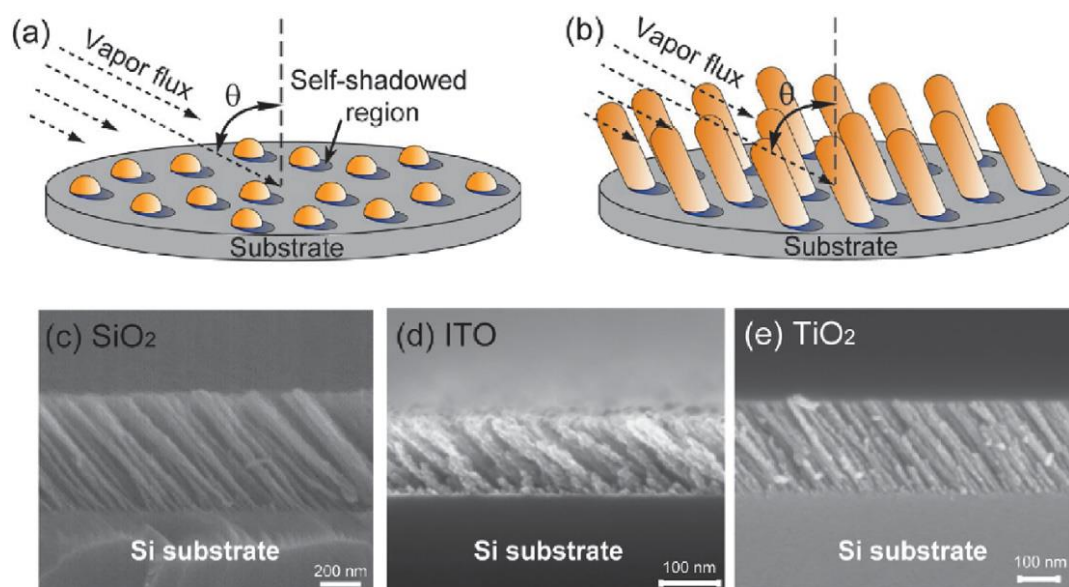


Fig. 5.16 Schematic diagram of oblique incidence film deposition; (a) and (b) the growth of an array of directed nanorods. Cross sectional images of (c) SiO_2 , (d) ITO, and (e) TiO_2 nanorods deposited by oblique incidence film deposition (J. L. Plawsky et.al¹⁵⁵).

5.4.2 Fabrication process

The author presented many types of chemical dealloying of Cu–Cr; the process including high-temperature coarsening (in chapter 2), including low-temperature coarsening (in chapter 3), without thermal coarsening (in chapter 4). The first one requires thermal coarsening at 700 °C for 1 h, whereas the heat-resistant temperature of polyimide films is approximately 350 °C, therefore the author's second or third technique seems to be suitable.

First, the author challenged to prepare the sensors via the chemical dealloying including low-temperature coarsening. Fig. 5.17 shows a sensor fabrication process. A glass substrate was first prepared through the ultrasonic cleaning in acetone for 5 min, and then in ethanol for 5 min, subsequently rinsed in water for 5 min. Next, the substrate was dried through the air blow and heat-treatment on a hot plate in air at 110 °C for 5 min (Fig. 5.17(a)).

Afterwards, the masked glass substrate was loaded in sputtering system, and a Cr adhesion layer was deposited, which was immediately followed by Au sputtering (Fig. 5.17(b) and (c)). The total film thickness was approximately 500 nm. The metal mask was removed after Au sputtering (Fig. 5.17(d)), then a polyimide film (2.0 μm thick) was patterned via lithography following Table 5.2 (Fig. 5.17(e)).

In the next step, the masked wafer was loaded in NFTS, and Cu and Cr were simultaneously

sputtered onto the polyimide film with an area with dimensions $3.5 \text{ mm} \times 2.4 \text{ mm}$ (Fig. 5.17(f)). This resulted in a 500 nm thin film of $\text{Cu}_x\text{Cr}_{100-x}$; this process is further described later. Moreover, the coarsening was conducted at $300 \text{ }^\circ\text{C}$ for 1 h prior to dealloying (Fig. 5.17(g)). Due to the heat-treatment, Cu and Cr were thermally diffused with the grain growth, allowing the excellent Cu etching. The annealed sample was dealloyed by immersing it for 15 h in 32.5% HNO_3 at room temperature, producing a nanoporous film structure (Fig. 5.17(h)).

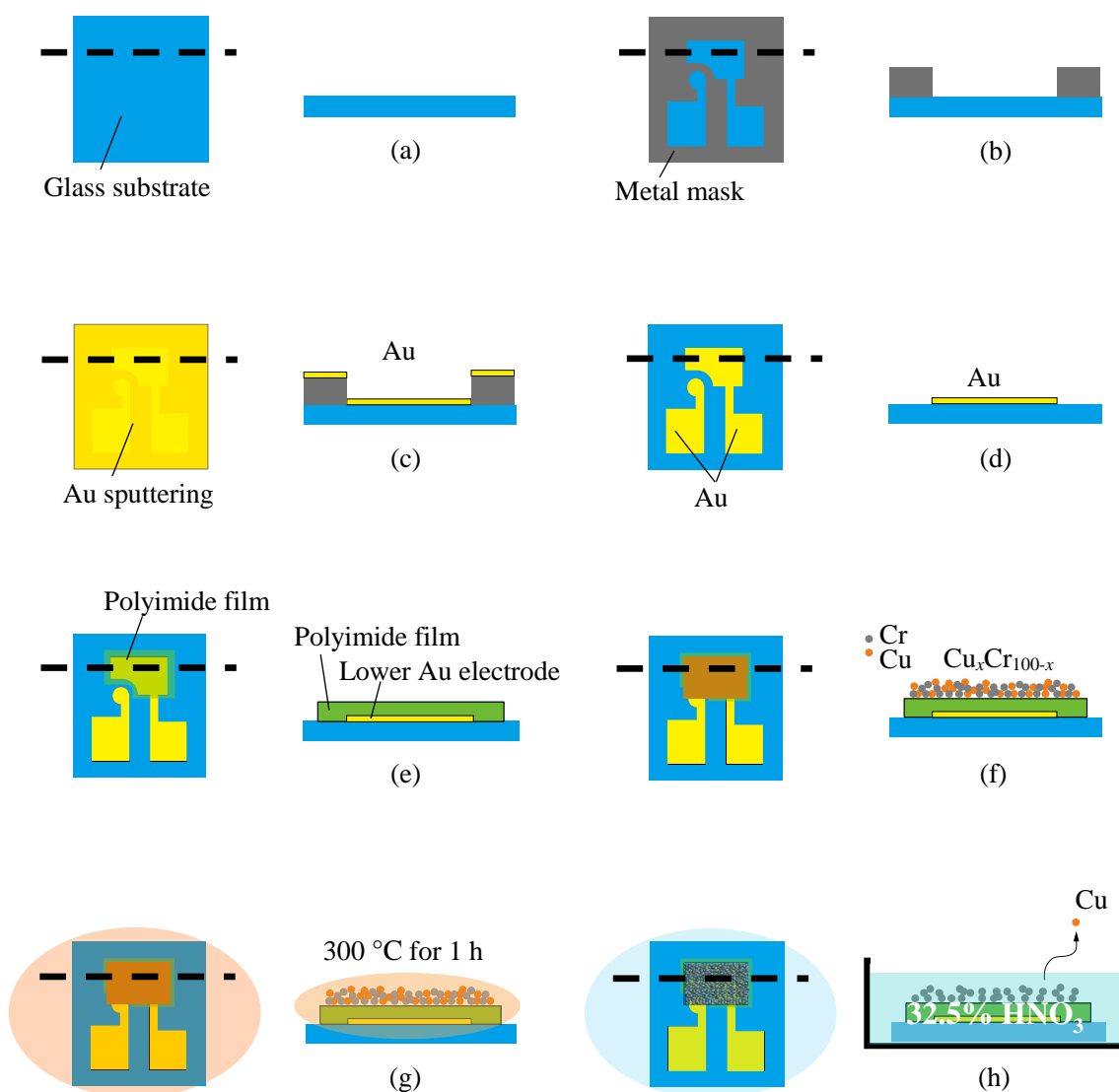


Fig. 5.17 Sensor fabrication process via chemical dealloying including thermal coarsening; (a) substrate cleaning, (b) masked substrate using metal mask, (c) deposition of lower Au electrode film, (d) removal of metal mask, (e) deposition of polyimide film, (f) co-sputtering of Cu–Cr, (g) thermal coarsening in a high-vacuum atmosphere, and (h) Cu dealloying at room temperature.

Cu–Cr alloys with initial compositions ($\text{Cu}_x\text{Cr}_{100-x}$) determined by the previously reported combinatorial search were tested. The results shown in Fig. 5.18 could be obtained in chapter 3, and helpful to identify optimal fabrication conditions for sensors. Because region A could produce the excellent Cu dealloying, and because the pore size for upper nanoporous electrode film filter was targeted in 10–50 nm, the author could successfully determine $\text{Cu}_{72}\text{Cr}_{28}$ as the optimal alloy for the process. Table 5.4 summarized sputtering conditions for NFTS.

The alloy compositions before and after dealloying were first characterized by EDX. Moreover, FE-SEM was used to examine the surface structures of the Cu–Cr film. Sensor performances were also determined following the system shown in Fig. 5.12.

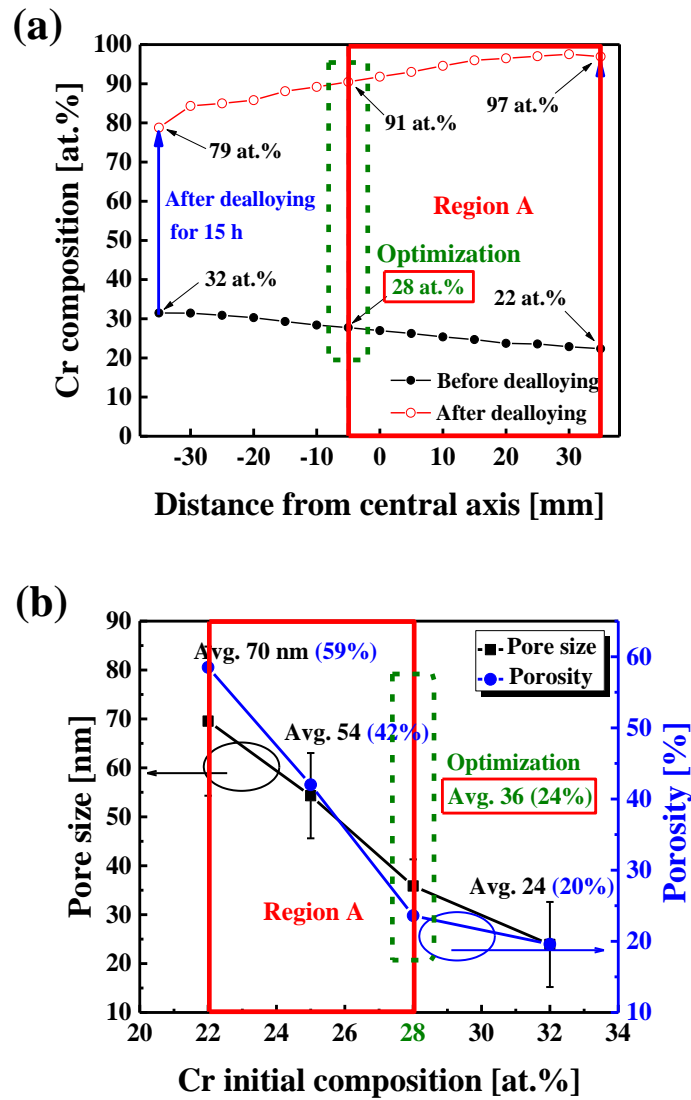


Fig. 5.18 Optimal fabrication conditions for sensors identified in the combinatorial search; (a) the corresponding Cr composition, and (b) final pore size and porosity.

Table 5.4 Sputtering conditions in NFTS

Initial alloy composition (at.%)	Cu ₇₂ Cr ₂₈
Film thickness (nm)	500
Sputtering pressure (Pa)	0.5
Sputtering power (W)	Cu target: 202
	Cr target: 168
Sputtering time (min)	15
TS distance (mm)	82
Deposition area	3.5 × 2.4

5.4.3 Experimental results and discussion

Fig. 5.19 shows the sensor samples fabricated via dealloying process; (a) before dealloying, and (b) after dealloying. In most of sensor samples, upper Cu–Cr films were unfortunately delaminated from the polyimide films during the dealloying service. As seen from the photo (b), the dealloyed Cu–Cr film was broken into fragments, and also the remained parts were easily delaminated by air blow. Therefore, the dealloyed film had the poor mechanical toughness, which have resulted from the heat shrink of the polyimide film (Fig. 5.20). The polyimide films are prone to deformation at a high temperature, and this experimental result showed that the heat shrink was happened at 300 °C for 1 h, which was even within the allowable heat-treatment. The above Cu–Cr film was hardly bound by the bottom polyimide film, thus the heat shrink of the polyimide film generated numerous cracks on the Cu–Cr film surface, resulting in the poor mechanical toughness. Such fragile Cu–Cr films were finally broken down during Cu dealloying.

The survived Cr nanoporous film above the polyimide film had an elemental composition of Cu₁₇Cr₈₃, according to EDX analysis. The deformed Cu–Cr film might hinder the smooth Cu dealloying, resulting in the insufficient Cu etching. Fig. 5.21 shows the white light interferometer (Zygo Inc., Model NewView 5000) image taken after the dealloying process, and it indicates there was uneven adhesion. This can be explained by deformation of the polyimide due to the high temperature atmosphere. Thus, it decreased adhesion between the top Cr nanoporous film and the bottom polyimide film.

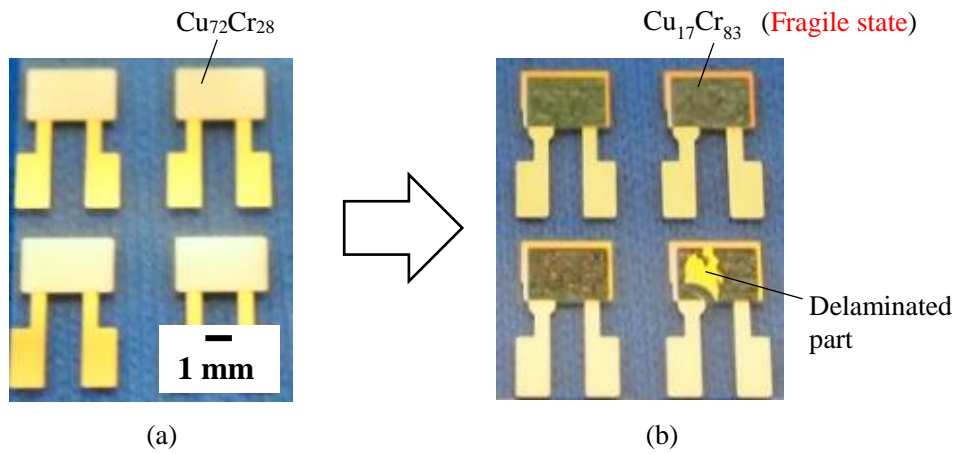


Fig. 5.19 Fabricated sensors; (a) before Cu dealloying, and (b) after Cu dealloying. As seen from the photo (b), upper electrode film was partially delaminated from polyimide film.

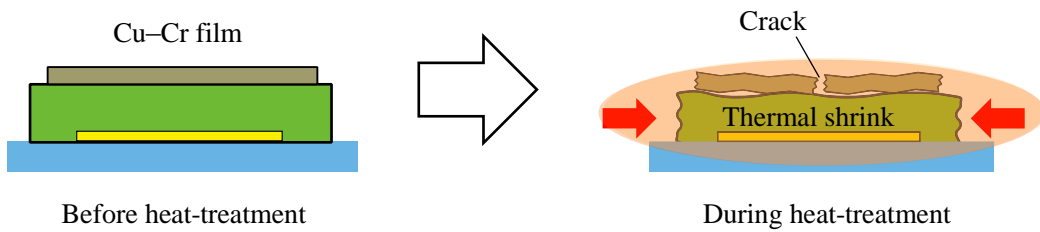


Fig. 5.20 Thermal shrink by polyimide film damaging top Cu–Cr film

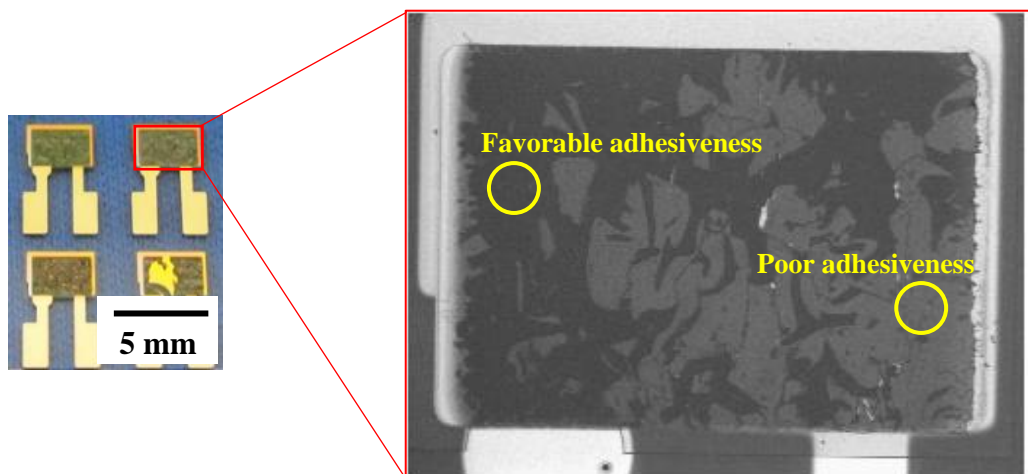


Fig. 5.21 White light interferometer image showing the formation of the surface morphology.

Fig. 5.22(a) shows the FE-SEM (JEOL Inc., Model JSM-6301F) top view taken before the dealloying process and it shows the smooth surface of the Cu–Cr thin film, and Fig. 5.22(b) shows visible porosity after the dealloying process. The time-series response and hysteresis of this sensor were evaluated in air where it is easy to control the RH. Fig. 5.23 shows the electrostatic capacity versus time for 50%–90% RH at 25 °C in the bath. The fabricated sensor followed the changes in RH, but showed the poor responsiveness. It is markedly to note that the sensor performance at the dehumidification was especially low, which resulted from the poor filtration property. Moreover, Fig. 5.24 shows the electrostatic capacity versus RH for the sensor during exposure to 50%–90% RH at 25 °C, and the hysteresis of the sensor was 35.8% FS (the target hysteresis was below 10.0% FS), remaining a lot of problems.

The remained all problems were attributed to the thermal coarsening. This thermal coarsening deformed the polyimide films, weakening the final nanoporous film stability. The fabricated unstable sensor certainly showed the low performances, and an improvement of the sensor is required.

The only way to improve the sensor properties is to skip thermal coarsening step. The chemical dealloying established in chapter 4 allow to execute all steps at room temperature. The author introduces a further improved sensor fabrication process, which is mentioned in the next section.

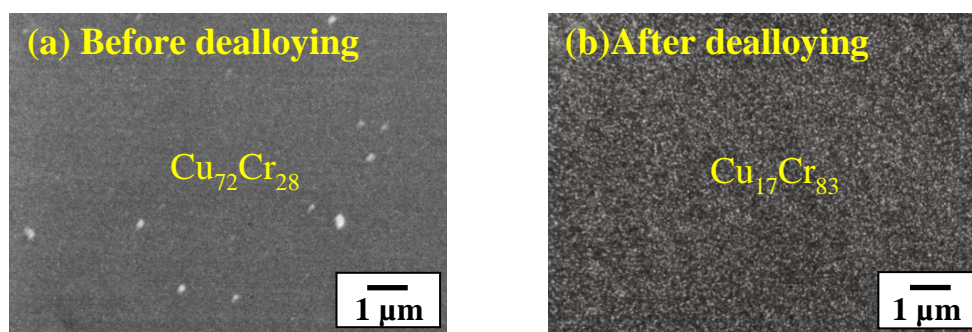


Fig. 5.22 FE-SEM images of Cu–Cr film; (a) before Cu dealloying, and (b) after Cu dealloying. Before Cu dealloying, the top-view showed a smooth structure. By contrast, the top-view showed a visible porosity.

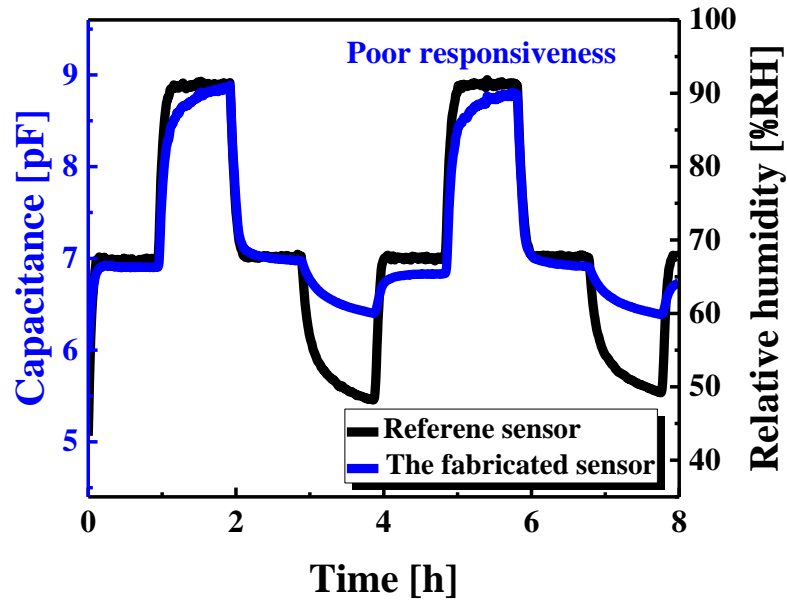


Fig. 5.23 Time-series response of the fabricated sensor with the unfavorable Cr nanoporous electrode film filter. The result showed the poor repeatability. Especially, performances in dehumidification was markedly unfavorable.

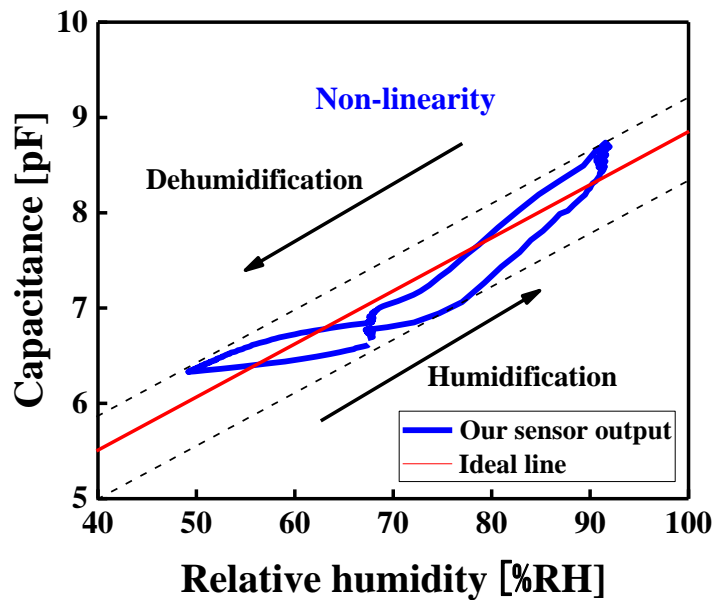


Fig. 5.24 Hysteresis of the fabricated sensor in air at 50%–90% RH and 25 °C.

5.5 Sensors developed via the chemical dealloying without thermal coarsening

5.5.1 New sensor design

The author first redesigned the sensor shape. As mentioned in the section 5.2.2, the old design shown in Fig. 5.4 could cause reduction of sensor output owing to the error in the alignment of the metal mask and substrate. This is because the same dimension of the upper and lower electrode film (dimension: 3.5 mm \times 2.4 mm). The author resolved the problem by designing the upper electrode film to be larger (dimension: 5.0 mm \times 3.6 mm) than the lower electrode film. The wide margin may prevent the reduction of the effective surface (S) even when a trouble is occurred by a position alignment error. The predicted sensor output was approximately 117–134 pF for 50%–90% RH (i.e., estimated sensitivity is same ca. 17/40 pF/% RH).

Fig. 5. 25 shows the new sensor design. Basic structure is the same as Fig. 5.4. To prevent the upper electrode film from being electrically connected with the lower electrode film, the margin of 0.5 mm wide was prepared. Sensor fabrication process was mentioned in more details below.

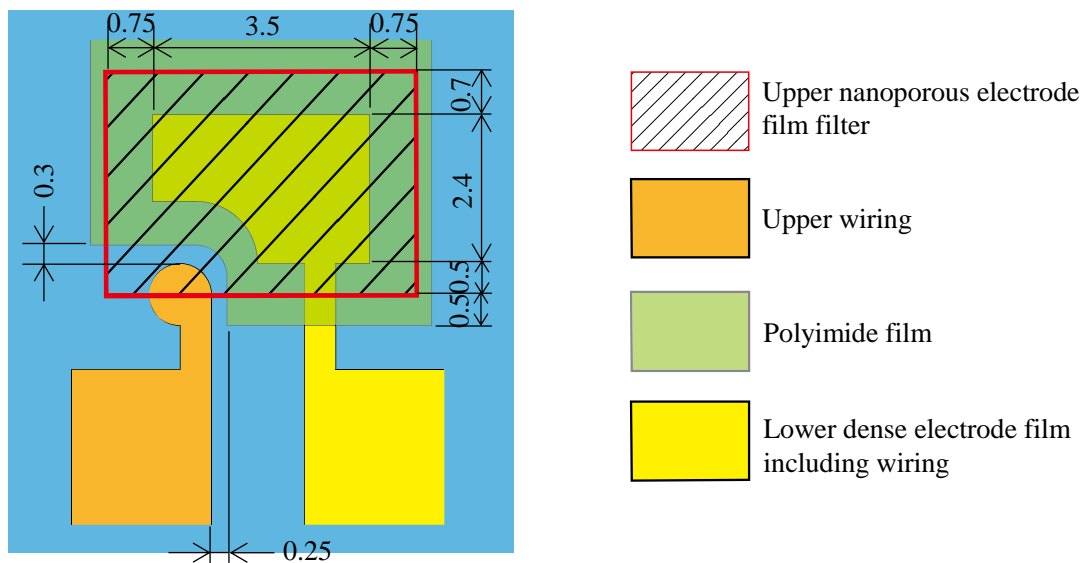


Fig. 5.25 Newly proposed sensor design

5.5.2 Fabrication process

Fig. 5.26 shows a newly proposed sensor fabrication process. A starting glass substrate was first prepared through the ultrasonic cleaning (Honda Electronics Inc., Model W-113) in acetone

for 5 min, and then in ethanol for 5 min, subsequently rinsed in water for 5 min. Afterwards, the substrate was dried through the air blow and heat-treatment in air at 110 °C for 5 min (Fig. 5.26(a)).

In the previous work, the lower electrode film was patterned using metal mask. However, preparation of metal masks was costly, thus liftoff process using photoresist was employed (Fig. 5.26(b)). Negative photoresist (ZEON Inc., Model ZPN1150-90) was spin-coated (Mikasa Inc., Model MS-A150) on the substrate and patterned following the Table 5.5. The coated substrate was prebaked and then treated by exposure apparatus (Union Inc., Model PEM-800), and subsequently post-exposure baked after the exposure step. In the final, the treated sample was developed using alkaline development solution (Tokyo Ohka Kogyo Inc., Model NMD-3), and rinsed with pure water (Fig. 5.26(b)).

A lower electrode film was then deposited by sputtering system (Shibaura mechatronics Inc., Model CFS-4ES-231) in accordance with the Table 5.6. The wafer was first cleaned by reverse sputtering at 100 W for 50 s. Afterwards, a Cr adhesion layer was deposited, which was immediately followed by Au sputtering (Fig. 5.26(c)). The total film thickness was approximately 300 nm thick. Uniform film thickness was achieved by rotating the wafer at 10 rpm during the deposition. Lift-off was carried out acetone immersion for more 10 h to remove the remaining photoresist, thus revealing the lower electrode pattern (Fig. 5.26(d)).

After cleaning the wafer in acetone, ethanol, and pure water immersion, a polyimide film (2.0 μm thick) was prepared via lithography following Table 5.2 (Fig. 5.26(e)). Next, NFTS deposited $\text{Cu}_x\text{Cr}_{100-x}$ film of 350 nm thick onto the polyimide films (Fig. 5.26(f)); sputtering conditions are referred later. Before co-sputtering in NFTS, the surface of the polyimide film was then roughened using polishing sheets (Fig. 5.27) to facilitate a higher bonding force at the interface between the Cu–Cr and polyimide films by the Anchor effect¹⁵⁶, thereby preventing delamination of the Cu–Cr film from the polyimide film during the Cu dealloying.

After Cu–Cr film deposition, Cu dealloying of the deposited $\text{Cu}_x\text{Cr}_{100-x}$ film was performed by immersion in 22.5% HNO_3 at room temperature, yielding a Cr_2O_3 based transparent film with nanoscale pores (Fig. 5.26(g)). This can be explained by considering that the as-deposited Cu–Cr film was composed of small Cr grains, which easily oxidized in the HNO_3 solution. The obtained transparent nanoporous has insulating properties, therefore new eighth step was included into the fabrication process; finally Au was thinly sputtered (20–30 nm thick) on the transparent film to be used as the upper electrode of the sensor (Fig. 5.26(h)).

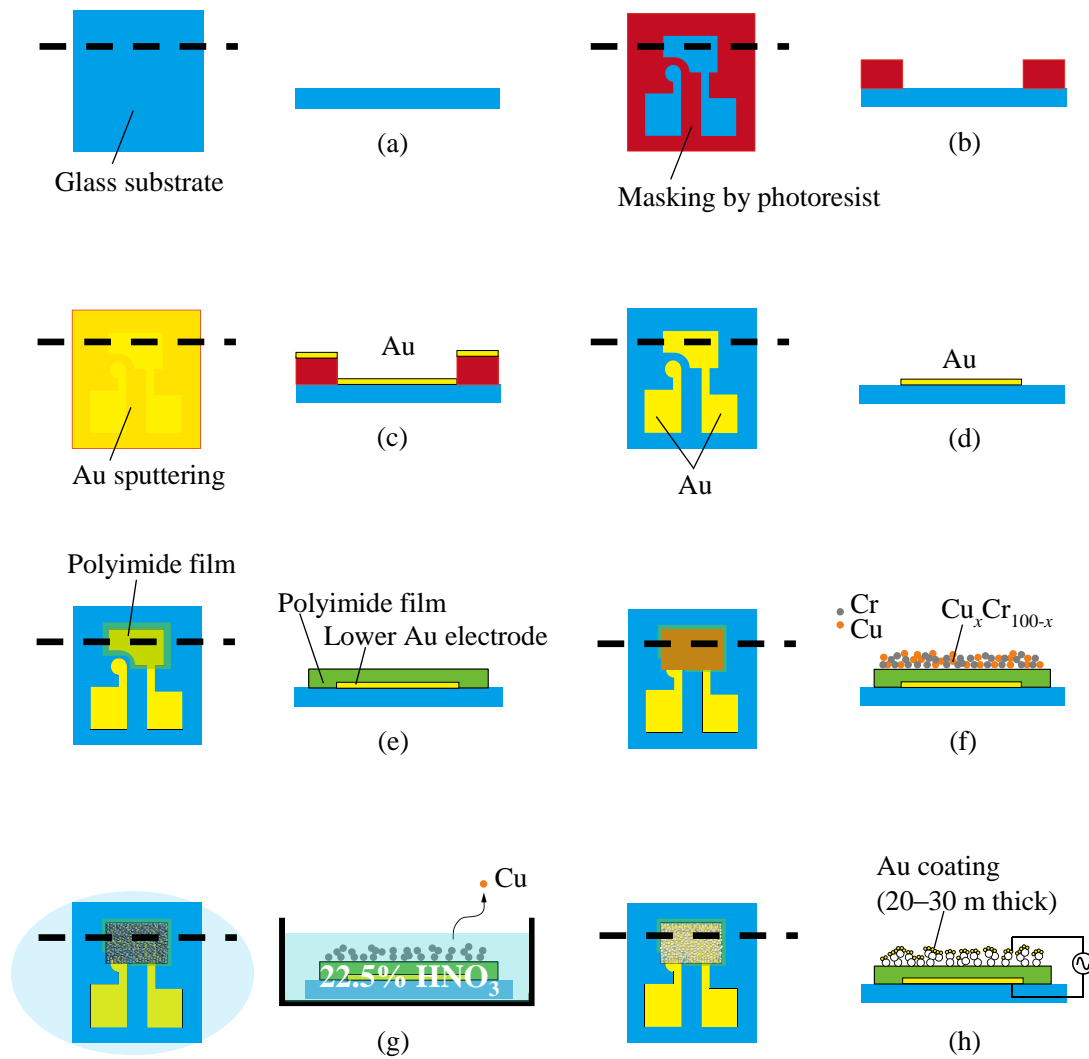


Fig. 5.26 Sensor fabrication process via chemical dealloying without thermal coarsening; (a) substrate cleaning, (b) masked substrate using photo resist, (c) deposition of lower Au electrode film, (d) lift-off process, (e) deposition of polyimide film, (f) co-sputtering of Cu–Cr, (g) Cu dealloying at room temperature, and (h) Au sputtering.

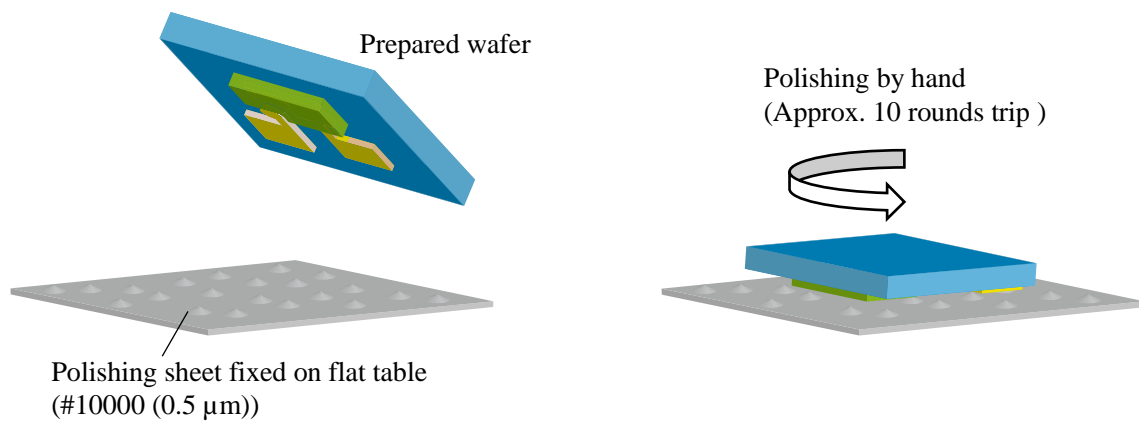


Fig. 5.27 Surface of polyimide film roughened using polishing sheet, facilitating higher bonding force at interface between Cu–Cr and polyimide film by Anchor effect¹⁵⁶.

Table 5.5 Fabrication conditions of mask using photoresist

Spin coat	500 rpm × 5 s → 2000 rpm × 20 s → 2300 rpm × 0.3 s
Pre bake	90 °C × 2 min
Exposure	7.7 mW/cm ² for 7 s
Post-exposure bake	110 °C × 110 s
Development	NMD-3

Table 5.6 Sputtering conditions for lower Au electrode film

Sputtering pressure (Pa)	0.6
Sputtering power (W)	Cr target: 200
	Au target: 200
Sputtering time (min)	Cr: 70 s
	Au: 660 s
Total film thickness (nm)	300

Cu–Cr alloys with initial compositions ($\text{Cu}_x\text{Cr}_{100-x}$) were identified in the previously reported combinatorial search shown in Fig. 5.28. This fabrication map reported in chapter 4 enable the effective and rapid sensor fabrication. Fig. 5.28 reveal that an initial Cr composition of 18 at.% results in sufficient Cu dealloying without film dissolution. Thus, $\text{Cu}_{82}\text{Cr}_{18}$ was selected as the optimal alloy A and used to fabricate nanoporous films and sensors (herein referred to as sensor A).

To evaluate the relationship between the sensor performance and the level of Cu dealloying (corresponding to the pore size), an alloy with a composition that does not yield sufficient Cu dealloying ($\text{Cu}_{80}\text{Cr}_{20}$) was also selected as alloy B and used to fabricate nanoporous films and sensors (herein referred to as sensor B). Sputtering conditions for the two Cu–Cr films in NFTS were summarized in Table 5.7. Hence, sensors A and B were fabricated through the same process but with chemical dealloying of $\text{Cu}_{82}\text{Cr}_{18}$ and $\text{Cu}_{80}\text{Cr}_{20}$, respectively; they were compared in terms of several metrics of sensor performance.

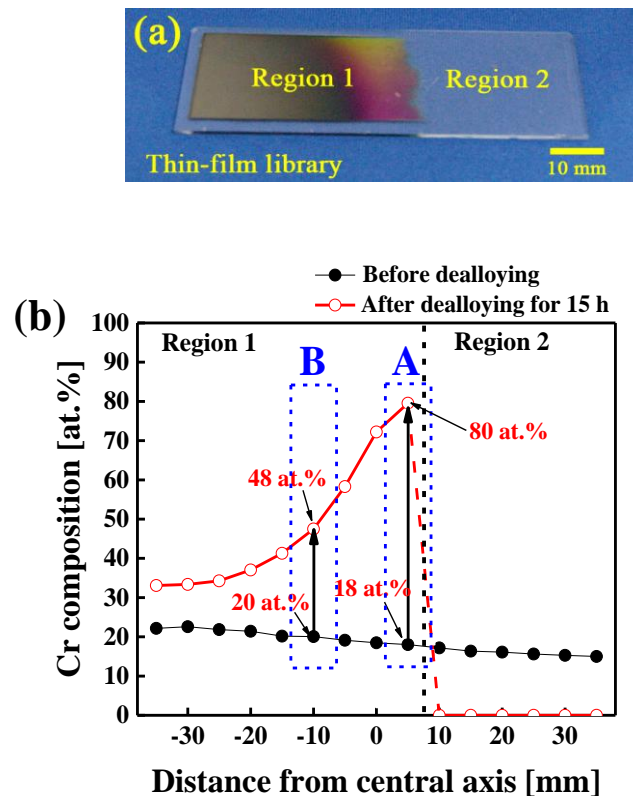


Fig. 5.28 Optimal fabrication conditions for sensors identified in the previously reported combinatorial search.

Table 5.7 Sputtering conditions in NFTS

		Alloy A: Cu ₈₂ Cr ₁₈	Alloy B: Cu ₈₀ Cr ₂₀
Sputtering pressure (Pa)		2.5	2.5
Sputtering power (W)	Cu	175	175
	Cr	80	94
Sputtering time (min)		35	35
TS distance (mm)		82	82
Deposition area (mm)		3.6 × 5.0	3.6 × 5.0
Film thickness (nm)		350	350

5.5.3 Evaluation system in air

The fabricated sensors were first studied in air (because it is difficult to control the RH in oil) and then in oil. The newly constructed measurement setup, shown in Fig. 5.29, comprised a humidity- and temperature-controlled chamber (ESPEC Inc., Model SH-242, Controllable range: 30%–90% RH), an excellent reference moisture sensor (Tateyama Kagaku Industry Inc., Model SPF-54, measurement accuracy: $\pm 3.0\%$ RH, 90% response time: 15 sec), a logger (National Instruments Inc., Model NI myDAQ) and an LCR meter (HIOKI Inc., Model 3532-50, Measuring frequency: 100 kHz) connected to a PC (Software: LabVIEW).

The time-series responsiveness and hysteresis of each fabricated sensor was evaluated using the same electrostatic-capacity-transient method, in which the change in the electrostatic capacity was measured between different RH values (40%–90% RH) at 25 °C. The target value for the hysteresis was less than 10.0% FS.

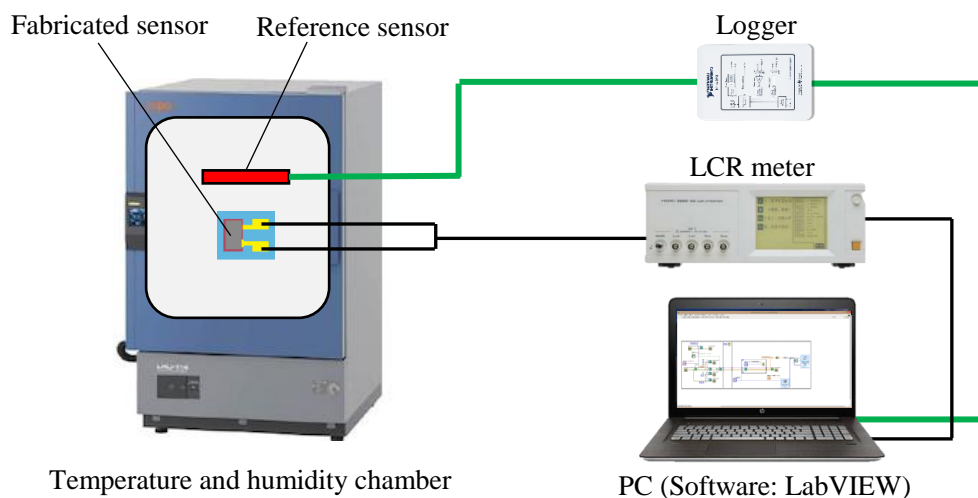


Fig. 5.29 Measurement setup for testing the sensors in air.

5.5.4 Experimental results and discussion

The nanoporous electrode film filters for sensor A were fabricated via sputtering of $\text{Cu}_{82}\text{Cr}_{18}$ on a polyimide film under the condition shown in Table 5.7, followed by chemical dealloying in 22.5% HNO_3 . The $\text{Cu}_{82}\text{Cr}_{18}$ film was dealloyed to $\text{Cu}_{25}\text{Cr}_{75}$; its color changed from brown to transparent (Cr_2O_3) after 7 min of dealloying, as shown in Fig. 5.30, but its thickness remained unchanged. Further Cu etching is normally not possible because prolonging the dealloying time resolved the transparent nanoporous film. This Cu etching performance almost corresponded with the combinatorial analysis shown in Fig. 5.28; final obtained Cr composition was 80 at.% at the combinatorial analysis, and 75 at.% at the sensor fabrication through the same process, indicating that the author's combinatorial analysis was a reliable. The author considered the total dealloying time depending the Cu–Cr film size. The $\text{Cu}_{82}\text{Cr}_{18}$ film used for the sensor fabrication had the small dimension ($3.6 \text{ mm} \times 5.0 \text{ mm}$), in which side etching was enhanced, resulting in the shorter dealloying time.

In the last step of fabrication, Au was thinly sputtered on the transparent $\text{Cu}_{25}\text{Cr}_{75}$ film to be used as the upper electrode of the sensor. Fig. 5.31 shows the obtained sensor. The FE-SEM images shown in Fig. 5.32(a) depict the surface structures of the as-deposited $\text{Cu}_{82}\text{Cr}_{18}$ film prior to dealloying and the Au thinly sputtered on the $\text{Cu}_{25}\text{Cr}_{75}$ film. Nanoporous structures with pores of approximately 20–40 nm were successfully observed after dealloying and Au sputtering, as the FE-SEM images reported in chapter 4 (see Fig. 4.24(b)). Summary, sensors with novel transparent

nanoporous films were fabricated via chemical dealloying of a Cu–Cr alloy with a composition optimized via the combinatorial method. As mentioned in chapter 4, however, some cracks were created on the film surface (Fig. 5.32(b)), remaining a problem.

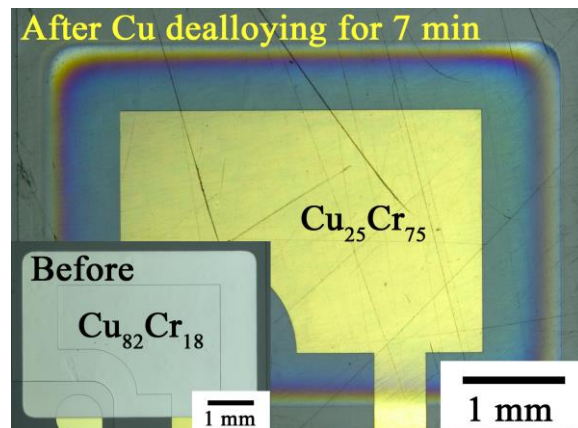


Fig. 5.30 Images of the Cu–Cr film before and after Cu dealloying (sensor A)

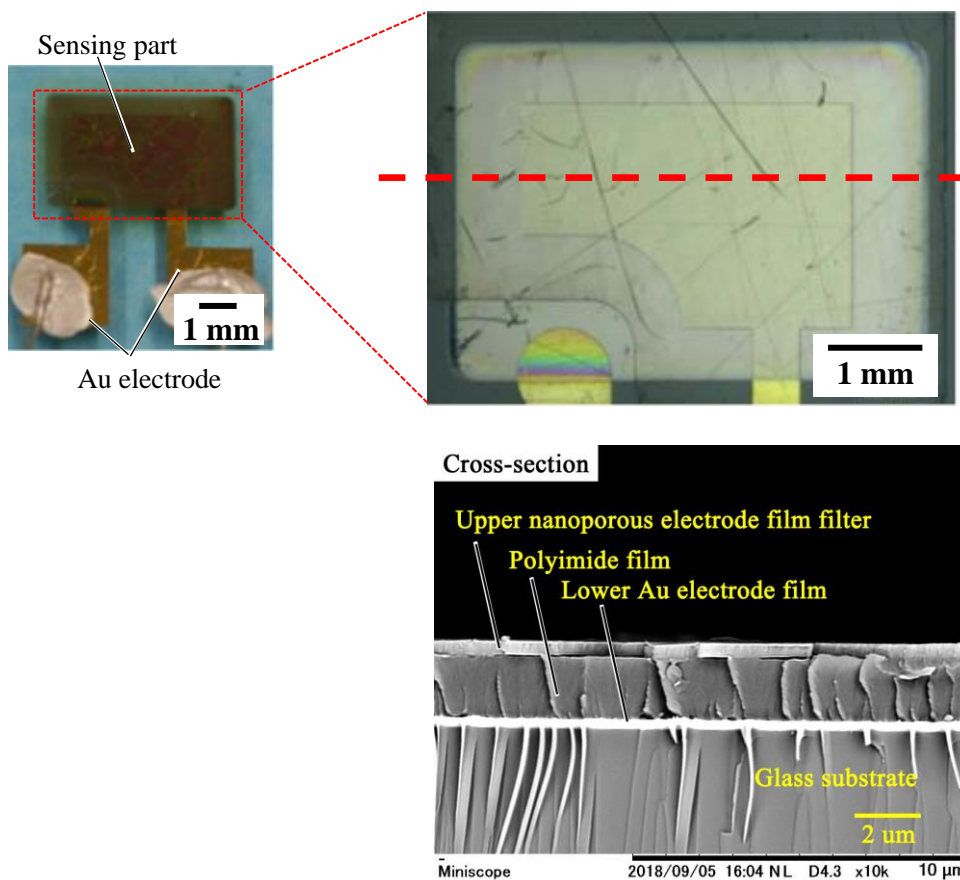


Fig. 5.31 Fabricated oil-moisture sensor A

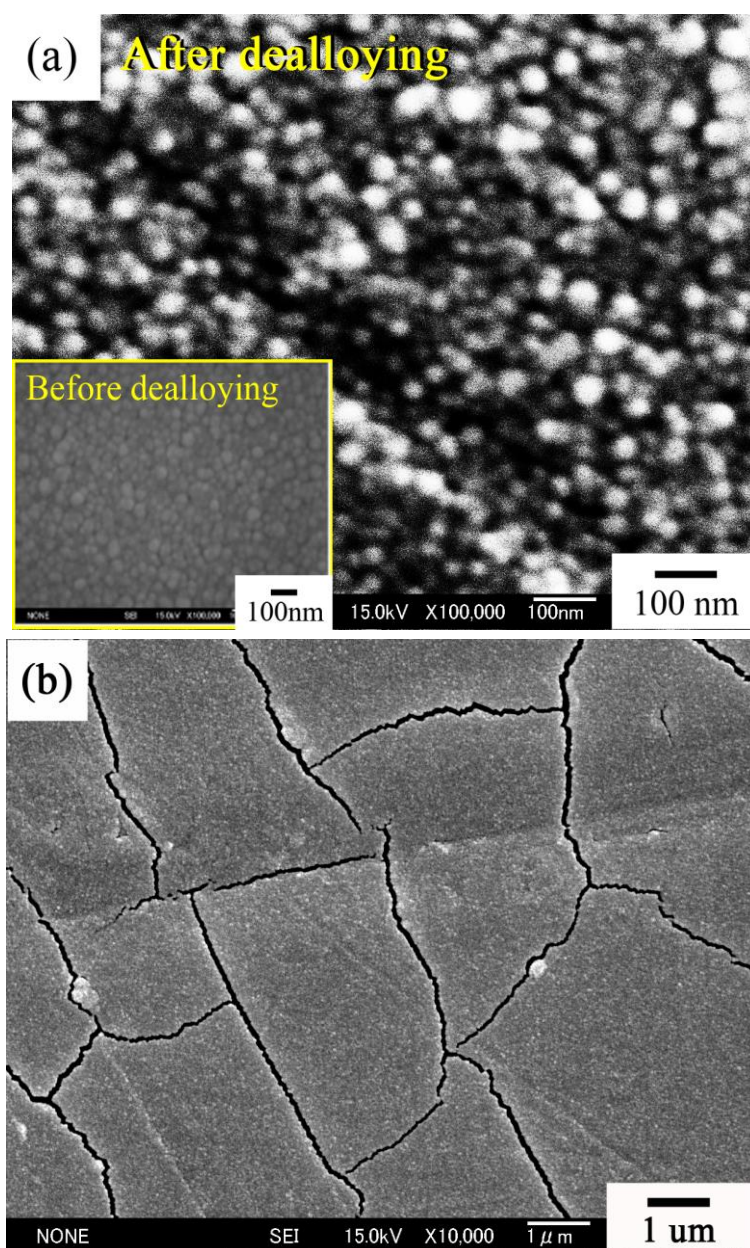


Fig. 5.32 (a) Surface structure before and after dealloying, and (b) film cracks created on the final obtained $\text{Cu}_{25}\text{Cr}_{75}$ film surface.

Next, to investigate the relation between the level of Cu dealloying and sensor performance, another replicate of sensor B was fabricated as shown in Fig. 5.28. Table 5.7 shows the sputtering conditions. The chemical dealloying of $\text{Cu}_{80}\text{Cr}_{20}$ was performed in the same conditions (22.5% HNO_3 for 7 min). Over 7 min of dealloying, the Cu in the $\text{Cu}_{80}\text{Cr}_{20}$ film was gradually etched to yield $\text{Cu}_{46}\text{Cr}_{54}$, and the appearance of the film changed from silver to black, but the thickness

remained unchanged (Fig. 5.33). As indicated by the combinatorial analysis shown in Fig. 5.28, it was not possible to achieve sufficient Cu dealloying.

In the final step of fabrication, Au was thinly sputtered on the $\text{Cu}_{46}\text{Cr}_{54}$ film to be used as the upper electrode film. Fig. 5.34 shows the obtained sensor B. The FE-SEM images in Fig. 5.35(a) and (b) show the surface- and cross sectional structure of the dealloyed Cu–Cr film, respectively. The observed porous structure was unclear, which can be attributed to the insufficient Cu dealloying. The pores were estimated to be smaller than 20 nm. Moreover, even in the chemical dealloying of $\text{Cu}_{80}\text{Cr}_{20}$, a lot of cracks were seen on the film surface (Fig. 5.36). Because the Cu dealloying did not advance in the sample B, the amount of cracks was less than that of sample A. As the Cu dealloying proceeds, relief of internal stresses in the film were gradually enhanced, therefore film cracking was increasingly created throughout the surface.

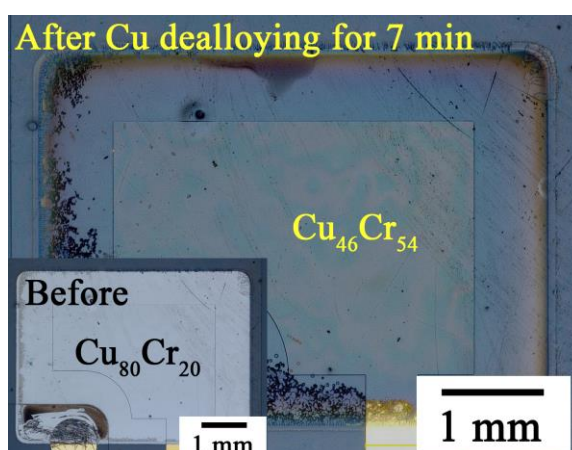


Fig. 5.33 Images of the Cu–Cr film before and after Cu dealloying (sensor B)

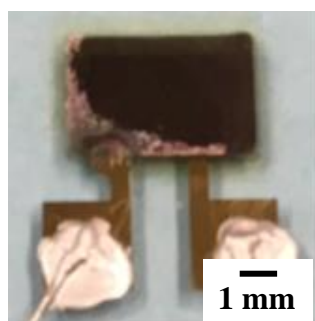


Fig. 3.34 Fabricated oil-moisture sensor B.

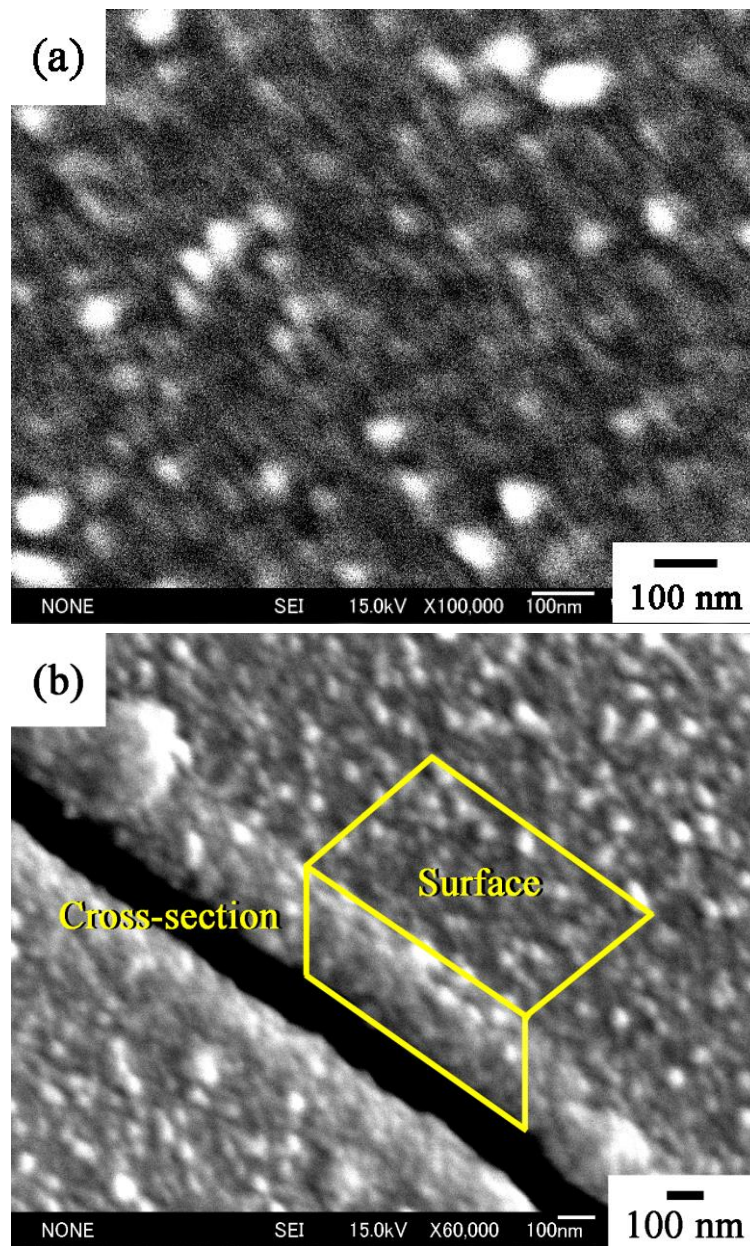


Fig. 5.35 (a) Surface structure and (b) cross-sectional structure of the final obtained $\text{Cu}_{46}\text{Cr}_{54}$ film, unfortunately showing there were no visible pores.

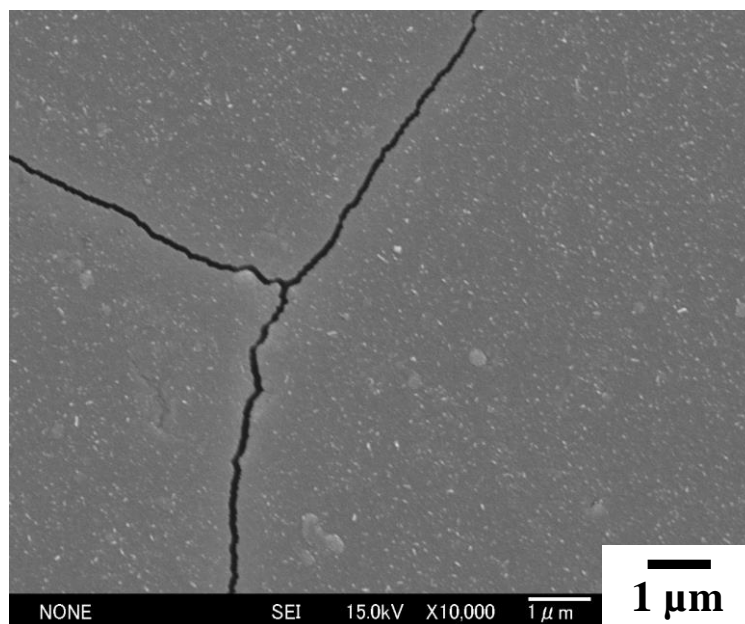


Fig. 5.36 Film cracks were also seen on the final $\text{Cu}_{46}\text{Cr}_{54}$ film surface

Sensor A was first evaluated in air. Fig. 5.37(a) shows the time-series response of the sensor. In this study, the author shortened the evaluation time to investigate the fabricated sensor as soon as possible, but the adequate evaluation time was considered, where minimum two cycles including 90% RH holding for 15 min were carried out. In this evaluation, tracking and keeping of sensor output at each stage (humidification→ 90% RH holding→ dehumidification) were carefully evaluated with respect to the perfect reference sensor. The data indicate that the fabricated sensor exhibited outstanding responsiveness and repeatability in air.

The sensor output range was approximately 130–145 pF at 50%–90% RH, indicating that the sensitivity was ca. 15/40 pF/% RH, which was close to the predicted sensitivity (17/40 pF/% RH). The author considered that the small deviation was caused by the nanostructured upper electrode film. The predicted sensitivity described was estimated when considering a normal capacitor having dense upper and lower electrode films. By processing the pure film into a nanoporous film, the effective surface (S) area of the capacitor or electrical conduction property of the upper sensor electrode was altered, likely resulting in the shift from the designed sensor characteristics. Moreover, as shown in Fig. 5.37(b), the measured hysteresis was 7.4% FS, which was within the target range of <10.0% FS; this confirms that the sensor also exhibited excellent linearity.

By contrast, sensor B was also evaluated in air, and remained a problem on the sensor

responsiveness. Fig. 5.38(a) shows the time-series response of sensor B, which indicates that the sensor output was delayed in response to dehumidification from 90% RH to 40% RH. The sensor output range was approximately 170–188 pF at 50%–90% RH, indicating the favorable 18/40 pF/% RH (predicted sensitivity: ca. 17/40 pF/% RH) based on the almost dense upper film structure. However, as shown in Fig. 5.38(b), the hysteresis of sensor B was 13.3% FS, which is above the target range of <10.0% FS, indicating that the sensor exhibited non-linearity. These results can be attributed to the insufficient Cu dealloying of the upper nanoporous electrode film under condition B, which might hamper its permeability to water molecules.

Although the insufficient Cu dealloying negatively impacted the sensor performances, Fig. 5.38(b) demonstrated that the nanostructures produced by chemical dealloying was very helpful for the separation of water molecules from oil. Fig. 5.39 summarized the performances of the sensor 2 having the dense and cracked upper electrode film, and sensor B. The amount of cracks was nearly the same between two sensors, however sensor B exhibited greater responsiveness, where the hysteresis was approximately 63% down. This improved sensor property could be achieved by the sub-nanoporous islands. In addition, the sensitivity was also drastically improved; the sensitivity of sensor 2 was 2.5/40 pF/% RH, whereas that of sensor B was 18/40 pF/% RH, which surely obeyed the designed value (17/40 pF/% RH).

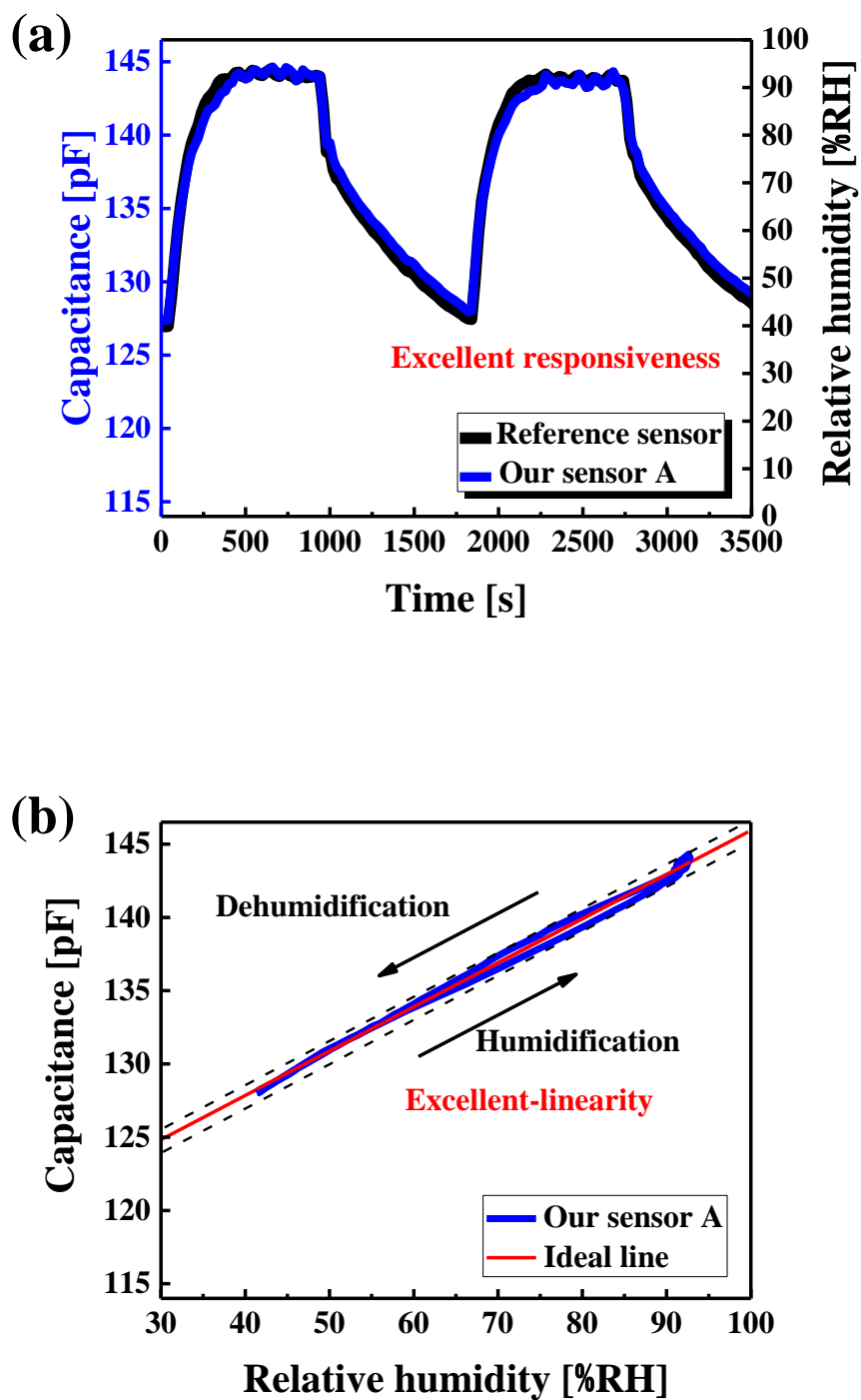


Fig. 5.37 (a) Time-series response and (b) hysteresis of sensor A in air at 40%–90% RH and 25 °C.

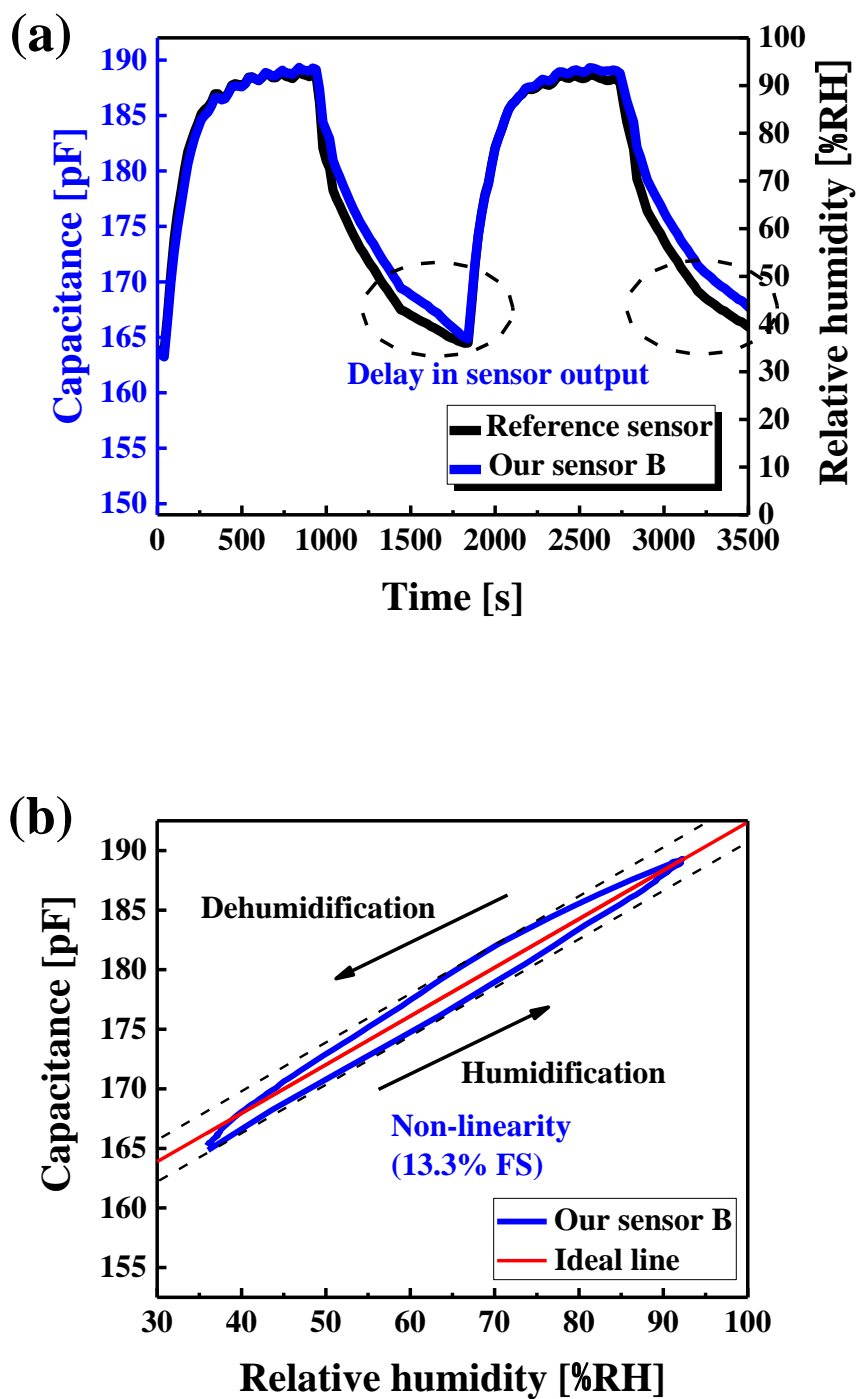


Fig. 5.38 (a) Time-series response and (b) hysteresis of sensor B in air at 40%–90% RH and 25 °C.

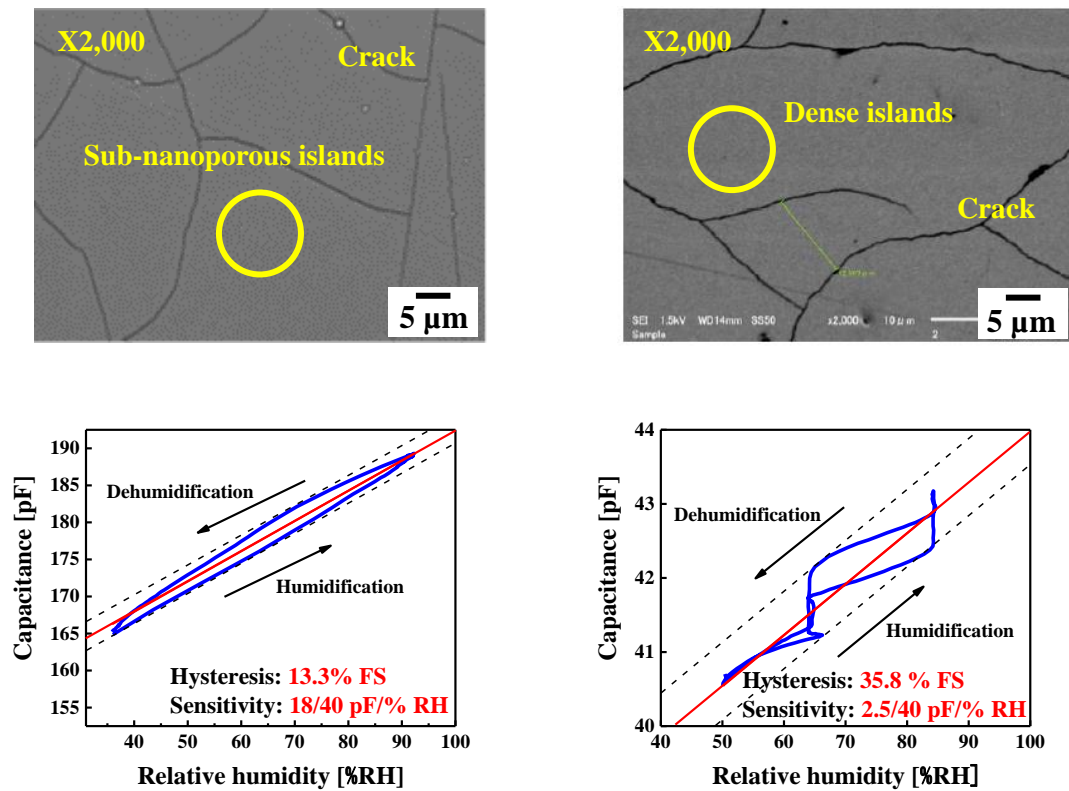


Fig. 5.39 Comparing the moisture permeability property between sub-nanoporous electrode film and dense electrode film. In the situation that the amount of cracks were same between them, the dramatic improved hysteresis and sensitivity could be attributed to the increased film porosity.

Fig. 5.40 shows the summary of the sensor performances in air. Greater film porosity promised the easy moisture permeability; water molecules transport through the upper electrode film was smoothly performed at humidification and dehumidification, leading to excellent linearity. The target hysteresis less than 10.0% FS was successfully achieved by the chemical dealloying using $\text{Cu}_{82}\text{Cr}_{18}$ alloy film. Summary, the optimal pore size for the sensor could be determined by minimum 20–40 nm, which can be clearly observed in the level of FE-SEM resolution.

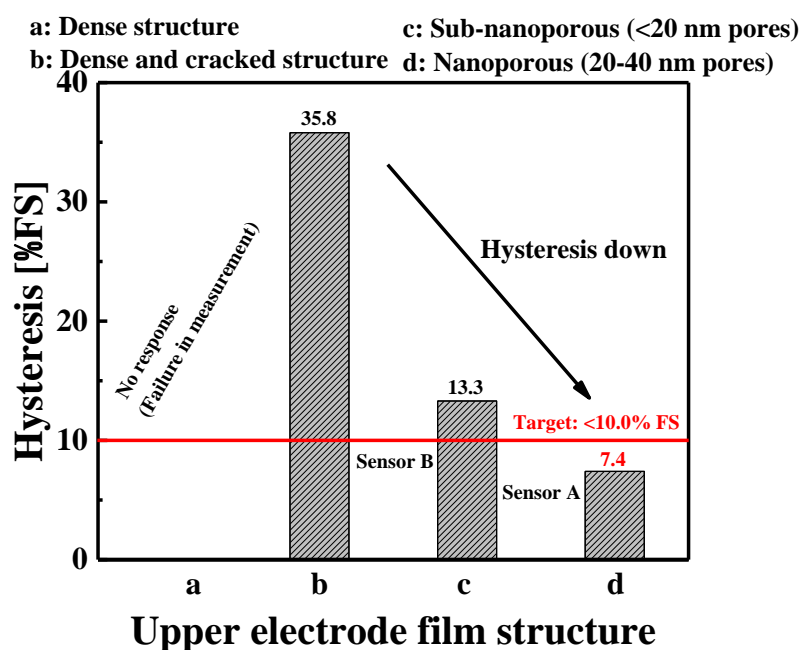


Fig. 5.40 Hysteresis at different upper electrode film structure

5.6 Final evaluation for sensors

5.6.1 Evaluation system in oil

Furthermore, the performance of the fabricated sensors in oil was determined based on the transient moisture content in oil. Fig. 5.41 shows the measurement setup for oil, comprising an oil bath (fresh industrial lubricating oil (Oil type: RO150) was used) placed on a hot stirrer (AS ONE Inc., Model DP-1S), a reference moisture sensor for oil (Nabtesco Inc., Model N-WIO-006H, 90% response time: approx. 10 min), a logger (National Instruments Inc., Model NI myDAQ) and an LCR meter (HIOKI Inc., Model 3532-50, Measuring frequency: 100 kHz) connected to a PC (Software: LabVIEW).

The fabricated sensors were placed in the oil at 30 °C along with the reference sensor. Then,

purified water was gradually added to the oil (30%–100% RH) which was stirred at a high speed. The data from the newly proposed sensors and the commercial reference sensor were simultaneously recorded by the LCR meter and logger, and compared in terms of performance. The reference sensor output format (4–20 mA (=0%–100% RH)) is converted to the voltage value (0.4–2.0 V), which can be fetched by the logger (National Instruments Inc., Model NI myDAQ).

The 90% response time in oil was also measured as the time taken by the fabricated sensor output to reach 90% of the maximum output; the target value was less than 10 min. Experimental procedure is as follows;

First, the reference sensor and the author's sensor were simply compared, in which the purified water was constantly added to the oil at approximately 3.5% RH/min. This test immediately revealed which sensor was superior.

Second, the speed run of the sensor responsiveness was determined, which can be identified by comparing each sensor's 90% response time. The reference sensor as well as the author's sensor were arranged at the bottom of the oil bath, therefore a slight lag time occurred as it took time for the added water to reach the sensing area. Thus, the author assisted the mixing of water and oil by using a stirring stick, which immediately resulted in the formation of a uniform, single layer.

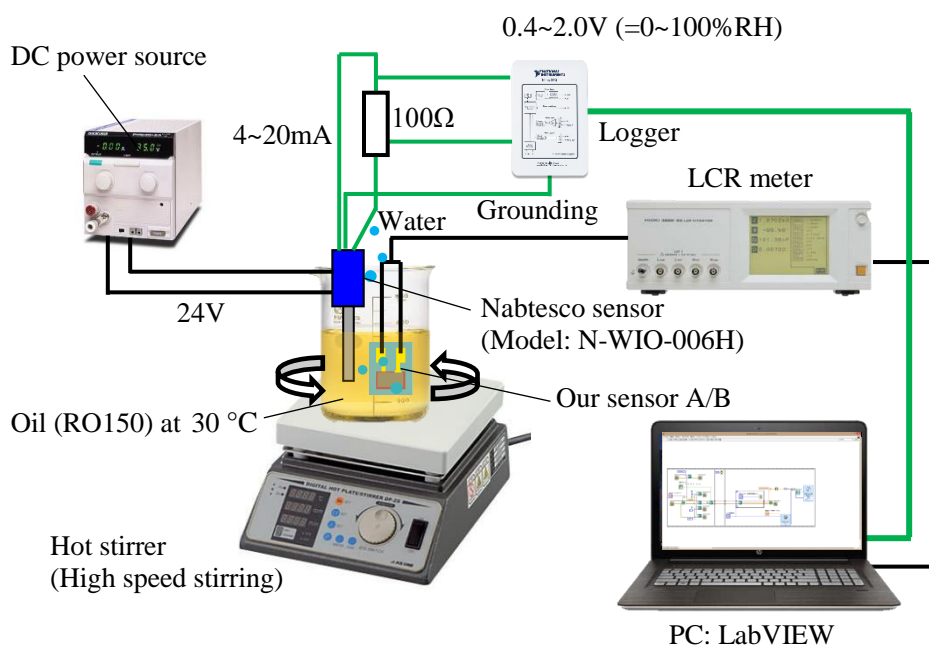


Fig. 5.41 Measurement setup for testing the sensors in oil.

5.6.2 Experimental results and discussion

Sensor A showing the best hysteresis in air (7.4% FS) was first tested. As purified water was gradually added to the oil at approximately 4.0% RH/min, and the results were compared with the measurements from the reference sensor. A glass beaker (max. 300 ml) was used for the oil bath. The rotating speed of the oil was 150 rpm. Fig. 5.42 shows the responsiveness of each sensor in oil, indicating this sensor is superior to the reference sensor. Thus, the novel nanoporous films fabricated via chemical dealloying of $\text{Cu}_{82}\text{Cr}_{18}$ are promising as effective molecular filters.

Sensor B showing the unsatisfied hysteresis in air (13.3% FS) was also evaluated in oil and compared to the reference sensor. Purified water was added at approximately 3.0% RH/min. The rotating speed of oil was same 150 rpm. Fig. 5.43 shows that sensor B was superior to the reference sensor; however, the change in sensor output as the RH increased was relatively slow. The measured sensitivity at the starting phase was approximately 4.1% RH/min for sensor A, whereas the sensitivity for sensor B was approximately 1.1% RH/min, indicating that the sensor A was superior to sensor B.

As seen from the graph curve, the reaction of the reference sensor initially delayed, which may have resulted from the poor water diffusion in oil around the reference sensing area. Later, the graph curve sharply rose, catching up its proper output. To prevent this lag, a smaller oil bath and higher rotating speed were implemented and used to determine the 90% response time.

Finally, the 90% response times of all sensors were measured. A smaller glass beaker (max. 100 ml) was used for the oil bath, and the rotating speed of the oil was 900 rpm, quickly becoming the favorable mixing state of the water and oil. The enough purified water was added rapidly to the oil. As shown in Fig. 5.44, each sensor output changed from 0% to 100%, and the 90% response time was 8 min for sensor A, 10 min for sensor B, and 12 min for the reference sensor. Thus, sensor A exhibited the best performances in both air and oil.

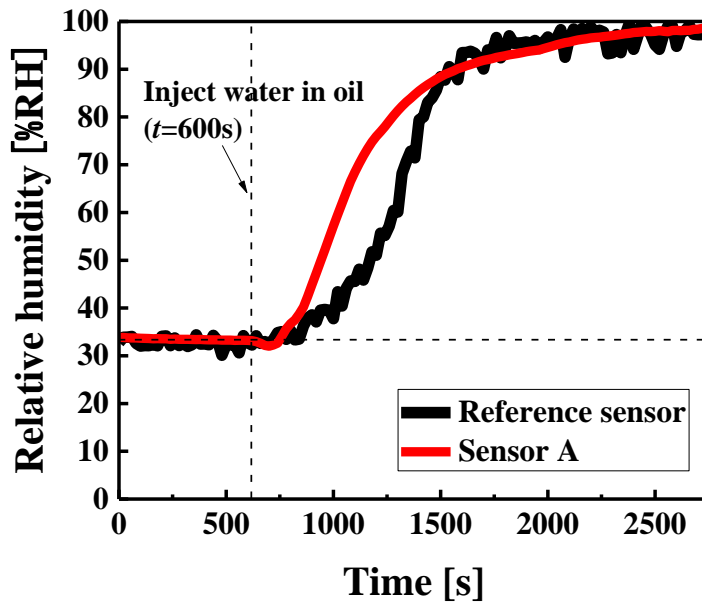


Fig. 5.42 Comparison of sensor A to the reference sensor for moisture measurement in oil.

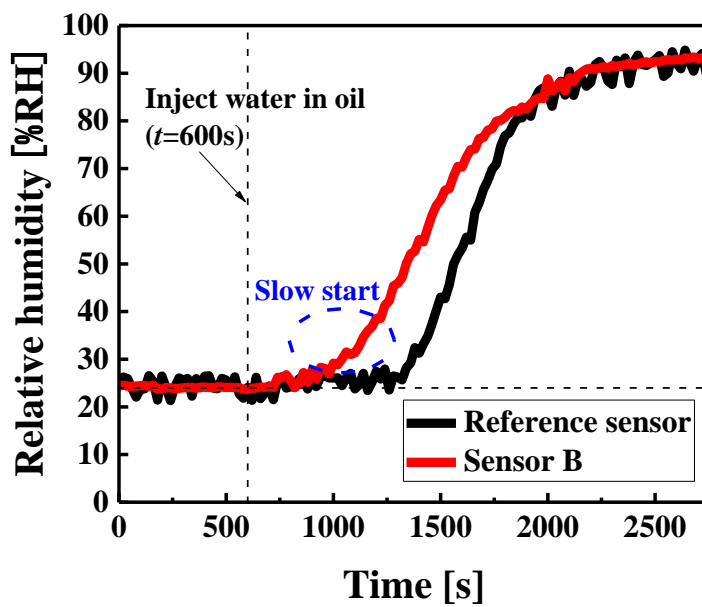


Fig. 5.43 Comparison of sensor B with the reference sensor for moisture measurement in oil.

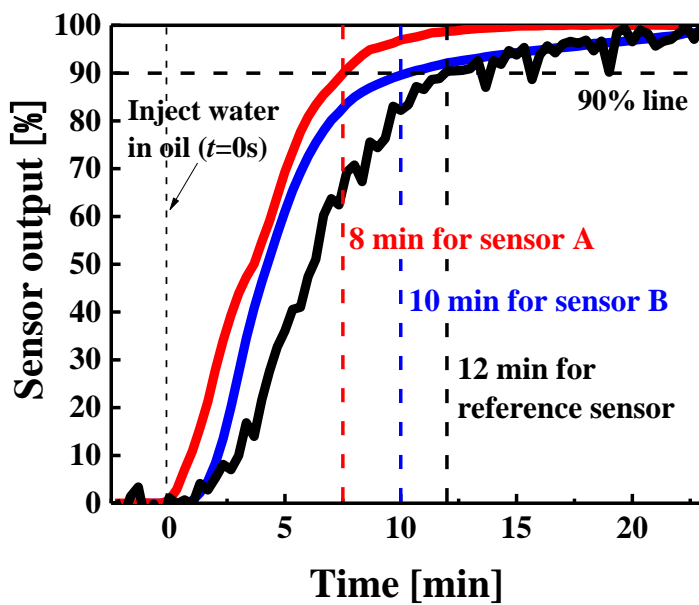


Fig. 5.44 90% response time of each sensor for moisture measurement in oil.

5.6.3 Summary of sensor performances in air and oil

Fig. 5.45 shows the summary of sensor performances in air and oil, indicating the performance rank characterized by evaluation in air was reflected in that in oil. Sensor A exhibited the best performances in both air (excellent sensitivity, repeatability and 7.4% FS for linearity) and oil (8 min for 90% response time). This result could be achieved via novel chemical dealloying of Cu–Cr alloys as optimized by a combinatorial analysis.

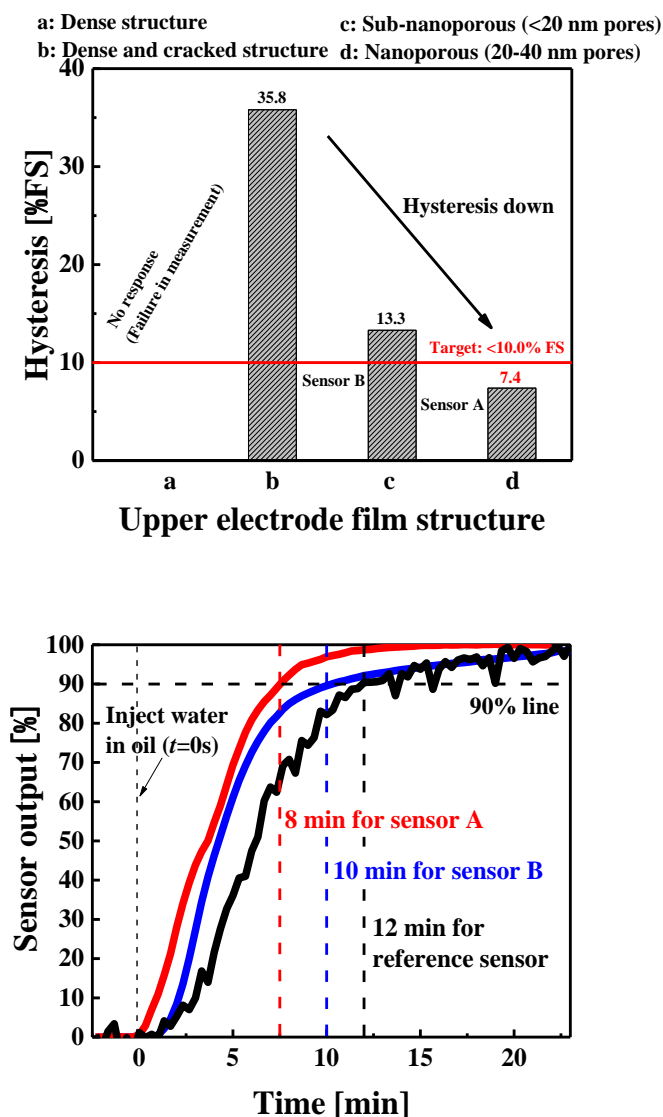


Fig. 5.45 Summary of sensor performances. The best sensor performance (hysteresis (7.4% FS) in air and 90% response time (8 min) in oil) was found out using combinatorial approach.

5.6.4 Future works

The fabricated sensor A exhibited the outstanding hysteresis (7.4% FS) in air at 25 °C, however the sensor could not keep the level (within 10.0% FS) with increase of measuring temperature. The measured hysteresis was 13.8% FS at 35 °C, and 29.5% FS at 50 °C, gradually becoming non-linearity. The oil temperature used in an engine system normally becomes ca. 50 °C, therefore the improvement of the heat-resistance property is required.

The author considered that the poor heat resistance was attributed to the film cracks created on the nanoporous electrode film filter (Fig. 5.32(b)). The cracked sensor electrode film has the poor mechanical toughness, and might be deformed by the thermal shrink of the polyimide film. The deformed nanoporous films may hamper the moisture permeability, resulting in the large hysteresis. Accordingly, removing film cracks must be necessary, and research is now ongoing.

5.7 Summary

In this chapter, the author aimed the nanoporous film for application in MEMS moisture sensor for oil. The sensor fabrication was conducted based on sputtering/lithography/chemical dealloying. The process parameters were effectively identified in the previously reported combinatorial analysis. The fabricated sensors were compared with the reference sensor in terms of several metrics of sensor performance.

At the beginning, the motivations of this work were mentioned, and then the author explained the principle of the proposed sensor. Moreover, the sensor structure was carefully designed.

As preliminary test, the densely structured electrode film was applied to the sensor. However, the final sensor entirely did not operate. This was due to that the dense film hindered the moisture permeability. The sensor having the additionally cracked upper film also did not work, and showed the poor linearity (=35.8% FS). These findings demonstrated that the nanoporous film was a key-material for realizing the moisture sensor for oil. Consequently, the author prepared many types of nanoporous films for the sensor via the chemical dealloying.

In the first step, chemical dealloying including low-temperature coarsening was employed. The sensor fabrication process was explained using a schematic sequence. Initial Cu–Cr alloy composition for the chemical dealloying was determined from the combinatorial analysis, based on focusing the level of Cu dealloying performance as well as pore size. Cu₇₂Cr₂₈ alloy promising the excellent Cu dealloying and final avg. 36 nm pores was selected as a candidate.

Unfortunately, the fabricated sensor was fragile, because the heat-treatment deformed the polyimide film and reduced adhesion between the top nanoporous film and the bottom polyimide film. The sensor was subsequently evaluated in air as a moisture sensor in order to assess a time-series response and hysteresis. The sensor followed the changes in RH, but the sensor had problems with a high hysteresis (35.8% FS).

Reflecting such problem, the author proposed chemical dealloying without thermal coarsening. Based on the prior combinatorial analysis aimed at materials discovery, $\text{Cu}_{82}\text{Cr}_{18}$ and $\text{Cu}_{80}\text{Cr}_{20}$ were selected in chemical dealloying experiments as candidates for incorporation in sensors for the first time. The $\text{Cu}_{82}\text{Cr}_{18}$ film was effectively Cu-dealloyed, altering its composition to $\text{Cu}_{25}\text{Cr}_{75}$ after 7 min of dealloying. The dealloyed $\text{Cu}_{82}\text{Cr}_{18}$ film exhibited a Cr-based nanoporous structure with 20–40 nm pores.

In contrast, the $\text{Cu}_{80}\text{Cr}_{20}$ film could not be fully Cu-dealloyed, which was consistent with the results of the combinatorial search. Sensors A and B were fabricated via chemical dealloying of $\text{Cu}_{82}\text{Cr}_{18}$ and $\text{Cu}_{80}\text{Cr}_{20}$, respectively, and evaluated with respect to the reference sensor in both air and oil. The measured hysteresis in air was 7.4% FS for sensor A, which was below the acceptable limit of 10.0% FS, whereas that for sensor B was 13.3% FS.

Moreover, the author revealed that the measured 90% response time in oil was 8 min for sensor A and 10 min for sensor B as compared to 12 min for the reference sensor; thus, the response time of sensor A was below the acceptable limit of 10 min. Although the fabricated sensor showed the poor heat resistance, the fabrication process was systematically optimized by the author's combinatorial approach, demonstrating the prepared nanoporous films can be utilized as molecular filters at the low temperature. The author also proved the combinatorial method has a lot of possibilities for the materials discovery as well as MEMS manufacturing.

Chapter 6 Conclusions and future works

6.1 Conclusions

In this contribution, the author proposed further systematic chemical dealloying for MEMS applications. Proposed chemical dealloying combined with the combinatorial thin film synthesis was helpful in accelerating the fabrication of nanoporous films. Moreover, the fabricated novel nanoporous films had excellent moisture permeability and could be used for sensor electrodes as well as molecular filters. Novelties of this work are as follows:

- (1) Chemical dealloying of Cu–Cr alloy
- (2) Combination of chemical dealloying and combinatorial method
- (3) Fabrication conditions and final obtained morphologies dependence
- (4) Nanoporous films for application in nanofilter used in MEMS sensor

The author summarized this study in accordance with the thesis structure.

Chapter 1 Introduction

The author introduced many types of nanoporous formation technology. To date, feasible methods have succeeded in fabricating the random or uniform network nanostructures. However, the majority of previous reports required special equipment, heat treatment, or additional processing. The author has been focused on fabricating moisture sensing device for oil, and chemical dealloying was the better suited process. While chemical dealloying is recognized as an easy process, and wide applicable materials and substrate types are very attractive, this process has also some disadvantages; it needs a lot of sacrificial materials, and finding possible process parameters is normally difficult. In this work, the author dealt with those negative aspects by employing the following ideas:

First, inexpensive Cu was selected as a sacrificial material, overcoming one negative points of chemical dealloying. Moreover, Cr is suitable nanoporous metal because of its excellent chemical resistance, inexpensive metal, and hydrophilicity. The author mentioned that the chemical dealloying of Cu–Cr alloy might be a promising approach for the proposed MEMS sensor.

Second, the author proposed chemical dealloying as optimized by combinatorial method. Combinatorial method provides a time effective pathway for materials discovery. Thus, this

technique must be helpful to determine process parameters for chemical dealloying.

Moreover, the author proposed nanoporous films for application in MEMS sensor. The author considered fabricated nanoporous films via chemical dealloying can be expected to be molecular filters. The experimental sequence of this challenging work was described, and final destination was also clarified.

Chapter 2 Chemical dealloying including high-temperature coarsening

The author fabricated Cr nanoporous films via chemical dealloying of Cu–Cr including thermal coarsening. At the beginning, the author revealed characteristics of NFTS system while comparing the conventional FTS system, and the distribution of traveling target particles was also explained using schematic diagram. Furthermore, the author mentioned about the first chemical dealloying procedure as well as its fabrication conditions. Measurement equipment used (EDX, stylus step profiler, FE-SEM) and their detection principle were also explained.

Unfortunately, first tried Cu dealloying was not possible, which resulted from the high initial Cr composition (32 at.% Cr) and the dense film structure (sputtering pressure: 0.5 Pa in argon). Owing to the above film properties, HNO₃ solution could not enter to the interior of the Cu–Cr film. The author demonstrated that the thermal coarsening at 700 °C for 1 h provided an efficient Cu dealloying. Cu was successfully removed from the Cu₆₈Cr₃₂ film via the dealloying treatment. Final obtained alloy composition was almost Cr (98 at.%). Moreover, the obtained Cr based-material showed 200–300 nm open pore structure, indicating the first test was successfully achieved.

The effective Cu etching performance and large pore growth could be explained by thermal grain growth. The obtained porous materials are expected in the use of catalysts, absorbent materials, or nanofilters. In this method, however, heat treatment at 700 °C atmosphere limited possible applications, and the author described the need of new chemical dealloying that can be accomplished through low-temperature coarsening.

Chapter 3 Chemical dealloying including low-temperature coarsening

The author proposed new chemical dealloying assisted by the low-temperature coarsening. In this section, the author was motivated to fabricate nanoporous films on polyimide films. On considering that the heat-resistant temperature of polyimide film was approximately 350 °C, the

coarsening temperature must be reduced from 700 °C to 300 °C. The results obtained from the previous work showed that Cu dealloying from Cu₆₈Cr₃₂ film was not possible by thermal coarsening at 300 °C for 1h, since this heat temperature was extremely small and unsatisfied for a grain growth.

The author considered that the optimization of initial Cu–Cr compositions may assist the Cu etching performance. It was easy to predict that low Cr concentration may enhance the Cu etching. Combinatorial method was employed for determination of an optimal initial Cu–Cr composition, which have demonstrated the adaptability of a newly developed chemical dealloying.

The author first revealed the one-dimensional compositional gradient technology in NFTS. The study showed that the compositional gradient (Δx at.%/mm) increased as the sputtering pressure was increased. The widest compositional gradient created by NFTS was approximately 10/76 at.%/mm at 2.5 Pa in argon. Based on the finding, thin-film library containing the initial composition of 32–22 at.% Cr (Avg. 450 nm thick) was prepared in NFTS on a single glass substrate with dimensions 26 mm × 76 mm.

The so fabricated thin-film library was thermal coarsened at 300 °C for 1 h under high-vacuum atmosphere, subsequently Cu was dealloyed by immersing the library in 32.5% HNO₃ for 15 h. After dealloying process, film properties (alloy composition, film thickness, nanostructure, pore seize, and porosity) were carefully studied. Final film properties were position-dependent, showing that the initial Cr composition in the range of 28–22 at.% successfully yielded favorable nanostructures (residual Cu composition: 9–3 at.% without film dissolution, pore size: avg. 36–70 nm, and porosity: 24–59%). Summary, combinatorial technology accelerated the process parameters optimization.

Next, the author's motivations were oriented to the further developed chemical dealloying that can be completed without thermal coarsening. The author believed that this newly proposed technique would open up future applications.

Chapter 4 Chemical dealloying without thermal coarsening

The author presented a new chemical dealloying, eliminating the need for thermal coarsening. The author's preliminary test suggested the possibility of Cu dealloying at room temperature by reducing the initial Cr composition to below 22 at.%.

Therefore, thin-film libraries (dimension: 26 mm × 76 mm) containing the initial 22–15 at.%

Cr (Avg. 380 nm thick) were prepared by NFTS, and initial Cu–Cr alloy compositions were successively searched. Through the combinatorial analysis, the author revealed that $\text{Cu}_{82}\text{Cr}_{18}$ resulted in sufficient Cu dealloying without film dissolution. Thus, $\text{Cu}_{82}\text{Cr}_{18}$ was selected as the optimal alloy and used to fabricate nanoporous films.

Moreover, the author also studied the influence of film density on Cu etching rate. At the beginning of this study, the author mentioned the relationship between as-deposited $\text{Cu}_{82}\text{Cr}_{18}$ film density and sputtering pressure. Sputtering pressures of 0.5 and 2.5 Pa in argon were tested. The structures obtained under different sputtering pressures showed that the resulting surface was coarser at the higher sputtering pressure. The Cu etching rate was 0.1 at.%/min under 0.5 Pa and 30 times higher (3.0 at.%/min) under 2.5 Pa, resulting in $\text{Cu}_{22}\text{Cr}_{78}$ for only 20 min. The author demonstrated that two controllable process parameters {initial Cu–Cr alloy composition and sputtering pressure (i.e., Cu–Cr film density)} were key to achieve effective Cu dealloying without the help of thermal coarsening.

Interestingly, an appearance of the Cu–Cr film changed from Cu brown to transparency after dealloying, which have resulted from the formation of Cr_2O_3 . FE-SEM observation showed that the dealloyed film had cracks throughout the film, and no clear nanopores were observed. The author concluded that the film cracking was attributed to internal stress in the as-deposited film. Moreover, invisible pores were explained by the theory; diffusion coefficient of Cr was relatively small and the Cu–Cr film was strongly restricted by the hard glass substrate, hindering the growth of the pore scales.

Based on the findings, the author attempted to fabricate a nanoporous Cu–Cr film on a softer polyimide film under the same dealloying conditions. While the dealloyed film on the glass substrate had no clear visible pores, the dealloyed film on the polyimide exhibited numerous pores with diameters of 20–40 nm. This result proved that the polyimide films emphasized the dealloyed Cu–Cr film porosity. Although some cracks (approximately 100 nm wide and several μm long) were created on the film surface, the fabricated nanoporous film is expected to be applied as a nanofilter.

Chapter 5 Nanoporous film for application in MEMS device

The fabricated nanoporous film in the best condition was used for electrode film in MEMS moisture sensor for oil. First of all, the author mentioned the motivations of this work, and then

gave explanation for the sensor structure and its mechanism. The author fabricated sensors having the dense upper electrode films, which predictably did not operate. This have resulted from the poor moisture permeability. The author confirmed that additional cracks slightly allowed the water infiltration, but the sensor did not totally function (linearity: 35.8% FS). For the better application, the sensors required nanostructured upper electrode film (ideal pore size: 10–50 nm), which were prepared via the chemical dealloying.

In the first challenge, chemical dealloying including low-temperature coarsening was employed. The sensor fabrication process was described using a schematic sequence. Moreover, initial Cu–Cr alloy composition for the chemical dealloying was identified in the author's combinatorial analysis; the author selected $\text{Cu}_{72}\text{Cr}_{28}$ because this composition yielded favorable nanoporous film properties (residual Cu composition: <10.0 at.%, final pore size: avg. 36 nm) .

Unfortunately, the author learned that thermal coarsening process shrank polyimide films, therefore Cu–Cr films fixed on polyimide films cracked throughout the film surface. Finally, the so unstable Cu–Cr films were easily delaminated from the sample during the dealloying step. Furthermore, the survived sensor showed the poor responsiveness, as well as non-linearity (35.8% FS). Based on the results, the author utilized the chemical dealloying with no requirement of thermal coarsening.

In order to assess the pore size and sensor performance dependence, the author selected $\text{Cu}_{82}\text{Cr}_{18}$ and $\text{Cu}_{80}\text{Cr}_{20}$ for sensor fabrication conditions, which were referred to as sensor A and B, respectively. While sensor A had favorable nanoporous electrode film with 20–40 nm pores, sensor B had unclear nanostructured electrode films (estimated pore size was less than 20 nm). The author clarified that the pore size highly depended on each sensor performance; hysteresis in air was 7.4 % FS for sensor A and 13.3% FS for sensor B, and 90% response time in oil was 8 min for sensor A and 10 min for sensor B as compared to 12 min for the commercial reference sensor.

Summary, the author successfully realized the superior moisture sensors for oil via novel chemical dealloying of Cu–Cr alloys with compositions that were optimized by a combinatorial method. To the best of our knowledge, this is the first such study. Moreover, this novel transparent nanoporous film is further expected to be useful as a nano-filter, catalyst, or absorbent material and in other MEMS.

6.2 Future works

The author has successfully designed the outstanding sensor via challenging chemical dealloying, and almost accomplished the research goals. This study, however, remained some problems, and the research is now ongoing. The remained research tasks are as follows:

(1) Improving heat resistance property of sensor

As mentioned in chapter 5, the fabricated sensors exhibited poor heat resistance, in which the sensor hysteresis became larger with increase of measuring temperature. This negative sensor property have resulted from the film cracking appeared on the upper nanoporous electrode film filter. The desired nanostructure for films is a 3D interconnected network of Cr particles and open pores, with no film cracks. In order to eliminate film cracks, the author proposes further controlling of initial alloy composition or film thickness. There are some research that setting the initial alloy composition could mitigate the as-deposited film stress, thereby may avoid cracking in dealloyed films.

The established combinatorial approach by the author will promise the development of nanoporous films. Moreover, the author is now interested in other binary alloys for chemical dealloying. In other words, there are still a lot of possibilities to improve the sensor property.

(2) Demonstration of filtration performance

In this contribution, the data did not quite show the water filtration procedure in oil. In this study, the filtration performance was evaluated based on the sensor performance in air and oil. However, the evaluation focusing nanofilters is more promising and desirable. For example, it may be ideal that water removal from oil would be determined based on water concentration in oil, where oil including water is flushed away through the prepared membrane.

For another method, dyed water by water-soluble colorant will be helpful to visually judge the separation of water from oil. Summary, filtration property with respect to nanoporous materials are more needed.

(3) Effect of oil type on sensor performance

In the sensor evaluation, a fresh lubrication oil was used. However, most of them, lubrication

oil used in mechanical system is generally contaminated by oxidation, gas, dust, metal piece, or chemical substance. Those adulterants may influence on the sensor responsiveness, therefore, the author additionally must evaluate sensors in such environment. Moreover, relationship between sensor performance and oil type must be important information.

Appendix

Chemical dealloying of Cu–Cr alloy, as well as that dealloying process as optimized combinatorial method are very attractive and profound. Therefore, there are still a lot of works. In this contribution, unexplained phenomena were also remained, which have to be cleared in the future. The author summarized unsolved tasks below:

(1) Novel combinatorial approach for chemical dealloying

Structure color produced from dealloyed film was alloy composition dependent, as seen from Fig. 1. Although the success rate was extremely low, Cu could be more dealloyed from the best $\text{Cu}_{25}\text{Cr}_{75}$ reported in chapter 5. Prolonging dealloying time may dissolve the Cu–Cr film, thus the processing has to be carefully treated. The author currently judges the Cu dealloying process by visual observation by oneself. However, this is not systematic and quantitative. For the better chemical dealloying, dealloying time and final alloy composition need to be well controlled.

The author proposes a novel chemical dealloying system (Fig. 2). Each color information can be replaced in an RGB value using imaging processing software, which can be also as a function of alloy composition. Final alloy composition linked to the software can be controllable, and the combination moving substrate with the above system promises newly developed chemical dealloying.

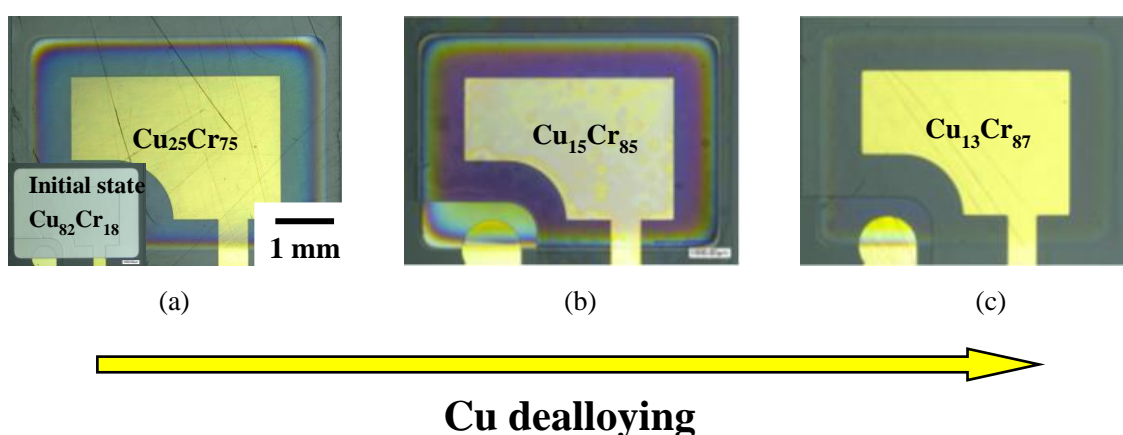


Fig. 1 Structure color of dealloyed film depending the level of Cu dealloying; (a) at $\text{Cu}_{25}\text{Cr}_{75}$, (b) $\text{Cu}_{15}\text{Cr}_{85}$, and (c) $\text{Cu}_{13}\text{Cr}_{87}$.

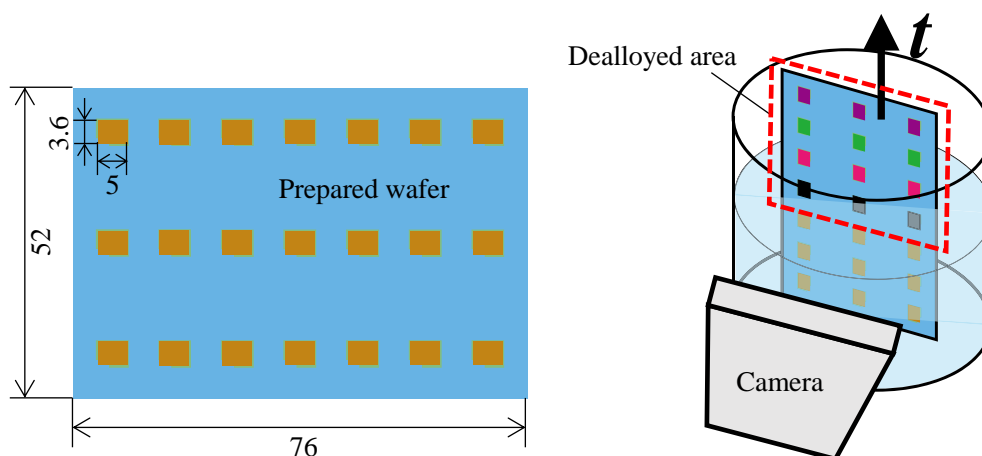


Fig. 2 Newly proposed novel chemical dealloying system.

(2) Investigation of nanoporous structures produced via Cr deposition

This study remained a curious phenomenon upon the chemical dealloying. Fig. 3 shows the chemical dealloying sequence, and Table 1 summarizes sputtering conditions. A dense $\text{Cu}_{82}\text{Cr}_{18}$ film (400 nm thick) was deposited on a polyimide film (4.0 μm thick). The dealloyed dense $\text{Cu}_{82}\text{Cr}_{18}$ film expanded after Cu dealloying, and the film thickness changed from initial 400 nm to 760 nm. FE-SEM top-view showed approximately 100–300 nm open pores (Fig. 4(a)). Moreover, FE-SEM side-view revealed that the dealloyed film was comprise of two layer; while the bottom layer was dense structure, the top layer exhibited porous structure (Fig. 4(b)).

Fig. 5 shows the XRD patterns of the Cu–Cr film before and after the Cu dealloying. After the dealloying of Cu, peaks corresponding to Cr were newly observed, suggesting that Cr was deposited on the initial Cu–Cr film. Many parts of this study remained unexplained, and the author is researching now. This interesting phenomenon may not be “chemical dealloying”?

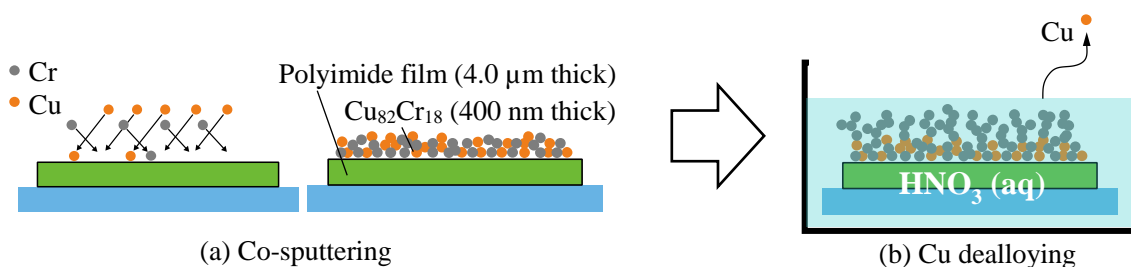


Fig. 3 Fabrication process; (a) co-sputtering, (b) Cu dealloying with 22.5% HNO_3 for 15 h.

Table 1 Sputtering conditions in NFTS

Initial alloy composition (at.%)	Cu ₈₂ Cr ₁₈
Sputtering pressure (Pa)	0.5
Sputtering power (W)	Cu target: 223
	Cr target: 113
Sputtering time (min)	15
TS distance (mm)	82
Deposition area	3.6 × 5.0

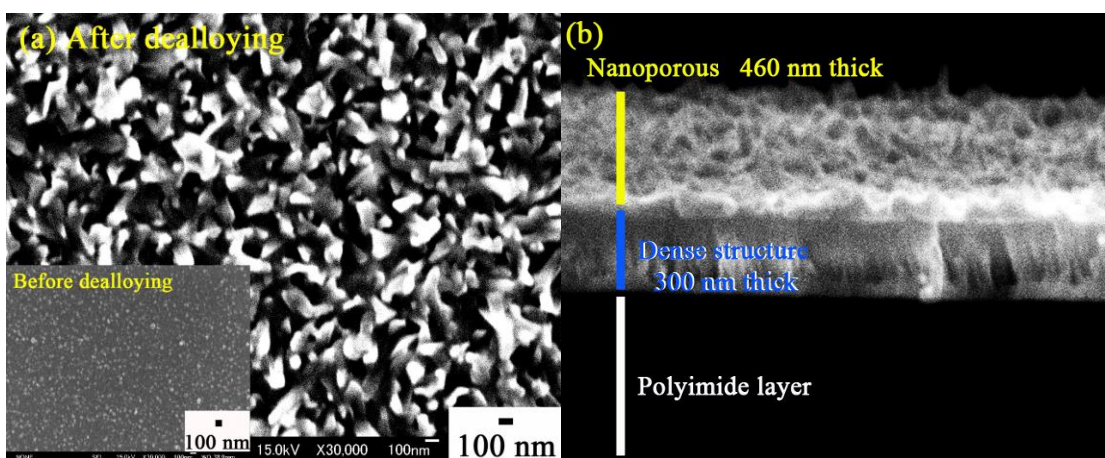


Fig. 4 FE-SEM images; (a) top-view and (b) side-view of dealloyed Cu–Cr film.

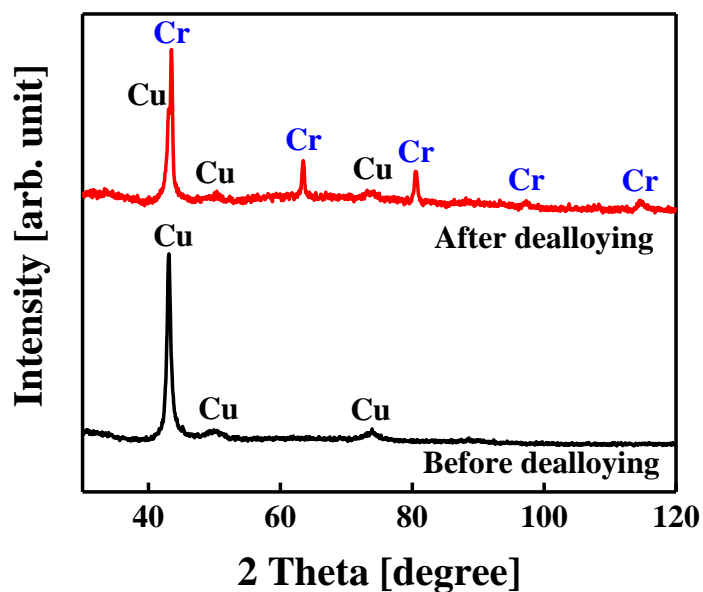


Fig. 5 XRD analysis before and after Cu dealloying.

Reference

- 1) 伊藤章：膜分離工学 ～分離膜の種類～ (1993) [Online].
Available: http://chemeng.in.coocan.jp/memb/m_mb1.htm
- 2) 袴田昌高, 千野靖正, 馬淵守, “合金化/脱合金化法による白金板表面へのナノポーラス構造形成”, *日本金属学会誌*, 第75巻, 第1号, (2011), 42-46
- 3) A. Abburi and W. J. Yeh, “Temperature and Pore Size Dependence on the Sensitivity of a Hydrogen Sensor Based on Nanoporous Platinum Thin Films”, *IEEE Sensors Journal*, **12**, (2012), 2625-2629
- 4) W. C. Li and T. J. Balk, “Preparation and Hydrogen Absorption/Desorption of Nanoporous Palladium Thin Films”, *J. Materials*, **2**, (2009), 2496-2509
- 5) S. T. Mostafavi, M. R. Mehrnia, and A. M. Rashidi, “Preparation of nanofilter from carbon nanotubes for application in virus removal from water”, *Desalination*, **238**, (2009), 271-280
- 6) F. Bunge, C. Habben, S. Driesche, and M. J. Vellekoop, “INTEGRATION AND CHARACTERIZATION OF NANOPOROUS ALUMINUM OXIDE MEMBRANES IN MICROFLUIDIC CHIPS”, in *Proc. IEEE 31th Annual Int. Conf. on Micro Electro Mechanical Systems (MEMS2018)*, (2018), 1237-1240
- 7) T. Ota, M. Nakayama, Y. Kanno, T. Suzuki, and N. Miki, “IN VITRO AND IN VIVO TESTS OF NANOPOROUS MEMBRANE COATED WITH BIOCOMPATIBLE FLUORINE-DOPED DIAMONDE-LIKE CARBON FOR HEMOFILTRATION TREATMENT”, in *Proc. IEEE 31th Annual Int. Conf. on Micro Electro Mechanical Systems (MEMS2018)*, (2018), 412-414
- 8) Y. Tanaka and Y. Yalikun, “A FOOT-TREADING TYPE ELECTRIC POWER GENERATOR USING MICRO/NANO CHANNELS IN A POROUS GLASS FILTER”, in *Proc. IEEE 31th Annual Int. Conf. on Micro Electro Mechanical Systems (MEMS2018)*, (2018), 677-680
- 9) 柳澤 和道, “水熱法によるセラミックス粉末の合成”, *ニチアス技術時報*, **2**, (2008), 1-7
- 10) A. Syed and E. Mastropaolo, “Hydrothermal growth of vertically-aligned zinc oxide nanowires on patterned seed layers”, in *Proc. Micro and Nano Engineering 2014*, (2014)
- 11) J. Wang, C. Chen, Z. Ren, and Z. Wang, “Seed-assisted hydrothermal synthesis of aligned single-crystalline anatase nanorods on FTO: synthesis and application”, *Semicond. Sci. Technol.*, **29**, (2014), 1-9
- 12) X. Peng, K. Koczur, S. Nigro, and A. Chen, “Fabrication and electrochemical properties of novel nanoporous platinum network electrodes”, *Chem. Commun.*, to be published. DOI:

- 10.1039/b412677g, (2004), 2872-2873
- 13) 遠藤治之, 泉田福典, 長谷川辰雄, 大嶋江利子, 米倉勇雄, 原田善之, 前田克巳, 新倉郁生, 柏葉安兵衛, “ZnO 単結晶基板の応用に関する研究”, *岩手県工業技術センター研究報告*, **12**, (2005)
 - 14) 小野幸子, 阿相英孝, “陽極酸化被膜 ～現場のための材料解析入門～”, 日本電子株式会社
 - 15) H. Kawashima, K. Fukiba, T. Ono, and S. Tokawa, “Effects of Aluminum Anodizing on Pre-Cooling Time”, in *Proc. of Space Transportation Symposium FY2017*, (2018), 1-6 (in Japanese)
 - 16) G. E. J. Poinern, N. Ali, and D. Fawcett, “Progress in Nano-Engineered Anodic Aluminum Oxide Membrane Development”, *J. Materials*, **4**, (2011), 487-526
 - 17) H. Masuda, K. Yada, and K. Osaka, “Self-ordering of cell configuration of anodic porous alumina with large-size pores in phosphoric acid solution”, *Jpn. J. Appl. Phys.*, **37**, (1998), 1340-1342
 - 18) S. A. Srivastava, S. Talapatra, R. Vajtai, and P. M. Ajayan, “Carbon nanotube filters”, *Nature Mat.*, **3**, (2004), 610-614
 - 19) C. Mihaela and M. C. Morris, “Carbon nanotube biosensors”, *Frontiers in Chemistry*, **3**, (2015), 1-21
 - 20) I. V. Zaporotskova, N. P. Boroznina, Y. N. Parkhomenko, and L. V. Kozhitov, “Carbon nanotubes: Sensor properties. A review”, *Modern Electronic Materials*, **2**, (2016), 95-105
 - 21) X. Zhang, H. Cui, Y. Gui, and J. Tang, “Mechanism and Application of Carbon Nanotube Sensors in SF₆ Decomposed Production Detection: a Review”, *Nanoscale Res. Lett.*, **12**, (2017), 1-12
 - 22) J. Erlebacher and K. Sieradzki, “Pattern Formation During Dealloying,” *Scripta Mat.*, **49**, (2003), 991–996
 - 23) A. Dursun, D. V. Pugh, and S. G. Corcoran, “Dealloying of Ag–Au Alloys in Halide-Containing Electrolytes”, *Journal of The Electrochemical Society*, **150**, (2003), 355-360
 - 24) X. Lu, L. Au, J. McLellan, Z. Li, M. Marquez, and Y. Xia, “Fabrication of Cubic Nanocages and Nanoframes by Dealloying Au/Ag Alloy Nanoboxes with an Aqueous Etchant Based on Fe(NO₃)₃ or NH₄OH”, *NANO Lett.*, **7**, (2007), 1764-1769
 - 25) J. Erlebacher, “An Atomistic Description of Dealloying”, *Journal of The Electrochemical Society*, **151**, (2004), 614-626

- 26) J. K. Chang, S. H. Hsu, I. Wen, and W. T. Tsai, "Formation of Nanoporous Nickel by Selective Anodic Etching of the Nobler Copper Component from Electrodeposited Nickel–Copper Alloys", *J. Phys. Chem.*, **112**, (2008), 1371-1376
- 27) J. Jayarai, B. J. Park, D. H. Kim, W. T. Kim and E. Fleury, "Nanometer-sized porous Ti-based metallic glass", *Scripta Materialia*, **55**, (2006), 1063-1066
- 28) T. Fujita and L. Chen, "Development of Nanoporous Metal for Catalysis Using Dealloying Process", *Annual Report*, **24**, (2010), 242-243 (in Japanese)
- 29) C. Hou, X. Y. Lang, G. F. Han, Y. Q. Li, L. Zhao, Z. Wen, Y. F. Zhu, M. Zhao, J. C. Li, J. S. Lian, and Q. Jiang, "Integrated Solid/Nanoporous Copper/Oxide Hybrid Bulk Electrodes for High-performance Lithium-Ion Batteries", *Scientific Reports*, to be published. DOI: 10.1038/srep02878, (2013), 1-7
- 30) 日本潤滑学会編：潤滑ハンドブック (1980, 養賢堂)
- 31) P. C. Stair, C. Marshall, G. Xiong, H. Feng, M. J. Pellin, J. W. Elam, L. Curtiss, L. Iton, H. Kung, M. Kung, and H. -H. Wang, "Novel, uniform nanostructured catalytic membranes", *Topics in Catalysis*, **39**, (2006), 181-186
- 32) W. Chen, X. Gui, B. Liang, R. Yang, Y. Zheng, C. Zhao, X. Li, H. Zhu, and Z. Tang, "Structural Engineering for High Sensitivity, Ultrathin Pressure Sensors Based on Wrinkled Graphene and Anodic Aluminum Oxide Membrane", *ACS Appl. Mater. Interfaces*, **9**, (2017), 24111-24117
- 33) M. Aramesh, O. Shimoni, K. Fox, T. J. Karle, A. Lohrmann, K. Ostrikov, S. Prawer, and J. Cervenka, "Ultra-high-density 3D DNA arrays within nanoporous biocompatible membranes for single-molecule-level detection and purification of circulating nucleic acids", *Nanoscale*, **7**, (2015), 5998-6006
- 34) G. Jeon, S. Y. Yang, and J. K. Kim, "Functional nanoporous membranes for drug delivery", *J. Mater. Chem.*, **22**, (2012), 14814-14834
- 35) W. Liu, S. Zhang, N. Li, J. Zheng, S. An, and Y. Xing, "Dealloying of Dual-Phase Al 15 at.% Cu Alloy in an Acidic Solution", *International Journal of ELECTROCHEMICAL SCIENCE*, **7**, (2012), 2240-2241
- 36) X. Lu, T. J. Balk, R. Spolenak and E. Arzt, "Dealloying of Au–Ag thin films with a composition gradient: Influence on morphology of nanoporous Au", *Thin Solid Films*, **515**, (2007), 7122-7126
- 37) Z. Qi, C. Zhao, X. Wang, J. Lin, W. Shao, Z. Zhang and X. Bian, "Formation and Characterization of Monolithic Nanoporous Copper by Chemical Dealloying of Al–Cu Alloys", *J. Phys. Chem. C*, **113**, (2009), 6695

- 38) L. Sun, C. L. Chien and P. C. Searson, "Fabrication of Nanoporous Nickel by Electrochemical Dealloying", *Chem. Mater.*, **16**, (2004), 3125-3129
- 39) M. C. Dixon, T. A. Daniel, M. Hieda, D. M. Smilgies, M. H. W. Chan and D. L. Allara, "Preparation, Structure, and Optical Properties of Nanoporous Gold Thin Films", *Langmuir*, **23**, (2007), 2414-2422
- 40) W. C. Li and T. J. Balk, "Achieving finer pores and ligaments in nanoporous palladium–nickel thin films", *Scripta Materialia*, **62**, (2010), 167-169
- 41) R. Morrish, K. Dorame and A. J. Muscat, "Formation of nanoporous Au by dealloying AuCu thin films in HNO₃", *Scripta Materialia*, **64**, (2011), 856-859
- 42) T. Fujita, Y. Kanoko, Y. Ito, L. Chen, A. Hirata, H. Kashani, O. Iwatsu, and M. Chen, "Nanoporous Metal Papers for Scalable Hierarchical Electrode", *Adv. Sci.* to be published. DOI: 10.1002/advs.201500086, **2**, (2015)
- 43) J. N. Cawse, "Experimental Design for Combinatorial and High Throughput materials Development", *GE Global Research ~Technical Report~*, **2002GRC253**, (2002), 4
- 44) I. Takeuchi, J. Lauterbach and M. J. Fasolka, "Combinatorial materials synthesis", *materialstoday*, **8**, (2005), 18-26
- 45) M. Y. M. Chiang, R. Song, A. J. Crosby, A. Karim, C. K. Chiang, E. J. Amis, "Combinatorial approach to the edge delamination test for thin film reliability—adaptability and variability", *Thin Solid Films*, **476**, (2005), 379-385
- 46) Ji-Cheng Zhao, "Combinatorial approaches as effective tools in the study of phase diagrams and composition–structure–property relationships", *Progress in Materials Science*, **51**, (2006), 557-631
- 47) S. S. Mao and P. E. Burrows, "Combinatorial screening of thin film materials: An overview", *Journal of materiomics*, **1**, (2015), 85-91
- 48) S. S. Mao, "High throughput growth and characterization of thin film materials", *Journal of Crystal Growth*, **379**, (2013), 123-130
- 49) T. Gebhardt, D. Music, T. Takahashi and J. M. Schneider, "Combinatorial thin film materials science: From alloy discovery and optimization to alloy design", *Thin Solid Films*, **520**, (2012), 5491-5499
- 50) P. J. McGinn, "Combinatorial electrochemistry-Processing and characterization for materials discovery", *Materials Discovery*, **1**, (2015), 38-53
- 51) T. H. Muster, A. Trinchi, T. A. Markley, D. Lau, P. Martin, A. Bradbury, A. Bendavid and S. Dligatch, "A review of high throughput and combinatorial electrochemistry", *Electrochimica Acta*, **56**, (2011), 9679-9699

- 52) E. W. McFarland and W. H. Weinberg, “Combinatorial approaches to materials discovery”, *Trends in Biotechnology*, **17**, (1999), 107-115
- 53) R. Takahashi, H. Kubota, M. Murakami, Y. Yamamoto, Y. Matsumoto and H. Koinuma, “Design of Combinatorial Shadow Masks for Complete Ternary-Phase Diagramming of Solid State Materials”, *J. Comb. Chem.*, **6**, (2004), 50-53
- 54) H. Chang, I. Takeuchi and X. D. Xiang, “A low-loss composition region identified from a thin-film composition spread of $(\text{Ba}_{1-x-y}\text{Sr}_x\text{Ca}_y)\text{TiO}_3$ ”, *J. Appl. Phys. Letter*, **74**, (1999), 1165-1167
- 55) D. Pei, “On-Bead Library Screening Made Easier”, *Chemistry & Biology*, **17**, (2010), 3-4
- 56) S. Borman, “Combinatorial chemistry”, *Chemical and Engineering News*, **24**, (1997), 43-62
- 57) B. Jandeleit, D. J. Schaefer, T. S. Powers, H. W. Turner, and W. H. Weinberg, “Combinatorial Materials Science and Catalysis”, *Angew. Chem. In. Ed.*, **38**, (1999), 2492-2532
- 58) X. D. Xiang, X. Sun, G. Briceno, Y. Lou, K. Wang, H. Chang, W. G. W. Freedman, S. W. Chen, P. G. Schultz, “A Combinatorial Approach to Materials Discovery”, *Science*, **268**, (1995), 1738-1740
- 59) P. J. McGinn, “Combinatorial electrochemistry —Processing and characterization for materials discovery”, *Materials Discovery*, **1**, (2015), 38-53
- 60) M. Y. M. Chiang, R. Song, A. J. Crosby, A. Karim, C. K. Chiang, and E. J. Amis, “Combinatorial approach to the edge delamination test for thin film reliability—adaptability and variability”, *Thin Solid Films*, **476**, (2005), 379-385
- 61) J. Drelich, E. Chibowski, D. D. Meng, and K. Terpilowski, “Hydrophilic and Superhydrophilic Surfaces and Materials”, *Soft Matter.*, **7**, (2011), 10
- 62) 一般社団法人 日本印刷産業連合会 [Online]
Available: <https://www.jfpi.or.jp/webyogo/index.php?term=1177>
- 63) 伊藤 昭夫：薄膜材料入門 (1998, 裳華房)
- 64) 金原 粲：薄膜の基本技術 (2008, 東京大学出版会)
- 65) C. Lehmann and P. Sigmund, “On the Mechanism of Sputtering”, *Phys. stat. sol.*, **16**, (1966), 507-511
- 66) E. Alfonso, J. Olaya, and G. Cubillos, “Thin Film Growth Through Sputtering Technique and Its Applications”, *Crystallization*, **15**, (2012), 397-432
- 67) J. E. Greene, “Tracing the recorded history of thin-film sputter deposition: From the 1800s to 2017”, *J. of Vacuum Science and Technology A*, **35**, (2017), 1-60
- 68) 井上泰志, 高井治, ”プラズマ CVD における薄膜堆積過程”, *プラズマ・核融合学*

- 会誌, 第76巻, 第10号, (2000), 1068-1073
- 69) 白藤 立, "プラズマ CVD の化学反応工学", *高温学会誌*, 第37巻, 第6号, (2011), 281-288
- 70) C. Woodford : Electroplating (2018) [Online].
Available: <https://www.explainthatstuff.com/electroplating.html>
- 71) Z. Li, H. Bian, C. M. Lee, X. Chen, and Y. Y. Li, "Nickel nanotube array via electroplating and dealloying", *Thin Solid Films*, **658**, (2018), 1-6
- 72) 幸塚 広光, "ゾル-ゲルコーティング技術の基礎", *NEW GLASS*, **25**, (2010), 40-45
- 73) J. Siegel, O. Lyutakov, V. Rybka, Z. Kolska, and V. Svorcik, "Properties of gold nanostructures sputtered on glass", *Nanoscale Research Letters*, **6**, (2011), 1-9
- 74) J-M. Ting, and P. Chen, "Dependence of compositions and crystallization behaviors of dc-sputtered TiNi thin films on the deposition conditions", *J. Vac. Sci. Techno. A*, **19**, (2001), 2382-2387
- 75) S. Swann, "MAGNETRON SPUTTERING", *Phys. Technol.*, **19**, (1998), 67-75
- 76) P. J. Kelly, R. D. Arnell, "Magnetron sputtering: a review of recent developments and applications", *Vacuum*, **56**, (2000)159-172
- 77) J. Musil, P. Baroch, J. Vicek, K. H. Nam, and J. G. Han, "Reactive magnetron sputtering of thin films: Present status and trends", *Thin Solid Films*, **1-2**, (2005), 208-218
- 78) M. N. Alam, M. Vasilie, V. Kotovb, and K. Alameh, "Recent developments in magneto-optic garnet-type thin-film materials synthesis", *Procedia Eng.*, **76**, (2014), 61-73
- 79) D. G. Constantin, M. Apreutese, R. Arvinte, A. Marin, O. C. Andrei, and D. Munteanu, "MAGNETRON SPUTTERING TECHNIQUE USED FOR COATINGS DEPOISTION; TECHNOLOGIES AND APPLICATIONS", in *Proc. 7th International Conference on Materials Science and Engineering (BRAMAT2011)*, 12, (2011), 29-33
- 80) D. K. Maurya, A. Sardarinejad and K. Alameh, "Recent Developments in R.F. Magnetron Sputtered Thin Films for pH Sensing Applications—An Overview", *Coating*, **4**, (2014), 756-771
- 81) A. Katagiri, S. Ogawa, T. Shimizu, M. Matsushima, K. Akiyama, and H. Funakubo, "High Temperature Reproducible Oreparation of Mg₂Si Films on (001)Al₂O₃ substrates Using RF Magnetron Sputtering Method", *Mater. Res. Soc. Symp. Proc.*, **1642**, (2014), 1-6
- 82) J. L. Vossen, "Control of Film Properties by rf-Sputtering Techniques", *Journal of Vacuum Science and Technology*, **8**, (1971), 12-30
- 83) M. Hughes : What is Sputtering? Magnetron Sputtering? (2014) [Online].
Available: <http://www.semicore.com/what-is-sputtering>

- 84) C. Lin, D. C. Sun, S. L. Ming, E. Y. Jiang, and Y. G. Liu, "Magnetron facing target sputtering system for fabricating single-crystal films", *Thin Solid Films*, **279**, (1996), 49-52
- 85) X. S. Li, T. Tanaka, and Y. Suzuki, "Lead Zirconate Titanate (PZT) Thin Film Deposition in Facing Target Sputtering", *J. Vac. Soc. Jpn.*, **42**, (1999), 257-260
- 86) H. Ma, J. S. Cho, and C. H. Park, "A study of indium tin oxide thin film deposited at low temperature using facing target sputtering system", *Surface and Coating Technology*, **153**, (2002), 131-137
- 87) Y. Hoshi, H. Kato, and K. Funatsu, "Structure and electrical properties of ITO thin films deposited at high rate by facing target sputtering", *Thin Solid Films*, **445**, (2003), 245-250
- 88) J. A. Jeong, H. S. Shin, K. H. Choi, and H. K. Kim, "Flexible Al-doped ZnO films grown on PET substrates using linear facing target sputtering for flexible OLEDs", *J. Phys. D: Appl. Phys.*, **43**, (2010), 1-6
- 89) Z. Zhang, M. F. Hossain, T. Arakawa, and T. Takahashi, "Facing-target sputtering deposition of ZnO films with Pt ultra-thin layers for gas-phase photocatalytic application", *Journal of Hazardous Materials*, **176**, (2010), 973-878
- 90) A. Iljinas, J. Dudoni, R. Brucas, and A. Meskauskas, "Thin Ferromagnetic Films Deposition by Facing Target Sputtering Method", *Nonlinear Analysis: Modelling and Control*, **10**, (2005), 57-64
- 91) O. Kamiya, Y. Onai, H. Kato, and Y. Hoshi, "ITO films deposited by facing target sputtering", *J. Mater. Sci.: Mater Electron*, **18**, (2007), 359-362
- 92) K. Wasa, M. Kitabatake, H. Adachi : Thin film materials technology: sputtering of control compound materials, (2004, William Andrew Inc.)
- 93) S. Kadokura, M. Naoe, and Y. Maeda, "Advanced sputtering techniques for high rate-, plasma free-deposition and excellent target utility with uniform erosion", *Vacuum*, **51**, (1998), 683-686
- 94) R. Behrisch and W. Eckstein : Sputtering by Particle Bombardment: Experiments and Computer Calculations from Threshold to MeV Energies, (2007, Springer-Verlag Berlin Heidelberg)
- 95) E. Suzuki and Y. Hoshi, "Computer Simulation of Sputter-Deposition Processes", *Journal of The Magnetics Society of Japan*, **21**, (1997), 43-46
- 96) V. Orlinov, G. Mladenov, and I. Petrov, "Angular distribution and sputtering yield of Al and Al₂O₃ during 40 keV argon ion bombardment", *Vacuum*, **32**, (1982), 747-752
- 97) D. R. M. Kaminsky : ATOMIC AND IONIC IMPACT PHENOMENA ON METAL SURFACES, (1965, ACADEMIC PRESS Inc.)

- 98) 加藤雅敏, 榊 孝, ”金属クロムの硝酸中における腐食”, *日本金属学会誌*, **第 56 卷**, 第 9 号, (1992), 1050-1055
- 99) 村石治人, 原田 稔, 北原重登, ”硝酸と銅との反応についての再検討”, *化学と教育*, **第 35 卷**, 第 5 号, (1987), 68-71
- 100) 山野昭人, ”X 線回折装置の原理と応用”, 一般社団法人 日本分析機器工業会
- 101) 加藤範夫: 回折と散乱 (1978, 朝倉書店)
- 102) 大橋裕二: X 線結晶構造解析 (2005, 裳華房)
- 103) 高橋昇, 浅田千秋, 湯川夏夫: 金属材料学 (1996, 森北出版)
- 104) 小橋眞, 高田尚記: 構造材料学: 第 7 回 再結晶と粒成長の速度論 (2018, 名古屋大学講義資料)
Available: <http://www.numse.nagoya-u.ac.jp/P6/kobashi/policy.html>
- 105) S. K. Nakatani, T. Fujita, K. Uchisawa, D. Umetsu, Y. Kase, Y. Kowata, K. Chiba, T. Tokunaga, S. Arai, Y. Yamamoto, N. Tanaka, and M. Chen, “Environment-Sensitive Thermal Coarsening of Nanoporous Gold”, *Materials Trans.*, (2014), 1-5
- 106) M. Hakamada and M. Mabuchi, “Thermal coarsening of nanoporous gold: Melting or recrystallization”, *J. Mater. Res.*, **24**, (2009), 301-304
- 107) J. Wang, R. Xia, J. Zhu, Y. Ding, X. Zhang, and Y. Chen, “Effect of thermal coarsening on the thermal conductivity of nanoporous gold”, *J. Mater. Sci.*, **47**, (2012), 5013-5018
- 108) 長崎誠三, 平林眞: 二元合金状態図集 (2008, アグネ技術センター)
- 109) TORAY Industries Inc., “Positive Tone Photosensitive Polyimide “Photoneece” PW-1500 series”, Japan [Online].
Available: https://www.toray.jp/electronic/semicon/fot/pdf/phn_a003.pdf
- 110) 森 直哉: 新対向ターゲット式スパッタ法を用いたコンビナトリアル探索 (平成 23 年度 東京工業大学修士論文)
- 111) 菊池直人, 草野英二, ”スパッタリング成膜における薄膜構造制御”, *J. Vac. Soc. Jpn.* (Japanese), **第 50 卷**, 第 1 号, (2007), 15-21
- 112) 中野 武雄, ”中高圧下のスパッタリングにおける粒子輸送過程”, *J. Vac. Soc. Jpn.* (Japanese), **第 45 卷**, 第 9 号, (2002), 699-705
- 113) D. Brune, R. Hellborg, H. J. Whitlow, and O. Hunderi: Surface Characterization, (1997, WILEY-VCH)
- 114) Y. Taga, “Modification of Thin Film Properties by Sputtered Particles”, *R&D Review of Toyota CRDL*, **28**, (1993), 3

- 115)大川恭志, 早川幸男, 北村正治, ”グリッド損耗評価試験技術の現状” *イオン加速グリッド耐久認定用数値解析 JIEDI (JAXA Ion Engine Development Initiatives) ツールの研究開発ワークショップ 2006 年度報告書*, JAXA-SP-06-019, 13-19
- 116)J. Williams, M. Johnson, and D. Williams, “Differential Sputtering Behavior of Pyrolytic Graphite and Carbon-Carbon Composite Under Xenon Bombardment”, in *Proc. 40th AIAA Joint Propulsion Conference*, (2004), AIAA-2004-3788
- 117)K. A. Zoeb, J. Williams, D. D. Williams, and A. P. Yalin, “Differential Sputtering Yields of Refractory Metals by Xenon, Krypton, and Argon Ion Bombardment at Normal and Oblique Incidences”, in *Proc. 29th International Electric Propulsion Conference*, (2005), 1-25
- 118)A. P. Yalin, J. Williams, V. Surla, J. Wolf, and, K. A. Zoeb, “Azimuthal Differential Sputter Yields of Molybdenum by Low Energy Xe⁺ Bombardment”, in *Proc. 42nd AIAA/ASME/SAE/ASEE Joint Propulsion Conference & Exhibit*, (2006), 1-19
- 119)T. Motohiro and Y. Taga, “Monte Carlo Simulation of The Particle Transport Process in Sputter Deposition”, *Thin Solid Films*, **112**, (1984), 161-173
- 120)A. M. Myers, J. R. Doyle, and J. R. Abelson, “Monte Carlo simulations of magnetron sputtering particle transport”, *J. Vac. Sci.*, **9**, (1991), 614-618
- 121)S. Mahieu, G. Buyle, D. Depla, S. Heirwegh, P. Ghekiere, and R. D. Gryse, “Monte Carlo simulation of the transport of atoms in DC magnetron sputtering”, *Nucl. Instr. and Meth. in Phys. Res.*, **243**, (2006), 313-319
- 122)岡田美広, 伴厚志, 渡辺典子, 四宮時彦, 岡本昌也, ”プラスチックカラーTFT 液晶の開発”, *シャープ技報*, 第 85 号, (2003), 30-33
- 123)Y. Han, B. Matthews, D. Roberts, K. R. Talley, S. R. Bauers, C. Perkins, Q. Zhang, and A. Zakutayev, “Combinatorial Nitrogen Gradients in Sputtered Thin Films”, *ACS Comb. Sci.*, **20**, (2018), 436-442
- 124)I. Takeuchi, R. B. van Dover, and H. Koinuma, “Combinatorial Synthesis and Evaluation of Functional Inorganic Materials Using Thin-Film Techniques”, *MRS Bulletin*, (2002), 301-308
- 125)P. D. Rack, J. D. Fowlkes, and Y. Deng, “Combinatorial RF Magnetron Sputtering for Rapid Materials Discovery: Methodology and Applications”, *Microsc. Microanal.*, **10**, (2004), 58-59
- 126)Y. Liu, J. Padmanabhan, B. Cheung, J. Liu, Z. Chen, B. E. Scanley, D. Wesolowski, M. Pressley, C. C. Broadbridge, S. Altman, U. D. Schwarz, T. R. Kyriakides, and J. Schroers, “Combinatorial development of antibacterial Zr-Cu-Al-Ag thin film metallic glasses”, *Sci. Rep.*, **6**, (2016), 1-8

- 127)K. Jin, R. Suchoski, S. Fackler, Y. Zhang, X. Pan, R. L. Greene, and I. Takeuchi, “Combinatorial search of superconductivity in Fe-B composition spreads”, *APL Mater.*, **1**, (2013), 1-6
- 128)S. V. Roth, H. Walter, M. Burghammer, C. Riekkel, B. Lengeler, C. Schroer, M. Kuhlmann, T. Walther, A. Sehrbrock, R. Bomnick, and P. M. Buschbaum, “Combinatorial investigation of the isolated nanoparticle to coalescent layer transition in a gradient sputtered gold nanoparticle layer on top of polystyrene”, *Appl. Phys. Lett.*, **88**, (2006), 1-3
- 129)H. Xiang, B. Zhao, Y. Wang, X. Zhang, Y. Ren, N. Yan, T. Gao, J. Li, L. Zhang, and H. Wang, “Rapid Construction of Fe-Co-Ni Composition-Phase Map by Combinatorial Materials Chip Approach”, *ACS Comb. Sci.*, **20**, (2018), 127-131
- 130)G. Gamez, G. Mohanty, and J. Michler, “Ultrafast elemental mapping of materials combinatorial libraries and high-throughput screening samples via pulsed glow discharge optical emission spectroscopy”, *J. Anal. At. Spectrom.*, **28**, (2013), 1016-1023
- 131)深川雄貴：水分センサ用ポーラス薄膜成膜条件のコンビナトリアル探索 (平成 27 年度 名古屋大学修士論文)
- 132)井上泰宣, 鎌田喜一郎, 濱崎勝義：薄膜物性入門 (内田老鶴團)
- 133)草野英二：はじめての薄膜作製技術 (2012, 森北出版)
- 134)C. Colinge, J. Bagdahn, H. Baumgart, K. D. Hobart, H. Moriceau, and T. Suga “Semiconductor wafer Bonding 11: Science, Technology, and Applications – In Honor of Ulrich Goesele”, *ECS transactions*, 33, (2010), 64,65
- 135)H. Matsuyama, Japan patent No. JP2009060777 (4 March 2010)
- 136)R. E. Cantley, “The effect of water in Lubricating Oil on Bearing Fatigue Life”, *ASLE Trans.*, **20**, (2008), 244-248
- 137)N. Dittes, : Mixing grease with water, (2015, Lulea tekniska universitet)
Available: <http://www.diva-portal.org/smash/get/diva2:1004920/FULLTEXT01.pdf>
- 138)A. Jamaluddin, D. H. S. Law, S. D. Taylor, and S. U. Andersen : HEAVY OIL EXPLOITATION, (2018, PennWell Corporation)
- 139)堂園吉彦, ”「全酸化」(TAN: Total Acid Number)”, *日本造船学会誌*, 第 710 巻, (1988), 525
- 140)C. Parisotto, M. F. Ferrao, A. L. H. Mueller, E. I. Mueller, M. F. P. Santos, R. C. L. Guimaraes, J. C. M. Dias, and E. M. M. Flores, “Total Acid Number Determination in Residues of Crude Oil Distillation Using ATR-FTIR and Variable Selection by Chemometric Methods”, *Energy Fuels*, **24**, (2010), 5474-5478
- 141)一般社団法人 潤滑油協会：作動油の水分と劣化の関係について [Online]

- Available: <http://www.jalos.jp/jalos/qa/articles/005-325.htm>
- 142) J. Sander : Water Contamination: Management of Water During the Lubricant Life Cycle, (2009, Lubrication Engineers Inc.)
- 143) H. Bloch : PRACTICAL LUBRICATION FOR INDUSTRIAL FACILITIES, (2009, The Fairmont Press)
- 144) M. Day and C. Bauer : Water Contamination in Hydraulic and Lube Systems, (2007, Practicing Oil Analysis)
- 145) 福永香, 倉橋真司, "プリント配線板用絶縁材料の高周波誘電特性にあたる水分の影響", *エレクトロニクス実装学会講演大会論文集*, **21**, (2007), 85-86
- 146) 吉井雄佑 : 新しい薄膜金属フィルタを用いた油中水分センサ (平成 25 年度 東京工業大学修士論文)
- 147) Y. He, J. Fu, and Y. Zhao, "Oblique angle deposition and its applications in plasmonics", *Front. Phys.*, **9**, (2014), 47-59
- 148) Y. Shim, V. Borovikov, and J. G. Amar, "Effects of shadowing and steering in oblique-incidence metal (100) epitaxial growth", *Physical Review*, **77**, (2008), 1-13
- 149) P. Nuchuary, T. Chaikereee, N. Kasayapanand, N. Mungkung, S. Arunrungrusmi, M. Horprathum, P. Eiamchai, S. Limwichean, V. Patthanasettakul, N. Nuntawong, C. Oros, S. Denchitcharoen, B. Samransuksamer, and P. Chindaudom, "Preparation and Characterization of ITO Nanostructure by Oblique Angle Deposition", *Materials Today*, **4**, (2017), 6284-6288
- 150) C. Gruener, S. Liedtke, J. Bauer, S. G. Mayr, and Bernd Rauschenbach, "Morphology of Thin Films Formed by Oblique Physical Vapor Deposition", *ACS Appl. Nano Mater.*, **1**, (2018), 1370-1376
- 151) K. M. A. Sobahan, Y. J. Park, J. J. Kim, Y. S. Shin, J. B. Kim, and C. K. Hwangbo, "Nanostructured optical thin films fabricated by oblique angle deposition", *Adv. Nat. Sci.*, **1**, (2010), 1-6
- 152) Z. Cao : Thin film growth—Physics, materials science and applications—, (2011, Woodhead Publishing)
- 153) A. Zribi and J. Fortin : Functional Thin Films and Nanostructures for Sensors, (2009, Springer)
- 154) H. Kwon, S. H. Lee, and J. K. Kim, "Three-Dimensional Metal-Oxide Nanohelix Arrays Fabricated by Oblique Angle Deposition: Fabrication, Properties, and Applications", *Nanoscale Research Letters*, (2015), 1-12
- 155) J. L. Plawsky, J. K. Kim, and E. F. Schubert, "Engineered nanoporous and nanostructured

- films”, *Materials Today*, **12**, (2009), 36-45
- 156)小原田一真, 安田光伸: 樹脂膜/金属間の接着力発現メカニズム解析, (2013, 東レリサーチセンター)

Acknowledgments

I would like to state that I have great pleasure to complete the doctoral thesis. I am immensely grateful to my faculty at the Graduate School of Micro-Nano Systems Engineering of Nagoya University, Professor Seiichi Hata, Associate Professor Junpei Sakurai, Assistant Professor Mizue Mizoshiri, and Assistant Professor Chiemi Oka. Without their support, collaboration and guidance, my doctoral research would not have been the same.

Especially, I am deeply grateful to Professor Seiichi Hata and Associate Professor Junpei Sakurai. I received generous support and tips for living a life. Advices given by them have been a great help in planning my life. I felt encouraged and I will work harder in future and put my full efforts to next project.

In addition, I would like to acknowledge Professor Kazuhiro Kitamura from Aichi University of Education, Professor Kenji Fukuzawa and Senior Lecturer Yuhki Toku from the Graduate School of Nagoya University for comments on earlier version of this thesis. Their useful and insightful comments helped me to brush up my thesis.

Furthermore, I would also like to acknowledge with much appreciation with Nabtesco Inc. staff of Mr. Tsutomu Takahashi, Mr. Takashi Mizoguchi, and Mr. Nobuyuki Mukai, who gave the technical supports and the permission to use required equipment to complete the sensor evaluation.

A special thanks goes to secretary, Ms. Yumiko Hasebe, who helped me to coordinate my office work and travelling overseas. Without her support, my daily tasks would not have been smoothly achieved.

I gratefully express my deepest appreciation to all past and present members of our laboratory. I had a great time here for three and a half years, and never forget the moments. A special gratitude I give to Mr. Yuuki Fukagawa, whose contribution, really helped me to achieve my research goals. I have to appreciate the guidance given by other supervisor as well as the panels especially in my project presentation that has improved my presentation skills thanks to their comment and advices.

Last but not least, many thanks go to my family, friends in Japan and Germany. Professor Frank Altrock was my anchor, and I would like to offer my special thanks to you (Vielen Dank für Ihre damalige Hilfe in Deutschland, und dank Ihres ineren Haltes konnte ich meine Doktorarbeit erzielen! Irgendwann will ich unbedingt wieder nach Münster zurückkehlen:))

Thank you for everything,

17. 01. 2019

Yusuke Yoshii